Structural characterization and molecular modeling of the active aromatic polyamide layer in reverse-osmosis membranes

Xuefan Song

Thèse de doctorat

NNT : 2020UPASB024

Caractérisation de la structure et modélisation moléculaire de la couche active en polyamide aromatique des membranes d'osmose inverse

Structural characterization and molecular modeling of the active aromatic polyamide layer in reverse-osmosis membranes

Thèse de doctorat de l'Université Paris-Saclay

École doctorale n° 581, agriculture, alimentation, biologie, environnement et santé (ABIES)

Spécialité de doctorat : Génie des procédés

Unité de recherche : Université Paris-Saclay, INRAE, AgroParisTech, UMR 0782 Paris-Saclay Food and Bioproduct Engineering research unit, 91744, Massy, France.

Référent : AgroParisTech

Thèse présentée et soutenue à Paris-Saclay, le 16 décembre 2020, par

Xuefan SONG

Composition du Jury

Violaine ATHÈS Professeur, AgroParisTech	Présidente
Anthony SZYMCZYK Professeur, Université de Rennes 1	Rapporteur & Examinateur
Emeric BOURASSEAU Chercheur sénior, CEA-IRESNE	Rapporteur & Examinateur
Cyrille SOLLOGOUB Professeur, Le CNAM	Examinateur
Estelle COUALLIER Chargée de recherche, CNRS, Université de Nantes	Examinatrice

Direction de la thèse

Claire FARGUES Maître de conférences, Université Paris-Saclay	Directrice de thèse
Bernard ROUSSEAU Directeur de recherche, CNRS-Inst. Chimie Physique	Co-Directeur & Examinateur
Wafa GUIGA Maître de conférences, Le CNAM	Co-Encadrante & Examinatrice

To my lovely family.

Acknowledgements

Firstly, I would like to express my gratitude to my supervisor M. Bernard Rousseau, who guided me along my PhD course, providing invaluable suggestions to help me through the difficulties in research.

I would also like to thank all the members in the group ThéoSim, for their warm welcome and kindness. I am grateful to Mme. Carine Clavaguéra, who is always caring and helpful.

I would like to thank Mme. Claire Fargues and Mme. Wafa Guiga for their company and help during three years. I would also like to thank M. Jean-Marie Teuler and Jehan Waeytens, who offered important aid for the advancement of my project. I would also like to thank the committee and jury members of my project, their review of my work and advice has been instructive.

I would like to address my thanks to the École doctoral ABIES: M. Alexandre Pery, M. Pierre Larraufie, Mme. Corinne Fiers and Mme. Christine Duvaux-Ponter, who have offered me countless help during my PhD course.

I would like to express my gratitude to Mme. Martine Decloux and M. Pierre Giampaoli, who provided me a lot of help and encouragement during my Master course, from who I was first inspired and decided to pursue research.

Credit goes to my colleagues Hai, Francesco, Céline, Karwan and Jessica, for their support and company that made my stay in the lab smooth and joyful.

I am indebted to my friends and my family, who give me unconditional love, support, and understanding.

Contents

List of Figures

List of Tables

Abbreviaiton

List of symbols

a	number of trimesoyl chloride (TMC) unit of the new set of aromatic polyamide chemical units
a_n	constant in torsion energy function
$\vec{a_i}$	acceleration of atom i
a_w	water activity
$acc(o \rightarrow n)$	acceptance probability of a move from an old configuration to a new one
A	a certain thermodynamic quantity
AFM	Atomic Force Microscopy
AFM-IR	Atomic Force Microscopy-based Infrared Spectroscopy
AOI	angle of incidence (°)
APA	aromatic polyamide
ATR-FTIR	attenuated total reflection Fourier transform infrared spectroscopy
Avg	average
b	number of m-phenylenediamine (MPD) unit of the new set of aromatic polyamide chemical units
BET	Brunauer-Emmett-Teller
c	number of hydroxyl terminal unit of the new set of aromatic polyamide chemical units
$\bar{c}$	parameter related to the water molecule energy difference between the first layer and higher layers
C	the carbon content (%)
C_{L}	Langmuir constant
C_{FH}	Flory-Huggins parameter
C_{P}	solute concentration in the solution at permeate side ($\mathrm{mol{\cdot}m^{-3}}$)
C_{R}	solute concentration in the solution at retentate side ($\mathrm{mol{\cdot}m^{-3}}$)
C_{w}	average water concentration in the active APA layer ($\mathrm{mol{\cdot}cm^{-3}}$)
Ccbla	carbon atom in carboxylic acid group
CPA2-ts	APA top-surface of CPA2 after dissection

CPA2-ots	original APA top-surface of CPA2 (undissolved)
CPA2-bs	APA back-surface of CPA2 after dissection
d	number of hydrogen terminal unit of the new set of aromatic polyamide chemical units
d_{areal}	areal density ($\text{g}\cdot\text{cm}^{-2}$)
d_{dense}	volumetric density of the dense regions of aromatic polyamide film ($\text{g}\cdot\text{cm}^{-3}$)
d_{typical}	typical width or diameter of ridges or chimney-like structures (μm)
$d_{\text{volumetric}}$	apparent volumetric density ($\text{g}\cdot\text{cm}^{-3}$)
d_{polymer}	dry density of the apparent film
d_{water}	density of water
D	solute diffusion coefficient in membrane ($\text{m}^2\cdot\text{s}^{-1}$)
D_{w}	water diffusion coefficient ($\text{m}^2\cdot\text{s}^{-1}$)
DMF	N,N-dimethylformamide
DVS	Dynamic Vapor Sorption
e	charge of electron
eq	equilibrium state
E	total energy
E_{ad}	adsorption energy (J)
E_1	sorption heat on the first layer (J)
E_{l}	heat of liquefaction (J)
EMA	effective-medium approximation
f	parameter measuring the difference between the chemical potential of molecules in the second absorption layer and in pure liquid state
f_{ac}	connection degree of acyl groups
f_{am}	connection degree of amine groups
f_{ij}	factor determining the way to apply the intermolecular interactions for two atoms (i and j) in an intramolecular case
f_{scale}	factor for scaling
f_{void}	void fraction of the apparent aromatic polyamide film
$\vec{F}_i$	sum of forces acting upon atom i
FE-SEM	Field Emission Scanning Electron Microscopy
FTIR	Fourier transform infrared spectroscopy
F-C	fully-crosslinked structure
F-L	fully-linear structure
G_{11}	cluster function

GAB	Guggenheim-Anderson-De Boer
$\vec{g_i}$	gradient of potential energy of system state i
$g_{\alpha\beta}(r)$	partial pair distribution function of particle α and β at distance r
h	size of sample block
$\boldsymbol{i}$	imaginary unit
iso	pressure control in an isothermal-isobaric ensemble is performed isotropically
$iso-stress$	pressure control in an isothermal-isobaric ensemble is performed anisotropically
I	infrared absorption density
Inter	intermolecular
Intra	intramolecular
IP	interfacial polymerization
IR	infrared
IUPAC	International Union of Pure and Applied Chemistry
J_{s}	solute flux ($\mathrm{mol{\cdot}m^{-2}{\cdot}s^{-1}}$)
J_{w}	water flux
k	absorption index
k_{B}	Boltzmann constant ($1.38{\times}10^{-23}$ $\mathrm{J{\cdot}K^{-1}}$)
k_{film}	absorption index of the apparent aromatic polyamide film (=0)
K	solute partition coefficient between membrane material and solution
K_r	constant in bond stretching energy function
K_θ	constant in angle bending energy function
K_ϕ	constant in improper torsion energy function
L	wet thickness of the film
L_0	dry thickness of the film
m	mass (g)
m_i	mass of atom i
m_{polymer}	dry polymer mass
m_{water}	water mass uptake at a certain water activity
$M(t)$	total dipolar moment-time signal of the system
$\mathrm{M_{num-avg}}$	average molecular number in one simulation polymer box
$\mathrm{M_{size-avg}}$	average molecular size (average atom number in one molecule) in one simulation polymer box
MCS	mean cluster size
MD	molecular dynamics
MPD	m-phenylenediamine

MRD	mean relative percentage deviation modulus
MW	molecular weight of water (18.01528 g· mol^{-1})
n	refractive index
n_{ad}	number density of the adsorbed molecules
n_{film}	refractive index of the apparent aromatic polyamide film
n_h	number of sample blocks, each sample block is of size h
n_{polymer}	refractive index of pure dense aromatic polyamide polymer
$n_{\mathrm{void,air}}$	refractive index of void (or air) (=1)
n_{CONH}	number of amide bonds
n_{COOH}	number of acyl groups
$n_{\mathrm{NH_2}}$	number of amine groups
N	nitrogen content (%)
N	total number of atom, particle or sample
N_A	Avogadro's number
$N_c(R)$	coordination number of particle in the sphere of radius R around the given particle
$N_{c\ \alpha_{(\beta)}}(R)$	coordination number of particle α around particle β
$N_{c\ \beta_{(\alpha)}}(R)$	coordination number of particle β around particle α
N_f	degrees of freedom of the system (= 3N−3)
N_i	independent sample number
N_x	number of points in X dimensions of a target area
N_y	number of points in Y dimensions of a target area
N_α	total number of particle α
N_β	total number of particle β
Namd	nitrogen atom in amide bond
Namn	nitrogen atom in amine group
NF	nanofiltration
O	oxygen content (%)
Oamd	oxygen atom in amide bond
OPLS-AA	The optimized potential for liquid state - all atoms, force filed
p	water vapor pressure
p_0	water saturation vapor pressure
p_{β_α}	pair number of particles β-α at the distance r from particle α
P	pressure
P_{xx}	pressure tensor element in X direction
P_{yy}	pressure tensor element in Y direction

P_{zz}	pressure tensor element in Z direction
PALS	Positron Annihilation Lifetime Spectroscopy
PBC	periodic boundary conditions
PES	polyethersulfone
PSf	polysulfone
PVA	poly vinyl alcohol
q	charge in electron charge unit
Q	fictitious mass of the extra degree of freedom (a time scale parameter for the fluctuation)
QCM	quartz crystal microbalance
r	bond length or distance between two non-bonded atoms
r^N	a particular configuration point
$r_{[\mathrm{C-N}]\mathrm{min}}$	distance between the nearest carbon atom in carboxylic acid group and nitrogen atom in amine group in the present system
r_p	reflectivity of polarized light in plane
r_s	reflectivity of polarized light out of plane
$r_{m:t}$	ratio of m-phenylenediamine (MPD):trimesoyl chloride (TMC)
$\vec{r_i}$	position of atom i
r0.25	simulated APA system generated from initial MPD:TMC ratio at 0.25
$\mathrm{r0.25_{rep}}$	average value of 11 repetitions of simulated APA systems generated from initial MPD:TMC ratio at 0.25
r0.5	simulated APA system generated from initial MPD:TMC ratio at 0.5
r0.75	simulated APA system generated from initial MPD:TMC ratio at 0.75
r1	simulated APA system generated from initial MPD:TMC ratio at 1
r1.2	simulated APA system generated from initial MPD:TMC ratio at 1.2
r1.3	simulated APA system generated from initial MPD:TMC ratio at 1.3
r1.5	simulated APA system generated from initial MPD:TMC ratio at 1.5
$\mathrm{r1.5_{rep}}$	average value of 11 repetitions of simulated APA systems generated from initial MPD:TMC ratio at 1.5
r1.8	simulated APA system generated from initial MPD:TMC ratio at 1.8
r1.9	simulated APA system generated from initial MPD:TMC ratio at 1.9
r2.0	simulated APA system generated from initial MPD:TMC ratio at 2.0
r2.5	simulated APA system generated from initial MPD:TMC ratio at 2.5
r3	simulated APA system generated from initial MPD:TMC ratio at 3
r3.5	simulated APA system generated from initial MPD:TMC ratio at 3.5

r4	simulated APA system generated from initial MPD:TMC ratio at 4
r5	simulated APA system generated from initial MPD:TMC ratio at 5
$r5_{rep}$	average value of 11 repetitions of simulated APA systems generated from initial MPD:TMC ratio at 5
R	the ideal gas constant (8.314 $J{\cdot}K^{-1}{\cdot}mol^{-1}$)
R_c	cut-off distance
RBS	Rutherford backscattering spectrometry
RDF	the radial distribution function
RH	relative humidity (%)
RMSE	root-mean-square error
RO	reverse osmosis
s	statistical inefficiency
S	sulfur content (%)
S	film surface (cm^{-2})
S_q	root-mean-square roughness (nm)
$S_{q-\mathrm{AFM}}$	root-mean-square roughness measured by Atomic Force Microscopy (nm)
$S_{q-\mathrm{Pro}}$	root-mean-square roughness measured by profilometry (nm)
SEM	scanning electron microscopy
SPES	sulfonated polyethersulfone
SPSf	sulfonated polysulfone
STD	standard deviation
SW	swelling degree
Syn	synthesized sample
Syn -20°C	free-standing APA film synthesized at -20°C
Syn 0°C	free-standing APA film synthesized at 0°C
Syn 15°C	free-standing APA film synthesized at 15°C
Syn 29°C	free-standing APA film synthesized at 29°C
S.E.	standard error
t	time
T	temperature (K)
TEA	triethylamine
TEM	transmission electron microscopy
TFC	thin film composite
TMC	trimesoyl chloride

U	potential energy
U_{angle}	angle bending energy
U_{bond}	bond stretching energy
$U_{\text{electrostatic}}$	electrostatic (the Coulombic) energy
$U_{\text{improper torsion}}$	improper torsion energy (out-of-plane bending term)
$U_{\text{Lennard-Jones}}$	Lennard-Jones potential
U_{torsion}	torsion energy
$\vec{v_i}$	velocity of atom i
V_{film}	volume of the apparent film
V_{water}	volume of water
V_1	partial molar volume of water
w	frequency
w_{a_w}	water mass per dry polymer mass at a certain water activity
w_i	experimental value
w_{ip}	predicted value
w_m	water adsorption capacity as water mass per polymer mass when the first layer is saturated
X	X direction
X	crosslinked fraction of the conventional aromatic polyamide chemical structure hypothesis
$< \text{X} >$	average of the thermodynamic quantity X
$< \text{X} >_h$	average of the sample block with a size h of the thermodynamic quantity X
XPS	X-ray Photoelectron Spectra
Y	Y direction
Y	linear fraction of the conventional aromatic polyamide chemical structure hypothesis
Z	Z direction
Z_{ij}	height profile of point at position i and j respectively in X and Y directions

Greek letters

α	angle or particle
β	torsion angle or particle
β'	reciprocal temperature ($1/k_{\mathrm{B}}T$)
γ_i	scalar constant
γ	water adsorption site number per gram of polymer
δ	membrane thickness
δ_{AFM}	average film thickness measured by Atomic Force Microscopy
δ_{base}	base thickness
δ_{Pro}	average film thickness measured by profilometry
Δ	phase shift
Δt	integration time step
ϵ_0	absolute dielectric permittivity of classical vacuum
ε	depth of the Lennard-Jones potential well (kcal·mol^{-1})
θ	angle
κ	integer extend parameter
λ	wavelength (nm)
μ	average height of a target area
μ_{wafer}	average height of blank wafer
μ_{film}	average height of film region on avoiding the edge
ξ	thermodynamic friction coefficient
ρ	probability density
ρ_β	bulk density of particle β
$\rho_{\beta_\alpha}(r)$	local density of particle β around α at distance r
σ	distance at which the Lennard-Jones potential is zero (Å)
$\boldsymbol{\sigma}$	standard deviation
$\boldsymbol{\sigma_h}$	block variance
ϕ_1	water volume fraction (%)
ϕ_2	polymer volume fraction (%)
χ	conventional descriptor of crosslinking degree
ψ	amplitude component
Ψ	virial

Résumé

Les membranes d'osmose inverse (OI) sont des membranes composites, dont la couche active de surface, directement responsable des performances de rétention, est en polyamide aromatique réticulé (PAA, épaisseur ∼200 nm), polymérisé sur un support poreux en polysulfone lui-même déposé sur une couche en polyester non tissé. L'osmose inverse est un procédé de plus en plus utilisé pour le traitement des effluents industriels mais le comportement des petits solutés organiques neutres reste difficile à prédire. Ce travail combine une approche expérimentale de caractérisation structurale de ce polymère avec une approche par modélisation moléculaire, afin d'améliorer la compréhension des phénomènes à l'échelle moléculaire.

Nous avons étudié une membrane commerciale (CPA2) ainsi que des films auto-supportés, synthétisés au laboratoire à différentes températures du solvant organique (-20 °C, 0 °C, 15 °C et 29 °C). Leurs propriétés structurales (morphologie, topologie, épaisseur, rugosité, fraction de vide, densité apparente, densité de la phase dense et structure chimique) ont été analysées par différentes techniques comme la Microscopie Electronique à Balayage, la Microscopie à Force Atomique (AFM), la profilométrie, l'ellipsométrie, la sorption dynamique de vapeur, la spectrométrie photo-électronique X et la spectroscopie AFM à Infra-Rouge. Les deux familles de films sont constituées d'une base dense sur laquelle se trouve : une structure de type "crête-et-vallée" pour la CPA2 ; une structure avec des motifs "cheminées" pour les échantillons synthétisés. L'épaisseur moyenne et la taille des cheminées augmentent avec la température. A partir d'un taux de vide moyen de 35% et d'une densité apparente de 0,81 g·cm^{-3} obtenus pour le PAA de la CPA2, on calcule pour sa phase dense une densité de 1,25 g·cm^{-3} pour le polymère sec, et de 1,48 g·cm^{-3} quand il est humide, ce qui représente une des très rares déterminations expérimentales pour le PAA dense d'une membrane commerciale. De nouveaux descripteurs ont été utilisés pour étudier le taux de réticulation de ce polymère. Dans le cas de la CPA2, ils permettent de déceler une hétérogénéité chimique dans l'épaisseur. Le film synthétisé à -20 °C présente un taux de prise en eau important de 65 % à 91 %HR, ce qui pourrait être attribué aux nombreuses petites "cheminées" en surface.

Plusieurs constructions tout-atome du PAA ont été réalisées en créant des liaisons amides entre le chlorure de trimesoyle (TMC) et le *m*-phenylènediamine (MPD), pour des rapports initiaux en monomères variant entre 0,25 et 5. On souhaite mimer ainsi les hétérogénéités de composition dans les membranes et comprendre l'influence des concentrations initiales en réactifs sur la structure du film. Plusieurs étapes de modélisation ont été nécessaires pour atteindre l'équilibre, en particulier une longue simulation (plusieurs microsecondes) à

tenseur de pression et température constantes. La composition en monomères dans les structures construites varie entre 0,68 et 2,61, correspondant à des fractions de groupements acyl/amine ayant réagi, respectivement de 0,45/1,0 à 0,99/0,57. Ces résultats sont cohérents avec les structures de films de PAA expérimentaux. La densité moyenne des boîtes de simulation est pratiquement indépendante du détail de la structure, de l'ordre de 1,26 g·cm^{-3}, en accord avec nos résultats sur la CPA2.

Des isothermes de sorption d'eau ont ensuite été réalisés pour l'ensemble des films expérimentaux et par Monte Carlo dans l'ensemble osmotique pour plusieurs matrices polymères simulées. A faible activité en eau, les résultats simulés sont cohérents avec ceux des films expérimentaux, validant ainsi l'ensemble de la méthodologie de modélisation. A forte activité en eau, la prise en eau est inférieure à celle observée expérimentalement. Ceci pourrait être attribué à la présence de "vides" dans les matériaux réels. Enfin, on note une quasi absence de gonflement en simulation, en accord avec nos résultats expérimentaux pour la CPA2.

Mots-clés : polyamide aromatique, caractérisation structurale, sorption d'eau, modélisation moléculaire

Abstract

Commercial reverse osmosis (RO) membranes typically consist of an active aromatic polyamide layer (APA, thickness ∼200 nm), polymerized on a porous polysulfone support, itself attached to a polyester backing fabric. RO membranes are widely used in industrial waste-water treatments and their performances are essentially dominated by the active APA layer. However, neutral organic molecules rejections and the corresponding transfer behaviors are difficult to predict. In this work, we combined experimental structural characterizations and molecular modeling investigations on APA films, in order to improve transfer understanding at molecular level. APA layer of commercial CPA2 RO membrane and a set of free-standing APA films synthesized at four organic solvent temperatures (-20°C, 0°C, 15°C and 29°C) were investigated. Their structural properties including the morphology, topology, thickness, roughness, void fraction, effective density, dense layer density and chemical structure were characterized via various techniques such as Field Emission Scanning Electron Microscopy (FE-SEM), Atomic Force Microscopy (AFM), Profilometry, Spectroscopic Ellipsometry, Dynamic water sorption (DVS), X-ray photoelectron spectra (XPS) and Atomic force microscopy-based infrared spectroscopy (AFM-IR). Both film types had a multi-level topological structure with a dense base upon which generates: a valley-ridge structure for CPA2 or a chimney-like structure for synthesized samples, for which thickness and chimneys size increased with temperature. Based on the obtained average void fraction of 35% and the apparent volumetric density of 0.81 g·cm^{-3}, the density of the dense regions of CPA2 APA layer was calculated at 1.25 g·cm^{-3} when dry and 1.48 g·cm^{-3} when hydrated. This completes the very few experimental density values found for the dense part of commercial APA films. With the help of a new set of chemical structure descriptors, the chemical depth-heterogeneity of CPA2 APA layer was investigated. The film synthesized at -20°C performed a remarkable water uptake of 65% at 91%RH, which might be attributed to its orderly distributed and small-size chimney morphology on top-surface. All-atoms molecular models of APA polymer were constructed by forming amide bonds between trimesoyl chloride (TMC) and *m*-phenylenediamine (MPD) with a set of initial MPD:TMC monomers ratios, varying from 0.25 to 5. The purposes were, on one hand, to mimic APA's possible depth-dependent heterogeneous structures with boxes of different cross-linking degrees; on the other hand, to understand the effect of different initial monomer proportions during the IP on APA film's structure. Several steps were necessary in order to obtain equilibrated samples, including a very long (several microseconds) constant stress and temperature molecular simulation. Final MPD:TMC (connected)

ratios ranging from 0.68 to 2.61 were observed, corresponding to systems with acyl/amine group connectivity degrees at 45%/100% or 99%/57%, respectively. These results were consistent with chemical structure evaluation of real APA films. A similar density around 1.26 g·cm^{-3} were observed for all systems, consistent with the experimental density of CPA2 APA.

Water sorption isotherms were computed using Monte Carlo method in osmotic ensemble for several simulated polymer matrixes and were obtained via DVS for experimental layers. At low water activity, water sorption behaviors of simulated polymers were in agreement with experimental data, validating the overall simulation methodology. At high water activity, water absorption was underestimated by molecular simulations. This could be attributed to the existence of void space in real APA films. No significant swelling was observed in simulations, which was in agreement with our experimental results for CPA2.

Key words: aromatic polyamide, structural characterization, water sorption, molecular modeling

General introduction

The membrane-based reverse osmosis (RO) process is widely applied in effluent treatment in various industrial fields, such as plating, textile, sugar and distillery industries[37, 49, 102], or in the removal of trace level of micro pollutants, such as pharmaceutical compounds[72, 73, 113] and pesticide residues[31, 79]. However its application is not well controlled in face of filtration of uncharged small organic solutes (molecular weight below 180 g·mol^{-1}). The rejections of these molecules are affected not only by molecular weight or size[8, 102, 125], but also by specific solute-membrane interactions such as hydrogen bonds or $\pi-\pi$ interactions[30, 44, 76], linked to solutes' as well as membranes' chemical properties. In previous studies in our laboratory, it was observed as well that the rejections of several organic molecules didn't follow the size-exclusion trend: 2,3-butanediol, butanoic acid and furfural have similar molecular masses, but their rejection degrees by aromatic polyamide (APA) based RO membranes were 100%, 80% and 40%, respectively[30, 102]. To take these phenomena into account, transfer of organic solutes through RO membranes is commonly represented by a solution-diffusion model[119]:

$$J_s = \frac{KD}{\delta}(C_R - C_P) \tag{1}$$

where J_s is the solute flux (mol·m^{-2}·s^{-1}), K is solute partition coefficient between membrane material and solution, D is solute diffusion coefficient in membrane (m^2·s^{-1}), C_R is solute concentration in the solution at retentate side (mol·m^{-3}), C_P is solute concentration in the solution at permeate side (mol·m^{-3}) and δ is membrane thickness (m). Based on above discussions, a good knowledge on the membrane's structure and hydration state is indispensable to well understand the transport mechanisms of neutral organic solutes through it.

The RO membrane typically consists of an aromatic polyamide skin layer (APA, thickness ∼200 nm) and two porous support layers, polysulfone (PSf, thickness ∼100 μm) and polyester (thickness ∼100 μm). The membrane performance is determined by the active APA layer, which exhibits a highly heterogeneous multi-level structure: a dense base with pores embedded in, upon which develops a void ridge-and-valley structure[91, 92, 124]. Moreover, some APA layers of commercial RO membranes might exhibit a depth-dependent heterogeneous chemical structure[17]. The dense regions, including the dense base and dense layers forming the ridge-and-valley structures, are believed to serve as the true selective barriers, determining the water and solutes' transport through the membrane. Nonetheless, the high heterogeneity and very thin thickness of the APA layer hinder applica-

tions of many characterization techniques. As a consequence, the APA layer's structure, such as thickness, void fraction, apparent density or chemical structure, still remains vaguely characterized. Moreover, the properties of the dense regions and the hydration of the apparent film are rarely studied.

The objective of this PhD project is to contribute to a detailed structural characterization of the APA layer and to provide supplementary information on its hydration properties, aiming to search for the structural properties-thermophysical properties relationships. Two approaches, experimental characterization and molecular modeling, were launched in parallel in order to give comprehensive understanding. The experimental approach gave insight into local structures of real APA films, which as well served as reference data to the molecular model building. Meanwhile, molecular modeling allowed of the design and characterizations of various APA structures, shedding light to structures-properties correlations at atomistic scale.

This thesis is divided into three chapters. In chapter 1, we present the experimental structural characterizations of the APA layer of commercial CPA2 RO membrane and a set of free-standing APA films synthesized at four organic solvent temperatures (-20°C, 0°C, 15°C and 29°C). Their structural properties including the morphology, topology, thickness, roughness, void fraction, apparent density, dense layer density and chemical structure were characterized via various techniques as Field Emission Scanning Electron Microscopy (FE-SEM), Atomic Force Microscopy (AFM), Profilometry, Spectroscopic Ellipsometry, Dynamic Vapor Sorption (DVS), X-ray Photoelectron Spectra (XPS) and Atomic Force Microscopy-based Infrared Spectroscopy (AFM-IR). The results from different techniques were compared in order to verify the reproducibility of the sample fabrication and to discuss and determine adaptable techniques for APA films' structural characterizations. The comparison of these various APA samples may help understand the influences of the presence of the support and synthesis temperature during the interfacial polymerization (IP) on the final structures and properties. The chemical structure characterization of APA films remains blurry in the literature due to the limited application of conventional crosslinking degree calculation. In face of such challenge, we also developed a new set of chemical structure descriptors, hence the chemical depth-heterogeneity of CPA2 APA layer was investigated.

In chapter 2, we report the design and structural characterizations of all-atoms molecular models of APA polymer. Taking APA layer's possible depth-dependent heterogeneous structure and various chemical structures of different APA layer types into account, we intended to construct a variety of molecular models by forming amide bonds between *m*-phenylenediamine (MPD) and trimesoyl chloride (TMC) with different initial MPD:TMC ratios, varying from 0.25 to 5. We also developed a polymer relaxation protocol, which allowed the strains, generated from the polymerization process, to be relaxed successively and also avoided unexpected box exploration. After a final relaxation stage in molecular dynamics *NPT iso-stress* (1 bar, 298.15 K) ensemble up to several μs, the molecular models' the local structures and thermophysical properties were examined. These models are supposed to represent the dense regions of real APA layers. Thereby, the obtained results not only gave insight into the properties of the true selective barriers (the dense regions), but also revealed the effect of different initial monomer portions during the IP on APA films' final structures. More importantly, they allowed

of the first systematical investigation on the structural properties-thermophysical properties correlations of APA polymer.

In the last chapter, we introduce the hydration of real APA films and APA molecular models. The water sorption isotherms of real APA films were obtained at a range of water activity varying from 0 to 0.9 at 20°C via Dynamic Vapor Sorption equipment, complementing the few available water sorption data base of uncoated APA films. Water molecules were inserted into three typical APA molecular models, polymerized from initial MPD:TMC ratios at 0.25, 1.5 and 5, using Monte Carlo method in osmotic ensemble at a range of water activity varying from 0 to 0.99 at 25 °C. We selected these three systems with similar initial dry densities but various chemical structures, expecting to compare the affinity of different chemical groups to water molecules. Besides, the water cluster formation in real APA films was investigated. The results of water sorption isotherms, together with the swelling and water mass uptakes, of real APA films and APA molecular models were compared. On the basis of a good knowledge of APA systems' topological and chemical structures (particularly for APA molecular models), the structural properties-water sorption behaviors correlations were revealed.

Xuefan Song was supported by the doctoral school Agriculture, alimentation, biologie, environnment et santé (ABIES) through finances from AgroParisTech acting as her employer. This PhD project was based on the collaboration between the team ProBioSSep at UMR 0782 Paris-Saclay Food and Bioproduct Engineering and the team ThéoSim at Institut de Chimie Physique (ICP, UMR 8000). The ensemble of this project was realized under partnerships with different research teams or laboratories. The syntheses of APA films were realized with the help of Mme. Anne Jonquières at Laboratoire de Chimie Physique Macromoléculaire, INPL, Nancy; AFM-IR analysis was carried out with the help of M. Alexandre Dazzi and Jehan Waeytens in the team BioPhysique at ICP; analyses of Profilometry, FE-SEM and Ellipsometry were realized with the help of M. Raphaël Weil, M. Zhizhong Li, M. Frédéric Restagno and Marion Grzelka at Laboratoire de Physique des Solides, Université Paris-Saclay; XPS analysis was carried out with the help of Mme. Diana Dragoe at Institut de Chimie Moléculaire et des Matériaux d'Orsay, Université Paris-Saclay.

Chapter 1

Experimental structural characterization of aromatic polyamide films

1.1 State of the Art

1.1.1 General introduction on RO membrane and its application

In recent years, about two-thirds of world population are already subjected to the water scarcity[81]. Water scarcity has become a worldwide issue since the late of 20th century due to various factors as climate change, population growth[117], inadequate socio-economic investment and governance[38]. Consequently, water management plays a crucial role in developing a sustainable society. In face of such concern, different physical-chemical treatments allow to purify and reuse water. Among them, membrane-based treatments and especially reverse osmosis (RO) are extensively used for pure water production and industrial waste-water treatment, thanks to advantages such as continuous process, easy scaling-up[109], relatively low energy cost compared to thermal processes such as distillation[104] and low chemical requirement[2]. RO occupies more than 50% of seawater global desalination plants[104]. It is also implemented for the treatment of effluents of various industrial fields, in order to achieve water reuse. For example, in plating industry, it is used to remove mixed chromic acid to produce rinsing water of high quality[37]; in textile industry it is applied for water reclamation[49]; in beet sugar and distillery industry, it is studied for the removal of small organic solutes from distillery condensates, to be reused as dilution water into the fermentation step[102]. Its broad applicability in industrial waste-water treatment also includes the removal of trace levels of micro pollutants, such as pharmaceutical compounds[72, 73, 113] and pesticide residues[31, 79]. Nonetheless, there remain still membrane performance challenges in some aspects. For example, RO removal performances of uncharged organic solutes with low molecular weights (below 180 g/mol) and transfer mechanisms appear difficult to predict.

Commercial RO membranes typically consist of an active aromatic polyamide layer (APA, thickness ∼200 nm), a porous polysulfone (PSf, thickness ∼100 μm) support, which afterwards is attached to a polyester

backing fabric (thickness ∼100 μm). The membrane performances are essentially dominated by the active APA layer. Previous studies has demonstrated water flux was attributed to APA layer's hydrophilicity [62, 100], thickness[62], void state[20, 62] and density [20]. With respect to solutes transfer such as organic molecules, their rejections were effected not only by molecular weight or size[8, 102, 125], but also by specific solute-membrane interactions such as hydrogen bonds or $\pi - \pi$ interactions[30, 44, 76], linked to solutes' as well as membranes' chemical properties. In order to explain such complex phenomena, transfer of organic solutes through the APA layer is commonly represented by a solution-diffusion model even though electrostatic interactions can be significant when the membrane and the solutes are charged, which assumes that the solutes firstly dissolve into the membrane matrix before diffusing through it[119]. Hence, a good knowledge of the structural properties turns out essential, upon which the membrane's structures-thermophysical properties correlations and solvent-membrane or solute-membrane interactions could be further revealed.

Up to date, in order to develop a more controlled synthetic pathway and optimize the membrane performance, remarkable efforts have been given to fabricate novel APA thin film composite membranes under different synthesis conditions[20, 32, 43, 55, 56, 59, 61, 95, 96, 100, 123]. Meanwhile, considerable quantity of structural characterizations on APA films of both commercial and laboratory synthesized membranes have been implemented[17, 25, 35, 63, 67, 74, 75, 114, 115, 124]. These studies are of great importance, which shed light to APA layer's formation mechanism and basic structures, offering a solid base for advancing the understanding of solvent/solute transfer mechanism through the membrane.

In following sections, the commercial and synthesized APA layer's formation (fabrication) pathways, including conventional interfacial polymerization and free-standing interfacial polymerization, are introduced at first. Next, the current advancement on structural characterizations on the APA film's morphology and topology, thickness and roughness, density and chemical structures are reviewed progressively. Successively the current major questions are addressed. In the end, the objectives of this study are presented.

1.1.2 Conventional interfacial polymerization of APA film with support

Interfacial polymerization (IP) was firstly introduced by Mogan *et al.,* in 1959[85], based on which the first commercial thin film composite (TFC) was invented in 1975. This film was generated from the interfacial polymerization between polyepiamine and isophthaloyl chloride for a military RO purification use[99]. Then it was replaced by the first commercial fully aromatic polyamide RO membrane, which was successively generated from similar concept, as a thin selective APA layer was deposited on a porous polysulfone (PSf) support layer in 1980[14]. The fabrication process of conventional interfacial polymerization for a typical commercial APA RO membrane is presented in figure 1.1, image from Park *et al.,* (2017)[94].

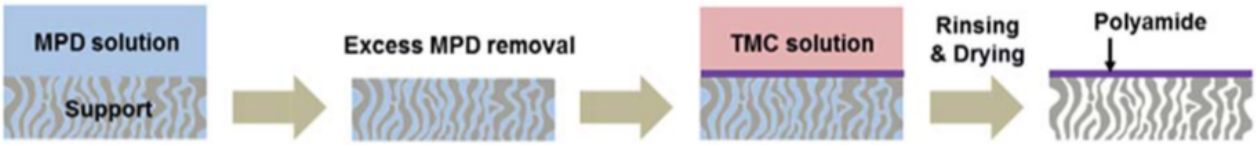

Figure 1.1: Schematic illustration of the fabrication of APA TFC membranes via conventional IP, from Park *et al.,* (2017)[94].

The interfacial polymerization occurred between trimesoyl chloride (TMC) and *m*-phenylenediamine (MPD). TMC is dissolved in organic solution while MPD in an aqueous solution. Then a PSf porous support layer is firstly immersed in the MPD aqueous solution until saturated with MPD solution. After removing excess MPD, it was brought to contact (by immersing it into TMC organic solution or by pouring TMC organic solution upon its surface). Since the two solutions are immiscible, the APA layer only grows at the interface region, and finally forms on the support's surface. In addition, treatments such as curing at high temperature could be implemented afterwards [96, 123].

Despite the wide application of the RO commercial membranes, studies were performed to optimize the IP process with presence of support. Ghosh *et al.,* (2008) illustrated that the diffusivity and solubility of MPD, which was related to organic solvent's temperature and type, influenced the film's water permeability and crosslinking state. They observed a thinner and more crosslinked membrane performed a higher water permeation[43]. Qiu *et al.,* (2009) synthesized the APA TFC with presence of PSf support by modifying the monomer concentrations (1∼2.4 wt% for MPD and 0.05∼ 0.3 wt% for TMC) and proportions (MPD:TMC ranging from 5.3 to 40). The authors demonstrated that variation of TMC concentration dominated the final film properties. Moreover, they highlighted that addition of isopropyl alcohol enhanced the water flux, which was probably explained by a direct modification of film's physicochemical properties during the synthesis[98]. Similar study was launched by Xu *et al.,* 2017[123], the authors demonstrated that the monomer concentration and molar ratio would affect the APA layer's morphology and thickness, which further impacted the membrane performance.

Khorshidi *et al.,* (2015) synthesized APA films on a polyethersulfone support at a range of temperatures of organic phase varying between -20°C and 50°C. The authors observed decreasing thickness and surface roughness, increasing crosslinking degree and better water permeation as a function of decreasing synthesis temperature. They explained the IP progressed under two competitive processes, the reaction between reactive acyl chloride and amine groups, and the hydrolysis of acyl chloride into unreactive acyl acid, which together resulted in a higher crosslinking state for film at -20°C[61]. On the contrary, Ghosh *et al.,* (2008)[43] investigated the organic phase temperatures varying from 8°C to 38°C and demonstrated a better water permeation at higher temperature. Moreover, studies also demonstrated the chemistry and structure of the support layer, such as hydrophilicity, porosity and pore size, affected the polymerized APA film's morphology and performance[41, 108].

1.1.3 Free-standing interfacial polymerization of APA film

Although the conventional polymerization with support generates APA TFC membranes with promising performance, it remains difficult to correlate systematically and directly the APA layer's structural properties to the membrane's thermophysical properties and performance, as the presence of support normally dominates various characterization techniques. The isolation of APA layer is usually required, but the effect of the support layer dissection on the APA is not fully studied. Meanwhile, as aforementioned, the membranes fabricated via a conventional IP were reported to be strongly dependent to physical-chemical properties of PSf support layer[41, 108], which might be an origin for creating the heterogeneous structures of APA layers. To overcome these challenges, several studies have proposed the fabrication of free-standing APA layer via direct IP between TMC organic and MPD aqueous phases [15, 20, 55, 56, 95, 100]. A schematic of the direct IP at free aqueous-organic interface is presented in fig.1.2. It is notable that, on adhesion to a support layer, these free-standing films performed even better water/solvent permeation with the same solutes rejection than conventional APA films synthesized with support or commercial RO membrane[55, 95]. Some studies also proposed to fabricate free-standing APA films with the utilization of sacrificial support[32, 59], for which the synthesis mechanisms varied from that of the above studies considering the presence of the sacrificial support.

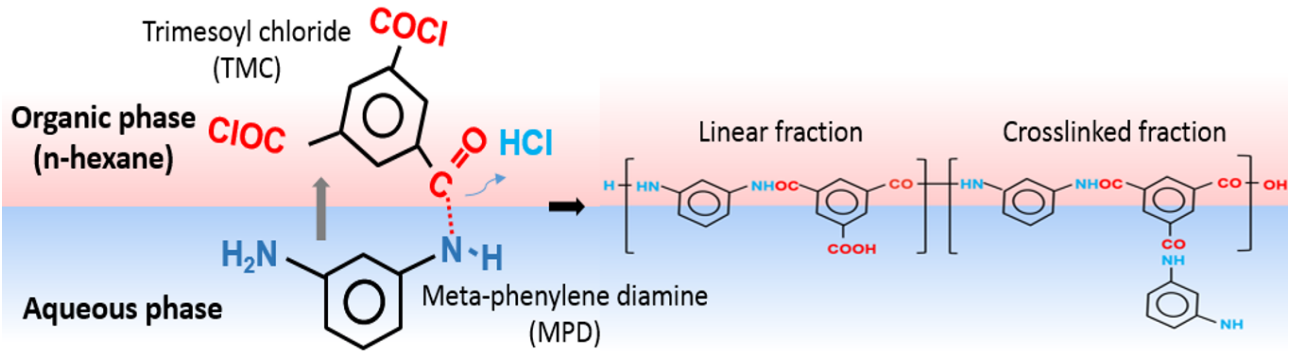

Figure 1.2: Schematic illustration of the fabrication of free-standing APA film via direct IP at free aqueous-organic interface.

Similar to the conventional IP, synthesis parameters of free-standing IP, such as monomer ratios and concentrations, reaction time, have been proven crucial to modify the APA film's properties. Based on Fourier transform infrared spectroscopy analysis, Jin *et al.,* (2009) found the chemical structure of the membrane could be modified by changing the synthesis conditions which directed affected the MPD diffusion. As reported, the film chemically exhibited more acyl groups with a higher TMC or lower MPD concentration, or longer reaction time and lower temperature[56]. Similarly, Dutta (2003) has observed an enhancement of vibration $-NH_2$ or $-COOH$ for system with high or low MPD:TMC molar ratio respectively[26]. Chai *et al.,* (1994) reported the film thickness was slightly increased with increasing TMC concentration at a fixed MPD concentration, but such effect was not observed by changing MPD concentration[15]. Dennison *et al.,* (2018) revealed an increase of film density and elastic constant with raising monomer concentration while maintaining the monomer proportion[20].

As mentioned previously, significant temperature effect on film's crosslinking state has been reported in conventional IP with a temperature variation ranging from -20°C to 50°C[61]. During IP, the reaction is governed by MPD diffusion from the aqueous phase into the organic phase. Since there exists no presence of support in free-standing IP, MPD diffusion is supposed to be no longer hindered by the support. Hence synthesis temperature is likely to play a more important role in free-standing IP than in the supported one. To our knowledge, the synthesis temperature effect in free-standing IP was only studied by Jin *et al.,* (2009)[56] up to date, where the temperatures was varied from 35°C to 65°C. It was revealed that a higher temperature led to a lower acyl group content. It should be noted this temperature range was smaller than that used by Khorshidi *et al.,* (2015). Hence more investigations are still interesting to enhance and understand the synthesis temperature effect during the free-standing IP.

1.1.4 Structural characterization advancement on APA films

1.1.4.1 Morphology and topology

In light of previous studies, the morphology of APA layer was reported to be closely correlated with membrane performance as salt rejection[42]. Several techniques such as scanning electron microscopy (SEM) or field emission scanning electron microscopy (FE-SEM), transmission electron microscopy (TEM) and atomic force microscopy (AFM)[63] are capable to illustrate the morphological structures [43, 48, 63, 67, 91, 92, 114, 124]. APA films exhibited highly heterogeneous morphological structures. For typical APA active layers of commercial RO membranes (synthesized with support) or of laboratory-made TFC from conventional IP, they were revealed to exhibit a similar typical ridge-and-valley structure on the top-surface, while the back-surface was flat and embed with pores. An example of top- and back-surface morphology of active APA layer of ESPA2 RO membrane is presented in fig.1.3, image from Yan *et al.,* (2015)[124].

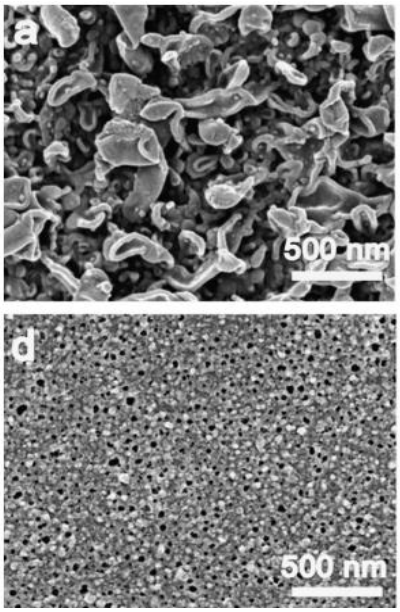

Figure 1.3: SEM images of (a) top- and (d) back-surface of active APA layer of ESPA2 RO membrane, from Yan *et al.,* (2015)[124].

The pores were supposed to allow of the migration of MPD in view of the formation of barrier layer at the interface[13], or they might arise from the presence of water drops at the interface, which re-established the organic-aqueous interface at the drop edge[54].

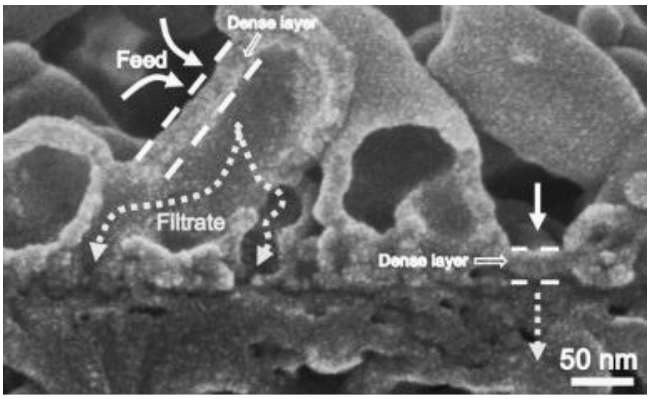

Figure 1.4: SEM cross-section image of active APA layer of ESPA2 RO membrane, cutting lines show the position of a dense layer and dotted lines show passages for filtrate to go through under pressure, from Yan *et al.,* (2015)[124].

Based on SEM and TEM cross-section images[91, 92, 124], this typical ridge-and-valley structure was proven to not be solid, but as a exterior dense layer forming void cavities. An example of SEM cross-section image of active APA layer of ESPA2 RO membrane is presented in fig.1.4, image from Yan *et al.,* (2015)[124]. What is clearly shown in this SEM cross-section image is that for active APA layer of ESPA2, the pores observed in the back-surface in fig.1.3 were supposed to be connected with the larger void cavity of the ridge-and-valley structures of the top-surface. The authors suggested the dense layer forming the cavity served as the selective barrier during the filtration. Once filtrates enter the dense layer, they diffused out of the APA through the

connected cavities and pores. It should be addressed such a cavity-pore connection structure has not been clearly identified for other RO membranes to our knowledge. On the other hand, a dense bottom, embed with pores, of a thickness around 20 nm was identified in fig.1.4, upon which developed the ridge-and-valley structure. Similar dense bottom was also reported for APA active layer of ESPA3 via TEM cross-section image[91]. It should be noted the above ESPA2 and ESPA3 are fabricated by Hydranautics, the same manufacturer as for the commercial RO membrane sample investigated in our study (CPA2).

In addition, since APA layers of RO membrane were revealed to exhibit a void nature as presented in fig.1.4, efforts have been contributed for an estimation of the void fraction. In a recent study, the APA layers of RO membranes XLE, ESPA3 and SWC4+ were reported to have a void fraction varying from 15 to 32% by applying and comparing various analyses such as TEM cross-section image, ellipsometry and water uptake by quartz crystal microbalance (QCM)[75]. Meanwhile, the voids were supposed to be not uniform as well given the high film heterogeneity. Previous Positron Annihilation Lifetime Spectroscopy (PALS) analysis showed that APA layer of FT30 RO membrane performed a bimodal distribution of void radii, around 2.1-2.4Å and 3.5-4.5 Å, which were supposed to represent the size of void space between intra-molecular chain segments and between nodule aggregates respectively [63].

With respect to free-standing samples, various morphological structures have been reported. Dennison *et al.,* (2018) observed compacting protrusions spreading on a flat top-surface, and noted the protrusions increased with monomer concentration[20]; Jin *et al.,* (2009) described their films' top-surfaces as a 'coarse surface with large holes exposed', and the back-surface as 'smooth, dense and porous'[56]; According to SEM images obtained by Cui *et al.,* (2017), chimney-like structures spreading on flat top-surfaces were observed, the size for which varied according to monomer concentration, while the back-surfaces were generally dense[18]. Typical FE-SEM/SEM images of these samples were presented in fig.1.5. The morphological variation might be attributed to significant differences of synthesis parameters such as temperature and time.

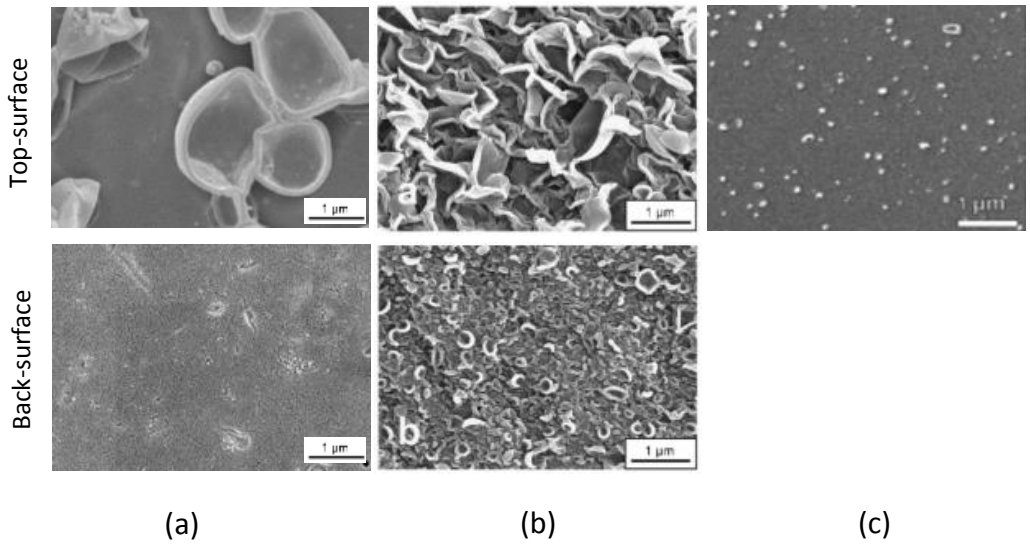

Figure 1.5: (a) FE-SEM images of top- and back- surface of free-standing IP film sample, 1 wt% MPD and 0.1 wt%TMC, from Cui *et al.,* (2017) [18]. (b) FE-SEM images of top- and back- surface of free-standing IP film sample, from Jin *et al.,* (2009)[56]. (c) SEM images of top-surface of free-standing IP film sample, 1 wt% MPD and 0.05 wt% TMC, from Dennison *et al.,* (2018)[20].

1.1.4.2 Thickness and roughness

AFM and profilometry detect directly the cross-section profiles, thus they are widely applied in the thickness and roughness characterization of APA films up to date [25, 34, 35, 60, 74, 93]. SEM and TEM cross-section image analyzes[74, 93, 107, 124], as well as spectroscopic ellipsometry[3, 20, 74], may give access to the thickness estimation of the APA layer, as well as to the void fraction it contains. Meanwhile, successful thickness estimations have also been reported by implementing other techniques such as combination of neutron and X-ray reflectivity analysis[32], or by recalculating the thickness from a pre-assumption on film density and an areal mass obtained by Rutherford backscattering spectrometry (RBS) or quartz crystal microbalance (QCM)[74].

According to previous studies, APA layers of commercial RO membranes exhibited a thickness ranging around 100 nm to 200 nm, meanwhile with a notable roughness ranging from 60 to 130 nm[74]. With respect to conventional and free-standing synthesized APA films, the thickness might be around sub-10 nm [20, 32, 59, 95] or up to 500 nm[56] according to different synthesis conditions. Exceptionally, an ultra-thick free-standing APA film was formed with a polymerization time up to 7 days, with film thickness more than 50μm, in order to investigate the bulk polymer's properties such as porosity formation[71].

Given the APA layer's thin and heterogeneous morphological feather (as presented in fig.1.4 and 1.5), an accurate thickness characterization remains challenging. A selection of a most adaptable thickness analysis method turned out crucial, as each of these techniques performs proper limits. AFM and profilometry demand the separation of the active layer, risking not completely eliminating of support layer or modifying the sample

morphological structure during the support dissection. The application of QCM or RBS requires supplementary density parameter, thus the confidence of result largely depends on the parameter accuracy. The SEM/TEM cross-section analyses are based on eye-estimation, while it should also underline that the possible existence of mechanical cutting would cause sample deformation (compression or folding), thus introducing analysis defaults. It has been reported that the SEM/TEM cross-section analyses only gave rough estimation compared to AFM, profilometry and ellipsometry[74]. Meanwhile, ellipsometry is very selective for the tested sample, as it requires the sample surface extremely flat. Studies have reported ellipsometry was not able to perform analysis (of thickness or other parameters such as refractive index) on the APA layer due to large roughness of the membranes investigated (ESPA1 and FT30)[8, 127].

The swelling degree is calculated as the ratio between the variation of initial and swelling thickness, and the initial thickness. Various swelling behaviors of APA layers were observed in the literature. For APA layer of SWC3 RO membrane, its swelling was reported too slight to be detected[70]. In other studies[25, 34], slight swelling of APA layers of RO membranes such as ESPA1, SWC1 and SWC4+ were reported around 3%∼14% via AFM analysis, but these analyses fell into the thickness analysis error. Meanwhile, the APA layer of XLE showed a significant swelling degree up to 53%. A high swelling degree up to 20% was also observed for a synthesized sub-10 nm thin APA film via neutron and X-ray reflectivity analysis[32]. On the basis of above analyses, it was supposed that the swelling behavior of APA layer depended largely to its proper structure, such as the crosslinking state or void fraction[25].

1.1.4.3 Density

To our knowledge, there existed only three experimental analyses on the density of APA layers of commercial RO membranes. Kotelyanskii *et al.,* (1998) reported the first hydrated density of APA layer of FT30 RO membrane at 1.38 g·cm^{-3} with a water content at 23% [66]. Based on this wet density value, a dry density was deduced around 1.06 g·cm^{-3} in later studies, with assumption that no swelling occurred when the film was hydrated [83, 127]. Zhang et *et al.,* (2010)[127] corrected the hydrated density of FT30 APA layer reported by Kotelyanskii as 1.24 g·cm^{-3} with a water content of 11.2 wt%, and the authors also reported a hydrated density of 1.22 g·cm^{-3} with a water content of 12.8 wt% for LF10 membrane. Meanwhile, it should note that these commercial layers are coated by poly vinyl alcohol (PVA). Recently, Lin *et al.,* (2016)[74] calculated dry densities of APA layers of ESPA3, XLE and the APA film's from the thickness results via ellipsometry and areal density reuslts via QCM. They observed these APA films performed with densities varying between 1 and 1.53 g·cm^{-3}. The authors also suggested these densities were not significantly different, and gave a representative average value at 1.26 g·cm^{-3}.

With respect to synthesized APA films, the reported apparent densities ranged between 0.59 to 2 g·cm^{-3} depending on synthesis conditions[20, 55, 59]. Studies of synthesized revealed the correlation between the synthesis conditions and the density. Karan *et al.,* (2015) observed the density increased from 0.59 to 1.44

along with extension of reaction time [59]. Dennison *et al.,* (2018) reported an about 20% density raise (from 1.1 to 1.3 g·cm^{-3}) when the monomer concentrations were doubled (from TMC 0.005wt% + MPD 0.1 wt% to TMC 0.1 wt% + MPD 2 wt%)[20]. Similar positive monomer concentration-density correlation was also observed by Jiang *et al.,* (2018). The authors reported an increasing density trend from 1.2 to 2.02 g·cm^{-3} with increasing monomer concentrations with a fixed molar ratio (from TMC 0.05wt% + MPD 0.025 wt% to TMC 3 wt% + MPD 0.15 wt%)[55]. In these above studies, the thickness and areal mass were all analyzed from AFM and QCM respectively. It should be addressed that a density more than 2 g·cm^{-3} for a APA structure based film remained questionable, compared to the density (1.45 g·cm^{-3}) of linear para-linked aromatic polyamide p-phenylene terephthalamide (Kevlar), which is supposed to be denser than APA film. This obtaining of unrealistic density value highlighted the difficulties for an accurate thickness characterization of the thin heterogeneous film with pronounced roughness and even question the notion of thickness for these films.

In addition, given the existence of notable void fraction in the APA layer, the dense regions (more precisely, the dense layer and dense bottom in fig.1.4 for example) are supposed to serve as the real selective barriers during the filtration [124]. As a consequence, the knowledge of the corresponding density allows of a better/deeper understanding of the water/solutes transfer mechanism through the membrane. Moreover, it provides very interesting information on the properties of the bulk APA polymer. The density of dense region could be deduced from the apparent density and void fraction. Nonetheless, to our knowledge, such an important information has not be reported by experimental studies up to date.

1.1.4.4 Chemical structure

The chemical structure of APA films is accessible via X-ray photoelectron spectra (XPS) or Rutherford backscattering spectrometry (RBS)[17, 114, 115]. These two techniques gave information on elemental composition, which were used to identify and distinguish APA layer by plotting nitrogen/oxygen element map[115] or to analyze the crosslinking state. For the latter, the chemical structure of APA film is considered as a combination of crosslinking and linear fractions. The crosslinking degree is defined as the corsslinking fraction. It could be deduced on the basis of two fractions' chemical formulas and elemental concentrations[1, 41, 51, 59, 62, 68]. Applying this descriptor, Kwak *et al.,*(2001) reported the FT-30 exhibited a crosslinking degree around 49%[68], and Kwon *et al.,*(2008) reported the APA layers of commercial LE and XLE RO membranes exhibited a higher crosslinking degree around 34% compared to that NF90 nanofiltration (NF) membrane at 25.6%. Besides, the crosslinking state of APA films synthesized at different conditions have been compared [51, 59, 62]. For example, Khorshidi *et al.,* (2016) addressed a more crosslinked structure with a lower synthesis temperature as mentioned previously[62]. It should be addressed that the successful application of this descriptor requires to neglect chain ends in APA structure. However, this assumption seems unrealistic for a real APA film, hence the application of such descriptor should be taken with caution.

During the synthesis, with the MPD diffusion, the MPD concentration declines, which may finally resulted

in a chemical composition deviation along the film thickness. Therefore, it is interesting to verify whether such depth-dependent chemical deviation exists. Since XPS is a highly surface sensitive (sampling depth $1 \sim 10$ nm) while RBS quantifies the volumetric elemental concentration, Coronell *et al.,* (2011) implemented the two techniques together to study the chemical heterogeneity of APA layers of several RO/NF membranes[17]. They finally claimed the existence of both homogeneous and heterogeneous chemical structures. In a later study, the chemical compositions of top- and back-surface of APA layer of SW30 RO membrane were investigated[70]. However, this result was not capable to demonstrate the heterogeneity of APA layer as SW30 is coated by PVA.

Besides, the chemical structure of the APA films can also be directly identified by analyzing typical chemical group vibrations via attenuated total reflection Fourier transform infrared spectroscopy (ATR-FTIR) or Fourier transform infrared spectroscopy (FTIR). By using these techniques, studies have confirmed the existence of coating layers (presence of intense peak of $-$OH and aliphatic $-$CH) of certain RO membranes [114, 115] and identified them as PVA in most cases. It also allowed to distinguish the chemical nature of the RO and NF membranes, as for semi-aromatic NF membranes, a clear absence of Amide II peak could be observed [36]. In addition, it allowed to verify the success of support dissection, polymer grafting [36] or modification/degradation of film's chemical structure in the application of specific effluent[26]. As mentioned previously, FTIR has been applied to distinguish the effect of synthesis monomer portions on final group concentrations (rich in $-NH_2$ or $-$COOH) of synthesized APA films [26, 56].

1.1.5 The major questions to be addressed

As reviewed above, despite the remarkable investigations that have launched to understand the formation and structural properties of APA films, many interesting aspects remain still not fully understood. For instance, the synthesis temperature effect on the IP at free aqueous-organic interface is rarely studied; the thickness analysis was proven challenging in face of the thin and heterogeneous feather of APA fims, therefore a selection of a relevant characterization techniques is needed; the density of APA's dense regions, which is supposed to govern the filtration process, waits still to be investigated.

In face of these challenges, in this study the free-standing films were synthesized respectively at -20°C, 0°C and 29°C, in order to offer more information on temperature effects during the IP at free aqueous-organic interface. On the other hand, CPA2 (Hydranautics, Nitto Group Company, USA) RO membrane, a standard membrane generally used for waste-water engineering studies[102], was chosen as conventional IP case-study to compare with the free-standing ones, while its APA layer's structure has not yet been characterized up to date. The structural properties, such as morphology, topology, thickness, void fraction, apparent density and that of the dense regions, water uptake and chemical structure were investigated with combination of various techniques as SEM, AFM, profilometry, ellipsometry, DVS, XPS and AFM-IR, aiming to contribute to a better understanding of morphological and thermophysical properties of APA layers of both conventional IP synthesized commercial CPA2 RO membrane and free-standing films. Meanwhile, a new set of chemical

descriptor was presented in this study, which permits to include all possible chemical configurations of APA film and to indicate the detailed quantities such as monomeric unit and amine/acyl group connection degrees with the help of chemical composition quantification via XPS.

1.2 Materials and methods

1.2.1 Chemicals

All reagents and chemicals were of analytical grade and were used as received: sodium metabisulfite ($Na_2S_2O_5$, Sigma-Aldrich), potassium nitrate (KNO_3, Sigma-Aldrich, ≥99 %), ammonium chloride ($NHCl_4$, Sigma-Aldrich ≥99.5 %), sodium bromide (NaBr, VWR Prolabo, 100 %), sodium iodide (NaI, Sigma-Aldrich, ≥99%), potassium hydroxide (KOH, Sigma-Aldrich, ≥85 %), trimesoyl chloride (TMC, Sigma-Aldrich, 98 %), *m*-phenylenediamine (MPD, Sigma-Aldrich, 99 %), triethylamine (TEA, Sigma-Aldrich, ≥99 %), *N,N*-dimethylformamide (DMF, Sigma-Aldrich, ≥99.9 %), chloroform (stabilized with ethanol, Carlo Erba, ≥99 %), *n*-hexane (Carlo Erba, analytic grade for HPLC). Ultrapure water was produced in the laboratory via MilliQ water system (resistivity≥18 MΩ-cm,Millipore).

1.2.2 APA layer preparation

1.2.2.1 APA layer isolation from commercial CPA2 membrane

CPA2 RO membrane was purchased from Hydranautics (Nitto Group Company, USA) as spiral wound module in wet state. It has an uncoated and fully aromatic polyamide active layer. Membrane samples were initially cut into A4 coupons and then stabilized with 1 wt% sodium metabisulfite solution and conserved at 4°C under vacuum. Before analysis, the membrane was rinsed by KOH at 0.4 $g{\cdot}L^{-1}$ and then by enough ultrapure water until the neutral pH was reached. To isolate the free APA active layer from the membrane, at first the support layer polyester was carefully peeled off by hand so that only APA+PSf remained, then PSf was removed by chemical treatment. The dissection method was adopted from Freger *et al.,* (2004)[34] but with some modifications. The active top-surface and back-surface (facing the support) of APA layer were obtained via different methods. For the back-surface, the APA+PSf coupon was pressed on a glass wafer with PSf facing up, ensuring the APA side stuck to the substrate. Then chloroform was dropped to dissolve the PSf until the APA became transparent, then a few droplets of DMF were placed for completing the removal of PSf. DMF was applied to swell and soften the APA layer, preventing it from deformation such as folding or wrinkling[34]. The dissolution is considered finished when the remaining layer stayed completely transparent after the solvent evaporated.

In order to obtain isolated APA top-surface, the PSf+APA coupon was immersed in DMF solvent with the help of a clip fixing the two boards of the coupon with the top-surface facing up. The PSf was dissolved in

DMF and the solvent was renewed progressively. With enough DMF washing quantity, the PSf was completely dissolved and only little trace remained in the solvent at the end according to XPS analysis. The remaining APA film was recovered by introducing underneath a silicon wafer of 1×1 cm^2 and then was raised out from the liquid by the wafer.

The ensemble APA+Wafer was air-dried and then conserved at 4°C out of direct light for future use. The original APA top-surface of CPA2 (undissolved) was named 'CPA2-ots'. The back-surface after dissection was specified as 'CPA2-bs' and the top-surface after dissection was as 'CPA2-ts'.

1.2.2.2 APA film synthesis

The free-standing aromatic polyamide films were synthesized via interfacial polymerization from TMC and MPD, which was adapted from the literature [28, 62].

20 mL of MPD aqueous solution (3% w/v) containing of 1% w/v TEA was poured into a Petri dish (diameter: 8.5 cm). Then 10mL of TMC (1% w/v) *n*-hexane organic solution was added delicately upon the aqueous surface with the help of a glass plate (size: 2 cm × 5.5 cm). The Petri dish was then covered with a glass plate to limit solvent evaporation during interfacial polymerization. After 15 min's contact, a continuous film was obtained at the interface and the polymerization reaction was stopped: the upper organic solution and lower aqueous phase were removed, while 2 mm depth of aqueous phase was maintained to avoid the film adhesion to the Petri dish bottom. Then, the top-surface was rinsed three times with 20 mL *n*-hexane and the back-surface was rinsed three times with 20 mL ultrapure water by always keeping a thin layer of water at the end of each washing step to let the synthesized film float on its surface. Two sets of synthesis were performed at different moments and by different experimenters in order to offer enough materials for characterization. As for sample set 1, the syntheses were achieved at three temperatures (-20, 0 and 29°C) by maintaining the initial aqueous and organic solutions as close as possible to corresponding temperatures. Due to freezing effect for aqueous phase at negative temperatures, the aqueous solution was controlled around 0°C for synthesis at -20°C. As for sample set 2, the syntheses were performed at four temperatures with an additional temperature at 15°C.

The synthesized samples were labeled in the form of 'Syn'+'synthesis temperature' as 'Syn -20°C', 'Syn 0°C', 'Syn 15°C' and 'Syn 29°C'. The top- and back-surface were specified with a suffix as '-ts' and '-bs', respectively. For SEM, AFM, profilometry and XPS characterizations, the CPA2 and synthesized film samples were all prepared on a silicon wafer around 1×1 cm^2, and analyses were realized by avoiding the film folding part and the edge.

1.2.3 APA film structural characterization

1.2.3.1 Field emission scanning electron microscopy (FE-SEM)

In conventional SEM analysis, a focused electron beam is produced by thermionic emitter and scan the sample surface. The electron excites the atom on the surface, emitting secondary electron, whose signal intensity is detected via Everhart-Thronley detector and produces the topological contrast, where the bright area indicates a high signal. The conventional SEM analysis is incapable to produce high-resolution image due to the low brightness, besides the operation at a high voltage possibly leads to damage on heat intolerant samples. FE-SEM used a field emission emitter gun to produce a much focused electron beam, resulting in brightness higher than conventional thermionic emitter. Thus it allows of an ultra-high resolution imaging at low accelerating voltage.

FE-SEM (Zeiss SUPRA55-VP) was used for the APA top- and back-surface morphology analyses, with 2 secondary electron detectors, an in–lens and an Everhart-Thornley SE detector. Dry samples were mounted to the steel mesh without usual sputter-coating and then put under vacuum for the analysis. The analysis was performed under 1.5 kV to avoid heating damage and at a magnification of 4000. SmartSEM software was used for data acquisition.

1.2.3.2 Atomic force microscopy

AFM analyses were performed with a nanoIR2 system (Bruker nano, USA) to study thickness, morphology and roughness of the top- and back-surfaces of dry samples, placed on a silicon wafer. The measures were done in contact mode, with a gold-coated tip (30 nm diameter) (HQ: CSC38/CR-AU, MicroMasch) with a constant force around 20 nN. Data acquisition was realized with the software Analysis Studio (version 3.15, Bruker nano, USA).Images and data were treated with Analysis Studio and MountainsMap (Version 8, Digital Surf, France).

For thickness measurement, frame leveling was realized via the MountainsMap's 'Series of profile' analysis, which adjusted the cross-section height profile of blank wafer to horizontal level, line by line. The height profile, also called peak-to-valley distance, of each point in X, Y plane is defined as $Z_{ij} = Z(X_i, Y_j)$. With N_x and N_y the number of points in X, Y dimensions of a target area, the average height of the area is defined as:

$$\mu = \frac{1}{N_x N_y} \sum_{j=1}^{N_y} \sum_{i=1}^{N_x} Z_{ij} \tag{1.1}$$

The average heights of blank wafer (μ_{wafer}) and film region (μ_{film}) avoiding the edge (the film region within at least 2 μm distance is not analyzed) were calculated independently and the difference between the two was defined as the average film thickness measured by AFM (δ_{AFM}). Besides, the morphology (peak-to-valley distance distribution or height histogram) was analyzed on a detection region of film around 10×10 μm^2. The statistic roughness was quantified on 10 repetitions of 5×5 μm^2 regions and calculated as the root-mean-square

roughness:

$$S_q = \sqrt{\frac{1}{N_x N_y} \sum_{j=1}^{N_y} \sum_{i=1}^{N_x} (Z_{ij} - \mu)^2} \tag{1.2}$$

Roughness uncertainty was evaluated by the confidence interval at 95% confidence on the 10 repetitions. To investigate cross-section profiles of the top-surfaces, a half film-covered region on the silicon wafer of total surface 10×30 μm^2 or sometimes 30×30 μm^2 was analyzed. At least 16 different lines were recorded for each sample. An evaluation of the base thickness (δ_{base}), upon which roughness or irregularities develop, was estimated as the lowest level of the valleys detected by the AFM tip and averaged for different lines analyzed. For CPA2, its back-surface was also analyzed to compare with the top-surface profile.

1.2.3.3 Profilometry

The profilometry (DektakXT, Bruker, Germany) was applied in our study for the investigation of APA film thickness. The analyses were realized with a force of 1 mg and a tip with a diameter of 4 μm. Data acquisition and treatment were realized via software Bruker Vision64. In this study, data were saved with a spatial resolution of 0.11 μm, except for the sample conditioned at 95% relative humidity (RH), where the resolution was 1.11 μm.

For each analysis, the vertical height profile of a straight line around 2 mm long crossing half wafer and half sample region was analyzed, on which 100 μm or 200 μm regular and flat region of sample and silicon wafer profile were selected. The film thickness obtained by profilometry (δ_{Pro}) was calculated as the difference between the average sample and wafer heights of the selected region, and statistic roughness (S_q) was calculated using sample heights. For each APA film type, thickness and roughness uncertainties were evaluated by the confidence interval at 95% confidence for at least 4 analyzed lines. For CPA2 film, top- and back-surfaces were both analyzed. As for synthesized films, only top-surfaces were studied. Influence of the relative humidity (RH,%) on the APA film thickness was tested for CPA2 as well as for synthesized samples. Each sample was placed in a sealed cylindrical glass device with a volume around 0.5 L, inside which a cuvette of 15 mL volume containing over-saturated salt solution of potassium nitrate, ammonium chloride, sodium bromide, sodium iodide or potassium hydroxide to generate 95%RH, 79%RH, 59%RH, 40%RH and 9%RH at 20 °C, respectively[45]. An incubation time of 7 days was used for each RH to ensure the water sorption equilibrium. The synthesized samples of set 2 were only equilibrated at 9% RH. S_q analysis of profilometry was only performed for CPA2-ts, CPA2-bs and synthesized samples of set 2 at 9%RH.

1.2.3.4 Spectroscopic ellipsometry

Spectroscopic ellipsometry (Accurion EP3) was used to determine the refractive index (n_{film}) of the APA layer and deduce the void fraction it contains (f_{void}). Relatively dry samples were analyzed: as for profilometry, all

samples were conditioned at 9 %RH for 7 days before analysis, corresponding to around 2 wt% water content for each sample. Duplicate sample wafers were prepared and at least 5 locations were analyzed on each. Data acquisition was realized via software EP3View V235 and data modeling was via EP4Model 1.01.

The light focusing optics allow to adjust the polarization and offer an optimum condition for the analysis. Ellipsometry measures changes in light beam polarization upon specular reflection off sample, the reflectivities of polarized light in plane (r_{p}) and out of plane (r_{s}). Then it expresses these two parameters in terms of amplitude ratio upon reflection ($tan\psi$, ψ is the amplitude component) and phase shift (Δ), as given:

$$\frac{r_{\mathrm{p}}}{r_{\mathrm{s}}} = \tan(\psi)e^{i\Delta} \tag{1.3}$$

The variation of this reflectivity ratio is illustrated by a multilayer optical model, where each optical layer is described by its thickness (δ) and refractive index (n) as the fit parameters with respect to angle of incidence (AOI, °) and wavelength of analysis (λ, nm). As a function of AOI, the model-generated ψ and Δ values are numerically fitted to the measured data, delivering the optimum values of aim layer's δ and the refractive index (n). The model allows as well to determine one optimum adjustable parameter if either the δ or the n is known. The top APA layer was deposited on a silicon wafer modeled as a 2 nm silicon dioxide layer (that had been measured independently) and an infinite silicon bottom layer. Each optical layer was described by its thickness (δ), absorption index (k) and refractive index (n). A multi-layer optical model was used to obtain refractive index of the APA-layer. Two AOI values were used (60° and 70°) and the laser beam wavelength was 658 nm. Optical properties for middle and bottom layers were taken as $n = 1.456$, $k = 0$ and as $n = 3.829$, $k = 0.014$ respectively. The refraction index of the APA layer was fitted using a thickness value obtained either from AFM or from profilometry analysis and assuming $k_{\mathrm{film}} = 0$. The model fitting was accepted when root-mean-square error (RMSE) was inferior to 100.

According to effective-medium approximation (EMA) models, the void fraction (f_{void}) of APA film could be deduced based on the obtained apparent refractive index (n_{film}), pure dense APA polymer refractive index (n_{polymer}) and that of void ($n_{\mathrm{void}} = n_{\mathrm{air}} = 1$). The f_{void} values were determined by the following three models:

Parallele model:

$$n_{\mathrm{film}} = (1 - f_{\mathrm{void}})n_{\mathrm{polymer}} + f_{\mathrm{void}}n_{\mathrm{void}} \tag{1.4}$$

Series model:

$$\frac{1}{n_{\mathrm{film}}} = \frac{1 - f_{\mathrm{void}}}{n_{\mathrm{polymer}}} + \frac{f_{\mathrm{void}}}{n_{\mathrm{void}}} \tag{1.5}$$

And *Bruggeman* model:

$$1 - f_{\mathrm{void}} = \frac{\frac{n^2_{\mathrm{film}}}{n^2_{\mathrm{polymer}}} - \frac{n^2_{\mathrm{void}}}{n^2_{\mathrm{polymer}}}}{(\frac{n^2_{\mathrm{film}}}{n^2_{\mathrm{polymer}}})^{1/3}(1 - \frac{n^2_{\mathrm{void}}}{n^2_{\mathrm{polymer}}})} \tag{1.6}$$

The chosen value for pure dense APA polymer refractive index (n_{polymer}) is discussed in the Results section. Un-

certainty on f_{void} was estimated by the average variation between the average value and maximum or minimum ones, issued from the error on n_{film} analysis.

1.2.3.5 Density estimation

For the commercial CPA2 membrane, several dissected APA film with accurate known surface were progressively gathered and rinsed by 2 L of water. Then the samples was recovered as a pellet. For the free-standing APA films (Syn -20°C, Syn 0°C and Syn 29°C, sample set 2), each of them was synthesized in a Petri dish (diameter: 8.5 cm) as described previously and the entire surface was recovered together as a pellet.

The sample pellets were primarily conditioned in quite dry atmosphere (RH near 0%) to firstly eliminate free water. They were then transferred into a dynamic vapor sorption device (DVS, Intrinsic instrument) to measure precise masses at controlled RH (%) by DVS, with a systematic fluctuation of ±0.5%. 0% and 95%RH were investigated to search for the dry and hydrated density. For CPA2, the equilibrium time was set as 24 h for each RH (%) stage. The mass was recorded every 20 seconds and the last 5 points were averaged as the equilibrated sample mass. As for synthesized APA films, the equilibrium time was set as 48h and data were recorded every minute. The dry masses of the tested samples were between 2.4 mg and 9 mg. Considering the heterogeneity of the APA film, three density concepts were investigated to get a more complete understanding of the film structure and dense APA polymer property. They were estimated by combining the mass with thickness and void fraction values obtained from the AFM/profilometry and ellipsometry analyses. The mass of the material (m, g) and the film surface (S, cm^{-2}) allow the areal density (d_{areal}, g·cm^{-2}) to be calculated as:

$$d_{\text{areal}} = \frac{m}{S} \tag{1.7}$$

Apparent volumetric density ($d_{\text{volumeric}}$, g·cm^{-3}) is obtained as:

$$d_{\text{volumeric}} = \frac{d_{\text{areal}}}{\delta} \tag{1.8}$$

where δ (cm) is the thickness estimation. Eventually, the volumetric density of dense APA region excluding voids (d_{dense}, g·cm^{-3}) is calculated using the void fraction of the film:

$$d_{\text{dense}} = \frac{d_{\text{areal}}}{1 - f_{\text{void}}} \tag{1.9}$$

Uncertainties for the results of density calculations were estimated by the variation between the average and the maximum or minimum values.

1.2.3.6 X-ray photoelectron spectroscopy

Prior to analysis, the CPA2 original top-surface, dissected top and back-surfaces, and synthesized APA films' top and back-surfaces were rinsed thoroughly by ultrapure water and then air-dried. Their chemical compositions were analyzed by a ThermoFisher Scientific K-Alpha XPS spectrometer equipped with a monochromatic aluminum source (Al K_α, $h\nu = 1486.68$ eV) under ultrahigh vacuum condition (10^{-7} Pa range). The emission angle was set to 0° with an analysis depth up to 10 nm and the X-ray gun was operated at 10 kV and charge neutralization system was used to obtain high-resolution spectra. The survey spectra acquisition was realized with a sweeping range over 0 - 1350 eV, a pass energy of 100 eV and an energy step of 1 eV.

For each sample, at least 2 frames of 1 cm^2 were studied, and on each frame at least 3 irradiated zones of 1 mm^2 were analyzed, leading to between 6 and 14 studied zones. The elemental percentages were obtained from the photoelectron peak area using the Avantage and CasaXPS softwares after a Shirley type background subtraction and following normalizations of the peak areas with the Scofield sensitivity factors. The initial raw data were treated by eliminating the chemical compositions from the impurities. For samples of CPA2, a small amount of sulfur from PSf ($C_{27}O_4SH_{22}$) was detected, hence the associated oxygen and carbon contents were eliminated on the basis of PSf's chemical formula. All data were compared and averaged to ensure the sample representability as below.

1.2.3.7 Atomic force microscopy-based infrared spectroscopy (AFM-IR)

If the energy of the irradiating infrared (IR) beams corresponds to the energy change of molecular vibrational states, the light beams are absorbed and the corresponding excited states are reached. The stretching and bending modes for the viration are well described. The former changes the bond length and bond energy, thus it demands a higher energy and appears at higher wavenumber. It has two forms: symmetric and antisymmetric stretching. The bending mode changes the bond angle strain, hence it requires lower energy and appears at lower wavenumber. The bending owns four forms: scissoring (in plane), wagging (out of plane), rocking (in plane) and twisting (out of plane). Generally speaking, bonds with strong bond strength and lower mass vibrate at higher wavenumber, and vice versa. Only the vibration with dipole moment changes can be seen in IR spectroscopy. The intensities of adsorption depend on the molecule number and also on the scale of dipole moment changes.

AFM-IR uses an AFM probe tip to locally detect thermal expansion in a sample resulting from absorption of infrared radiation. In this study, the IR spectroscopy analysis was performed via nanoIR2 system (Bruker nano, USA) coupled with a multichip QCL source with tunable repetition rate range of 0 - 500 kHz and spectral resolution of 0.1 cm^{-1}. IR spectroscopy analysis range covered from 1325 to 1960 cm^{-1} of the mid-IR region with a repetition rate about 400 kHz. Gold-coated silicon probe was used to avoid effects linked to IR absorption of the silicon cantilever. Data treatments were realized via MountainsMap 7.3 and Microsoft Excel.

1.3 Results

1.3.1 Morphology and topology

The knowledge on the morphology of APA films' top-/back-surface and cross-section is of significance in understanding the whole structure, the synthesis process or the film performance such as water flux or organic molecule permeation. The samples' morphologies were examined via AFM and SEM, on the purpose to compare different techniques and to give comprehensive visualization.

1.3.1.1 Morphology analysis on top- and back-surface

The APA film's pronounced morphological heterogeneity has been reported previously in the literature. Commonly the APA layers of commercial RO membranes or synthesized APA films with support were found having a typical ridge-and-valley surface and a relatively flat back-surface. Meanwhile, it should be addressed that these previous images were all presented at a small scale around tens of square micrometer. Therefore, the morphologies of CPA2 original top-surface and dissected back-surface were investigated at a larger scale around 30×20 μm^2 via SEM in this study to offer a more general complementary information, fig.1.6.

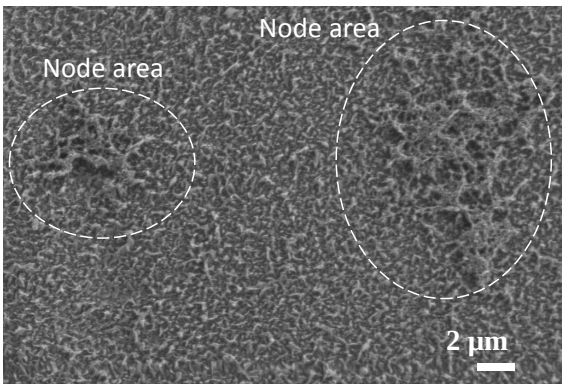

(a) CPA-ots

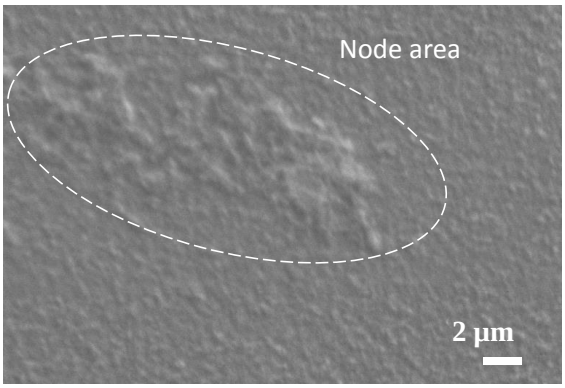

(b) CPA-bs

Figure 1.6: SEM image of CPA2 original APA top-surface and dissected APA back-surface.

As presented in fig.1.6(a), CPA2 APA layer doesn't exhibit a regular top-surface as expected at large image scale. Some node areas were determined, spreading around the top-surface. To our knowledge, these node structures have not been reported previously in the literature. Since this analysis was based on an original virgin top-surface, it could be deduced that these nodes were formed during the interfacial polymerization rather than being later created during the dissection process. Meanwhile, node areas were also observed on the dissected back-surface, fig.1.6(b). Since the regular regions remained dominant, they are considered more representative. In the following discussions only regular regions were selected and investigated. It is notable that the observation of the node areas on both sides of the CPA2 APA layer is interesting. Their formation mechanisms, appearance frequency and effects on membrane performances demand further exploration.

Fig.1.7 presents the morphology comparison of original top-surface, top-surface and back-surface after dissection treatment of PSf of CPA2 APA layer by zooming the regular regions.

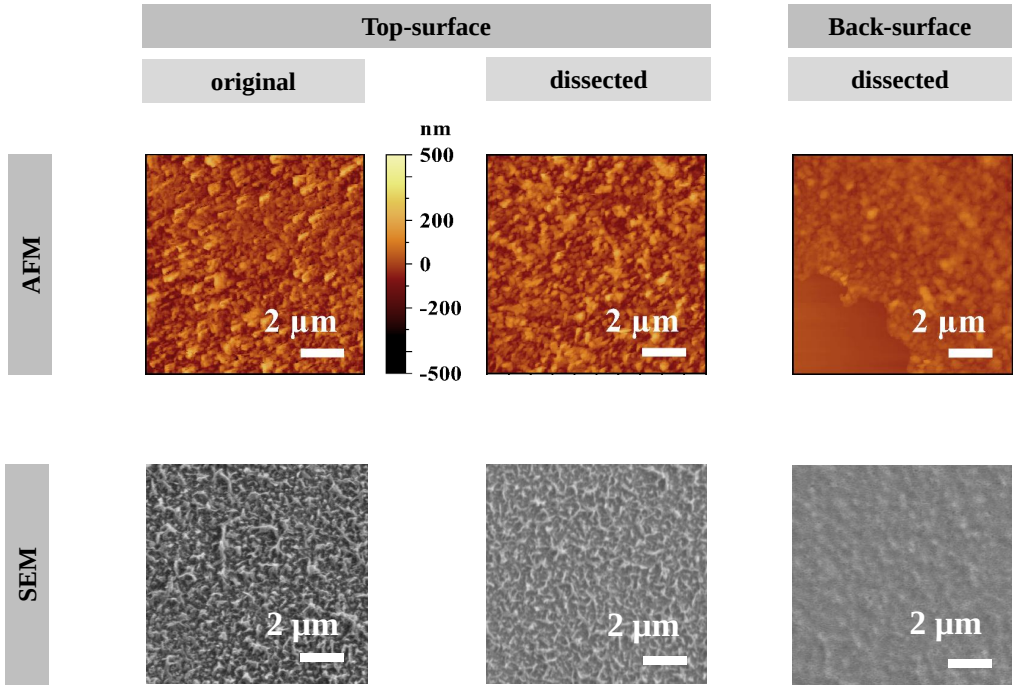

Figure 1.7: AFM and SEM images of CPA2 original APA layers', top-surface and back-surface.

The images of SEM and AFM were generally in consistence with each other for all the CPA2 samples. The regular region of top-surface exhibited a typical ridge-and-valley structure, which was reported via TEM or SEM analyses on other RO membranes [67] or synthesized APA thin films on support [43, 48]. Besides, in light of recent studies [91, 92, 114, 124], the ESPA2 and ESPA3 RO membranes from the same manufacturer as CPA2 had the same structure. In addition, it was proven that the dissection process didn't modify the film's morphological structure as no evident deformation was observed on CPA2 dissected top-surface when compared to the original one. This observation was also confirmed by later AFM roughness, with $S_{q-\mathrm{ori}} = 61 \pm 3$ nm and $S_{q-\mathrm{ts}} = 63 \pm 2$ nm.

On the other hand, the back-surface turned out to be much smoother and flatter than the top-surface. This flat feature could be mainly explained by the insolubility of TMC into the aqueous phase and by the existence of PSf support layer, which together prevented the APA film growing freely during the interfacial polymerization on the aqueous side. Nonetheless, previous studies have reported that the back-surface of the APA layers of ESPA2 and ESPA3 RO membranes were smooth but porous [91, 124]. These pores might arise from the presence of water drops at the interface, which re-established the organic-aqueous interface at the drop edge[54]. Cadotte *et al.,* (1985)[13] assumed that the pores allow of the migration of MPD in view of the formation of barrier layer at the interface. Nonetheless, as for CPA2, more evidences were demanded to verify the existence or inexistence of similar pores.

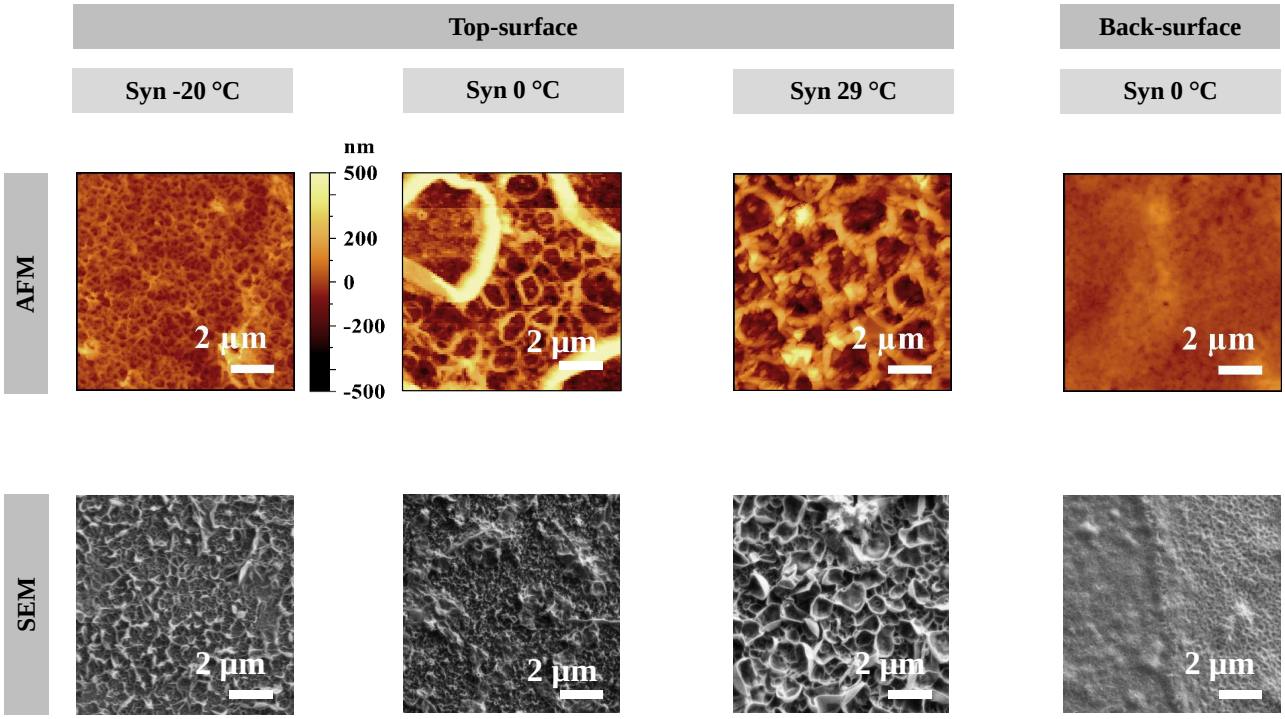

Figure 1.8: AFM and SEM images of Syn -20°C, Syn 0°C and Syn 29°C's top-surface and back-surface. AFM images were from sample set 2 and SEM images from sample set 1.

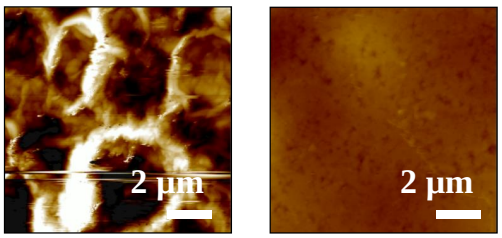

Figure 1.9: AFM images of Syn 15°C (sample set 2)'s top-surface and back-surface.

The morphology of the synthesized samples was significantly different from that of CPA2, fig.1.8 and 1.9. It should be addressed that SEM images correspond to sample set 1 while the AFM images are for sample set 2.

The comparison was possible for later added Syn 15°C in sample set 2, hence its AFM top- and back-surface images are presented individually in fig.1.9. On top-surfaces of all synthesized samples spread typical structures as hollow cylindrical walls forming open inner cavities, which were referred to as 'chimney-like structures' or 'chimneys' in this study. Similar chimney-like structures could be observed in the work of Cui *et al.,* (2017) for their free-standing synthesized APA films [18]. The formation of these specific structures might be linked to a freer MPD diffusion during the free-standing synthesis compared to the one with support, as MPD were supposed to migrate more slowly in the support's pore hence forming a more conservative ridge-and-valley structure. It could be observed the chimney-like structures' sizes were temperature-dependent. Syn -20°C exhibited the most regular chimney-like structures, with diameter around 0.5 μm. Then for Syn 0°C, the chimney structures became no longer uniform, as two sizes existed. The smaller chimney reached a diameter around 2 μm while the larger ones with a diameter around 6 μm covered smaller ones. At 15 °C, the chimneys became more uniform, as the majority exhibited a diameter around 3 μm while only few larger ones appeared, with a diameter up to 5.5 μm. As for Syn 29°C, the chimneys continued to grow as orderly as Syn -20°C, while the diameter remained around 2.5 $\sim$ 3 μm. In the study of Cui *et al.,* (2017), it was demonstrated that the chimney size increased along with the raise of TMC concentration. Nonetheless, in our study, the temperature impact on morphology was found complicated to explain. With increasing synthesis temperature, the chimneys firstly grew larger and uniform from a uniform state, then they unexpectedly became to decrease their sizes while generating again an ordered distribution. This complicated top-surface morphology evolution with temperature remained inexplicable based on current information.

All synthesized samples had a similar dense flat back-surface as Syn 0°C, half-covered by some tiny chimney-like structures.

It should be noted that the SEM and AFM images of Syn 0°C presented distinct morphology, as the large size chimneys were not present on the SEM image. This inconsistency might be explained by the sample's self-heterogeneity, or it might as well result from the uncontrollable factors during the manual fabrication since the samples for SEM and AFM analyses belonged to different sample preparation sets (set 1 for SEM and set 2 for AFM). During free-standing interfacial polymerization, the organic solution containing TMC was added on the aqueous-organic interface manually, which could introduce disturbance at the polymerization zone.

1.3.1.2 Topology analysis from cross-section profile investigation via AFM

Thanks to AFM's thin tip (with a diameter around 30 nm), it was possible to investigate detailed topological information of CPA2 (fig.1.10), Syn -20°C (fig.1.11), Syn 0°C (fig.1.12), Syn 15°C (fig.1.13) and Syn 29°C (fig.1.14) by analyzing the cross-section profiles.

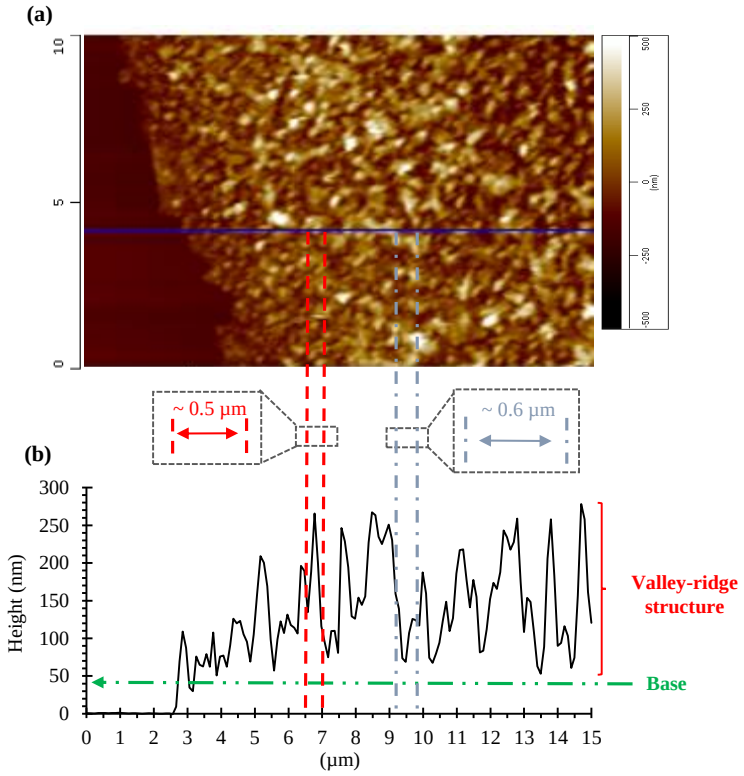

Figure 1.10: (a): AFM surface images of the top-surface of CPA2; (b): corresponding AFM height profile along the blue solid line. Analysis made on a 10×15 μm^2 half-covered sample.

For CPA2 (fig.1.10), wa can notice a base around 40 nm thick, determined as the lowest level of valleys, upon which developed the ridge structures. Such 'base+ridge' multi-level topology has been revealed for APA layers of ESPA3 and other RO membrane via TEM cross-section analysis[91, 92]. Moreover, the base bottom of ESPA2 APA layer has been quantified around 20 nm thick via SEM cross-section investigation[124], which was close to the base thickness obtained here.

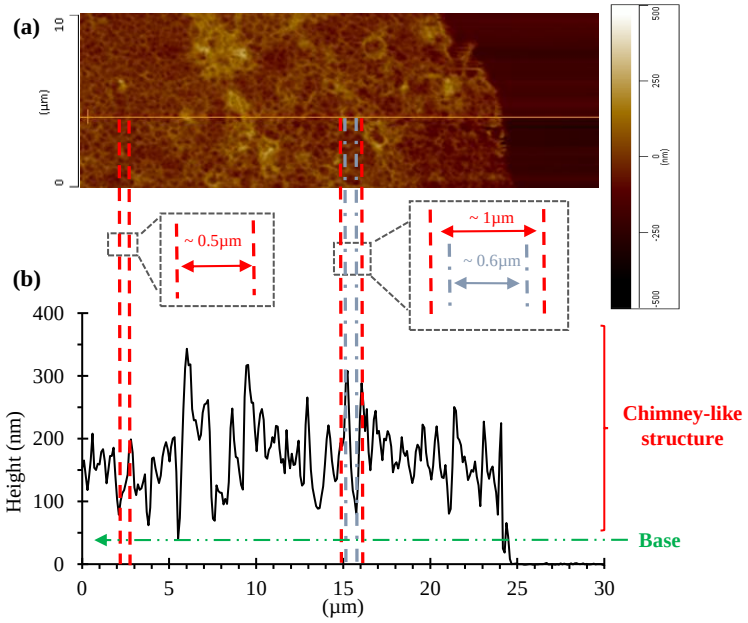

Figure 1.11: (a): AFM surface images of the top-surface of Syn -20°C; (b): corresponding AFM height profile along the orange solid line. Analysis made on a 10×30 μm^2 half-covered sample.

Multi-level topologies have been determined for free-standing synthesized sample as well. The chimneys structures of Syn -20°C were all developed upon a base around 60 nm thick as presented in fig.1.11. The chimney structures appeared uniform at this synthesis temperature, as the typical chimney wall height fell into a small range between 200 to 300 nm.

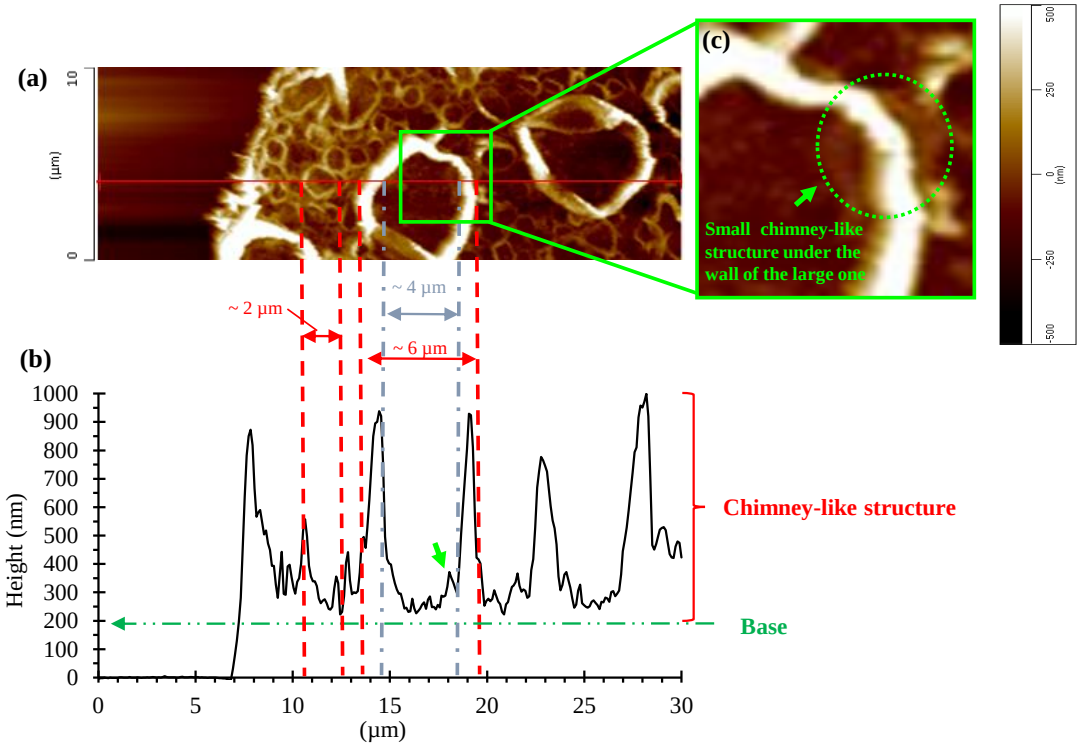

Figure 1.12: (a): AFM surface images of Syn 0°C film; (b): corresponding AFM height profile of red solid line in image (a); (c): corresponding enlarged image of the green solid box in image (a). Total analyzed surface of 30×30 μm^2.

As aforementioned, it was observed that the film growth was accelerated at 0°C, as the base thickness raised up to 160 nm. Two different chimney levels were observed with distinct diameters, wall thicknesses and heights as well. The small chimneys with a diameter at 2 μm, marked by green arrow in fig.1.12, had a typical wall thickness and height around 0.5 μm and 150 nm respectively, while the larger ones with diameter at 6 μm exhibited a notable wall thickness around 1 μm and height around 750 nm above the base. In addition, a complete small chimney could be observed lying under a part of one large chimney's wall, as zoomed in fig.1.12(c). The larger chimneys might develop upon the complete formation of smaller ones, or the two types might be generated simultaneously but connected afterwards. More investigations are required to reveal the formation mechanism of the two chimneys.

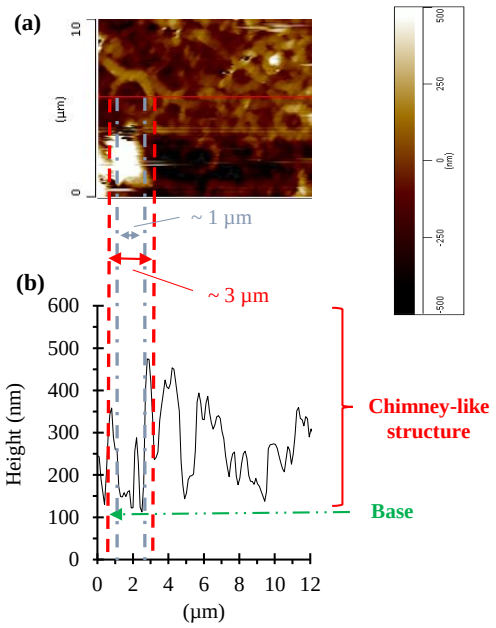

Figure 1.13: (a): AFM surface images of the top-surface of Syn 15°C; (b): corresponding AFM height profile along the blue solid line. Analysis made on a 10×30 μm^2 half-covered sample.

At 15°C, the chimneys become more orderly and with a diameter around 3 μm. A dense bottom was found around 100 nm thick.

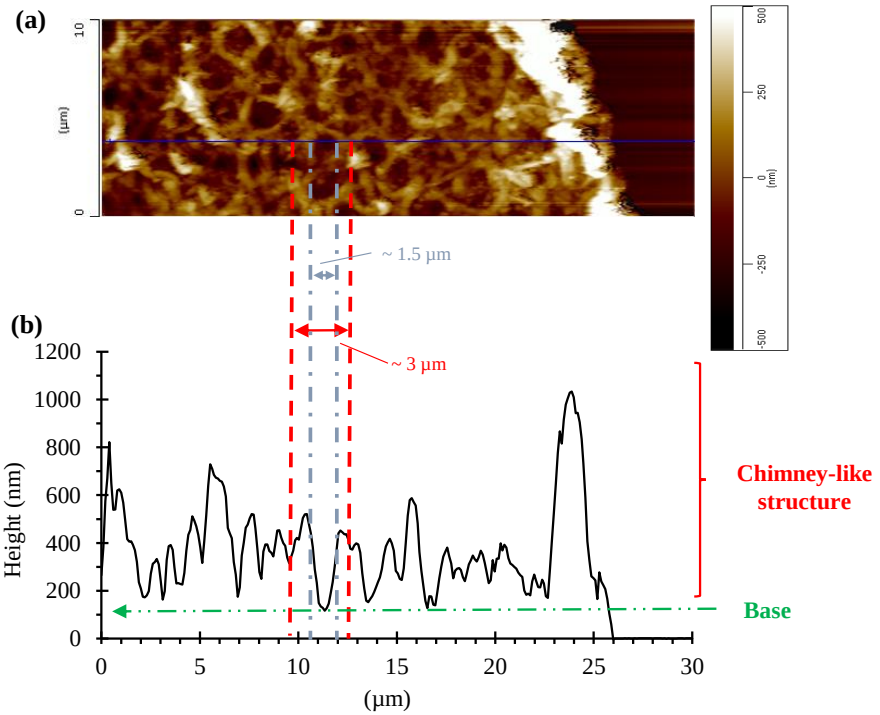

Figure 1.14: (a): AFM surface images of the top-surface of Syn 29°C; (b): corresponding AFM height profile along the blue solid line. Analysis made on a 10×30 μm^2 half-covered sample.

At 29°C, the chimneys become uniformly distributed again. Compared to Syn -20°C, the chimneys were of larger size, with a diameter, wall thickness and height above the base around 3 μm, 0.75 μm and 400 nm

respectively. The thickness of the base was found around 120 nm.

In summary, it was discovered that APA films, whether synthesized with or without support, all exhibited a multi-level topology as "base+ridge/chimeneys" structure. On the top-surfaces, CPA2 exhibited ridge-and-valley structures while free-standing synthesized samples exhibited chimney-like structures. The typical width or diameter of ridges or chimney-like structures (d_{typical}) are summarized in table 1.1. The varied top-surface might be attributed from the presence or not of the support layer during the interfacial polymerization. Meanwhile, all films had a smooth and flat back-surface. For free-standing synthesized samples, it was observed that the film morphological growth was temperature-dependent. Nonetheless, the related mechanism seems to be complicated and demands more investigations.

1.3.2 Average thickness and roughness

1.3.2.1 Investigation of relative humidity influence on thickness via Profilometry

The thickness evolution of CPA2 and synthesized samples (set 1) as a function of RH (%) is presented in fig. 1.15 and fig.1.16 respectively. In theory, there were risks that the surface morphology might be compressed when the thickness analysis was implemented with the back-surface facing up. To verify whether such influence existed, top-surface and back-surface samples were prepared respectively for each sample type and analyzed.

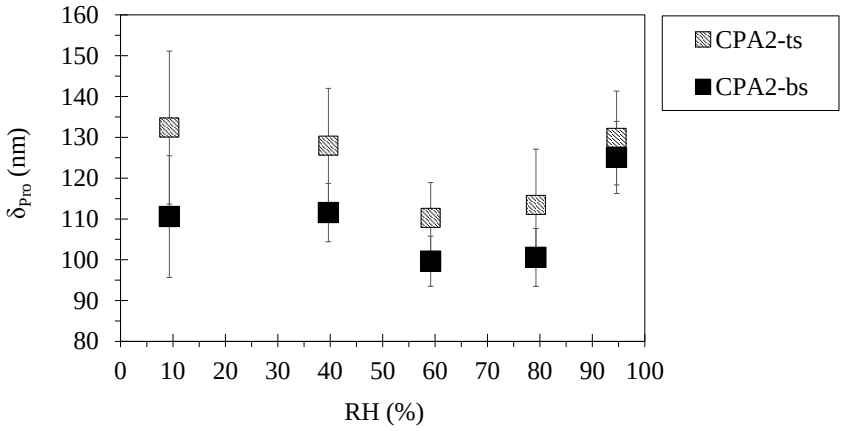

Figure 1.15: Influence of RH on thickness measured by profilometry for the CPA2 samples.

As shown in fig.1.15, for CPA2 the two sample surfaces had finally a similar thickness estimation ($\delta_{-\text{ts}} = 121 \pm 7$ nm and $\delta_{-\text{ts}} = 109 \pm 5$ nm). The S_q analysis performed at 9%RH demonstrated $S_{q-\text{ts}} = 10 \pm 1$ nm and $S_{q-\text{bs}} = 8 \pm 1$ nm. Hence it was concluded that existed no sample preparation effect on final thickness estimation under the profilometry analysis condition implemented in this study.

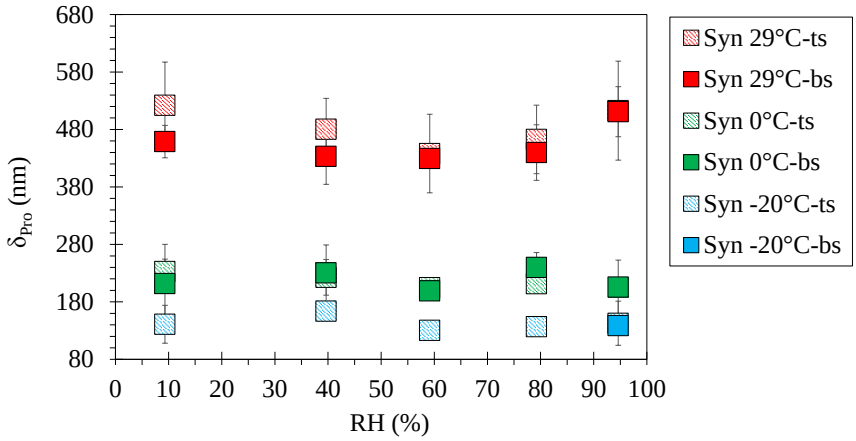

Figure 1.16: Influence of RH on thickness measured by profilometry for the synthesized samples.

As presented in fig.1.15 and fig.1.16, no significant swelling evolution was observed along with the increasing RH for both CPA2 and synthesized samples. According to previous studies, an accurate investigation of APA film swelling remained challenging due to the low thickness variation. Meanwhile, it was found that the swelling behavior might vary according to the proper crosslinking state of the APA sample. Slight swelling around 5%∼15% or evident swelling up to 53% were both reported for APA layers of various commercial RO membranes via AFM analysis[25, 36]. The former was not significant considering the high thickness analysis error. Due to the same reason, it was also reported that the swelling of commercial APA layer was not measurable[70]. In terms of synthesized APA samples, Foglia *et al.,* 2017[32] reported a high swelling degree up to 20% for their sub-10 nm thin APA films via neutron and X-ray reflectivity analysis. It should be highlighted that an aluminium humidity chamber was implemented to achieve RH controlling in-situ in their study, which allowed to observe progressive swelling evolution as a function of increasing RH. However, it should also be noted that the reflectivity analysis is only adaptable for extremely flat sample surface, as their APA films were around 10 nm thick and exhibited a sub-nm roughness. On the other hand, our profilometry thickness results of top-surface and back-surface demonstrated no significant difference. Based on above discussions, for each sample type, the thickness data at different relative humidities together with data of different sample surfaces were averaged. As for CPA2, average thickness and roughness were taken as $\delta_{\mathrm{Pro}} = 115 \pm 4$ nm and $S_{q-\mathrm{Pro}} = 9 \pm 1$ nm. The average profilometry thickness results for synthesized samples (set 1) are presented in fig.1.19.

1.3.2.2 Comparison of thickness and roughness analyzed by AFM and Profilometry

As introduced before, AFM and profilometry are relevant methods to give thickness estimation of thin films. The two methods are both based on direct investigation on sample's cross-section height profiles, meanwhile they own proper advantages and drawbacks. AFM is supposed to give more detailed profiles as it has a thinner tip (tip diameter of 30 nm in this study) compared to that of profilometry (tip diameter of 4 μm in this study). On the other hand, AFM analysis scale is limited to hundreds of $\mu\mathrm{m}^2$ (less than 30×30 $\mu\mathrm{m}^2$ in this study)

while profilometry investigates distance of hundreds of μm for each height profile (200 μm in this study). The AFM and profilometry characterization results are summarized in table 1.1.

Table 1.1: Summary of AFM and profilometry characterization of APA films.

APA film	$d_{\text{typical}}(\mu\text{m})$ [a]	Profilometry		AFM		
		δ_{Pro} (nm)	S_q(nm)	δ_{AFM} (nm)	δ_{base} (nm)	S_q (nm)
CPA2	$0.2 \sim 0.5$	115 ± 4	9 ± 1	136 ± 1	40	63±2
Syn -20°C	$0.5 \sim 1$	300 ± 30	180 ± 16	192 ± 2	60	50 ± 8
Syn 0°C	$1 \sim 2/6$ [b]	344 ± 25	137 ± 10	396 ± 11	160	176 ± 17
Syn 15°C	$2.5 \sim 5$	448 ± 36	181±36	282 ± 15	100	247 ± 13
Syn 29°C	$2 \sim 3$	487 ± 27	149 ± 22	368 ± 15	120	117 ± 5

[a] Width of the ridges for CPA2; typical chimney-like structure's diameter for synthesized APA samples. [b] For Syn 0°C, two chimney levels were observed.

A direct comparison of height profiles of dissected top-surface of CPA2 APA layer obtained via these two techniques is presented in fig.1.17. The dissected top-surface was implemented here instead of the original one because the existence of the irregular thick PSf support would make it impossible to launch thickness investigation on APA layer for both techniques.

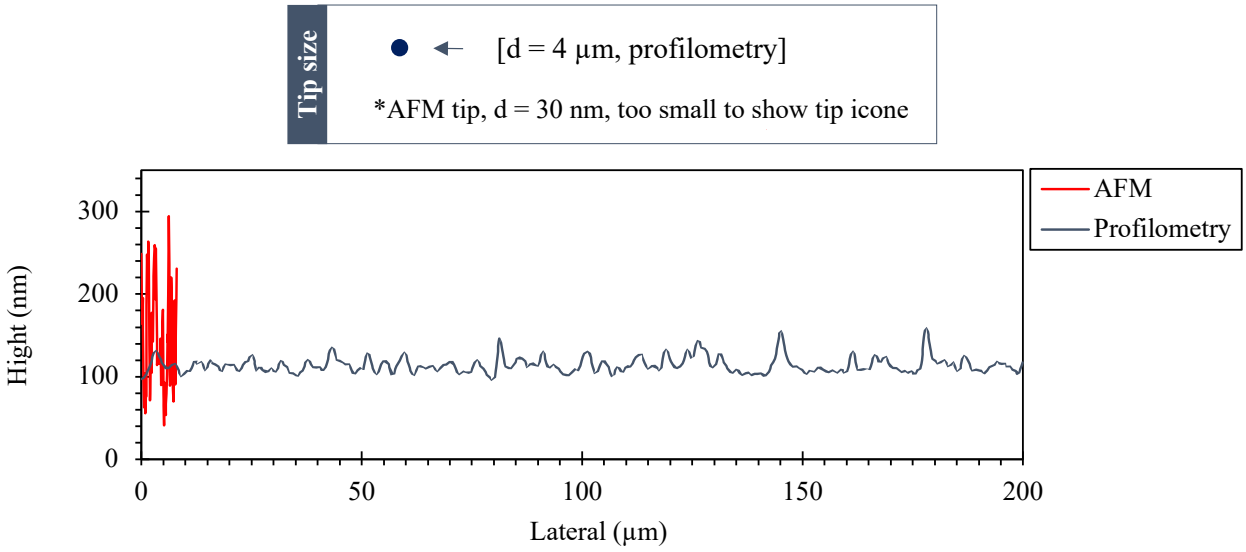

Figure 1.17: Representative topography profiles of dissected top-surface of CPA2 via profilometry and AFM. The two analyses were realized on different sample frames.

The profilometry generated a wider and distinct height profile compared to AFM. The profile obtained via AFM demonstrated a higher height fluctuation between 50 nm and 300 nm, which corresponded well to the base and ridge height level defined in fig.1.10. Meanwhile, the profilometry profile was much flatter. Its lowest height

level was around 100 nm, suggesting the profilometry was not capable to detect the base level of CPA2 around 50 nm as AFM did. This would be due to its large tip diameter (4 μm), which was wider than the typical interval distance between two ridge structures (less than 1 μm, fig.1.10). As a consequence, profilometry tip was blocked before entering the valley structures. Moreover, the highest height level detected by profilometry was 140 nm, unexpectedly lower than the ridge height around 300 nm detected by AFM. Hence profilometry tip is supposed to compress the ridge structures, given that the applied force of profilometry was around 10^4 nN, which was hundreds of times heavier compared to that of AFM around 20 nN. Consequently, the profilometry analysis led to a low roughness ($S_{q-\mathrm{Pro}} = 9\pm1$ nm) compared to AFM ($S_{q-\mathrm{AFM}} = 63\pm2$ nm). On the other hand, it seemed that the high ridge height was averaged by the low valley height for AFM analysis, hence the two techniques finally resulted in close thickness estimations, as $\delta_{\mathrm{Pro}} = 115 \pm 4$ nm and $\delta_{\mathrm{AFM}} = 136 \pm 1$ nm. In addition, being more sensitive compared to profilometry, AFM allowed to distinguish the roughnesses of CPA2's two surfaces, as $S_{q-\mathrm{ts}} = 63 \pm 2$ nm and $S_{q-\mathrm{bs}} = 25 \pm 1$ nm, which accorded well with the previous morphology observation in fig.1.7. Surprisingly, AFM gave as well various thickness estimations as $\delta_{-\mathrm{ts}} = 136 \pm 1$ nm and $\delta_{-\mathrm{bs}} = 97 \pm 2$ nm. This might be explained by the fact that CPA2 film was somehow compressed during the preparation of back-surface sample by tweezer. Overall, since CPA2 exhibited regular and relatively homogeneous profiles, the AFM analysis could overcome its drawbacks of only implementing small analysis scale. Overall, AFM demonstrated more advantages for thickness and roughness analyses than profilometry for the case of CPA2. Meanwhile, the thickness estimations from the two methods, $\delta_{\mathrm{AFM}} = 136 \pm 1$ nm and $\delta_{\mathrm{Pro}} = 115 \pm 1$ nm, were both taken as reference thickness in the following ellipsometry analysis in order to investigate the thickness estimation effect on the void fraction estimation.

The AFM and profilometry profiles comparisons for synthesized samples (sample set 2) are presented in fig.1.18.

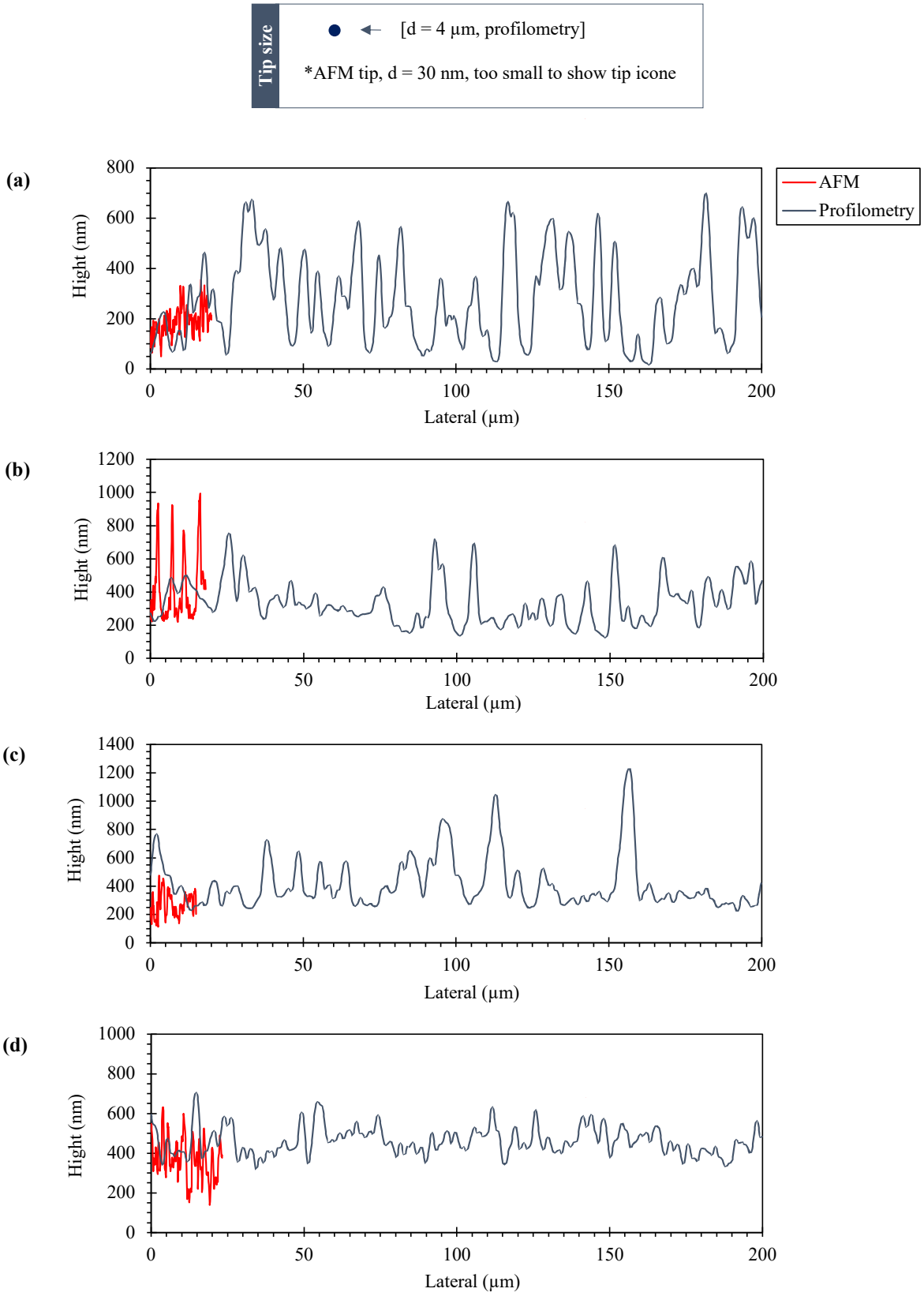

Figure 1.18: Representative topography profiles of top-surface of (a) Syn -20°C,(b) Syn 0°C,(c) Syn 15°C,(d) Syn 29°C, via profilometry and AFM. For each sample type, the two analyses were realized on different sample frames.

In contrast to CPA2, the profilometry profiles of all synthesized samples demonstrated noticeable fluctuations, which possibly corresponded to a general outline of the chimney-like structures. Synthesized samples are supposed to have a more rigid structure than CPA2, hence the profilometry tip's compression effect was not as evident as for CPA2. However, among all synthesized samples, only Syn 29°C showed a good agreement between its AFM and profilometry profiles, while both profiles of the others exhibited significant variations. For Syn 29°C, peak height profiles from profilometry almost overlapped with that from AFM, suggesting a good consistence in chimney wall height detection by both techniques. As the AFM tip was capable to enter inside the chimneys, AFM finally gave a relatively low thickness estimation than profilometry, as shown in fig.1.19 and table 1.1. Unexpectedly, the profilometry profiles of Syn -20°C and 15°C exhibited a significant higher height level than that of AFM. Some large peaks more than 700 nm high were detected by profilometry, which was not seen by AFM. Besides, Syn 0°C exhibited a lower profilometry profile compared to the AFM's. The possible explanation for these profile variations was that these samples were very heterogeneous. In other words, the profilometry revealed complementary morphological characters of theses samples thanks to its long analysis scale. During the free-standing interfacial polymerization, disturbance could be introduced during the manual addition of organic phase upon aqueous phase, which generated non-uniform reaction regions and finally led to a non-uniform film thickness. In addition, the high heterogeneity was highlighted during the profilometry analysis. For example, two Syn 15°C films, sampled from the same synthesis Petri dish, were found having different average thicknesses, with $\delta_1 = 508 \pm 41$ nm and $\delta_2 = 388 \pm 45$ nm. Moreover, it should be addressed that for synthesized samples, it was generally easy to find an equivalent short region within the profilometry profile, which corresponded well to the AFM profile. Hence AFM turned out to be less competitive in thickness/roughness analysis in the face of samples with high heterogeneity.

All thickness results are plotted in fig.1.19 to show better comparisons, between the two techniques and among different sample types as well.

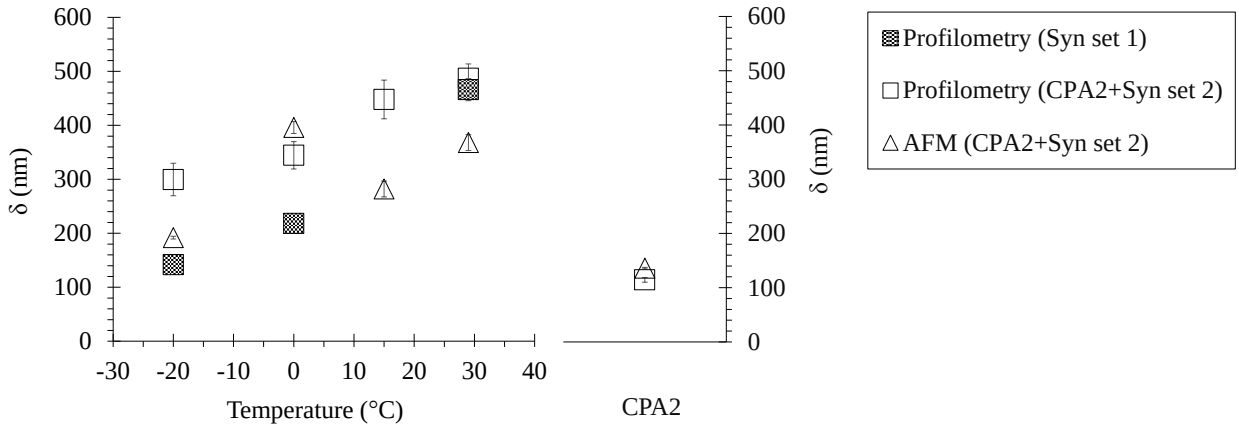

Figure 1.19: Thickness of CPA2, Syn -20°C, Syn 0°C, Syn 15°C and Syn 29°C, analyzed via AFM and profilometry.

APA layer of CPA2 had the lowest thickness compared to the synthesized ones. It was also proven to exhibit

a more regular and uniform feature (see S_q in table 1.1), probably thanks to the standard industrial fabrication. The high heterogeneity of the synthesized samples was attributed to unavoidable factors existing in the manual synthesis operation. What stands out in this figure is that the synthesized films' thicknesses raise as a function of temperature according to the profilometry thickness results of both sample sets. However, this positively temperature-dependent trend was not evident for AFM results, probably due to its low analysis representability as previously discussed. Returning briefly to the subject of the comparison between the two techniques, it has been revealed in this section that AFM is more accurate and adaptable for investigating the thickness and roughness of homogeneous samples as APA layer of CPA2. In spite of blurry profile description, profilometry was proven to be more relevant for analyzing highly heterogeneous samples as the free-standing synthesized ones in this study.

1.3.3 Void fraction estimation

The volumetric density is dependent on the void fraction, which plays an essential role in mass transport through the membrane. The estimation of void fraction f_{void} was achieved by following two steps: firstly the apparent refractive index of APA film (n_{film}) was determined via ellipsometry with knowing δ; then the f_{void} was obtained by applying effective medium approximations models (EMA) with n_{film} and n_{polymer}. As mentioned previously, both AFM and profilometry thickness estimations were taken as the reference thickness of CPA2 APA layer in ellipsometry analysis. For CPA2, it turned out difficult to achieve perfectly the model fittings, but an optimum value of n_{film} could still be found for each sampling. An average n_{film} was found at 1.36 ± 0.03 at wavelength of 658 nm. Very few information existed on n_{film} of commercial RO membrane's APA layer[3, 74]. The only reported commercial APA layer's n_{film} data were for XLE and ESPA3 membranes, with values at 1.48 and 1.43 respectively at 589 nm[74], which were close to what we obtained here. On the other hand, synthesized samples were found not suitable for ellipsometry analysis due to the pronounced surface roughness. Previous studies already revealed similar difficulty in determining the APA layer's thickness or n_{film}, due to the large roughness(ESPA1 or FT30)[8, 127].

The application of EMA models demands the knowledge of refractive index of sample's continuous phase (the dense regions, n_{polymer}) and the spread inclusion phase, the air in our case (n_{air}). Up to date, no experimental measurement has been reported on n_{polymer} of dry APA layer. In this study, three estimations of n_{polymer} have been tested: (1) 1.7, a theoretical estimation based on the group contribution method[116] and cited in different studies[8, 9]; (2) an experimental estimation of 1.6 via Cauchy model of a sub-10 nm synthesized APA dense film[59]; (3) another experimental estimation at 1.74 via Cauchy model as well on an APA nanofilm[20].

As presented in fig.1.20, CPA2 void fraction depended strongly on the choice of n_{polymer} and EMA model. The highest n_{polymer} value (=1.74) was selected as it corresponds to the densest APA film, supposed to be approximate to the dense bulk polymer. For a better comparison to data in the literature[75], the result generated from *Series* model was taken, resulting in an average void fraction (f_{void}) equal to 35%. This result

was relatively larger but still consistent with the previously reported void fractions ranging from 15% to 32% for APA layers of XLE, ESPA3 and SWC4+ RO membranes[75], which were obtained via various methods such as TEM cross-section image analysis, QCM water uptake and combination of ellipsometry analysis and *Series* model as well. $d_{\text{volumetric}}$

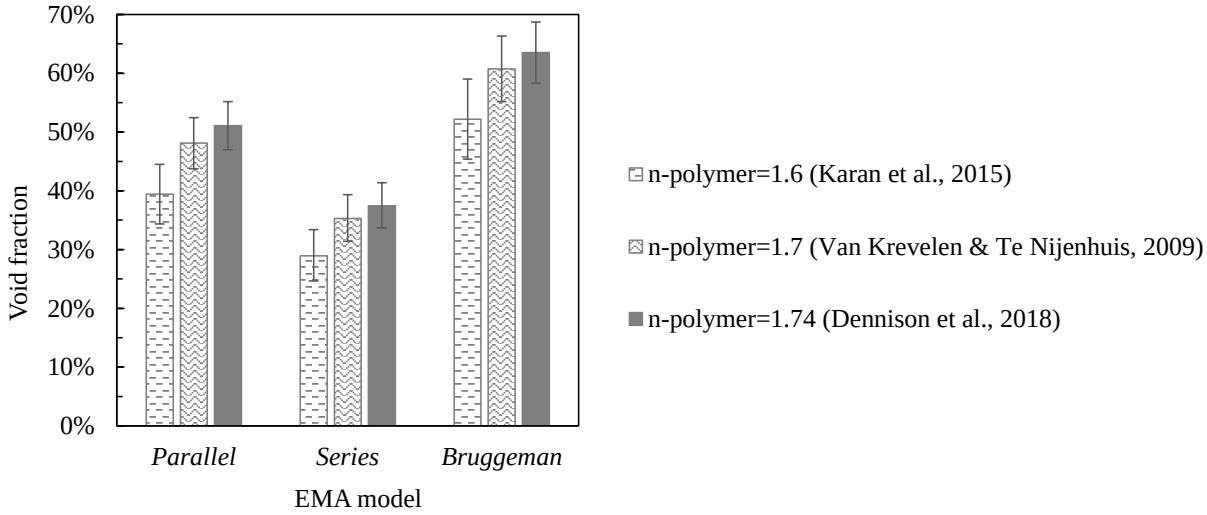

Figure 1.20: Void fraction estimation via EMA models for CPA2 APA layer by applying various n_{polymer}.

1.3.4 Density estimation

APA film's areal density (d_{areal}), apparent volumetric density ($d_{\text{volumetric}}$) and that of the dense region (d_{dense}) are summarized in table 1.2.

Table 1.2: Density estimation of APA layer of CPA2, Syn -20°C, Syn0°C and Syn 29°C. Synthesized samples are from sample set 2.

Membrane	$f_{\text{void}}(\%)^a$ AFM/Pro	RH(%)^b	d_{areal} (μg· cm^{-2})	Water uptake (wt%)	$d_{\text{volumetric}}$ (g· cm^{-3}) AFM/Pro	d_{dense} (g· cm^{-3}) AFM/Pro
CPA2	38±4 / 33±1	0	10.0±0.5	19	0.74±0.04 / 0.87±0.08	1.18±0.14 / 1.30±0.14
		88	11.9±0.6		0.88±0.05 / 1.04±0.09	1.40±0.17 / 1.55±0.16
Syn -20°C	NA	0	42.1±2.1	65	2.19±0.13 / 1.41±0.21	NA
		91	69.5±3.5		3.62±0.22 / 2.32±0.35	
Syn 0°C	NA	0	67.1±3.4	36	1.69±0.13 / 1.95±0.24	NA
		92	90.9±4.6		2.30±0.18 / 2.64±0.33	
Syn 29°C	NA	0	81.3±4.1	38	2.21±0.2 / 1.67±0.18	NA
		92	112.0±5.6		3.04±0.28 / 2.30±0.24	

[a] Estimated from ellipsometry analysis and *Series* EMA model (with $n_{\text{polymer}} = 1.74$). [b] No swelling took place between 0%RH and 92%RH.

For CPA2 APA layer, given that thickness estimations from AFM ($\delta_{\mathrm{AFM}} = 136$ nm) and profilometry ($\delta_{\mathrm{Pro}} = 115$ nm) were close, the apparent volumetric densities deduced from the two obtained thicknesses appeared finally close. As for dry CPA2 APA layer, the $d_{\mathrm{volumetric}}$ was at 0.74±0.04 g·cm^{-3} and 0.87±0.08 g·cm^{-3} respectively from AFM and profilometry analysis. An averaged dry density at 0.81 g·cm^{-3} was obtained. This value was relatively lower than the averaged density at 1.26 g·cm^{-3} for several commercial APA layers (ESPA3, XLE and SWC4) reported by Lin *et al.,* (2016), but close to the density of XLE around 1 g·cm^{-3}[74]. As discussed before, an accurate thickness characterization still remains challenging in face of the high heterogeneity and roughness of the APA layer. Hence the density variation might raise from different thickness characterization techniques, as the thickness was analyzed via ellipsometry in Lin's work compared to AFM in our study.

On the other hand, the variation might also be explained by different proper properties of these commercial layers. The group of Lin [75] have reported the areal densities of ESPA3, XLE and SWC4+ were at 13.8 μg·cm^{-2}, 14.06 μg·cm^{-2} and 13.4 μg·cm^{-2} respectively via QCM in another study. Moreover, Zhang *et al.,* (2009) reported dry areal densities of APA layers of FT30 and LF10 at 20.5 μg·cm^{-2} and 23.5 μg·cm^{-2} by using the same techniques[127]. It should be addressed as well that FT30 and LF10 are coated by PVA[17], which avoided an accurate areal density investigation for APA layers. Above all, it should be noted that the areal density ($d_{\mathrm{areal}} = 10.0$ μg·cm^{-2}) of CPA2 APA layer was significantly lighter than that of all above RO membranes, while the CPA2 showed an equivalent thickness (based on areal density data, if we suppose that CPA2 has similar dense structure as ESPA3, XLE or SWC4+, then it is supposed to only have a thickness less than 85 nm, which appears unrealistic according to our both profilometry and AFM analyses). Furthermore, it was also demonstrated in above ellipsometry analysis that CPA2 APA layer exhibited a relatively larger void fraction ($f_{\mathrm{void}} = 35\%$) than other RO membranes (ESPA3, XLE or SWC4+, f_{void} around $15\% \sim 32\%$). All above discussions (void fraction, volumetric and areal density comparisons) suggested a relatively looser structure with higher void fraction for the APA layer of CPA2.

With respect to CPA2's dense region, an averaged d_{dense} was found around 1.24 g·cm^{-3}. In the literature, densities ranging from 1.2 to 1.44 g·cm^{-3} have been reported for synthesized APA nanofilms by different authors[20, 32, 59]. They fabricated APA nanofilms with thickness around 10 nm, hence no aggregate void is supposed to form inside these films. Consequently, these reported densities were supposed to correspond to that of the dense regions for a thicker commercial APA layer (apparently ~ 100 nm thick). Moreover, the dense region density found in the present work was also consistent with the dry density of 1.2 g·cm^{-3} reported for a APA molecular model[64], which represented the bulk APA polymer.

The synthesized samples showed very high dry apparent volumetric densities, ranging from 1.69 g·cm^{-3} up to 2.21 g·cm^{-3} from AFM thickness analysis and 1.41 g·cm^{-3} to 1.95 g·cm^{-3} from profilometry. Similar questionable high density has also been reported by Jiang *et al.,* (2018), where the authors reported a density up to 2 g·cm^{-3}. To our knowledge, the APA film is not supposed to have a density even higher than that of the linear para-linked aromatic polyamide p-phenylene terephthalamide (Kevlar, 1.45 g·cm^{-3}). The over-estimated

density results from AFM thickness analysis could be explained by the lack of representability of this technique in face of the very high heterogeneity of our synthesized samples, as discussed in previous section. However, it should be addressed that the thicknesses of synthesized samples were also sub-estimated by profilometry. An evident compression from profilometry tip on CPA2's top-surface has been noted in previous section. However, it turned out that such compression effect might also exist on synthesized sample, which was covered by the pronounced surface roughness thus has not been successfully revealed in previous discussions. On the other hand, the thickness increasing trend as a function of synthesis temperature was still verified by areal density data, as dry d_{areal} arose from 42 μg·cm^{-2} to 81 μg·cm^{-2} when temperature arose from -20°C to 29°C. Since our free-standing films had thicknesses of hundreds of nanometers, their areal densities turned out more than ten times heavier than that of synthesized APA nanofilms[20, 55].

The CPA2 performed a water sorption at 19 wt%, which was in the same range with reported water uptake for APA layers of SW30 and FT30 at 20.1% (95%RH)[70] and 23% (unknown RH)[66] respectively. Meanwhile, it should also be noted that these two RO membranes are coated with PVA[17, 70], which might affect the apparent water sorption behavior. The average hydrated d_{dense} of CPA2 (from AFM and profilometry thickness analysis) was estimated at 1.48 g·cm^{-3} at 88%RH, which fell into the range of hydrated densities of APA nanofilms fabricated by Foglia *et al.,* (2017), varying between 1.35 $\sim$ 1.52 g·cm^{-3}[32] at 100%RH. However, this value should be taken with caution, as it was only valid when the water uptake behavior was homogeneous inside the film (in both void and dense regions), which seemed questionable at high RH. Meanwhile, Foglia *et al.,* (2017) reported that water uptakes for their nanofilms varied between 9 wt% and 24.4 wt%, with an average value around 15 wt%. This relatively lower water uptake compared to that of commercial APA layers could be explained by less presence of void space, which reduced the water adsorption sites.

Free-standing films had a significantly higher water sorption than that of commercial APA layers or synthesized nanofilms, with 65 wt%, 36 wt% and 38 wt% for Syn -20°C, Syn 0°C and Syn 29°C (sample set 2). These notable water sorption abilities are supposed to be correlated with the chimney-like structure on the top-surface, which provided a large number of adsorption sites. As for Syn -20°C, it exhibited the most orderly and smallest chimney-like structures, which formed the largest adsorption surface and finally led to a remarkable water uptake at 65 wt%.

1.3.5 Chemical structure of CPA2 aromatic polyamide active layer

1.3.5.1 Conventional and newly proposed chemical structure descriptors

The conventional chemical structure hypothesis of APA comes from the classical chemical crosslinking of linear polymers. It considers the APA film as the combination of two structural fractions as presented in fig.1.21: the crosslinked fraction (X) and linear fraction (Y), the sum of which is equal to 1 ($X + Y = 1$).

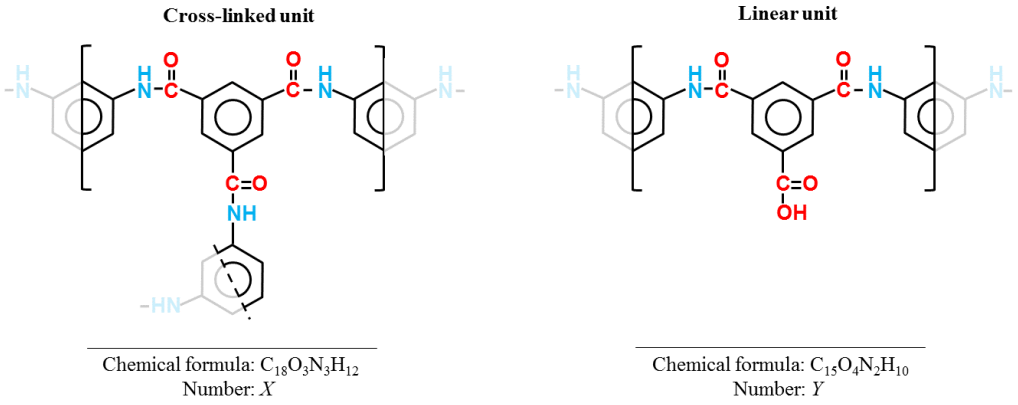

Figure 1.21: Chemical units in the conventional scheme for APA.

The conventional descriptor of crosslinking degree (χ), is defined as the crosslinked structure proportion in the system [1, 59, 62, 68, 93, 115]. According to the chemical formula, the oxygen content (O, %) of the polymer is proportional to $3X + 4Y$ while the nitrogen content (N, %) is proportional to $3X + 2Y$, then χ could be calculated from:

$$\chi = \frac{X}{X+Y} = \frac{6}{1+\frac{O}{N}} - 2 \tag{1.10}$$

However, this method could not escape from several drawbacks. Firstly, χ is only determined by O/N ratio, hence such method is unable to distinguish the systems with similar O/N but various carbon contents. Besides, the conventional structural hypothesis doesn't consider the possible existence of monomers, oligomers or terminals. As a consequence, it is unable to describe precisely a real APA structure containing non negligible amount of head and tail ends.

The present study proposes a new set of chemical units, containing a TMC unit, a MPD unit, a hydroxyl terminal unit belonging to an unreacted TMC acid group and a hydrogen terminal unit belonging to an unreacted MPD amine group. The number of such units is called a, b, c, and d, respectively. These units are shown in fig.1.22.

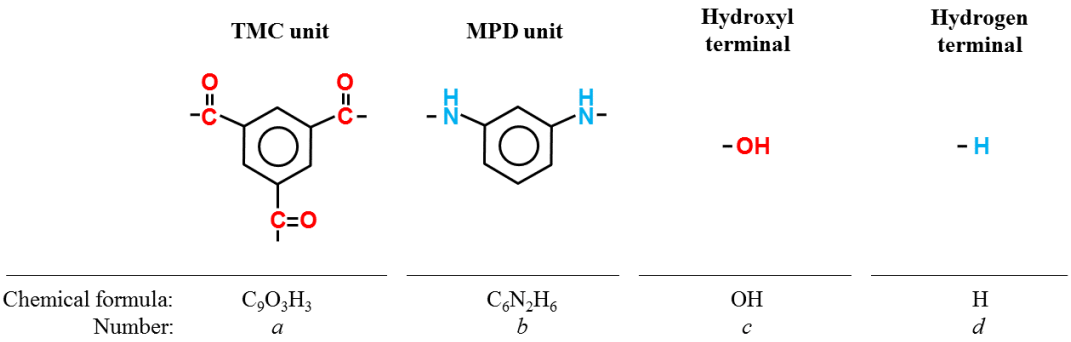

Figure 1.22: Chemical units in the new scheme for APA.

The elemental composition can be expressed by the numbers of units:

$$\begin{aligned} \mathrm{C} &= 9a + 6b \\ \mathrm{N} &= 2b \\ \mathrm{O} &= 3a + c \end{aligned} \tag{1.11}$$

where C is the carbon content (%). The number of $-$CO terminals of TMC frameworks which are not connected with hydroxyl terminals from the amide linkage, should be equal to the number of $-$NH terminals in MPD frameworks which are not connected with hydrogen terminals:

$$2b - d = 3a - c \tag{1.12}$$

On the basis of above equations, the connection degree of acyl groups (f_{ac}) or amine groups (f_{am}), which is equivalent to the crosslinking degree, is defined as total amide linkages out of corresponding potential sites to form amide bonds:

$$\begin{aligned} f_{ac} &= \frac{n_{\mathrm{CONH}}}{n_{\mathrm{COOH}} + n_{\mathrm{CONH}}} = \frac{3a - c}{3a} = (2 - \frac{3\mathrm{O}}{\mathrm{C} - 3\mathrm{N}}) \\ f_{am} &= \frac{n_{\mathrm{CONH}}}{n_{\mathrm{NH_2}} + n_{\mathrm{CONH}}} = \frac{2b - d}{2b} = (\frac{2\mathrm{C} - 3\mathrm{O}}{3\mathrm{N}} - 2) \end{aligned} \tag{1.13}$$

where n_{CONH} is the number of amide bonds, n_{COOH} is the number of acyl groups and $n_{\mathrm{NH_2}}$ is the number of

amine groups. The MPD to TMC ratio ($r_{m:t}$), could be simply given by:

$$r_{m:t} = \frac{b}{a} = (\frac{9\mathrm{N}}{2\mathrm{C} - 6\mathrm{N}}) \tag{1.14}$$

These newly proposed descriptors f_{ac}, f_{am} and $r_{m:t}$ are capable to give more detailed and comprehensive information on the chemical structure of APA layer, hence they have been applied together with χ in the chemical analysis of top- and back-surface of CPA2 APA layer below.

1.3.5.2 Chemical structure analysis via XPS

In the XPS analysis, little quantity of sulfur (S) of elemental percentage less than 1% was detected for all CPA2 samples. On one hand, this observation suggested that there existed some heterogeneous regions for CPA2, where the APA layer's thickness is supposed to be sub-dozens nm, hence allowing the support layer to be detected by XPS from the original top-surface. On the other hand, it also suggested that a part of the support was somehow trapped into the APA structure, hence this quantity has not been successfully eliminated during the dissection process, as sulfur was also detected for dissected top- and back-surface samples.

Given the presence of sulfur, the chemical composition of APA layer should be corrected by eliminating the corresponding elemental contributions of C and N from the support according to the support's chemical formula. In the literature, the support layer's chemical composition of FT30 RO membrane was reported as that of theoretical polysulfone (PSf) via RBS analysis[16, 83]. In recent studies, the support layer of other commercial or synthesized thin film composite RO membranes was also conventionally considered as PSf[75, 105, 126]. However, it should be addressed that support layers of RO membranes might vary according to the membrane manufacturer. Baker (2012)[7] indicated the support layer of NF membrane fabricated by Hydranautics (CPA2 membrane's manufacturer) was sulfonated polysulfone (SPSf). Moreover, the information given by Hydranautics on CPA2 support layer's type remains blurry. According to our exchanges with the manufacturer, the support layers might not be identical for all membrane types. With respect to CPA2, the support might be PSf or sulfonated polyethersulfone (SPES).

In order to verify whether the nature of support would have significant influence on final APA chemical compositions after the correction, correction tests have been performed with assumptions of six different support types: PSf, SPSf (with one or two sulfonated aromatic rings), polyethersulfone (PES) and SPES (with one or two sulfonated aromatic rings). Detailed results are presented in Appendix.A1. The results demonstrated that the support type affected much the chemical composition correction of APA layer, as the obtained elemental percentages performed a variation range around 4% for C (%) and 2 % for N (%) and O (%) (with presence of sulfur less than 1% in this study). Notably, these variation ranges represented quantification errors around 16% and 6% for N (%) and O (%), respectively, which would clearly lead to various chemical structure estimation

results for APA. All above discussions highlighted the importance of a good knowledge of support layer type for APA chemical composition determination, which has not been considered in previous publications. Nonetheless, in face of lack of such information, in our study the chemical composition correction was finally realized by taking support's chemical formula as that of polysulfone's ($C_{27}O_4H_{22}S$), which was conventionally used in the literature for other RO membranes. The corrected average elemental percentages (C, O and N) of CPA2 active layer are presented in table 1.3. The hydrogen is not quantifiable by XPS thus its percentage is not presented.

Table 1.3: Chemical composition of CPA2 active layer. Elemental percentages exclude hydrogen because hydrogen is not quantifiable by XPS.

CPA2 acrive layer	C (%)	O (%)	N (%)
original top-surface	72.1±0.8	17.0±0.9	10.9±0.5
dissected top-surface	73.1±0.5	15.4±0.4	11.5±0.4
back-surface	70.3±0.4	15.0±0.4	14.7±0.4

The CPA2 had an elemental composition roughly around 72/16/12 for C/O/N. No relevant difference was observed between original top-surface and the dissected one, which confirmed together with the observation in fig.1.7 that the dissection process did not modify both morphological and chemical structures of APA layer. Meanwhile, there existed a significant difference between the top- and back-surface, as the top-surface was richer in carbon and oxygen but poorer in nitrogen. This observation was consistent with the chemical depth heterogeneity reported for certain active layers of commercial RO membranes in the literature[17].

The chemical descriptors introduced above are presented in table 1.4.

Table 1.4: Chemical structure descriptors for CPA2 active layer.

		O/N	χ	f_{ac}	f_{am}	$r_{m:t}$
CPA2 layer	orignial top-surface	1.56±0.16	0.34±0.14	0.70±0.15	0.84±0.26	1.25±0.12
	dissected top-surface	1.34±0.08	0.57±0.08	0.80±0.08	0.90±0.16	1.34±0.09
	back-surface	1.02±0.05	0.97±0.08	0.28±0.15	0.16±0.10	2.53±0.20
active layers, Coronell *et al.,* (2011)[17]	ESPA3 top-surface	1.25	0.66	0.98	1.20	1.22
	ESPA3 volume	1.10	0.86	0.71	0.60	1.76
	ESPAB top-surface	1.46	0.44	0.87	1.13	1.16
	ESPAB volume	1.00	1.00	0.86	0.75	1.71
	SWC5 top-surface	1.10	0.86	1.28	1.94	0.99
	SWC5 volume	1.02	0.98	0.86	0.77	1.68
	NF90 top-surface	1.25	0.66	1.10	1.53	1.08
	NF90 volume	1.10	0.85	0.89	0.88	1.51

The conventional crosslinking degree and new descriptors gave different estimations on CPA2 active layer's chemical structure. The top-surfaces had an average χ around 0.45 while the back-surfaces exhibited a double value around 0.97. On the contrary, the f_{ac} and f_{am} demonstrated that the top-surfaces exhibited a higher connection degree (more than 0.7) for both acyl and amine groups, while the corresponding connection degrees for back-surface were less than 0.3, which suggested a better reticulation state on the top-surface. Such contrast might be explained by the existence of chain ends, which weakened the applicability of the conventional crosslinking degree. Meanwhile, $r_{m:t}$ showed that the MPD:TMC monomer units ratios decreased from the bottom towards the top. This observation confirmed the hypothesis that MPD quantity declines along its diffusion direction, finally generating a film for which the top-side is rich in TMC while the back-surface (interface region) is rich in MPD[33, 35]. A lower back-surface reticulation might be related to the hydrolysis of acyl chloride group at the polymerization interface. Water could react with acyl choride groups in this region[71], hydrolyzing (deactivating) them into carboxylic acid groups and finally weakening the connection[62].

Similar chemical heterogeneity along the APA layer's thickness was studied by Coronell *et al.,* (2011). Instead of analyzing the top- and back-surface independently, the authors implemented Rutherford backscattering spectrometry (RBS) to investigate the layer's volume-averaged chemical composition, while XPS was used to study the top-surface's[17]. APA based active layers of several commercial RO/NF membranes were investigated in their study and the corresponding data were used to calculate the conventional crosslinking degree and the new descriptors, presented in table 1.4. It was interesting to note that these samples shared the same general trend as CPA2, as group connection degrees raised while the $r_{m:t}$ decreased from the back to the top side. Meanwhile, certain f_{ac} and f_{am} of XPS results in their study were found superior to 1, probably due to a high analysis error. It should be addressed that the authors declared the existences of both depth-heterogeneity and depth-homogeneity for these membranes, which differed from the observation obtained here. The authors quantified the acyl groups by performing Ag^+ probing at pH = 10 and observed the distribution of acyl group was heterogeneous for ESPAB and NF90 while homogeneous for ESPA3 and SWC5. More investigations remain to be assessed to offer explication on these different conclusions.

In addition, the final chemical composition quantification results of synthesized samples (set 1 and set 2) remained uninterpretable thus are not presented here. The interferences on the final chemical quantification of these samples arose from the addition of chemicals such as the neutralizer TEA and anti-oxidant sodium metabisulfite during the synthesis, or exterior pollution as silicon powder from the glass ware. Certain quantity of sodium metabisulfite was supposed to remain with the APA films of sample set 1 after the polymerization, because the element Na was detected. With respect to samples of set 2, element silicon was detected. Besides, their raw XPS data presented unrealistic APA chemical structures, as f_{ac} and f_{am} were superior to 1. This was possibly attributed to the presence of TEA. Tests demonstrated that these data only became realistic (as f_{ac} or f_{am} decreased into a normal range) under the assumption that TEA contributed around 23% of the final carbon element quantity. This value corresponded to TEA's carbon contribution at the initial interface. Nonetheless,

its carbon contribution is supposed to vary along with the polymerization time and also with different reaction regions. As a consequence, the remaining TEA quantity was unknown, hence the composition correction was not possible to be launched.

1.3.5.3 Chemical structure analysis via AFM-IR spectra

Due to high analysis errors of AFM-IR, only a qualitative analysis was performed based on the obtained AFM-IR spectra here, fig.1.23.

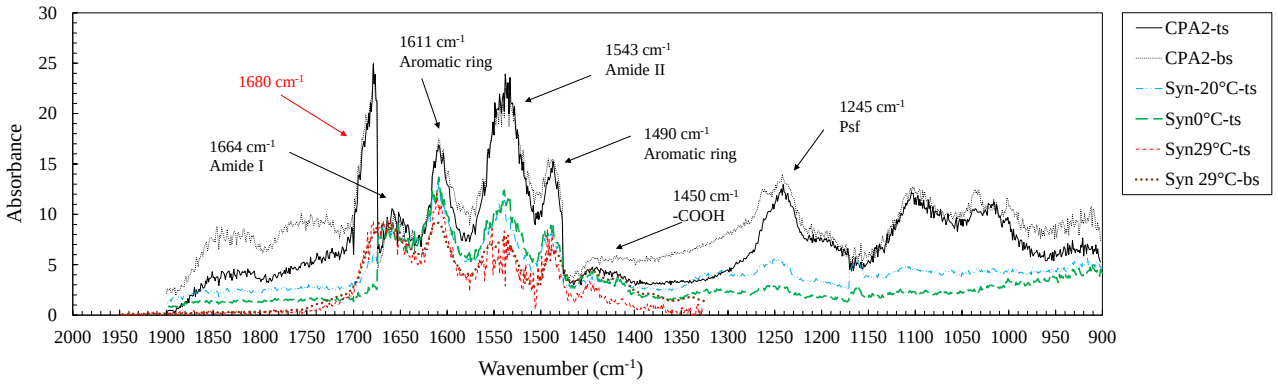

Figure 1.23: AFM-IR spectra of top- and back-surface of CPA2 APA layer, top-surface of Syn -20°C, top-surface of Syn 0°C, top- and back-surface of Syn 29°C (sample set 2).

The CPA2 APA layer and synthesized APA films gave similar typical peaks, with peaks of amide I at 1664 cm^{-1}, aromatic ring at 1611 cm^{-1} and 1490 cm^{-1}, and amide II at 1543 cm^{-1}. Meanwhile, the peak of carboxylic acid was also observed at 1450 cm^{-1}[84]. Based on current analysis, no qualitative difference was observed between top- and back-surface for CPA2 and Syn 29°C. Distinct from the synthesized samples, specific peaks were present around 1680 cm^{-1} and 1245 cm^{-1} for dissected CPA2 top- and back-surface. As mentioned previously, the element sulfur, which is supposed to be originated from the PSf support, was detected for CPA2 APA samples in XPS analysis. Hence the peak at 1245 cm^{-1} was probably attributed from C−O−C asymmetric stretching vibration of PSf[115]. However, peaks assignable for PSf are not supposed to be present at 1680 cm^{-1}. This peak might come from unknown composition used during the fabrication, which remained inexplicable here. More investigation are required to do the identification.

1.4 Conclusion

Similar to other RO membrane or conventional synthesized APA fims, a ridge-and-valley top-surface and a flat back-surface morphology was observed for the APA layer of CPA2. The ridge-and-valley structure formed on a dense bottom around 40 nm thick, extending upwards and finally giving a thickness around 136 nm. It turned out that AFM is only adapted for relative flat surface such as the top-surface of CPA2 APA layer. Meanwhile, it was revealed that profilometry tip compressed the sample's surface.

Compared to uncoated fully aromatic polyamide layers of other RO membranes (such as XLE, ESPA3 and SWC4+), CPA2 APA layer had a looser structure, larger void fraction (35%) accompanied with lower dry apparent volumetric density (0.81 g·cm^{-3}) and hydrated density (0.96 g·cm^{-3}). Moreover, the dry and hydrated densities of the dense regions were estimated respectively at 1.24 g·cm^{-3} and 1.48 g·cm^{-3}, both corresponding well to the data of very dense APA nanofilms in the literature.

Based on the application of new descriptors of chemical structure of APA, it was revealed that CPA2 was also chemically depth-heterogeneous. Its top-surface was proven to be richer in TMC units and more connected than the back-surface. The poorer connection of the back-surface was supposed to be attributed to the hydrolysis of reactive acyl chloride groups into unreactive carboxylic acid groups at the organic-aqueous interface (=back-surface of the film). This result was in contradiction with the tendency obtained from the classical crosslinking degree, suggesting that the latter may be not suitable for analyzing real APA films, which are supposed to have chains ends.

Free-standing films, synthesized directly at organic-aqueous interface without support at four different organic phase temperatures (-20°C, 0°C, 15°C and 29°C), exhibited as well a multi-level topology as 'dense bottom + chimneys-like structures'. Similar to commercial APA layer, their back-surface were flat. These films were extremely heterogeneous and had a pronounced roughness, which prevented the application of ellipsometry analysis. Moreover, neither AFM nor profilomery were capable to give a representative and accurate thickness estimation. The profilometry was also proven to have an compression effect on synthesized films' surfaces. From a rough estimation by profilometry, these films are supposed to be at least 300 nm thick, probably underestimated.

The synthesis temperature had an effect on film's morphology (such as the size and distribution of chimney-like structures), but the corresponding mechanism remained not clear. On the other hand, a positive thickness-temperature correlation was confirmed. Furthermore, based on the notable water uptake (up to 65 wt%), the formation of chimney-like structures on the top-surface turned out to play an important role for the film's water uptake behavior, since such structures offered a great adsorption sites for water molecules.

Besides, this work offered information on the selection of thickness characterization techniques (especially for AFM and profilometry) for APA samples.

In summary, this experimental work gave importance information on the active APA layer of commercial CPA2 RO membrane's chemical depth-dependent heterogeneity and dry/humidified densities of the dense regions, which served as reference data for the construction of APA molecular models in this PhD project. Nonetheless, structural properties of free-standing films, such as void fraction, chemical structure and density, wait to be further investigated.

Chapter 2

Design and characterization of an aromatic polyamide model of RO active layer membrane

2.1 State of the Art

The knowledge on the membrane's structure and the mechanism of water/solutes transfer is essential to improve the membrane performance in industrial application and also on the design of new efficient membranes. However, the acquisition of such knowledge is limited by experimental analyses. The water/solutes transport through the membrane takes place at the molecular level, therefore atomistic molecular modeling is able to give an accurate understanding of not only the RO membrane's atomistic structure, but also the structure properties-thermophysical properties correlations. For example, it performs detailed and quantitative analyses on membrane's microscopic spatial structures as chemical structures including functional group distribution and crosslinking degree, and as well the correlation between structures and the water/solutes sorption and further diffusion inside the membrane. Up to date, around thirty molecular modeling studies have been applied on RO membrane's active layer in order to investigate the transport mechanisms of water, salt or organic molecules through the membrane.

Aromatic polyamide is an amorphous polymer, hence the construction of such molecular model is complicated. There exist various ways to establish the APA molecular model in the literature, generally divided into two groups: some established the model by connecting APA linear chains, while others constructed the polymer structure by connecting the monomers to mimic the real interfacial polymerization (IP) process. Moreover, there exist also few studies in which the APA polymer was built via coarse-grained models.

In this section, the state of the art of dry APA molecular model constructions, together with obtained dry APA polymer structures in the literature are reviewed.

2.1.1 From linear chain to crosslinked network

The basic idea of chain bridging is to insert single or several linear polymer chains, which owns a given number of free acyl groups. Then an amount of monomers (especially MPD) are inserted. The linear chains are crosslinked by using MPD as bridge: one MPD is capable to form two amide bonds with two free acyl groups from either inter- or intra- chains.

The first APA molecular model was constructed by Kotelyanskii *et al.,* (1998)[66] via chains-bridging construction with the objective to mimic water and salt transport in RO FT30 membrane. The authors inserted in the simulation box a single linear polyamide chain (62 'MPD+TMC' repeat units) and some MPD monomer units at a preset density at 1.38 g·cm^{-3} and then 'crosslinked' the free acyl groups 7 ± 2 Å apart with the MPD as bridge. The authors finally realized six bridging. On the basis of this given information, their crosslinked samples exhibited a conventional crosslinking degree around 20%. Then water molecules were successively inserted into the box by respecting a water content at 23 wt% according to the experimental data of FT30's APA layer. In order to relax the polymer's configuration, the energy minimization was applied, followed by the annealation process via *NVT* (300 K) for 100 ps. Then the salt was inserted, followed by another minimization stage. The production stage was launched via *NVT* (300 K) or *NPT* (300 K, 1 bar) for 5 ns.

For both linear and crosslinked systems, the authors obtained a similar hydrated density around 1.295 g·cm^{-3} in *NPT* (300 K, 1 bar) ensemble. Through X-ray analysis of their samples, it was verified that there existed no periodicity in both linear and crosslinked samples. The authors finally demonstrated that water diffusion in the membrane followed a 'jump' diffusion process and concluded that the success of the salt rejection by FT30 was due to a lower mobility inside the membrane due to interactions with polar groups of the membrane.

In addition, in this study the acyl chloride groups were directly presented as carboxylic acid group, which remained protonated after the crosslinking process. Hence this simulation mimicked more the membrane state for a pH below 8.97[16]. Moreover, the authors reported experimental hydrated density for APA layer of FT30 RO membrane at 1.38 g·cm^{-3} with a water content at 23 wt%. The hydrated density at 1.38 g·cm^{-3} has been latterly taken as the preset density of initial dry monomer simulation boxes[47, 78, 112], as at this density the monomers stayed close to each other, which facilitated the successive monomer connections. Moreover, a dehydrated density has been deduced around 1.1 g·cm^{-3} from the study of Kotelyanskii *et al.,* (1998) as well. This estimated dry density has also been applied in simulation study as initial preset density[121, 122] or in experimental studies as reference parameter for structural characterizations such as thickness estimation [83, 84, 127].

Following the construction strategy of Kotelyanskii *et al.,* (1998), various APA models were constructed with larger size. In the study of Hughes *et al.,* (2010, 2012)[52, 53], the configuration of acyl group was taken as hydrolyzed and protonated form as well. 24 linear chains with 46 monomeric units at each (1104 monomeric units in total) were initially solvated in water under ensemble *NPT* (300K, 1 bar) for 2 ns by respecting a water content of 23 wt%, hence no dry structure was further investigated. Then MPD monomers were inserted to

bridge two TMC units, of which the acyl groups were 5∼9 Å apart. The authors preset 19.4% of TMC groups were crosslinked. After the connection, the polymer was equilibrated for another 1 ns, and the box obtained was around $50 \times 50 \times 100$ Å^3.

Xiang *et al.,* (2013)[121] prepared the system by folding 18 linear polymer chains (each containing around 24 monomeric units, hence around 430 monomeric units in total) via configurational-bias Monte Carlo algorithm. The dry polymer box had a dimension around $72 \times 36 \times 40$ Å^3 to match the experimental dry APA density at 1.1 g·cm^{-3}, which was deduced from the study of Kotelyanskii *et al.,* (1998). Different from Kotelyanskii *et al.,* (1998), the acyl groups were deprotonated and neutralized via the addition of ions in order to mimic the fouling condition with alginate. The chains' chemical composition were predetermined to reach authors' synthesized APA layer surface's O/N ratio around 1.6 by connecting two acyl groups by one MPD in each chain. Since authors only focused on the fouling molecules - APA surface interaction, the crosslinking within the system was not considered. According to the available chemical information, the conventional crosslinking degree is still be able to estimated at around 24%, with a MPD:TMC ratio at 1.16. In a later research [122], this group crosslinked the polymer chains by inserting MPD monomers, which served to form bridge between TMC units. According to the authors, the APA polymer finally exhibited a conventional crosslinking degree at 60%.

Ding *et al.,* (2014)[21, 22] inserted into the box 5 identical linear chains, each containing 50 monomeric units (250 monomeric units in total). The authors chose a low initial density at 1 g·cm^{-3} in order to leave more space for successive crosslinking. This density was very close to that used in the study of Xiang et al, 2013[121], at 1.1g·cm^{-3}. Then 250 MPD were inserted. MPD, for which two nitrogen in amine groups met the heuristic distance at 7.6 Å with the carbon in acyl group, were allowed to react. Finally a fraction of reacted acyl group at 80.8% was achieved. The box dimension was around $72 \times 36 \times 40$ Å^3. The membrane was solvated in a further step, hence the structure was not studied in a dry state. However, a dehydrated density around 1.01 g·cm^{-3} could be deduced from the hydrated density and water content value. This value should be taken with caution in view of the possible membrane swelling. Meanwhile, the average cavity diameter, in other words the free volume diameter, was found to be at 5.2 Å for the hydrated membrane.

The advantage of chain-bridging polymer construction is that MPD monomers are fully connected, which leads to a final structure close to that of conventional chemical units. Therefore the application of the conventional crosslinking degree χ remained interesting in these cases. On the other hand, a general drawback of above molecular models lies on the questionable production of thermophysical properties. As introduced, the water content and hydrated density reported for FT30 in the study of Kotelyanskii *et al.,* (1998) were generally taken as preset parameters for the construction, while the relaxation time for these models remained short (only hundreds of ns). Therefore there existed risks that the APA polymers were not well relaxed before the production of thermophysical parameters. It could be observed that even with various crosslinking degrees (varing from 10% to 60%), these models exhibited similar water content around 23 wt% and close hydrated densities varying from 1.32 to 1.38 g·cm^{-3}, which stayed very close to the corresponding preset values.

2.1.2 From monomers to crosslinked network

The chains-based construction permits to define the crosslinking degree of the film model. Conversely, it demands the artificial intervention on the design of polymer structure, where the linear chains are taken as the basis of the further crosslinked network. However, since a real APA film is synthesized from interfacial polymerization (IP), its crosslinking state should be less regular and more intricate.

From this assessment, Harder *et al.,* (2009)[47] invented a progressive amide covalent bond formation protocol by mimicking the real IP process. In their study, 250 MPD and 250 TMC monomers have been randomly inserted into the box, a target density at 1.38 g·cm^{-3} was obtained after energy minimization and a short molecular dynamics (MD) simulation. The TMC in this study had acyl chloride groups instead of carboxylic acid groups. Then amide bonds were formed in NVT ensemble (340K) every 1 ps if the distance between the carbon of free acyl chloride group and nitrogen of amine groups were within 3.25 Å, and this criteria was modified to 3.5 Å to expedite the crosslinking afterwards. With the advancement of polymerization, the free monomer residuals diminished, and intermolecular potential between the target carbon and nitrogen atoms were modified to increase attractions. In a next stage, in face of the self-limiting barrier formation, additional TMC monomers were inserted near free MPD in order to finally maximize the connection. Through all bond formation, the energy minimization was performed every 1 ps. In the end, unreacted monomers were removed and final MPD:TMC ratio was close to 1. According to authors, the generated membrane owned a conventional crosslinking degree at 37%, its free volume radius performed a bimodal distribution at 3 Å and 5 Å. The former and latter was in agreement with experimental network pore size at 2 Å and aggregate pore size at 4 Å of FT30 membrane[63], respectively. Nevertheless, it should be noted that Harder's model was a simple model. In real process, the acyl chloride groups are finally hydrolyzed into carboxylic acid groups, while such transition was not mentioned in Harder's work.

This progressive polymerization protocol was adopted with modifications by many later studies. In summary, the principle of Harder's construction method was to connect monomers at a heuristic distance, and the connection was further reinforced via specific methods such as modification of potential or addition of extra monomers.

Harder's group[78] later implemented this protocol to construct a system of 8 times larger scale but without the step of free MPD addition during bond formation stage. Their system ended with a higher MPD:TMC ratio at around 1.11 and it led to a hydrated density of 1.34 g·cm^{-3}. According to the authors, their polymer models performed a satisfying estimated rejection rate of salt at 99%, which proved the possible application of molecular model in simulating real membrane properties.

Araki *et al.,* (2015)[6] also constructed APA model via a step crosslinking among monomers, and the acyl chloride groups were finally substituted by carboxylic acid groups. After the crosslinking process, the model's energy was minimized and the cell length was reduced to achieve a target density. The authors finally obtained a dry and hydrated density for plain APA film at 1.33 and 1.27 g·cm^{-3}, respectively. These data remained

questionable, as the hydrated density was smaller than the dry density. The objective of their study was to investigate the effect of presence of single carbon nanotube inside the APA structure. The authors compared the plain APA model with another one reinforced with single carbon nanotube and found that the presence of carbon nanotube led to a smaller pore size and improved the salt rejection rate.

Wei *et al.,* (2016)[118] built the polymer starting with mixture of MPD and hydrolyzed TMC monomers at a range of ratios and densities using hierarchical protocol: crosslinking was firstly performed in a cubic box with a side of 20 Å, afterwards this box was duplicated, then more crosslinking was launched after. Such procedures were repeated until obtaining the target dimension (box length around 80 Å). Addition of hydrolyzed TMC monomers was realized to improve the crosslinking efficiency. And the polymer went through heating-annealing cycles at variation of temperature between 300K and 560K and became homogeneous after 100 ns in NVT ensemble. A dry density at 1.28 g·cm^{-3} was finally obtained. And the final ratio of MPD:TMC and oxygen/nitrogen ratio were both at 1.32. Three repetition boxes led to comparable results on pore-size distribution and water content. Besides, the authors also analyzed the packing of the benzene rings and reported the presence of three structural components: parallele stacked, T-shape and linearly bonded benzene rings.

Kolev *et al.,* (2014, 2015)[64, 65] connected 300 MPD, 200 TMC and 10 dimer, respecting a criteria distance at 7 Å. In their study, supplementary artificial intervention was introduced to have a polymer which met the desired structure, such as the monomers were only allowed to interact with the initial cluster but not among themselves to achieve a large polymer size, and supplementary MPD or MPD rich units were inserted to avoid acid excess. Finally they obtained a well crosslinked structure as both connection degrees of acyl (f_{ac}) and amine groups (f_{am}) were superior to 90% with a box dimension around $7 \times 7 \times 15$ nm^3. In view of the large box dimension, the authors reported two dry density of the APA polymer, one with large void at 1.2 g·cm^{-3} and the other at 1.3 g·cm^{-3}, excluding the voids. It should be also addressed in this study, the authors have applied a long trajectory up to 1000 ns to record the properties of the dry membranes. This time was significantly long compared to equilibrium time (less than 500 ns) in other studies.

Besides above studies, the monomer polymerization methods have also been applied in other studies[39, 40, 103, 112]. Different from the others, the group of Suzuki *et al.,* 2015[112] connected the monomers at different MPD:TMC ratios of 0.25, 1, 1.5 and 4 applying hybrid Monte Carlo/Molecular Dynamics cycles with box length around 50 Å. Five repetitions were applied for each ratio. The initial density was taken at 1.38 g·cm^{-3}, adapted from the previous work of Harder [47]. Compared to Harder *et al.,* (2009), their generation process combined Monte Carlo method to decide whether to accept or not a new amide bond formation. Finally, systems with evidently varied chemical structures have been achieved, as the final MPD:TMC monomer ratios ($r_{m:t}$) varying from 0.6 to 2.5. Comparing the experimental chemical composition data of FT30 membrane, the authors claimed that the system generated from initial MPD:TMC ratio at 0.25 could represent the top-surface while the one at 1 is supposed to represent the back-surface. The dry box of MPD:TMC at 1 was hydrated with water immediately hence only a hydrated density of 1.39 g·cm^{-3} was reported after a relaxation time

around tens of ns. To our knowledge, Suzuki *et al.,* (2015) performed the first atomistic study on APA film's heterogeneity via molecular modeling. However, in terms of the structural characterization of these various interesting systems, only free volume has been investigated. Probing a hard sphere with Van Der Waals radius of a water molecule at 1.4 Å, the authors found that the systems generated from middle initial MPD:TMC ratios (such as 1 and 1.5) performed with smaller free volume around 10.5%, while systems generated from extreme MPD:TMC ratios (0.25 and 4) owned larger value around 30%. The authors claimed that systems with smaller free volume represented more the regions responsible for the membrane performances.

2.1.3 Coarse-grained models and polymerization process

Atomistic study of APA film needs an expensive computational cost, thus size of simulation box of the atomistic system is limited. In the literature, the simulation box's lengths were commonly in the order of tens of Å[21, 22, 47, 112, 121], or hundreds of Å at maximum[52, 64, 65, 78], which represented less than tenth of the real active layer thickness of a reverse osmosis membrane. In view of the depth-dependent heterogeneity of the active APA layer[17, 33, 70, 110], simulations at angstrom scale could not escape from the drawback as being incapable to fully represent the changing properties along the film's thickness. In face of this difficulty, few studies have simulated the APA films via coarse-grained modeling. For example, Nadler et Srebnik (2008)[87] implemented a cluster-cluster aggregation model to simulate the polymerization process, replacing TMC and MPD monomers by different balls. The initial MPD:TMC monomer ratio was set as 3:2. The authors revealed the polymer film had heterogeneous structure with a dense core but looser ends after the polymerization. Muscatello *et al.,* (2017)[86] replaced the benzene ring as a rigid equilateral triangle, and the amine and acyl groups by cones. These side groups were allowed to rotate before being connected. Three ratios of initial MPD:TMC at 1:1, 3:2 and 3:1 were investigated, respectively. The monomers diffused by Brownnian motion and the amide bond was formed when the carbon atom in acyl group and nitrogen atom in amine group was less than 2.375 Å apart. The bond lengths in amide bond, such as that of C-N bond, were fixed. The authors demonstrated the polymerization was self-limiting. They finally obtained films with thickness of $5 \sim 10$ nm, which exhibited heterogeneous structures, with non-uniform pore distribution and opposite concentration gradients of acyl and amine groups, as there existed more acyl groups in the upper side while more amine groups in the lower part. Compared to initial monomer ratio MPD:TMC at 1:1 or 3:1, the ratio at 3:2 led to the largest oligomer size thanks to a good availability of both acyl and amine groups.

2.2 Questions raised in this work

Remarkable efforts have contributed to the development of APA polymer models. Nonetheless, the majority of the researches focused on the water diffusion or solutes diffusion, including salt and organic molecules, through the membrane[6, 21, 22, 39, 40, 47, 52, 53, 64–66, 78, 87, 103, 112, 118, 121]. The structure of dry APA molecular

model and the corresponding structure-properties correlation remain not clearly investigated.

The researches to date has tended to construct one single type of APA model based on the experimental chemical/thermophysical parameters of one real APA sample (APA layer of FT30 membrane in most cases). There exist several drawbacks. Firstly, it should be noted the APA layer of FT30 is coated with PVA[17, 83], hence its hydrated density (1.38 g·cm^{-3}) and water content (23 wt%) data reported firstly by Kotelyanskii *et al.,* (1998)[66], which were widely used in latterly simulation studies, remained questionable as there might exist a evident contribution from its hydrophilic coating. In face of such limit, it seems difficult to correlate these built molecular models to a real APA membrane. Secondly, most of these molecular models were hydrated by two water boxes at two sides while they exhibited a thickness only around several Å. As a consequence, such thin thickness was not able to avoid the interface effect, as the density profiles along the thickness were not really flat[6, 64]. Besides, the hydration also made it difficult to deduce accurately the dry density due to possible swellings of these models.

Moreover, as MPD concentration declines with its diffusion into the organic phase during the interfacial polymerization, it was suggested that APA films had possible depth-dependent chemical heterogeneity[17, 33, 35]. However, few simulation studies have taken account of such possible heterogeneous structure. As a consequence, the few reported thermophysical properties of dry APA film might lack of representability.

Another possible limitation is that the relaxation time applied previously seemed too short (hundreds of ns in most cases) to well relax the constraints generated during the polymerization of APA systems, which led to a bias on an accurate estimation of thermophysical properties.

In face of these challenges, our study intended to construct APA molecular models by forming amide bonds between hydrolyzed trimesoyl chloride (TMC) and *m*-phenylenediamine (MPD). APA polymer boxes were constructed from a range of different preset initial ratios between MPD:TMC (0.25, 0.5, 0.75, 1, 1.2, 1.3, 1.5, 1.8, 1.9, 2, 2.5, 3, 3.5, 4 and 5). The purposes were, on one hand, to mimic APA's possible depth-dependent heterogeneous structures[17, 35] with boxes of different crosslinking degrees; on the other hand, to understand the effect of different initial monomer proportions during the IP on APA film's structure. Moreover, the generation of various APA structures was expected to help distinguish the contribution of various chemical groups such as -COOH, -NH2 and -NHCO-, hence highlighting the correlation between APA chemical structures and thermophysical properties. For MPD:TMC ratios at 0.25, 1.5 and 5, 11 repetition boxes were launched respectively in order to investigate the repeatability of our polymer construction protocol. These systems were relaxed for at least several μs in molecular dynamics *NPT iso-stress* (1 bar, 298.15 K) to achieve constant thermophysical properties.

2.3 Molecular simulation procedure

2.3.1 Molecular dynamics principle

2.3.1.1 Solving Newton equations of motion

In molecular dynamics, the motion of each atom is determinative. According to classical mechanics, the sum of forces acting upon atom i, $\vec{F_i}$, is the opposite of the gradient of its potential energy U:

$$\vec{F_i} = -\nabla_i U = -(\vec{i}\frac{\partial}{\partial x_i} + \vec{j}\frac{\partial}{\partial y_i} + \vec{k}\frac{\partial}{\partial z_i})U \tag{2.1}$$

and according to Newton's laws of motion, the resulting acceleration of atom i is obtained by:

$$\vec{a_i} = \frac{\vec{F_i}}{m_i} \tag{2.2}$$

where m_i is the mass of atom i. With the obtaining of acceleration, it is thus possible to step forward in time t, updating the atom i's velocity, $\vec{v_i}$, and position, $\vec{r_i}$:

$$\frac{d^2\vec{r_i}}{dt^2} = \frac{d\vec{v_i}}{dt} = \vec{a_i} \tag{2.3}$$

There exist several methods for the numerical integration of Newton equations of motion (eq.(2.3)), among which the Velocity-Verlet's algorithm is the most widely used. In molecular dynamics computation, the t is signed as the integration time step Δt. The atom position at time $(t + \Delta t)$, $\vec{r}(t + \Delta t)$, is calculated firstly, then the corresponding acceleration, $\vec{a}(t + \Delta t)$, is derived from the potential energy at position $\vec{r}(t + \Delta t)$, next the velocity, $\vec{v}(t + \Delta t)$, could be successively updated:

$$\begin{aligned} \vec{r}(t + \Delta t) &= \vec{r}(t) + \vec{v}(t)\Delta t + \frac{1}{2}\vec{a}(t)\Delta t^2 \\ \vec{v}(t + \Delta t) &= \vec{v}(t) + \frac{1}{2}(\vec{a}(t) + \vec{a}(t + \Delta t))\Delta t \end{aligned} \tag{2.4}$$

In this work, the standard velocity-Verlet integrator is applied to integrate Newton equations of motion.

The selection of Δt should be done carefully, as a big time step size may result in a unrealistic molecular simulation while little size demands too much calculation time. The principle is to ensure Δt is inferior to 1/10 of the smallest motion period of the system studied. Usually Δt is taken between 5×10^{-16} s to 1^{-15} s.

2.3.1.2 OPLS-AA Force Field

The optimized potential for liquid state - all atoms (OPLS-AA) force field was applied for APA systems in this study. The OPLS-AA intra/intermolecular interaction functions originated from Jorgensen *et al.,* (1996)[58] and the parameters were taken from the version distributed by code TINKER, document *tinker 7.1.2 oplsaa.prm.*

These parameters were applied in functional terms of LAMMPS in this study.

The functions of bond stretching energy ($U_{\text{bond}}(r_{ij})$) and angle bending energy ($U_{\text{angle}}(\theta_{ijk})$) are of harmonic type, as that:

$$U_{\text{bond}}(r_{ij}) = K_r(r_{ij} - r_{eq})^2 \tag{2.5}$$

where K_r is the constant, r_{ij} is the bond length between atom i and j, r_{eq} represents the corresponding equilibrium bond length.

$$U_{\text{angle}}(\theta_{ijk}) = K_\theta(\theta_{ijk} - \theta_{eq})^2 \tag{2.6}$$

with K_θ is the constant, θ_{ijk} and θ_{eq} are respectively the angle among the atom i, j and k, and the corresponding equilibrium one.

The torsional potential term is of LAMMPS's *nharmonic dihedral* style. Due to a conversion process from NEWTON to LAMMPS, the functional form of NEWTON style *po19* was taken, and the corresponding OPLS-AA parameters were converted along into this form:

$$U_{\text{torsion}}(\beta_{ijkl}) = \sum_{n=0}^{8} a_n[cos(\beta_{ijkl})]^n \tag{2.7}$$

where a_n are the constants and β_{ijkl} is the torsion angle.

And the last intramolecular potential term is the improper torsion (out-of-plane bending term), the style *cvff* is implemented:

$$U_{\text{improper torsion}}(\phi_{ijkl}) = K_\phi[1 + dcos(n\phi_{ijkl})] \tag{2.8}$$

with ϕ_{ijkl} is the improper torsion angle and K_ϕ is the constant.

The intermolecular terms include electrostatic (the Coulombic) interaction:

$$U_{\text{electrostatic}}(r_{ij}) = (\frac{q_i q_j e^2}{4\pi\epsilon_0 r_{ij}}) f_{ij} \tag{2.9}$$

with q is the charge in electron charge unit, e is the charge of electron, r_{ij} is the distance between the charges on the two atoms, ϵ_0 is absolute dielectric permittivity of classical vacuum, and the ensemble $\frac{1}{4\pi\epsilon_0}$ is the Coulomb constant.

And the Lennard-Jones (LJ) potential is expressed as :

$$U_{\text{Lennard-Jones}}(r_{ij}) = 4\varepsilon_{ij}[(\frac{\sigma_{ij}}{r_{ij}})^{12} - (\frac{\sigma_{ij}}{r_{ij}})^6] f_{ij} \tag{2.10}$$

where r_{ij} is the distance between the two atoms i and j. r^{-6} is the attractive term while r^{-12} is the repulsive term. ε is the depth of the LJ potential well and σ is the distance at which the LJ potential is zero, for which

the standard geometric combining rules are applied as:

$$\varepsilon_{ij} = (\varepsilon_i \varepsilon_j)^{\frac{1}{2}} \tag{2.11}$$

$$\sigma_{ij} = (\sigma_i \sigma_j)^{\frac{1}{2}} \tag{2.12}$$

These interactions are applied as well for intramolecular cases when the atoms are separated by at least three bonds as that: $f_{ij} = 0$ if i, j are 1, 2 or 1, 3; $f_{ij} = 0.5$ if i, j are 1,4; otherwise $f_{ij} = 1$. The pair cut distance (R_c) was set at 10 Å in this study.

Details for applied OPLS-AA force field parameters are presented in Annexes A3.

2.3.1.3 The ensembles

In MD, the macroscopic thermodynamic quantities such as temperature, pressure, etc. are deduced from atomic properties and motions via the statistical thermodynamics. An ensemble is a statistical definition of a system with certain macroscopic thermodynamic properties.

The micro-canonical ensemble, also known as *NVE* ensemble, represents a system with fixed atom number N, volume V and total energy E, permitting the fluctuation of temperature T and pressure P. And a MD simulation by default conserves energy and corresponds to *NVE* ensemble[89].

The canonical ensemble, *NVT*, stands for a system where atom number, volume and temperature are fixed.

And for an isothermal-isobaric ensemble, *NPT*, the atom number N, pressure P and temperature T are fixed, while the volume fluctuates naturally. Since most of the experimental measurement are launched under certain pressure and temperature, the *NPT* ensemble is most relevant to the experimental data, compared with *NVE* or *NVT* ensembles. The pressure control in *NPT* ensemble could be performed in two ways, anisotropically (iso-stress/aniso) or isotropically (iso). Via iso-stress, the algorithm assigns the pressure tensor elements in all directions equal to the preset value. As consequence, the box dimensions are free to change independently, while the pressure tensor elements in all direction are almost equal. And via iso, the algorithm only ensures the average pressure tensor of different direction equal to the desired value, hence it permits the existence of pressure tensor variation among directions while box dimensions are compressed or exposed proportionally.

The choice of ensemble depends on the specific need. In this work, according to their proper characters,the three ensembles introduced above are implemented in different stages during the APA polymer box construction, so as in further box relaxation and data production.

2.3.1.4 Thermostat

A MD simulation conserves perfectly the total energy, corresponding to an NVE ensemble of statistical mechanics [89], where the kinetic and potential energies transform between each other but the total energy remains constant. Meanwhile, it should also be noted that this simulation condition differs from the real experimental conditions (under NPT or NVT ensembles, etc). Naturally the controlling of thermodynamic parameters such as temperature becomes crucial and indispensable. This controlling is called thermostatting, and the corresponding algorithms are computational thermostats.

The simplest thermostat is the velocity scaling [120]. As introduced previously, the atom's new position and velocity could be updated on the basis of Newton equations of motion (2.4), and the new instantaneous temperature T_{new} is calculated as:

$$T_{new} = \frac{\sum_{i=1}^{N} m_i(|\vec{v_i}|)^2}{3N_f k_{\mathrm{B}}} \tag{2.13}$$

where k_{B} is the Boltzmann constant (1.38×10^{-23} J·K^{-1}) and N_f (= 3N−3) is the degrees of freedom of the system. The velocity scaling thermostat compares T_{new} with target temperature T. If T_{new} is out of range of $0.9 \leq \frac{T_{new}}{T} \leq 1.1$, then the velocities of all atoms are scaled by multiplying a factor, $f_{scale} = \sqrt{\frac{T}{T_{new}}}$, in order to achieve the desired temperature. With correction at each time step, this method enables fast temperature controlling, however it turns out to be incorrect because it doesn't permit the temperature fluctuations generated from the kinetic/potential energy trading. To overcome this disadvantage, various other thermostats have been invented, such as Anderson thermostat[4], Berendsen thermostat[10], etc. Among these thermostats, the most widely used is the Nosé-Hoover thermostat, which is proposed originally by Nosé, 1984[89] and further developed by Hoover, 1985[50], allowing of the fluctuation of total energy of the system. This method is based on the adjustment of the atom velocity by a thermodynamic friction coefficient, ξ, thus the equations of motion are modified as:

$$\frac{d\vec{v_i}}{dt} = \frac{\vec{F_i}}{m_i} - \xi\vec{v_i} \tag{2.14}$$

and the ξ is obtained by:

$$\frac{d_\xi}{dt} = \frac{1}{Q}[\sum_{i=1}^{N} m_i|\vec{v_i}|^2 - (N_f+1)k_{\mathrm{B}}T] \tag{2.15}$$

where Q is fictitious mass of the extra degree of freedom, a time scale parameter for the fluctuation. T is the desired temperature. The obtained ξ serves in speeding or slow up the atom velocity. This method is believed to generate rigorous canonical ensemble. In this work, a Nosé-Hoover-chain thermostat was implemented.

2.3.1.5 Barostat

Similar to the temperature, the system's pressure computation is important and its controlling is imperative in many MD simulations. The pressure is computed based on the virial theorem. The virial, Ψ, is defined as the

sum of products between atom's coordinate $\vec{r_i}$ and acting force $\vec{F_i}$:

$$\Psi = \sum_{i=1}^{N} \vec{r_i}\vec{F_i} \tag{2.16}$$

For a real system, the total virial is consisted of an ideal gas part, $-3PV$, and a part of particle interactions, Ψ. According to virial theorem, the sum of the two parts equal to $-3Nk_{\mathrm{B}}T$, hence the pressure P could be computed:

$$P = \frac{1}{V}(Nk_{\mathrm{B}}T - \frac{1}{3}\Psi) \tag{2.17}$$

Ψ is sensitive to $\vec{F_i}$, since the force varies a lot, the pressure usually performs large fluctuation.

In general, the barostats are analogous to the corresponding thermostats, and the difference is based on the volume scaling, either in all directions or in one direction. In principle, the volume is scaled by a factor f, and this factor is determined differently according to algorithms on the basis of the variation between the desired and present system pressure. In this study, the Nosé-Hoover barostat[50] was applied. If the scaling are for all directions, the atom coordinates are scaled by a factor $f^{\frac{1}{3}}$.

2.3.1.6 Periodic boundary conditions (PBC)

To keep the total mass of the studied system constant, the periodic boundary conditions (PBC) are usually applied. A box is initially constructed with interested molecules in vacuum or in solvent, the application of PBC is to replicate this box image in all directions. All atoms in this box appear in other boxes with exactly the identical arrangements, properties and behaviors, and this is named as periodic mirror image system. When one atom move out from one boundary of the box, it would enter into the box from the opposite side. Overall, without application of PBC, the system studied is considered to have free surfaces, while with PBC, the effects of finite size and interface are removed.

For the periodic mirror image system, the calculations of inter/intra interactions follow the nearest mirror image rule: the interactions are calculated among the closest atoms. Hence, in certain cases, the calculation could be applied on atoms between two adjacent boxes rather than within the same box. Meanwhile, the cut-off radius, R_c, needs to be introduced to avoid the repeated calculation of non-bonded interactions: upon which the two atoms distance is superior to, the interactions are considered as zero thus not calculated. The set of cut-off radius should not exceed the half length of the box. Moreover, it should be noted that the non-bonded interaction potential at R_c is small but not equal to zero, thus a standard correction is applied to avoid the energy discontinuity at cut-off distance[58]. Meanwhile, a switching function could be used in the potential energy functions to achieve the same objective as well. In terms of long-range interactions, specific methods are also selected to compute them in infinite periodic systems. Long-range Coulombic interactions are usually computed via Ewald summation [29] in Fourier space, which has a more rapid convergence compared to the

summation in real space.

2.3.1.7 Temperature initialization

On starting a MD simulation, N atoms of masses m_i are inserted into a simulation box, adjusting the box volume fitting the preset density. Usually the atoms are inserted randomly or on lattice. To achieve a preset instantaneous temperature T, the atom initial velocities, $\vec{v_i}$ should make the system's total kinetic energy equal to the equipartition of kinetic energy:

$$\sum_{i=1}^{N} \frac{1}{2} m_i (|\vec{v_i}|)^2 = \frac{3}{2} N_f k_{\mathrm{B}} T \tag{2.18}$$

Hence, the principle of initial velocity setting is to ensure the total kinetic energy equal to $\frac{3}{2} N_f k_{\mathrm{B}} T$. The velocities might be chosen randomly from Gaussian distribution. For an atomic system:

$$\rho(\vec{v_{ix}}) = (m_i / 2\pi k_{\mathrm{B}} T)^{1/2} exp(-\frac{1}{2} m_i \vec{v_{ix}}^2 / k_{\mathrm{B}} T) \tag{2.19}$$

with $\rho(\vec{v_{ix}})$ is the probability density for velocity component $\vec{v_{ix}}$. Similar equations could be applied for the components of y and z, as well for the center-of-mass velocities in a molecular system. In an equilibrated system, the atom velocities follow the Maxwell-Boltzmann distribution. It should always check the system's overall momentum equal to zero.

2.3.1.8 Energy minimization

For a system containing N atoms, the potential energy of the systems of state i is a $3N$ Cartesian function:

$$U_i = f(x_1, y_1, z_1, x_2, y_2, z_2, ..., x_N, y_N, z_N) \tag{2.20}$$

The potential energy surface describes how the energy evolves along with coordinates, and the energy minimization/optimization is the process to look for the energy minimum point in this surface. Hence, the energy optimization is the process to search for the minimum of energy function. Among the various minimization algorithms, the conjugate gradients and damped dynamics algorithms [11] were applied in this work. Conjugate gradients algorithm is a first-order minimization algorithm. It moves the configuration in the direction of vector $\vec{v_i}$, which is conjugate, as computed from the gradient of potential energy (equation 2.20) $\vec{g_i}$ and the previous vector $\vec{v}_{i-1}$:

$$\vec{v_i} = -\vec{g_i} + \gamma_i \vec{v}_{i-1} \tag{2.21}$$

where γ_i is scalar constant obtained by:

$$\gamma_i = \frac{\vec{g_i} \cdot \vec{g_i}}{\vec{g}_{i-1} \cdot \vec{g}_{i-1}} \tag{2.22}$$

Subsequently the new coordinates are deduced:

$$\vec{r}_{i+1} = \vec{r_i} + \kappa \vec{v_i} \tag{2.23}$$

where κ is the integer extend parameter. With a series tests of κ, the resulting U_is are compared successively via line search method, and the lowest value of U_{min} is located as U_i when:

$$U_{i-1} > U_i < U_{i+1} \tag{2.24}$$

With continuation of the above processes, the configuration is updated progressively and finally arrives at lowest position of energy surface. In this work, the conjugate gradients algorithm of Polak-Ribiere method [97] was applied to align the newly formed amide bonds. Polak-Ribiere variant is supposed to be the most effective conjugate gradients method as it modifies γ_i as:

$$\gamma_i = \frac{(\vec{g_i} - \vec{g}_{i-1}) \cdot \vec{g_i}}{\vec{g}_{i-1} \cdot \vec{g}_{i-1}} \tag{2.25}$$

Besides, the damped dynamics algorithm[11], where the atoms' velocities are initiated at zero at beginning, was used to decrease the energy during the box relaxation process.

2.3.2 Analysis tools

2.3.2.1 Treatment of thermodynamic information

All MD simulations in this study were carried out by code LAMMPS. For LAMMPS MD simulation, three basic types of documents are the essentials: *data.system*, *in.system* and *ff.system*. *data.system* contains all system information such as atom types, charges, coordinates, connectivity and velocities, etc; *in.system* indicates the applied potential functions' types and specific simulation commands, etc.; and *ff.system* contains applied force field constant parameters.

The thermodynamic information such energy, temperature and pressure data, etc. during LAMMPS MD running are treated by local post-treatment tool LMPEVOL, which is developed specifically to analyze LAMMPS files. It calculates the corresponding mean value, standard deviation (STD, $\boldsymbol{\sigma}$) and standard error of the mean (S.E.). With N is the total sample number, the average of the quantity A is computed as:

$$< \mathrm{A} >= \frac{1}{N} \sum_{i=1}^{N} \mathrm{A}_i \tag{2.26}$$

and the standard deviation of A is obtained by:

$$\boldsymbol{\sigma} = (\frac{1}{N}\sum_{i=1}^{N}(\mathrm{A}_i - <\mathrm{A}>))^{1/2} \tag{2.27}$$

and the standard error of the mean is computed as:

$$\mathrm{S.E.} = \frac{\boldsymbol{\sigma}}{\sqrt{N_i}} \tag{2.28}$$

where N_i was independent sample number. Normally the results are divided into 5 $\sim$ 10 blocks, which are considered statistically independent. Otherwise, the N_i could be calculated from:

$$N_i = \frac{N}{s} \tag{2.29}$$

s is statistical inefficiency, which could be calculated by breaking the data into n_h blocks with size h as $N = hn_h$, then s is computed from :

$$s = \frac{h\boldsymbol{\sigma_h}^2}{\boldsymbol{\sigma}^2} \tag{2.30}$$

where $\boldsymbol{\sigma_h}$ is the block variance:

$$\boldsymbol{\sigma_h} = \frac{1}{n_h}\sum_{i=1}^{n_h}(<\mathrm{A}>_h - <\mathrm{A}>)^{1/2} \tag{2.31}$$

with $<\mathrm{A}>_h$ is the average over each block.

2.3.2.2 Angle and dihedral angle distribution

Given that abnormal configuration might be formed during simulated polymerization process, angle/torsion distributions were investigated to analyze configuration state of APA system by comparing it with system of 100 dimers.

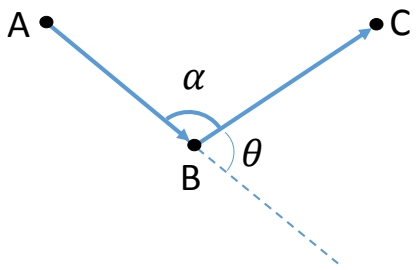

Figure 2.1: Angle calculation graphic.

With coordinates of three atoms in one angle interaction A (x_a, y_a, z_a), B (x_b, y_b, z_b), C (x_c, y_c, z_c) (figure

2.1), we have:

$$\overrightarrow{AB} \cdot \overrightarrow{BC} = |\overrightarrow{AB}||\overrightarrow{BC}| \cos\theta \tag{2.32}$$

Thus the angle of these two vectors θ, is computed as :

$$\theta = \arccos \frac{\overrightarrow{AB} \cdot \overrightarrow{BC}}{|\overrightarrow{AB}||\overrightarrow{BC}|} \tag{2.33}$$

the angle α is calculated as :

$$\alpha = \pi - \theta \tag{2.34}$$

The calculation of dihedral angle β of atoms A , B , C and D is based on the calculation of the normal vector of surface A-B-C $\overrightarrow{n}$ and that of surface B-C-D $\overrightarrow{m}$, figure 2.2.

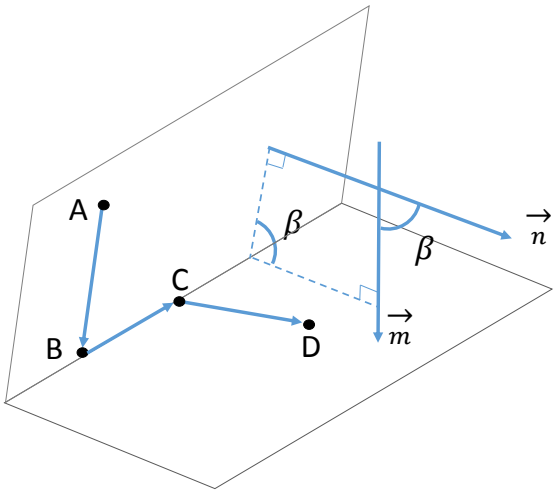

Figure 2.2: Dihedral angle calculation graphic.

The vectors $\overrightarrow{AB}(x_1, y_1, z_1)$, $\overrightarrow{BC}(x_2, y_2, z_2)$ and $\overrightarrow{CD}(x_3, y_3, z_3)$ are calculated from the four atoms coordinates. Then $\overrightarrow{n}$ is computed as the cross product of $\overrightarrow{AB}$ and $\overrightarrow{BC}$:

$$\overrightarrow{n} = \overrightarrow{AB} \times \overrightarrow{BC} \tag{2.35}$$

and $\overrightarrow{m}$ is computed as the cross product of $\overrightarrow{BC}$ and $\overrightarrow{CD}$:

$$\overrightarrow{m} = \overrightarrow{BC} \times \overrightarrow{CD} \tag{2.36}$$

With obtained $\overrightarrow{n}$ and $\overrightarrow{m}$, the dihedral angle β is computed directly by applying equation 2.33.

The number of angle/dihedral angle for a given resolution range is counted and normalized by the total angle/dihedral angle number.

2.3.2.3 Radial distribution function (RDF) and coordination number ($N_c(R)$)

The RDF function counts the number of two-atom species with specific distance, assuming the system is spherical. The partial pair distribution function $g_{\alpha\beta}(r)$ represents the local density of particle β around α, $\rho_{\beta_\alpha}(r)$, compared to the bulk density of β, ρ_β:

$$g_{\alpha\beta}(r) = \frac{\rho_{\beta_\alpha}(r)}{\rho_\beta} \tag{2.37}$$

where $\rho_{\beta_\alpha}(r)$ represents pair number of β-α at the distance r from particle α, p_{β_α}, divided by the corresponding spherical shell volume between r and $r + \mathrm{d}r$ and total number of particle α, N_α:

$$\begin{aligned} g_{\alpha\beta}(r) &= \frac{p_{\beta_\alpha}(r)}{4\pi/3[(r+\mathrm{d}r)^3 - r^3]N_\alpha}\frac{1}{\rho_\beta} \\ &= \frac{p_{\beta_\alpha}(r)}{4\pi r^2 \mathrm{d}r N_\alpha}\frac{1}{\rho_\beta} \\ &= \frac{p_{\beta_\alpha}(r)V}{4\pi r^2 \mathrm{d}r N_\alpha N_\beta} \end{aligned} \tag{2.38}$$

The $N_c(R)$ represents total number of particle in the sphere of radius R around the given particle, obtained by integrating the local density along the R. Hence, $N_c(R)$ of particle β around particle α, $N_{c\ \beta_{(\alpha)}}(R)$ is:

$$\begin{aligned} N_{c\ \beta_{(\alpha)}}(R) &= \int_0^R 4\pi r^2 \rho_{\beta_\alpha}(r)\mathrm{d}r \\ &= \int_0^R 4\pi r^2 \rho_\beta g_{\alpha\beta}(r)\mathrm{d}r \end{aligned} \tag{2.39}$$

In the same way, for $N_{c\ \alpha_{(\beta)}}(R)$:

$$N_{c\ \alpha_{(\beta)}}(R) = \int_0^R 4\pi r^2 \rho_\alpha g_{\alpha\beta}(r)\mathrm{d}r \tag{2.40}$$

Overall, β and α perform the same $g_{\alpha\beta}(r)$ but different coordination number.

2.3.2.4 Calculated Infrared absorption spectrum

To obtain the infrared absorption spectrum, the system's total dipolar moment-time signal is firstly recorded as:

$$M(t) = \sum_{i=1}^{N} q_i r_i(t) \tag{2.41}$$

where N is the total particle number with charge q_i at position r_i. The infrared absorption (IR) spectrum as a function of frequency w is calculated from its autocorrelation function followed by Fourier transformation:

$$I(w) = \int_{t=0}^{t} < M(t) \cdot M(0) > e^{-\boldsymbol{i}wt} \mathrm{d}t \tag{2.42}$$

where I is the infrared absorption density, $\boldsymbol{i}$ is imaginary unit and $< M(t) \cdot M(0) >$ is the autocorrelation function, which is used to describe the regularity of dipolar moment vibration signal occurring at the corresponding frequency w. If the dipolar moment signal point $M(0)$ is correlated with the corresponding point $M(t)$, the correlation degree is calculated as the dot product of $M(t) \cdot M(0)$. If it is correlated, the value is equal to 1. Then the correlation degree is averaged over time. The accuracy of IR spectrum is dominated by the applied parameters of force field, which might lead to displacement of the characteristic peak position in the spectroscopy comparing to the experimental data.

In this study, the attribution of IR spectrum of APA dimer was analyzed via the code NEWTON. The constraint method of NEWTON was used to fix certain chemical bonds in order to identify the corresponding IR spectrum peak. The trajectory of dipole moment was recorded every 0.5 fs time step for 1 ns under *NVE* MD ensemble. The IR spectra of APA polymer system were studied by LAMMPS. The trajectory of dipole moment was recorded every 0.5 fs time step for 2 ns under *NVT* (298.15 K) MD ensemble.

2.3.3 Building APA samples at the atomic level

2.3.3.1 General APA polymer construction protocol

To mimic the real interfacial polymerization process between the MPD and TMC, the APA polymer molecular model was generated by connecting the two types of monomers, after which various types of MD simulations were performed in order to equilibrate the polymer system. The APA polymer generation steps are demonstrated in figure 2.3.

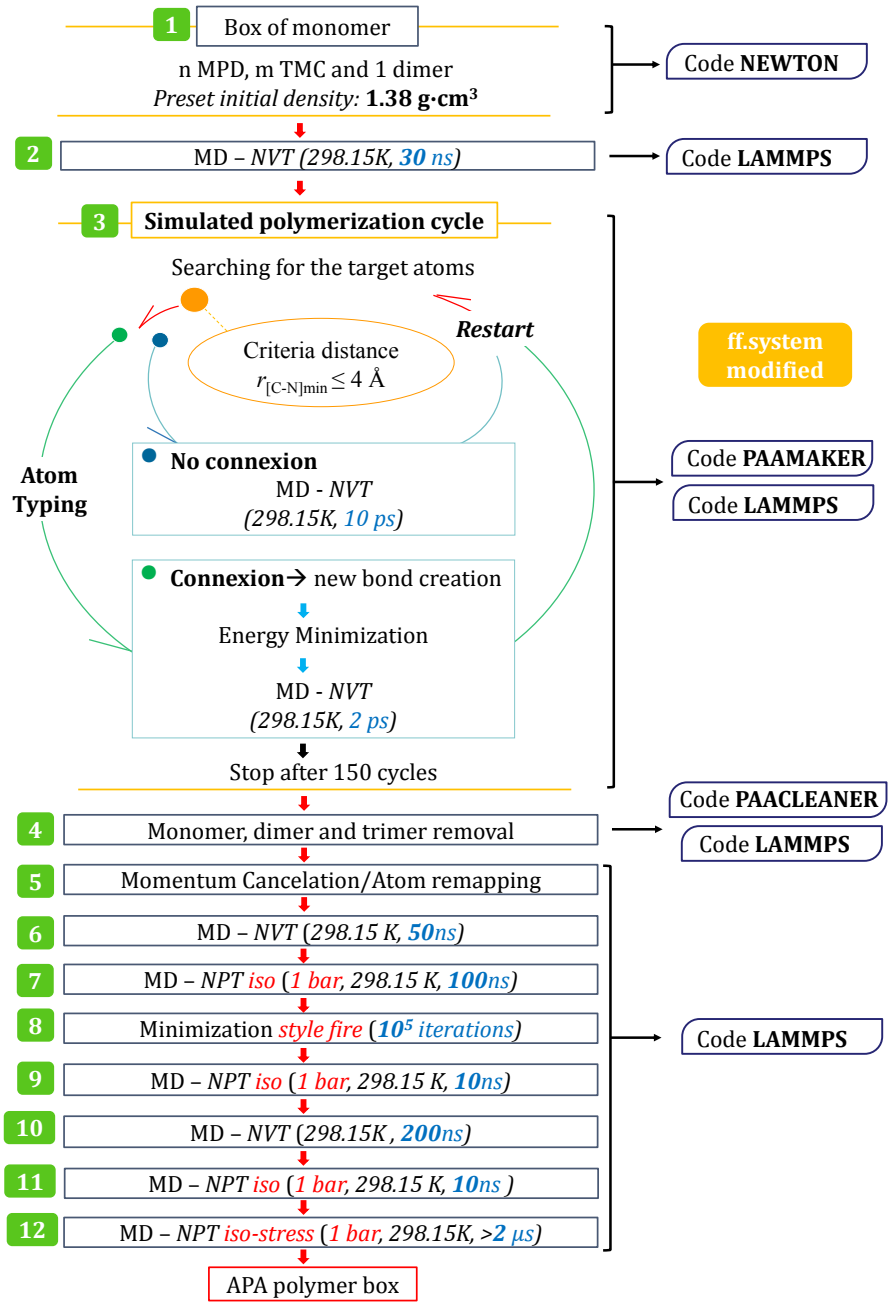

Figure 2.3: APA system generation method map.

The polymer model was inspired by mimicking interfacial polymerization between monomers[47]. In this work, simulations were based on boxes at relatively small size (box length around 30 Å), but with a set number of repetitions. The purpose was to clarify the possible structure variations originated from box construction processes and as well to ensure the systematical repeatability of the developed construction protocol.

During construction processes, all the molecular dynamics (MD) and energy minimization simulations were performed by LAMMPS. Nose-Hoover style non-Hamiltonian equations of motion was applied to control temperature or pressure. Meanwhile certain local codes were also developed and implemented to accomplish the construction.

Initially, around two hundred mixed TMC and MPD monomers at a certain ratio and one TMC-MPD dimer were firstly inserted at random lattice position in a cubic box at initial density of 1.38 g·cm^{-3} by NEWTON. This density was firstly simulated by Kotelyanskii *et al.,* (1998) as hydrated density of APA polymer with water content of 23 wt% [66], which was selected here to ensure close monomer distance for establishing the amide bond formation in a further step. 3D period boundary conditions were applied for the simulation box.

Then MD in *NVT* ensemble at 298.15 K was performed for 30 ns in order to generate a reasonable departing configuration for starting the polymerization. The free acyl groups from TMC (or dimer) and free amine groups from MPD (or dimer) were connected progressively by following the reaction - bond alignment - equilibration cycle, similar to the work of Kolev & Freger (2014) [64]. For each cycle, the nearest carbon atom in carboxylic acid group and nitrogen atom in amine group in the present system were firstly located by our local code Paamaker, and the amide bond was further created when their distance ($r_{[\mathrm{C-N}]\mathrm{min}}$) was smaller than 4 Å. The information concerning the related atom types, new bond, angle, dihedral and improper dihedral interactions was modified or added in system's database, while one corresponding 'water molecule' (1 oxygen and 2 hydrogen atoms) and the related information were removed by LAMMPS. Next, energy minimization for hundreds steps was performed to align the new bond, followed by *NVT* ensemble at 298.15 K for 2 ps to equilibrate the system while maintaining the box shape. It was noted that during bond alignment stage, the hydrogen and oxygen atoms in amide bond, between which performed attractive electrostatic force due to the opposite charges but with zero Lennard-Jones potential, turned to approach extremely close to each other and finally resulted in unreasonable configuration with high electrostatic potential. In order to prevent this problem, during the whole bond formation cycles, the Lennard-Jones potential parameters of the hydrogen atom in amide bond was modified as that in aromatic ring, aiming to add repulsive force between the two atoms. Detailed information on amide formation is presented later.

With the advancement of polymerization cycles, it would be no longer possible to find $r_{[\mathrm{C-N}]\mathrm{min}}$ which met the criteria, and the reaction - bond alignment - equilibration cycle would be replaced by direct equilibration in *NVT* ensemble at 298.15 K for 10 ps, aiming to relax the system for a longer time to create new possibility of bond formation. The completion of polymerization is supposed to be achieved after 150 cycles for systems at size in this work. Thereafter, the unreacted monomers, together with existing dimers and trimers, were removed from the systems by our local code PAACLEANER, because these small molecules are not supposed to exist in real APA membrane.

In order to release the important mechanical constraints generated during the bond formation process and also to contract the void formed from the small molecule removal, different progressive relaxing stages were demanded. The principle idea was to finally relax the box in *NPT iso-stress* ensemble at 298.15 K and 1 bar (mimicking the real experimental condition), while preventing the box from artifacts such as evident deformation.

The system's velocity was no longer equal to zero after the molecule removal, thus firstly the overall momentum was canceled by LAMMPS. Then *NVT* ensemble at 298.15 K for 50 ns was subsequently performed,

following *NPT iso* ensemble at 1 bar and 298.15 K for 100 ns to regulate the average of pressure tensor elements P_{xx}, P_{yy} and P_{zz} back to 1 bar while maintaining the cubic box shape. Next, energy minimization (style *fire*) for one hundred thousand steps was applied with purpose to decrease the energy, then system momentum was canceled again and *NPT iso* ensemble at 1 bar and 298.15 K for 10 ns was launched to regulate the average pressure. Upon this step, there existed still some mechanical constraint bias among X, Y and Z. The box lengths were foremost redefined according to the average values in the previous step, and *NVT* ensemble at 298.15 K for 200 ns was subsequently performed to release the bias. And also from this step, the system momentum was canceled systematically every 10 ns. After, it was noted that mean pressure drove slightly away again from the target pressure, thus *NPT iso* ensemble at 1 bar and 298.15 K was applied another time for 10 ns to regulate average pressure.

Finally *NPT iso-stress* ensemble at 1 bar and 298.15 K was performed until the energy and density equilibrium plateau was achieved. Since each bond formation was established randomly during the polymerization process, the mechanical constraints generation states also varied from system to system. Hence, the relaxation time demanded here varied from 1 to 4 μs according to proper properties of each system.

2.3.3.2 Detailed protocol of polymerization cycle

In OPLS-AA force field, the 'atom class', such as 'C411', is used to index the Lennard-Jones and coulombic parameters, while 'atom type', such as 'C', is used to index the other parameters. The principle of single simulated polymerization cycle was to localize the nearest group of free carbon atom (C411) of TMC carboxylic acid group and free nitrogen atom (N730) of MPD amine group in the present system. If the distance between these two atoms was smaller than the criteria value, which was set at 4 Å in present study, the amide group was subsequently formed by removing the corresponding hydrogen atom (H739) from the MPD side and the hydroxyl group (H211 and O211) from TMC side as one water molecule and followed by connecting the C411 with N730. After bond connection energy minimization was expected to release the constrains.

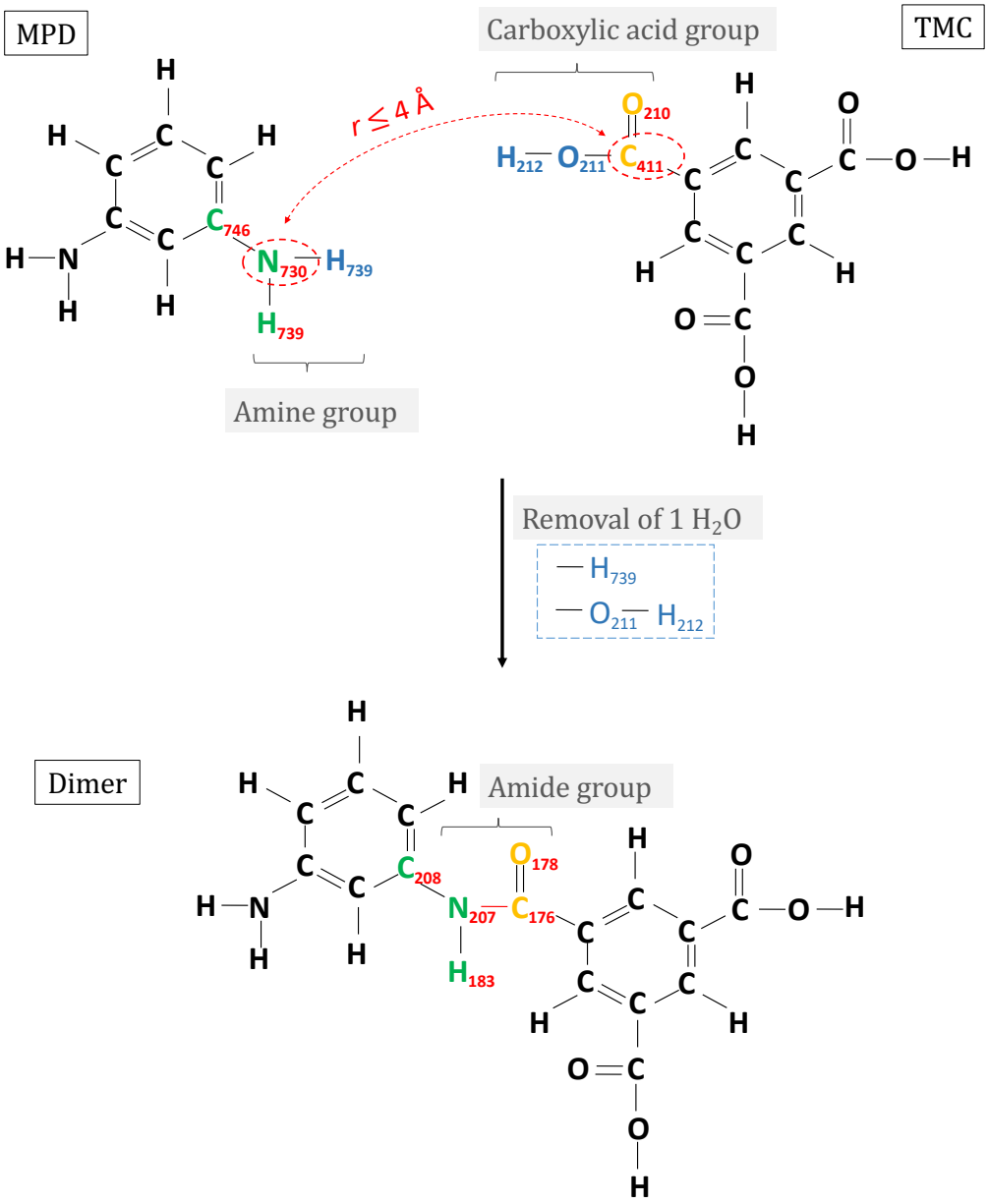

Figure 2.4: Principle of simulated polymerization cycle.

Atom class and type modification after new bond connection As shown in fig.2.4, with formation of amide bond, related atoms eventually changed their classes or even types. Table 2.1 summaries the corresponding modified atoms during the transformation from monomer into polymer. In order to compare, the atom information before and after polymerization is presented on pair, changed parameters are underlined in red.

Table 2.1: Atom class, charge, Lennard-Jones parameters and atom type modifications along with amide bond formation.

Atom Class	q(e)	ε (kcal/mol)	σ (Å)	Atom Type
N730	-0.9000	0.170	3.300	NT
N207	-0.3850	0.170	3.250	N
C746	0.1800	0.070	3.550	CA
C208	0.0850	0.070	3.550	CA
H739	0.3600	0.000	0.000	H
H183	0.3000	0.000	0.000	H
C411	0.6350	0.105	3.750	C
C176	0.6150	0.105	3.750	C
O210	-0.4400	0.210	2.960	O
O178	-0.5000	0.210	2.960	O

As illustrated in table 2.1, the related atoms have changed their classes, suggesting the modification of their charges. Meanwhile, the LJ parameters of the majority of the atoms remained the same, except for the nitrogen. Besides, only the nitrogen changed its atom type from NT to N, as shown in fig.2.5.

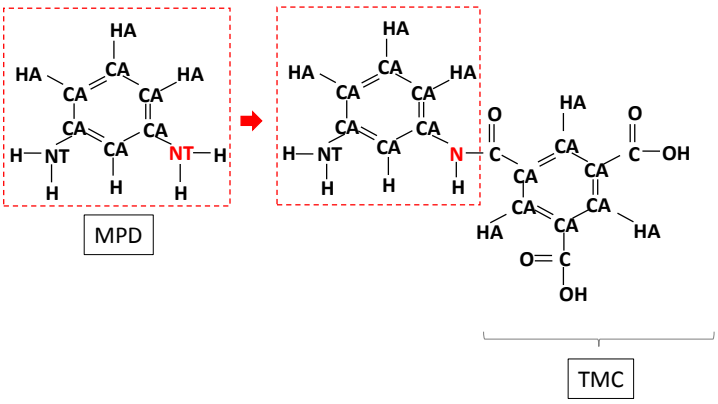

Figure 2.5: Atom type change during simulated polymerization.

More details on the comparison of the corresponding intramolecular parameters of N and NT are presented in Annexes A4, where the modified information are underlined in red.

In summary, as for the eight related atoms, their atom classes and charges were modified along with the bond creation. The corresponding LJ parameters were modified automatically along with the modification of the atom class. Besides, the parameters of one bond (NT-CA → N-CA), one angle (H-NT-CA → H-N-CA) and one dihedral interaction (H-NT-CA-CA → H-N-CA-CA) needed modifications as well. Moreover, corresponding improper torsions were also modified, but the details are not presented in this thesis.

Lennard-Jones parameter modification of atom H183 After one bond connection, minimization process was implemented. It was found in our study that modification of force field was needed for its application during the polymerization process, specifically in minimization stage, where the distance between the N-C atoms was forced to decrease to the equilibrated amide bond length. Meanwhile, according to force field of H183 ($\varepsilon = 0$ (kcal/mol)), table 2.2), no LJ repulsion existed between the H183 and O178:

Table 2.2: Force fieldparameter of O178, H183 and H91.

Atom	Atom Type	q(e)	ε (kcal/mol)	σ (Å)
O178	O	-0.5000	0.210	2.960
H183	H	0.3000	0.000	0.000
H91	HA	0.1150	0.030	2.420

Since the two atoms owned opposite charges, consequently the distance between the two atoms intended to approach to zero which produced unrealistic configuration and extremely high electrostatic energy. Hence, the LJ parameters of atoms of H183 were modified manually as that of H91 on the purpose to apply repulsive force between them only during the simulated polymerization process.

The realization of above polymerization process was accomplished via alternative applications of two codes: our local code PAAMAKER and LAMMPS code.

2.4 Results

2.4.1 Validation of the building procedure

2.4.1.1 Alignment and relaxation of newly formed amide bond

In our study, the amide bond was established between the nitrogen and carbon atoms which were more distant than in an equilibrated amide bond (≤ 4 Å compared to 1.35 Å). As a consequence, each amide bond connection would lead to an increase of strains inside the system. As presented previously, the conjugate gradients algorithm of Polak-Ribiere method was applied in order to align the newly formed amide bond once a new amide bond was connected, followed by a relaxation stage of MD under NVT (298.15 K) for 2 ps. With respect to polymerization cycle where no amide bond was formed, a relaxation stage of MD under NVT (298.15 K) for 10 ps was launched to leave the system more time reorganizing.

This analysis of alignment and relaxation of the newly formed amide bond was based on a system with medium initial MPD:TMC ratio at 1.5, r1.5_1 (repetition box n°1). 1.5 corresponds to the MPD:TMC monomer units ratio for a fully-crosslinked APA structure, hence in such system there exist equally abundant free acyl and amine groups. Before the polymerization, this system, containing only monomers, was relaxed in NVT (298.15 K) ensemble for 30 ns at a preset density of 1.38 g·cm^{-3}. At the end of this relaxation stage, it had

a potential energy around -121 KJ/mol, with bond, angle, torsion, Lennard-Jones and electrostatic energies at 35 KJ/mol, 30 KJ/mol, 45 KJ/mol, -32 KJ/mol and -192 KJ/mol, respectively. During the polymerization process, the energies of the systems generally increased due to the formation of amide bond except for Lennard-Jones potential (LJ), which declined due to the removal of atoms (O211 and H212 from acyl group and one H739 from amine group for one formation of amide bond). Among the increasing potentials, the bond and electrostatic energies raised the most sharply. The fig.2.6 demonstrates how the bond energy evolved during the polymerization process. The first twenty cycles out of 150 cycles were taken as example. During this initial stage of polymerization process, one new bond was always formed for each cycle.

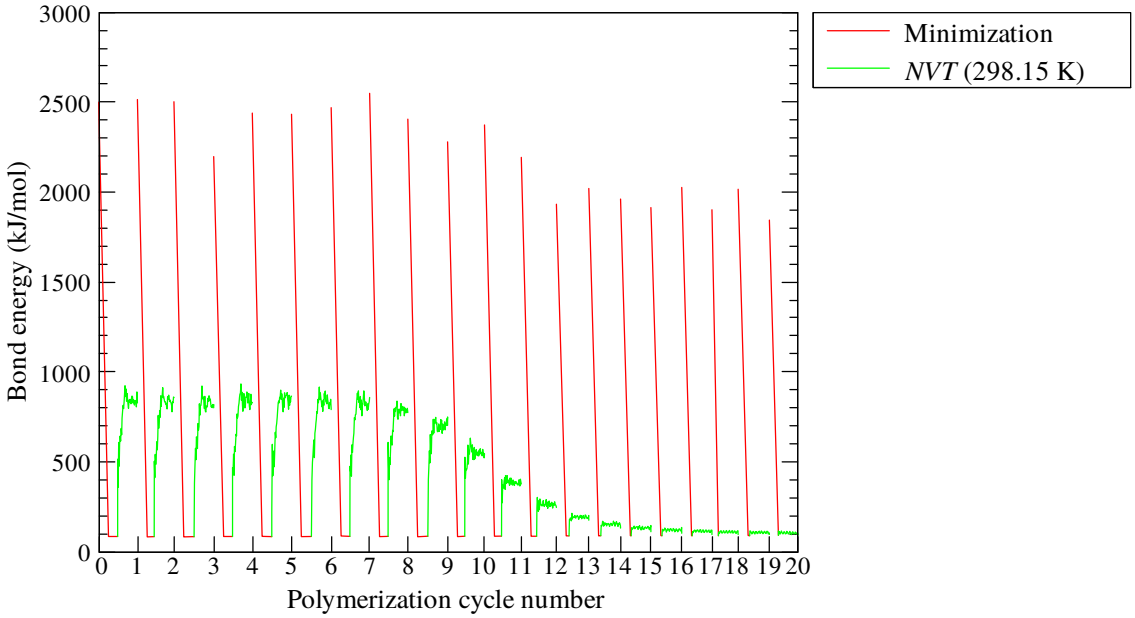

Figure 2.6: Bond energy evolution during the first twenty polymerization cycles of system r1.5_1.

For each polymerization cycle, the beginning point of each Minimization line represents the system's bond energy just after the new amide bond connection. In the first cycle, the bond energy raised to 2500 kJ/mol from 35 kJ/mol of the initial monomer state (data not shown in the figure) due to the amide bond connection. The minimization process intended to decrease the distance between the nitrogen and carbon atoms of the newly connected amide bond, which successfully brought the bond energy back down to 84 kJ/mol. In a next step, the system reorganized under MD ensemble NVT (298.15 K) for 2 ps, leading to an increase of bond energy which stayed relatively constant around 840 kJ/mol at the end. Then, the second polymerization began, the bond energy arose back to 2500 kJ/mol, then declined with the application of minimization and arose again during the relaxation stage...such similar cycles continued until the 8th one, where the bond energy increase during the relaxation stage became less evident. From the 16th cycle, this increase became even not notable in fig.2.6. From the 17th to 20th cycle, the bond energy during the relaxation stage seemed to only fluctuate around the value at the end of minimization stage, which was about 100 kJ/mol. As the system became more connected and rigid, it became more difficult to reorganize in a short relaxation time hence leading to less fluctuation of

bond energy. Fig.2.7 demonstrates the bond energy evolution at the end of polymerization process, from cycle 130 to 150 for r1.5. The polymerization of r1.5 became saturated at this stage (as presented later in fig.2.9). From the 130th to the 133rd cycle, there existed still new amide bond formations, hence the bond energy raised but then was brought down by the application of energy minimization (fig.2.7).

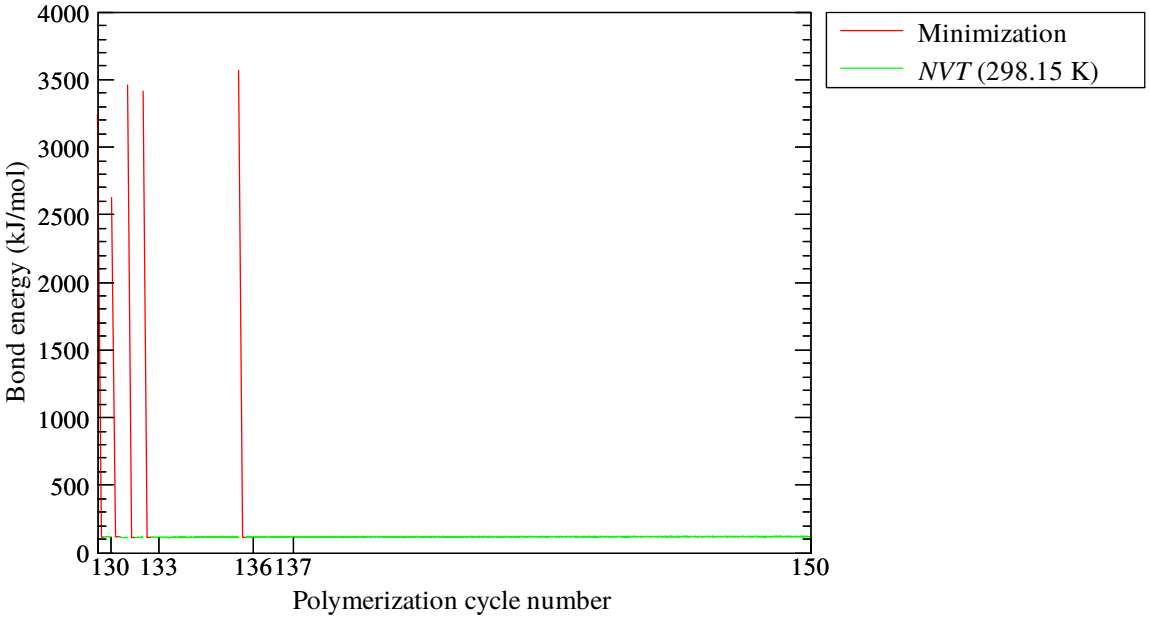

Figure 2.7: Bond energy evolution during the last twenty polymerization cycles of system r1.5_1.

Then after two cycles (134th and 135th) of relaxation under *NVT* (298.15 K) for 10 ps, another new amide bond was formed at the 136th cycle. The polymerization was saturated from the 137th cycle, from which only the relaxation stage was performed until the end of the polymerization process. Despite evident bond energy increase created by the bond formation and declining by the minimization, the bond energy of the system remained relatively stable during the relaxation stages. For instance, after each minimization, the bond energy only fluctuated little around 120 kJ/mol during the following relaxation stage. And it maintained around this value for the longer relaxation stage at the end of polymerization process. Hence, this was consistent with the observation of the receding increase of bond energy during relaxations stages of the first twenty cycles: since the system became more and more rigid thanks to the advancement of polymerization, less notable structural reorganization could be observed during a relatively short period (hundreds of ps) of relaxation under *NVT* (298.15 K).

The evolution of the electrostatic energy at the beginning and the end of the polymerization process, is presented in fig.2.8.

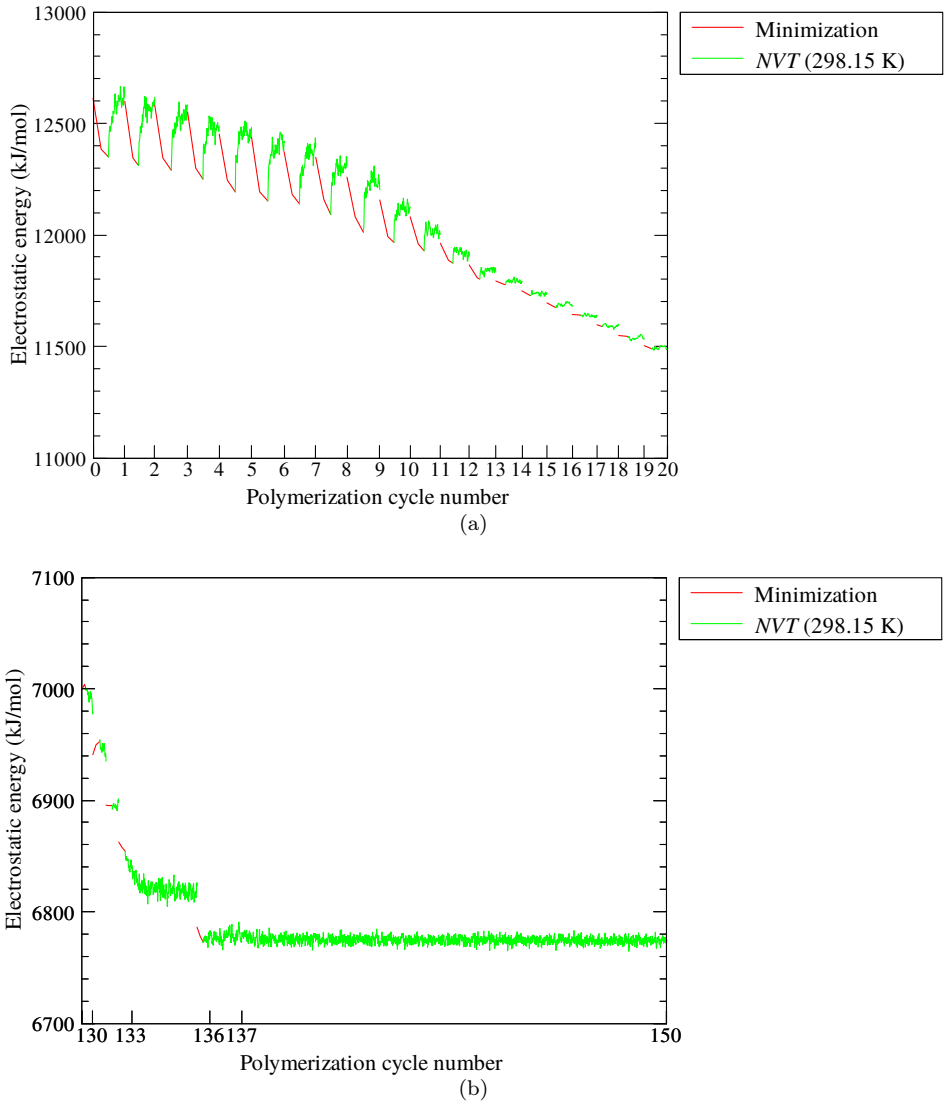

Figure 2.8: Electrostatic energy evolution during the first and the last twenty polymerization cycles of system r1.5_1.

As introduced above, before the polymerization, the system performed with an electrostatic energy around -192 kJ/mol. As shown in the fig.2.8(a), its electrostatic energy raised up to 12600 kJ/mol at the first cycle of polymerization process. Such evident raise was probably attributed to the removal of atoms and the modification of force field parameters of the atoms in the newly formed amide bond. Even though the overall electric charge of the system always remained neutral, the modification of the force field parameters of these atoms led to an evident increase of electrostatic energy due to the unstable configuration of the newly amide bond. During the first 13 cycles, the electrostatic energy decreased firstly during the energy minimization and rose again during the system's structural organization in NVT (298.15 K) ensemble. With the advancement of the polymerization, the polymer became more rigid, hence the structural organization during a short time became more difficult, which explained the weaker fluctuations of the electrostatic potential during the relaxation stage of the 14th and 20th cycles. In general, the electrostatic potential exhibited a decreasing trend thanks to the application

of energy minimization.

During the last twenty cycles of the polymerization, the electrostatic energy continued decreasing from the 130th to 136th cycle, fig.2.8(b). An evident structural relaxation in NVT (298.15 K) ensemble was observed during the 133th and 135th cycles. After the last connection at the 136th cycle, the electrostatic energy stayed constant around 6775 kJ/mol in NVT ensemble for a relaxation time of 142 ps until the end of the polymerization process.

Overall, the application of energy minimization and relaxation stages in NVT (298.15 K) ensemble during the polymerization process assisted in relaxing progressively the polymer structure, particularly the newly formed amide bonds. They were essential for a successful continuation of polymerization cycles and the generation of a reasonable polymer configuration at the end of polymerization process.

2.4.1.2 Amide bond connection and network formation

The amide bond formation numbers along with the advancement of polymerization cycles for three typical systems, with initial MPD:TMC ratios at 0.25 (repetition box n°0), 1.5 (repetition box n°1) and 5 (repetition box n°0), are presented in fig.2.9. At the beginning of the polymerization, the system r0.25_0 had 46 MPD, 184 TMC and one dimer, hence it owned a potential maximum amide number at 93; for r1.5_1, initially with 84 MPD, 56 TMC and one dimer, it had a potential maximum amide number at 169; and r5_0 had 200 MPD, 40 TMC and one dimer, hence it was potentially able to form 121 amide bonds in maximum.

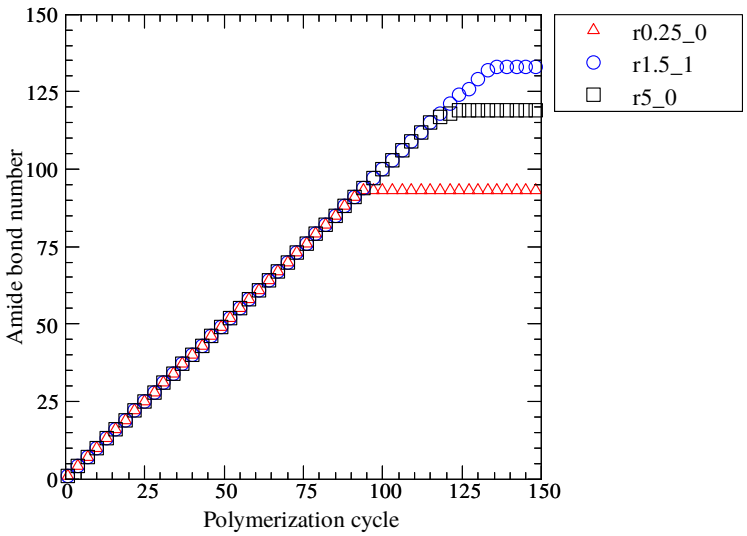

Figure 2.9: Amide bond formation along with the advancement of polymerization cycles of system r0.25 (repetition box n°0), r1.5 (repetition box n°1) and r5 (repetition box n°0).

At the beginning and during the middle of the polymerization (from the 1st to 90th cycle), the bond formation was similar for all systems, as the amide bond number curves of three systems overlapped with each other. In this stage, one new amide bond was always formed in each cycle. Afterwards, the polymerization became progressively saturated, as the polymerization stopped from the 95th, 137th and 123rd cycle for r0.25_0, r1.5_1

and r5_0, receptively. Besides, according to polymerization results of systems with other initial MPD:TMC ratios (results no shown here), 150 cycles were proven enough to saturate the polymerization, except for one system (r1.3), where the polymerization continued after the 150th cycle and ended in the 154th. Besides, tests have been done to know whether new bonds could be still formed after leaving the system reorganizing for a longer time. Eleven repetition boxes of systems r1.5 were relaxed under MD NVT (298.15 K) for 2 ns after the first polymerization process, then they were taken to launch a second polymerization process. However, the results showed no new bond was formed afterwards for all test boxes. Hence, the application of 150 polymerization cycles was proven efficiency for systems with box dimension used in our study.

On the other hand, even though r0.25_0 and r5_0 departed from a relatively larger box dimension (total initial atom number more than 4000 at a box dimension around $35 \times 35 \times 35$ Å^3 compared to r1.5_1 initially with around 2500 atoms at a box dimension about $29 \times 29 \times 29$ Å^3), more amide bonds were formed in the system r1.5_1. This was attributed to different potential connection sites for these systems. For an initial MPD:TMC at 1.5, there existed equally abundant free acyl and amine groups, this system naturally offered more bond formation sites. Meanwhile, for systems r0.25 and r5, the potential amide bond number were limited at 93 and 121 respectively due to the weaker number of one type of monomer, hence there existed a large excess of the other monomer type.

To compare the effect of initial MPD:TMC ratios during the polymerization process and on the final APA network formation, the snapshots of typical systems r0.25_0, r1.5_1 and r5_0 at three stages: before polymerization (Cycle 0), after polymerization (Cycle 150) and after the removal of oligomers, including monomers, dimers and trimers (Oligo-rem), are presented in fig.2.10. In this presentation, the atom number of each molecules is differentiated by different colors.

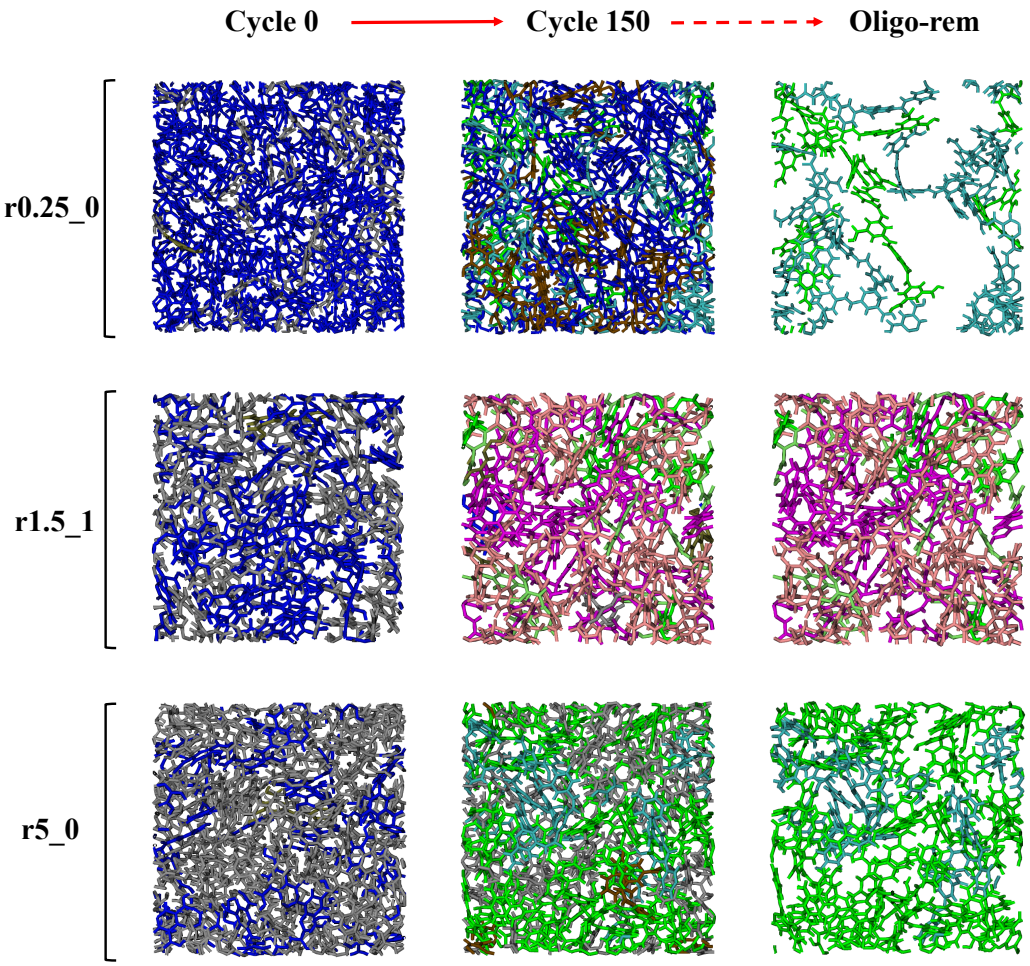

Figure 2.10: Snapshots of APA systems r0.25 (repetition box n°0), r1.5 (repetition box n°1) and r5 (repetition box n°0) at cycle 0, cycle 150 of polymerization process and after the removal of oligomers. The atom number of each molecules is differentiated by color, with atom number at 16 (MPD): silver; 21(TMC): blue; 34(dimer): tan; 47/52(trimer): ochre; 53-99: cyan; 100-199: green; 200-299: lime; 300-399: yellow; 400-499: pink; 500-599: orange; 600-699: magenta.

At Cycle 0, the systems were in form as a collection of monomers at a preset density at 1.380 g·cm^{-3}. The system r0.25 initially had 46 MPD, 184 TMC and one dimer. As shown in the figure, its snapshots was dominated by the color of TMC (blue). For r1.5, the two monomer's numbers were close (84 MPD and 56 TMC), hence the monomers' corresponding colors, blue for TMC and silver for MPD, both occupied a comparable portion in the snapshot. The color silver naturally became dominant for r5, as MPD number (200) was as five times as that of TMC (40). At the end of polymerization (Cycle 150), the three systems exhibited various polymerization states (various molecular sizes). For r0.25, a notable quantity of unreacted TMC monomers remained. Meanwhile, these excessive and unreacted TMC spread around the system, hence hindering as well the connection among the formed molecules. As a consequence, only trimers or small molecules with less than 200 atoms were formed in the end. The snapshot of Oligo-rem demonstrated the final molecules quantity of r0.25 after the removal of monomers and oligomers. As shown in the figure, the majority of materials have been removed due to small sizes. It should be addressed that snapshots of Oligo-rem didn't really exist for these three systems. During the

development of construction protocol, the monomers and dimers were firstly removed. After several relaxation stages, it was decided to remove as well the oligomers. Hence the presentations of Oligo-rem here only aims to demonstrate the remaining atom quantity which participated in forming relative large molecules, rather than to demonstrate the system configuration. Similarly, since r5 possessed an evident excess of MPD monomers, there still remained a lot of unreacted MPD at the end of cycle 150. Due to the presence of these monomers, no large molecules were formed neither, as the largest molecule owned an atom number less than 200. Different from r0.25, more materials remained after the removal of oligomers. This could be related to more potential connection sites of TMC than that of MPD. For r5, the TMC was surrounded by excessive MPD, hence its three free acyl bonds were able to connect with three MPD, finally forming relative large molecule as tetramer. On the contrary, MPD was surrounded by excessive of TMC for r0.25. Since one MPD, with two free amine bonds, was only able to connect with two TMC monomers, hence such connection naturally led to more formation of trimers, which were removed afterwards. Distinguished from r0.25 and r5, the system r1.5 had a much better polymerization state. At cycle 150, very few monomers remained unreacted (3 MPD and 1 TMC). Meanwhile, the formed molecules were all of relative large sizes, as the largest molecules had 693 atoms. As shown in Oligo-rem, the removal of oligomers had little effect, as the majority of initial materials participated in the formation of large APA networks for r1.5. Overall, the initial MPD:TMC ratio at 1.5 was proven to be much more favorable to construct large APA networks, while systems with extreme initial MPD:TMC ratios such as r0.25 and r5 demonstrated more tendency to generate smaller molecular pieces.

2.4.1.3 Molecular size distribution

The information of molecular size and number in each simulation box was obtained by our local code PAASTATS. The histogram of molecular size distribution of 11 repetition boxes, generated from initial MPD:TMC ratios at 0.25, 1.5 and 5 respectively, after the removal of oligomers is presented in fig.2.11. For each initial MPD:TMC ratio, the average molecular number ($M_{num-avg}$) and molecular size ($M_{size-avg}$, number of atom in the molecule) in one box upon 11 repetitions are indicated directly in the figure.

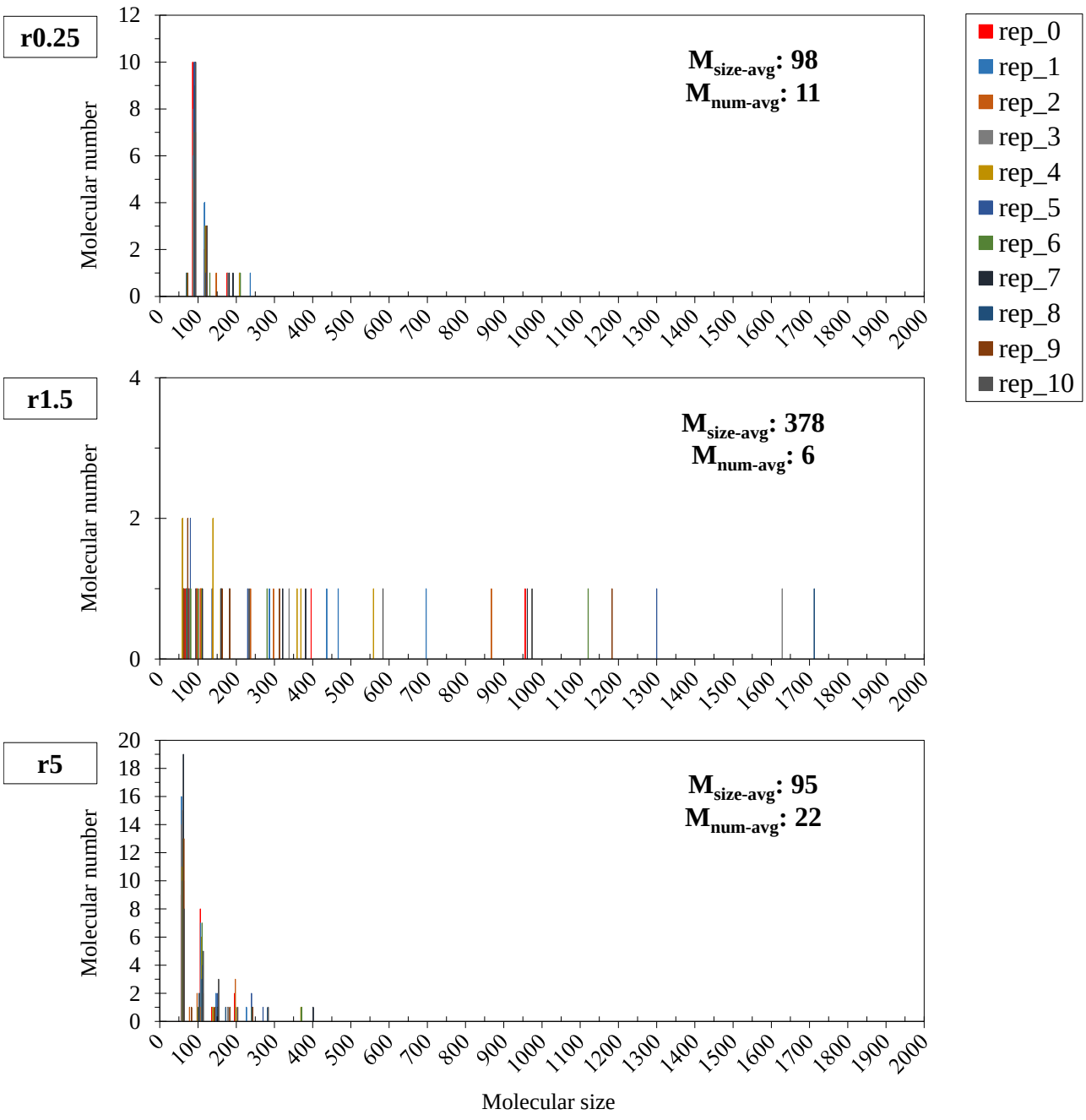

Figure 2.11: Histogram of molecular size distribution of 11 repetition boxes generated from initial MPD:TMC ratios at 0.25, 1.5 and 5 after the removal of oligomers. For each initial MPD:TMC ratio, the average molecular size $M_{size-avg}$ and molecular number $M_{num-avg}$ in one box upon 11 repetitions are indicated.

As shown in the figure, the systems fabricated from the extreme initial MPD:TMC at 0.25 and 5 consisted with a larger number ($M_{num-avg} > 10$) of small molecules ($M_{size-avg} < 100$). For these systems, their molecular sizes all distributed at the left side of the histogram. Hence, these systems were more like a gathering of molecular pieces rather than a whole polymer network. Meanwhile, the systems of r1.5 exhibited a wider molecular size distribution. Only few small molecules were found ($M_{num-avg} \leq 6$), and the systems mainly consisted of large molecules with $M_{size-avg} > 100$. For certain repetition boxes, very large molecules with atom number more

than 1500 were also observed. Thereby, systems of r1.5 were clearly better connected than the systems of r0.25 or r5, forming polymer networks.

Despite the molecular size, more detailed analyses on chemical structures of these remaining molecules, both large networks and relative small molecular pieces, are presented in later section 2.4.2.2.

2.4.1.4 Pressure tensor relaxation

During the polymerization or the oligomer removal process, the pressure became unequilibrated in X, Y and Z directions due to artificial bond formation between initially distant nitrogen and oxygen atoms or creation of volume vacancy. As presented in previous section 2.3.3, various equilibration stages were implemented successively in order to relax the pressure to 1 bar and also maintained the box shapes. Here pressure (P) and box length (L) evolution along with these relaxation stages of system r1.2 is presented as example in fig.2.12. Different stages are represented as serial numbers in fig.2.12 as: 1. last cycle of polymerization process; 2.removal of oligomers and cancellation of system's total momentum, followed by MD under *NVE* for 0.5 fs; 3. MD under ensemble *NVT* (298.15 K) for 50 ns; 4. MD under *NPT iso* (298.15 K, 1 bar) for 100 ns; 5. energy minimization for 100000 iteration steps; 6. MD under *NPT iso* (298.15 K, 1 bar) for 10 ns; 7. MD under *NVT* (298.15 K) for 200 ns. The box dimension was taken as the average value during the last 5 ns of the previous step; 8. MD under *NPT iso* (298.15 K, 1 bar) for 10ns; 9. MD under *NPT iso-stress* (298.15 K, 1 bar) for 1.6 μs. For all stages except for stage 1, 2 and 5, box length evolution data of every 10 ps are presented. Besides, due to large fluctuation of pressure, the pressure data were averaged over 1 ns. With respect to stage 1, one average value of pressure/box length during 10 ps *NVT* (298.15 K) is presented. As for stage 2, the pressure and box length data for one step time (0.5 fs) under *NVE* after oligomer removal and momentum cancelaton are presented directly. For stage 5, the pressure was averaged every 100 iterations, while the box length data are presented directly without being averaged.

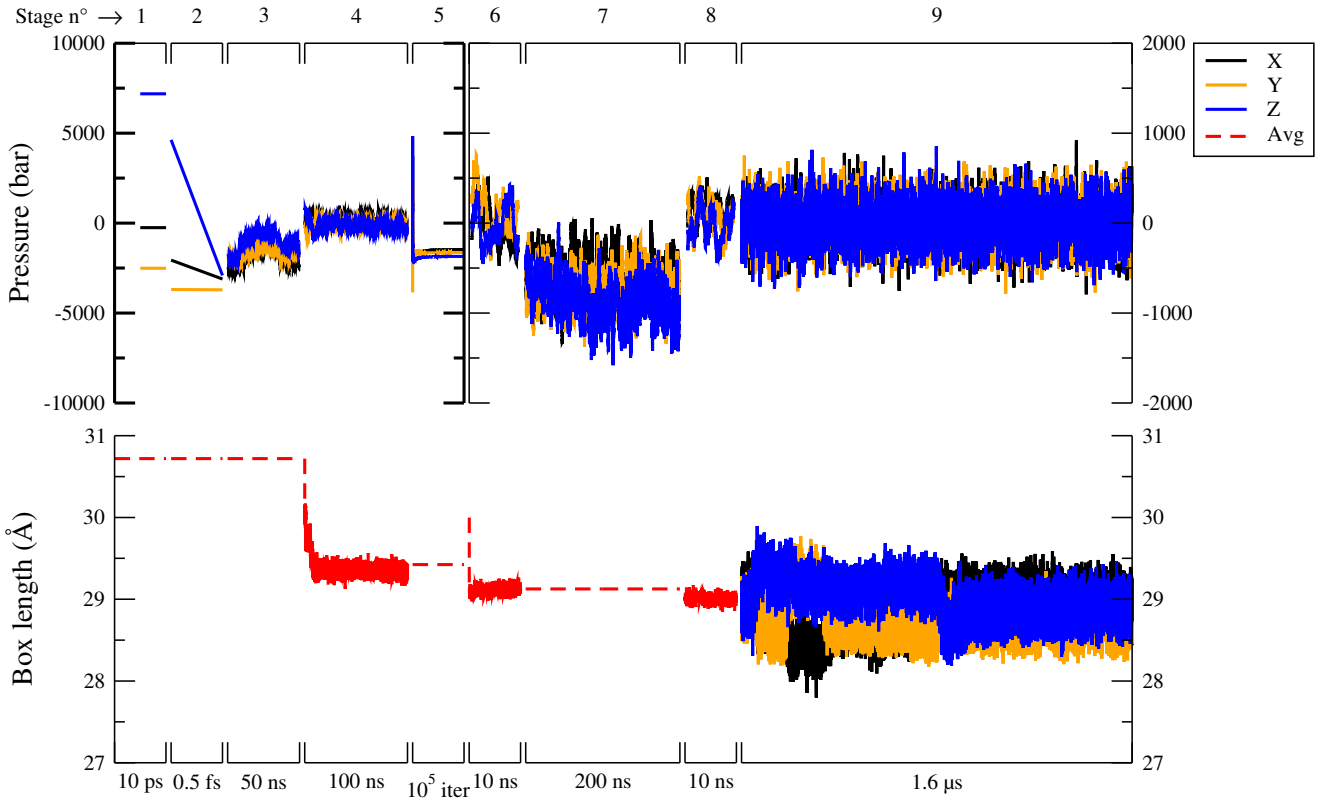

Figure 2.12: Pressure and box length evolution along with various relaxation stages after polymerization process of system r1.2. The serial numbers (n°) represent various stages as: 1. last cycle of polymerization process under *NVT* (298.15 K) for 10 ps ; 2. removal of oligomers and cancellation of system's total momentum, followed by MD under *NVE* for 0.5 fs; 3. MD under ensemble *NVT* (298.15 K) for 50 ns; 4. MD under *NPT iso* (298.15 K, 1 bar) for 100 ns; 5. energy minimization for 100000 iteration steps; 6. MD under *NPT iso* (298.15 K, 1 bar) for 10ns; 7. MD under *NVT* (298.15 K) for 200 ns; 8. MD under *NPT iso* (298.15 K, 1 bar) for 10ns; 9. MD under *NPT iso-stress* (298.15 K, 1 bar) for 1.6 μs.

As shown in the figure, there existed a large gap of pressure tensor elements at the end of polymerization, as the pressure tensor P_{xx} fluctuated around -250 bar, P_{yy} around -2500 bar while P_{zz} up to 7200 bar. As the amide bond formation artificially brought two initially distant atoms close, this process raised immediately the pressure. Meanwhile, due to the molecular movement during the bond formation, more free volume are supposed to be generated in Y direction hence leading to a pressure decline. The pressure tensor P_{xx} fell in a relatively normal range, hence there were probably less effects or the effects from bond formation and free volume creation have been finally averaged in this direction . It should be addressed that bond formation and free volume creation took place both randomly during the polymerization stage. Therefore the observation here only represented individual case. Meanwhile, large differences between pressure tensor elements were always observed for other systems.

In stage 2, the oligomers were firstly removed from the system. Together with the removal of atoms (

O211 and H212 from acyl group and one H739 from amine group for one formation of amide bond) during the polymerization, the removal of materials from the system led to an overall system momentum unequal to zero. Therefore, the cancellation of total system momentum was successively launched, followed by one time step of 0.5 fs MD under ensemble *NVE*. As demonstrated in fig.2.12, the starting pressure points of stage 2 was lower than the end pressure points of polymerization stage, which suggested the pressure tensor elements declined immediately due to oligomer removal. Then, as the momentum was canceled, the pressure tensor elements continued decreasing. According to supplementary tests, with or without removal of oligomers, the momentum cancellation always performed an evident effect on pressure. This demonstrated the momentum accumulation during the polymerization was evident and the polymerization did not take place at the expected temperature at 298.15 K.

Next, the system was relaxed under *NVT* (298.15 K) ensemble firstly for 50 ns in order to leave the system reorganizing while maintaining the box shape. During this stage, the molecules were able to mobile to fill the vacancies, hence the pressure tensor elements were able to evolve naturally under constant box volume. As shown in the figure (stage 3), the pressure tensor P_{xx}, P_{yy} and P_{zz} firstly increased and then decreased, which corresponded a serie of structure reorganizations inside the box. Meanwhile, it was also found the potential energy of the system decreased slowly and finally remained constant at the end of 50 ns. Nonetheless, the average pressure fluctuated around -2000 bar ($P_{xx} = -2152$ bar, $P_{yy} = -1863$ bar and $P_{zz} = -1202$ bar), which was much lower than the expected value. In order to raise the average pressure to 1 bar, the system was relaxed under *NPT iso* (298.15 K, 1 bar) successively (stage 4). The advantage of *NPT iso* ensemble is that it adjusts the average pressure by keeping the box length ratio constant. In other words, the box lengths in three directions are modified proportionally, which allows of the maintenance of box shape. As shown in fig.2.12, since the box remained cubic as before, all three box lengths decreased together from 30.7 Å to 29.4 Å. Meanwhile, it was worthy to note that the gap of pressure tensor elements decreased, as P_{xx} fluctuated around 212 bar, P_{yy} around -70 bar and P_{zz} around -150 bar, respectively. At the end of this stage, the system had a relatively reasonable configuration already, as the evident large vacancy could be no longer observed and the pressure approached to the target value. Therefore, a minimization stage of 10^5 iterations was launched to optimize this configuration.

Departing from the optimized configuration, a relatively long relaxation (= 200 ns) under ensemble *NVT* (298.15 K) was expected (stage 7), before which *NPT iso* (298.15 K, 1 bar) was implemented for 10 ns to raise the pressure to 1 bar (stage 6). The purpose was to leave the system reorganizing for a enough long time while maintaining the box dimension. According to our previous tests, there existed risks of producing unexpected box dimension if the system has not been pre-relaxed enough before being relaxed under ensemble *NPT iso-stress* (298.15 K, 1 bar). It was found for certain systems, the box lengths explored in one direction while decreasing under 20 Å in another. Since Lennard-Jones potential cut-off distance in our study was set as 10 Å, the minimum box length should be at least 2 times larger than this value. Hence a box length inferior than 20 Å

was not permitted. At this long relaxation stage (stage 7), the pressure tensor decreased evidently (particularly in P_{zz}), which demonstrated the structural reorganization. At the last 50 ns of this stage, the pressure tensor elements remained relatively constant and close, with P_{xx} fluctuated around -570 bar, P_{yy} around -730 bar and P_{zz} around -950 bar. Then, another stage of *NPT iso* (298.15 K, 1 bar) was launched to raise the average pressure to 1 bar (stage 8). Afterwards, the system was taken to the final relaxation stage (stage 9) under *NPT iso-stress* (298.15 K, 1 bar), which corresponded to the general real experimental condition of APA polymer structural characterization.

In *NPT iso-stress* ensemble, the pressure tensor elements are conditioned to the expected value, as $P_{xx} = P_{yy} = P_{zz}$, while the box lengths in different directions are allowed to fluctuate. As shown in fig.2.12, the pressure tensor curves in different directions overlapped well with each other as expected. Meanwhile, the box was no longer in a cubic shape as the box lengths in three directions fluctuated independently. The different box length fluctuations reflected that the constraints in different directions were finally equilibrated and released via reorganization. It should be noted this relaxation stage demanded a long time, as there still existed some box length fluctuations in Z direction after 800 ns. With the continuation of relaxation time up to 1.6 μs, the box lengths became constant at the end part of the stage.

2.4.1.5 Potential energy relaxation and density evolution

To mimic the thermophysical properties of the APA polymer system in real experimental condition, the polymers were finally relaxed under *NPT iso-stress* (298.15 K, 1 bar). In this section, the potential energy and density evolution along relaxation time in the final relaxation stage is presented, in order to demonstrate that long relaxation time up to 5.45 μs was indispensable to release the strains generated during polymerization process. Among all the polymer systems, the system of initial MPD:TMC at 0.5 demanded the longest relaxation time, hence its profiles are presented here as example.

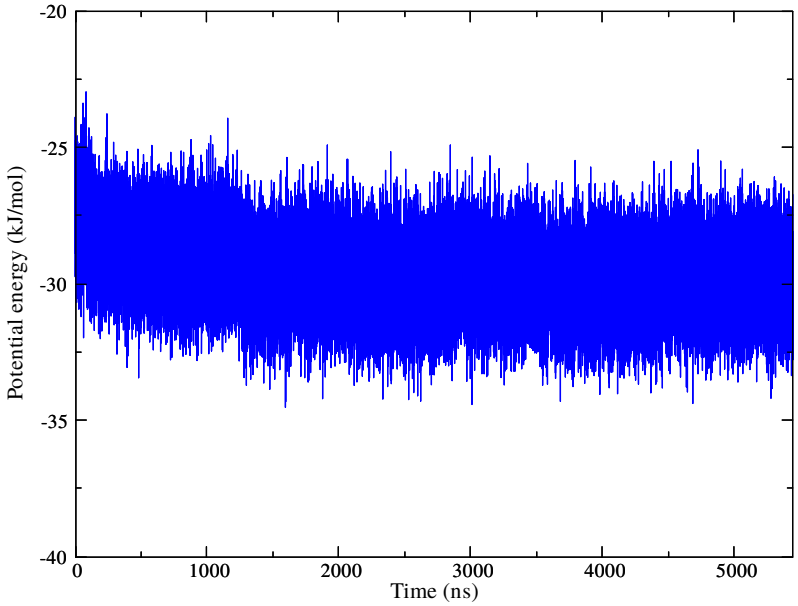

Figure 2.13: Potential energy evolution as a function of relaxation time under *NPT iso-stress* (1 bar, 298.15 K) of polymer system r0.5.

As presented in the figure 2.13, the system's potential energy passed a long declining stage for nearly 4 μs. Then it became constant for the last 1.45 μs.

The system's density kept increasing during the first 2 μs and continued to fluctuate in the following 2 μs, as shwn in figure 2.14. The evident density fluctuation during the first 4 μs corresponded well to the potential energy relaxation, as the system performed several structural organizations to release the constraints. After 4 μs, the potential energy became constant while there existed still some regional reorganization, the density continued to fluctuate and finally became stable from 4.7 μs.

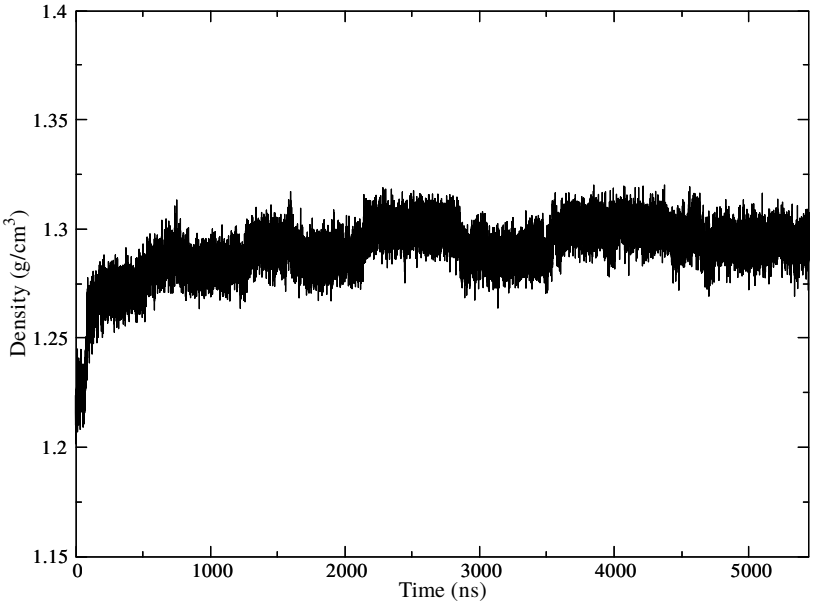

Figure 2.14: Density evolution as a function of relaxation time under *NPT iso-stress* (1 bar, 298.15 K) of polymer system r0.5.

Overall, the above discussions demonstrated for APA polymer systems with box dimension in our study (around $30 \times 30 \times 30$ Å^3), long relaxation time up to several μs under *NPT iso-stress* (298.15 K, 1 bar) is demanded to achieve a constant potential energy or thermophysical properties data, such as density.

2.4.1.6 Amide bond configuration analysis via angle/torsion distribution histogram

To verify whether the newly formed amide bonds exhibited reasonable configurations after the successive relaxation stages, the histograms of angle (N-C=O) and torsion (H-N-C=O) distributions of typical systems r0.25_0 (repetition box n°0), r1.5_1 (repetition box n°1) and r5_0 (repetition box n°0), at the end of the 150th polymerization cycle (Cycle 150) and at the end of last relaxation stage under *NPT iso-stress* (298.15 K, 1 bar) (Relaxation), are presented respectively in figure 2.15.

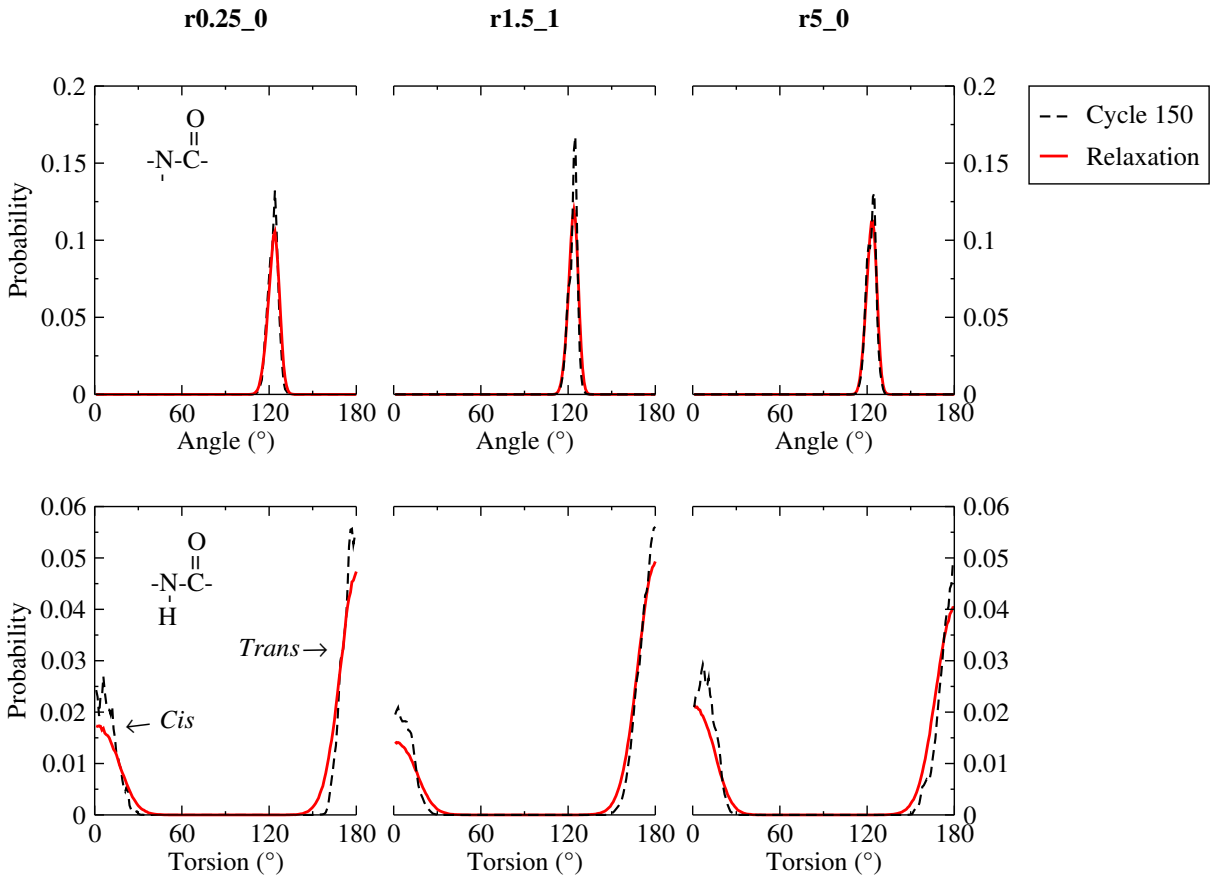

Figure 2.15: Histograms of N-C=O angle and H-N-C=O torsion distributions of systems r0.25_0 (repetition box n°0), r1.5_1 (repetition box n°1) and r5_0 (repetition box n°0) at the end of the 150th polymerization cycle (Cycle 150) and at the end of last relaxation stage under *NPT iso-stress* (298.15 K, 1 bar)(Relaxation).

As shown in figure 2.15, for all systems the N-C=O angles at the end of polymerization or at the end of relaxation stage were all around 124°, which was close to the equilibrium value at 123°. It should be addressed that systems had a lower probability at the equilibrium value after the relaxation. This could be explained by the existence of adjacent neighborhood chains in these polymer systems, which probably affected the N-

C=O angle configuration by establishing intermolecular interactions such as hydrogen bond during the various relaxation stages, hence leading to a wide angle configuration distribution in the end.

Meanwhile, the relaxation of amide bond is evidently shown by comparing the distributions of H-N-C=O torsion, as all distribution curves at the end of relaxation stages became much smoother than that at the end of polymerization. Since the amide bond performs a double bond nature, the four atoms (H-N-C=O) are supposed to stay in the same plane. Its conformation is restricted to one of two possibilities, either *trans* or *cis*, which corresponds to a torsion angle at 180° or 0° respectively. The amide bonds are generally in the *trans* conformation. The *cis* conformation is less favorable because of the steric interference between the side chains. For example, for a system of pure dimers, all amide bonds exhibited the *trans* configurations as in fig.2.16(a). Nonetheless, polymer systems in our study were found also exhibiting *cis* configurations. One of theses *cis* configurations in system r0.25_0 is presented in fig. 2.16(b) as example.

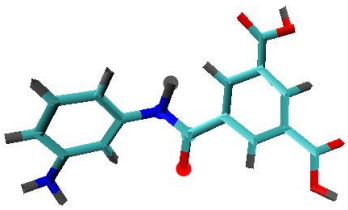

(a) *Trans* amide bond configuration at the end of relaxation under *NPT iso-stress* (298.15 K, 1 bar) in 50 dimer system

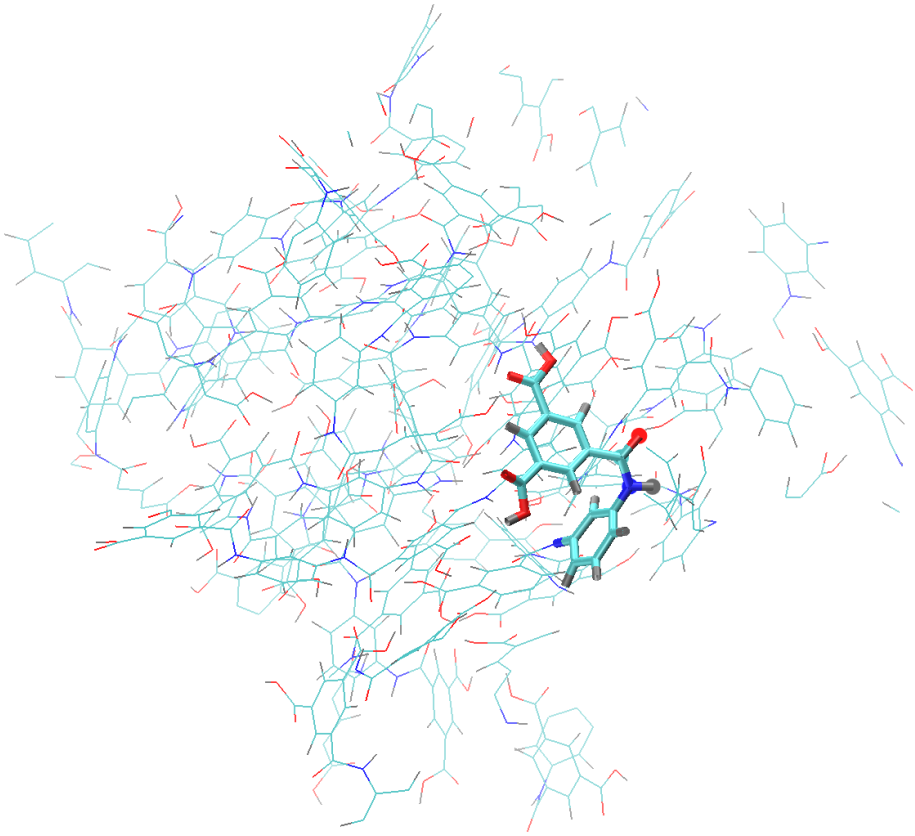

(b) *Cis* amide bond configuration at the end of relaxation under *NPT iso-stress* (298.15 K, 1 bar) in polymer system r0.25 (repetition box n°0)

Figure 2.16: Trans or cis amide bond configuration in dimer or r0.25 polymer system (repetition box n°0). Red cycle: oxygen atom in amide bond; grey cycle: hydrogen atom in amide bond.

According to the torsion histogram (fig.2.15), at the end of relaxation stages, nearly 60% of amide bonds were in *trans* configuration while the rest 40% were in *cis* configuration. During the crosslinking process, the amide bonds were formed once the distance between the potential carbon and nitrogen atoms met the criteria,

thus allowing of the possibility to generate *cis* configuration inside our polymer systems. Due to the fact that there doesn't exist experimental investigation (at least to our knowledge) on the *cis* or *trans* configuration of amide bond in real APA films, we compared one dimer in *trans* configuration with another one in *cis* via DFT analysis by GAUSSIAN. There existed an energy gap around 19 kJ/mol between *cis* and *trans*, a larger value compared to RT, where R is the universal gas constant (8.314 $J{\cdot}K^{-1}{\cdot}mol^{-1}$) and T is absolute temperature. More investigations are required to verify the presence or the absence of *cis* configuration in experimental conditions.

2.4.2 Chemical structure analysis

2.4.2.1 Chemical structure analysis via N/O map

Despite the various chemical structure descriptors introduced previously in previous chapter, an N/O map distribution[115] is another relevant method to analyze and compare the chemical structures of APA systems. In such map, APA system are plotted as a function of nitrogen (N,%) and oxygen (O,%) elemental percentages with hydrogen excluded. For instance, the fully-crosslinked system ($C_{18}H_{12}N_3O_3$) performs with a N(%) at 12.5 (%) and an O(%) at 12.5 (%), then it can be plotted on the N/O map accordingly as in fig.2.17. Similarly, the fully-linear structure ($C_{15}H_{10}N_2O_4$), with a N(%) at 9.55 (%) and an O(%) at 19.05 (%), can be plotted as well.

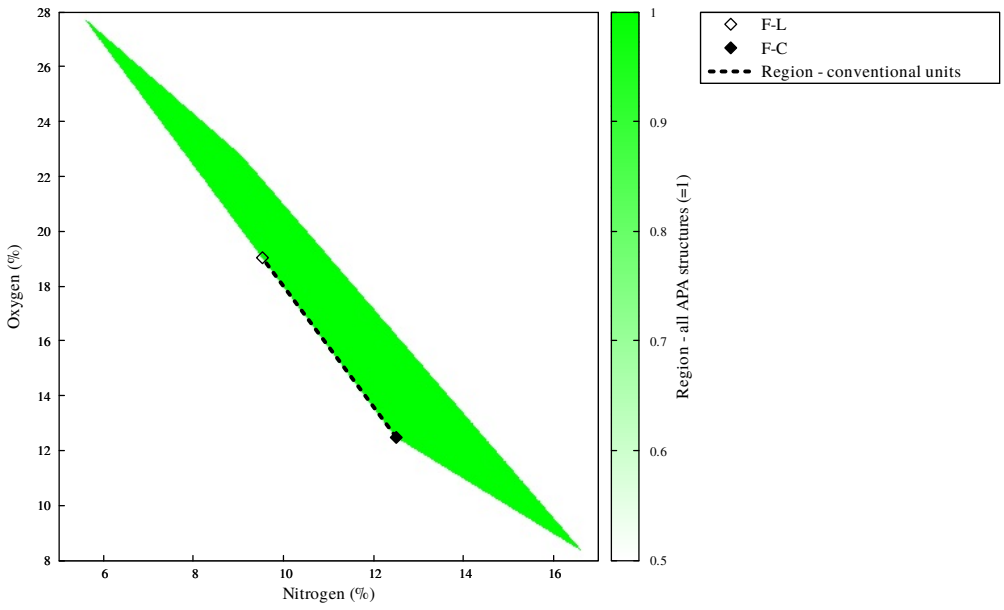

Figure 2.17: N/O map indicated with region of all possible APA structures. F-L represents the fully-linear point while F-C represents the fully-crosslinked point. The region fits the structural assumption of conventional chemical units schema is indicated by dotted line.

On the basis of the chemical units of the new descriptors presented previously (eq. (1.11) and (1.12)), for a APA polymer, the number of unit a ($= \frac{C-3N}{9}$) and b ($= 2N$) should be superior to zero, while the number

of unit c ($= \mathrm{O} - \frac{\mathrm{C}-3\mathrm{N}}{3}$) and d ($= \mathrm{N}+\mathrm{O} - \frac{2(\mathrm{C}-3\mathrm{N})}{3}$) should be equal or greater than zero. Moreover, under the experimental condition, generally APA film is washed at the end of IP, hence monomers are not likely to remain within the final polymer structure. Accordingly, under the assumption that there exists no monomer in APA polymer system, the fraction of acyl groups that has reacted, f_{ac} ($= 2 - \frac{3\mathrm{O}}{\mathrm{C}-3\mathrm{N}}$), is supposed to vary between 33.3% and 100%. More specifically, for the TMC monomer unit, 33.3% indicates that one out of three acyl groups is connected while 100% indicates that all three acyl groups are reacted. Similarly, the fraction of amine groups that has reacted f_{am} ($= \frac{2\mathrm{C}-3\mathrm{O}}{3\mathrm{N}} - 2$) should vary between 50% and 100%. 50% represents the cases where the MPD monomer unit only has one connected amine groups, while 100% indicates that MPD's both amine groups are connected. Respecting these above criteria, the region which covers all possible APA structures (without presence of monomer) could be defined in the N/O map with coloration, as presented in fig.2.17.

In addition, the region which fits the structural assumption of conventional chemical units scheme could be indicated in N/O map. This scheme assumes that APA polymer consists of two fractions, a linear one and a crosslinked one (fig.1.21 in chapter 1), in which all amine groups of MPD monomers are supposed to be connected. Accordingly, the corresponding APA structure region is the line between the fully-linear and fully-crosslinked structure points, presented as the dotted line in fig.2.17. It should be noted that this line is only a part of the boundary of the region of all possible APA structures, which underlines the limited applicability of the conventional chemical units.

Interestingly, N/O map could be further combined with the analyses of conventional and new chemical descriptors as well. On the same O/N map, the chemical descriptor values of χ, $r_{m:t}$, f_{ac} and f_{am} corresponding to each group of nitrogen and oxygen values can be calculated by applying the equations presented in the previous section 1.3.5.1. Then the obtained results can be presented as 2D color map for the possible region of APA structures on the N/O map.

In this study, the chemical structures of simulated polymers were investigated via N/O map plotting, combined with the analyses of chemical descriptors χ, $r_{m:t}$, f_{ac} and f_{am}. The element compositions of each APA molecular model such as N (%) and O (%) were analyzed and obtained by our local code PAASTATS. This code was developed specifically to collect chemical structure information of APA molecular models. In addition, experimental chemical composition data of various APA layers of RO/NF membranes in the literature were also plotted in N/O map (see Annexes A2). As shown in the fig.A1, chemical composition results given by different authors for one same membrane type varied from each other. Moreover, half of the experimental data presented in this figure dropped out of the possible region of all possible APA structures. These contradictions suggest that chemical compositions of real APA films still remain poorly studied, possibly due to a high analysis error of XPS/RBS. Hence, more investigations are required to give an accurate chemical structure description for real APA membranes.

2.4.2.2 N/O map analysis combined with chemical descriptors

In the fig.2.18, the simulated APA polymers generated from fifteen different initial MPD:TMC ratios (r0.25, r0.5, r0.75, r1, r1.2, r1.3, r1.8, r1.9, r2.0, r2.5, r3, r3.5, r4 and r5) are plotted in N/O maps. For each typical system with repetitions (r0.25, r1.5 or r5), one average value of 11 repetitions is presented with error bar as $r0.25_{rep}$, $r1.5_{rep}$ and $r5_{rep}$, respectively. As shown in the figure, these error bars were very small, demonstrating that, for all three typical ratios, their 11 repetitions exhibited very close chemical structures. These results suggested a good quality of our polymerization algorithm, which is able to produce polymer chemical structures with a good repeatability from a given initial monomer ratio.

In each sub-figure of fig.2.18, the specific region corresponding to possible APA polymer structures (under the assumption that no monomer remains) is colored. The color evolution signifies the evolution of chemical descriptors χ, $r_{m:t}$, f_{ac} and f_{am} in sub-figures (a), (b), (c) and (d), respectively.

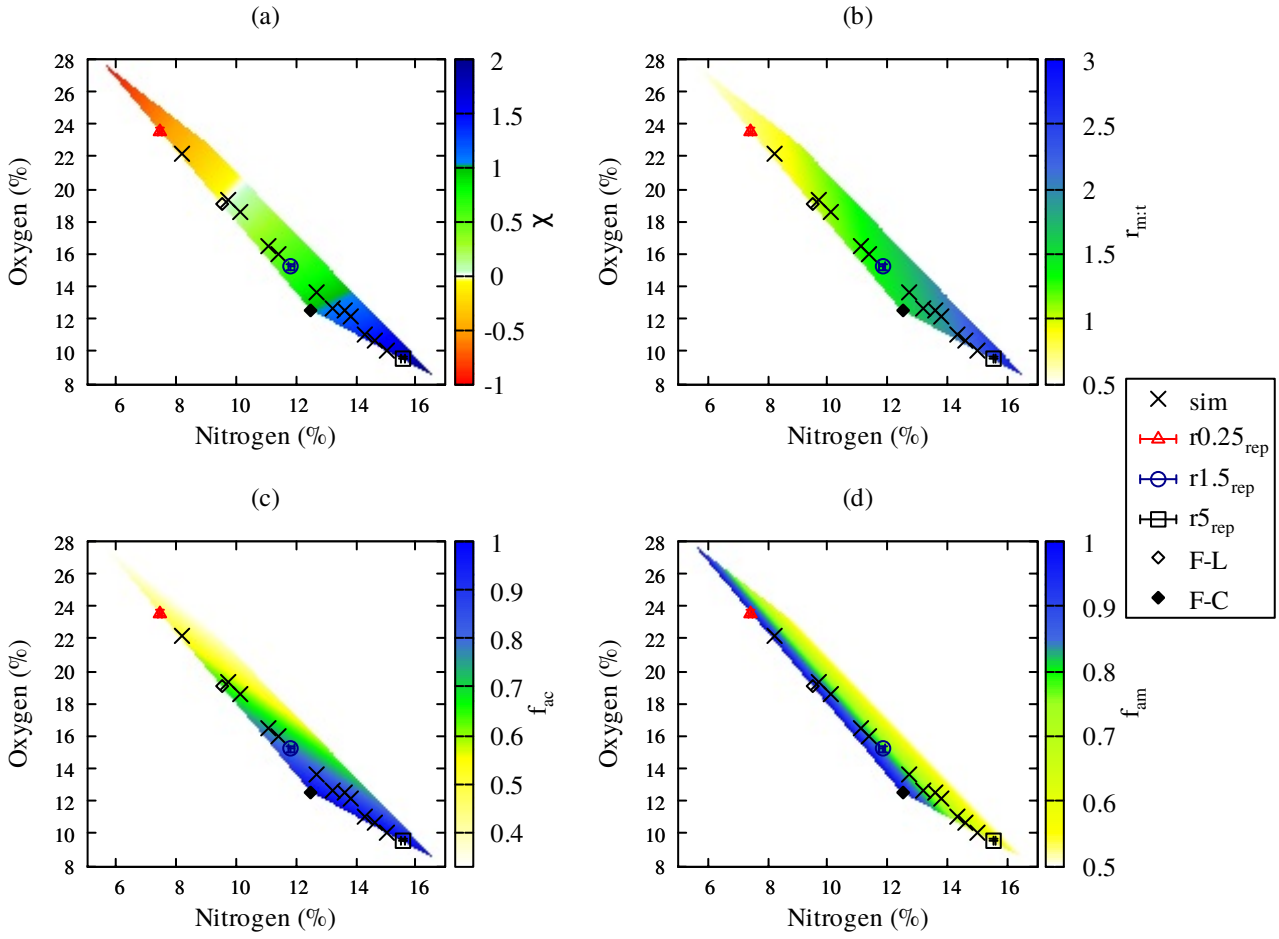

Figure 2.18: N/O map plotting with chemical structure descriptors χ, $r_{m:t}$, f_{ac} and f_{am} of simulated APA polymers. Cross symbols from left to right: r0.5, r0.75, r1, r1.2, r1.3, r1.8, r1.9, r2.0, r2.5, r3, r4 and r3.5. Triangle, cycle and square symbols represent the average values of 11 repetitions of r0.25, r1.5 and r5, respectively.

The conventional chemical descriptor χ is based on the conventional chemical units scheme, hence a good application of this descriptor is limited to APA structures located upon the line between the fully-linear and

fully-crosslinked points. In face of the simulated polymers in our study, which exhibited chains ends, this descriptor became meaningless. As shown in fig.2.18(a), from r0.25 to r5, their χ values increased progressively from -0.59 to 1.75 along with the progressive decline of their O/N ratios from 3.3 to 0.6. Only the systems between r0.75 and r1.8 had a physically meaningful range of χ ($0 \leq \chi \leq 1.0$). Moreover, it also turned out that χ values of our samples were not either quantitatively nor qualitatively comparable. According to the results, r0.75 performed with a χ value at zero, suggesting this system didn't exhibit any crosslinking node. However, according to our detailed chemical analysis via PAASTATS, r0.75 was verified to own six crosslinked fraction structures. On the contrary, r2.5 exhibited a χ around 1.2, but it only exhibited five crosslinked fraction structures. In face of such inconsistency, we found that the application of the conventional chemical descriptors χ should be taken with caution, as the majority of APA polymer systems might not fit its structural assumption. Meanwhile, the newly proposed descriptors don't have such limit, as they are applicable for all possible APA structures.

The fig.2.18(b) demonstrated the evolution of the final monomer ratio $r_{m:t}$ for our simulated samples. These samples exhibited a great variability of chemical structures with final $r_{m:t}$ ranging from 0.68 to 2.61, which crossed the vast majority of the possible APA polymer region. This validated our protocol to construct different APA structures by changing the initial MPD:TMC monomer ratios. During the IP, the MPD monomer concentration declines along with the diffusion in the organic phase, which might result in depth-dependent chemical heterogeneity. Such heterogeneity have been investigated previously via applying mathematical model of APA formation[33, 35]. Recently, both chemical heterogeneity and homogeneity were reported for APA layers of various commercial RO membranes via XPS and RBS analyses[17]. Meanwhile, it should be addressed that the chemical structures of commercial APA layers remained not clearly studied. According to the literature, elemental compositions of certain commercial APA layers have been analyzed by various studies, but these data were not consistent with each other probably due to large analysis errors of techniques as XPS[17, 24, 63, 69, 83, 114]. Hence, chemical structures of commercial APA layers remained blurry, as no accurate information was available on the chemical similarities or differences among different membranes.

The investigations with such abundant sample variability in this study are supposed to bring very interesting and complementary information. On one hand, our various models managed to represent possible heterogeneous regions of active APA layers along with the thickness; on the other hand, they were also able to represent APA layers of various commercial RO membrane types, which might be potentially different. Moreover, possible structures-properties correlations were able to be investigated directly by comparing these various structures.

As shown in figure 2.18(c,d), along with the increase of initial MPD:TMC ratio, f_{ac} rose up while f_{am} decreased. Systems generated from initial MPD:TMC ratios at 0.25 and 5 exhibited extreme f_{ac}/f_{am} around 45%/100% and 99%/57%, respectively. This indicated that with abundant initial TMC monomers (in case of r0.25), the final APA polymer exhibit an excess of free acyl groups while amine groups are well connected; vice versa, when MPD monomers are overdosed, the final APA structure exhibits evident free amine groups while free

acyl groups rarely exist. Such polymer generation result was consistent with the chemical structure evaluation of real APA films, where the authors synthesized APA films with various monomer portions and found a high concentration of free amine or acyl group respectively with a high initial MPD or TMC monomer portions[26]. Moreover, this generation result indicated a possible correlation between the final chemical structure and the depth along the film thickness. In real IP polymerization, as the quantity of MPD declines with its diffusion in the organic phase, there might exist an overdose of MPD at the interface between organic and aqueous phases (if MPD monomers are of high concentration), hence the resulting region (back-surface) is supposed to be rich in MPD monomer units and free amine groups. On the contrary, with abundant TMC monomers, the top-surface region is supposed to exhibit more TMC units and free acyl groups while less free amine groups. This estimation was generally confirmed by our experimental chemical structure analysis of CPA2, where its top-surface was found exhibiting a lower $r_{m:t}$ and a higher f_{am} than the back-surface. Meanwhile, it should be addressed that the CPA2 back-surface didn't exhibit a high f_{ac} as expected. This could be due to the complicated real synthesis condition at the interface with the presence of aqueous phase, where the active acyl groups are hydrolyzed by water hence leading to a weak connection degree.

As for medium initial MPD:TMC ratios such as r1.5, both relative high connection degrees were achieved around 80%, suggesting a better connection state of these systems. This result was in consistence with the observation in fig.2.10, where systems at extreme MPD:TMC ratios such as r0.25 and r5 consisted of molecules pieces while r1.5 generated large networks during the polymerization. Therefore, it could be deduced that for a real APA film, its most crosslinked structure is more probably generated in the regions where the quantities of two monomer are more or less equivalent, as more potential sites would be active to form the network. The formation of such monomer ratio is determined by various factors such as the initial monomer concentrations and ratio, synthesis temperature, organic solvent properties, etc.

According to the N/O map (fig.2.18), the system r1.8 was most adjacent to the fully-crosslinked structure, exhibiting $r_{m:t}$, f_{ac} and f_{am} at 1.61, 85% and 79% compared to that of fully-crosslinked structure at 1.5, 100% and 100%. Meanwhile, r0.75 was closet to fully-linear structure, with $r_{m:t}$, f_{ac} and f_{am} at 1.04, 62% and 89%. For these two simulated systems, neither acyl nor amine group was fully connected, suggesting that the formation of the polymer might also generate steric hindrance for the potential connection. To promote the connection, special treatment should be considered, such as more insertion of free monomers or application of extra attraction force[47].

Nonetheless, it should be addressed that during real IP, the mobility of monomers is supposed to be naturally restrained by the polymer formation. There is supposed to exist some regions with an overdose of one certain monomer type. Thereby the formation of large regions only consisted of fully-linear structure or fully-crosslinked structure, is not likely to be possible under real experimental conditions. As a consequence, it is natural for real APA films to have a certain quantity of free groups or chain ends.

2.4.3 Local structure analysis

2.4.3.1 State of amide group

The radial distribution function (RDF) of the pair between nitrogen (Namd) and oxygen (Oamd) atoms in amide bond $g_{\mathrm{NamdOamd}}(r)$ assists in investigating the crosslinking state such as the amide bond configuration and distribution in local structure. Since the polymer systems exhibited similar $g_{\mathrm{NamdOamd}}(r)$, the result of system r1.5_1 (repetition box n°1) was taken as example here and was compared to that of dimer system (50 dimers) in fig 2.19. The intramolecular and intermolecular contributions are demonstrated respectively along with the total RDF. More details on $g_{\mathrm{NamdOamd}}(r)$ of other polymer systems are presented in Annexes A5.

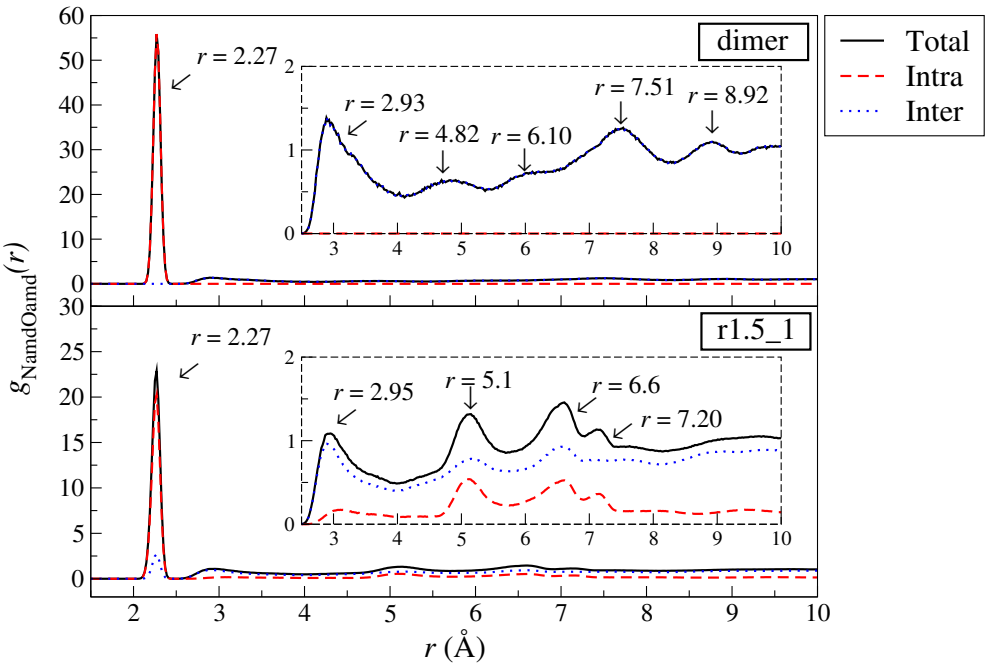

Figure 2.19: Radial distribution function (RDF) between nitrogen (Namd) and oxygen (Oamd) atoms in amide bond ($g_{\mathrm{NamdOamd}}(r)$) of 50 dimer system and polymer system r1.5_1 (repetition box n°1).

As presented in fig.2.19, all systems had a large first peak at 2.27 Å. For dimer system, this peak totally arose from intramolecular contribution, which represented the distance between the nitrogen and oxygen in amide bond of dimer. In contrast to dimer system, the peak of r1.5_1 consisted of both intramolecular and intermolecular components, while the intramolecular component was the dominant part. The same oxygen to nitrogen distance (2.27 Å) in amide bond was observed for the intramolecular contribution for both dimer and polymer systems, suggesting that the newly formed amide bonds in polymer systems finally exhibited a reasonable configuration as in dimer after the relaxation stages. The intermolecular component in polymer system represented the separation distance, the very close distance of oxygen and nitrogen atoms in adjacent amide bonds from different molecular chains, from which it could be deduced that the polymers were more packed than the dimer system.

After the first peak, the amplitude declined immediately for all systems, suggesting the probability of finding a pair of oxygen and nitrogen in amide bond decreased sharply and progressively approached to that of finding such a pair at a completely random distribution (=1). In seek for a better precision, the region of RDF from 2.5 Å to 10 Å is zoomed in each graphic.

As there existed no connection among the dimer molecules, the intramolecular contribution naturally remained at zero after the first peak and the peaks behind consisted of sole intermolecular component. Dimer system's second peak located around 2.93 Å as separation distance, which was nearly 0.7 Å further than that in r1.5_1 polymer system. Following the second peak, several peaks could be observed at 4.82 Å, 6.10 Å, 7.51 Å and 8.92 Å, which represented the progressive outward amide bond shells. However, it should be addressed that these peaks were dull, which demonstrated a loss of regularity of the intermolecular configuration along with the extension of radial direction.

With respect to the polymer system, after the first peak, the intermolecular component became the dominant contribution while the intramolecular component still existed due to the crosslinking. In general, it was noted that intra and intermolecular components exhibited the same evolution trend, suggesting a good relaxation of polymer structure. The second peak located around 2.95 Å, mainly consisted of the intermolecular component, suggesting the second intermolecular coordination shell. Meanwhile, weak intramolecular contribution could be observed. It was notable that neighboring amide bonds are not supposed to exist in such close distance, therefore this intramolecular contribution was thought to be from the chain folding. Similarly, the intramolecular contribution for the third peak located around 5.10 Å is supposed to be from the chain folding as well. The forth peak was observed around 6.55 Å to 6.62 Å, for which the intramolecular component was from the closest neighboring amide bond, as presented in Annexes fig.A4.

Moreover, the fifth peak at 7.08 Å, mainly deduced from intramolecular contribution, was observed closely adjacent to the forth one.

Similar to dimer system, from 4 Å, the intermolecular component of polymers exhibited dull peaks, while the peaks from intramolecular component remained sharp. This demonstrated that the intermolecular configuration was less regular than the intramolecular one in polymer systems.

Generally speaking, for a purely linear APA chain, the distance between any two amide bonds is supposed to be at least several times of one covalent bond length. Since the crosslinked polymer exhibited a complex 3D spatial configuration due to network formation (such as chain folding), it was reasonable to observe subtle amid bond distance variations such as that between the third and the forth peaks (around 1.5 Å) and between the forth and the fifth ones (less than 1 Å).

Overall, the analysis of $g_{\mathrm{NamdOamd}}(r)$ demonstrated that the polymer systems exhibited both close intermolecular and intramolecular distances, implying a highly packed state with respect to the dimer system.

The density of amide bond in various systems could be investigated and compared from the coordination number of oxygen atom around nitrogen atom in amide bond ($N_{c\ \mathrm{Oamd_{(Namd)}}}$), figure 2.20.

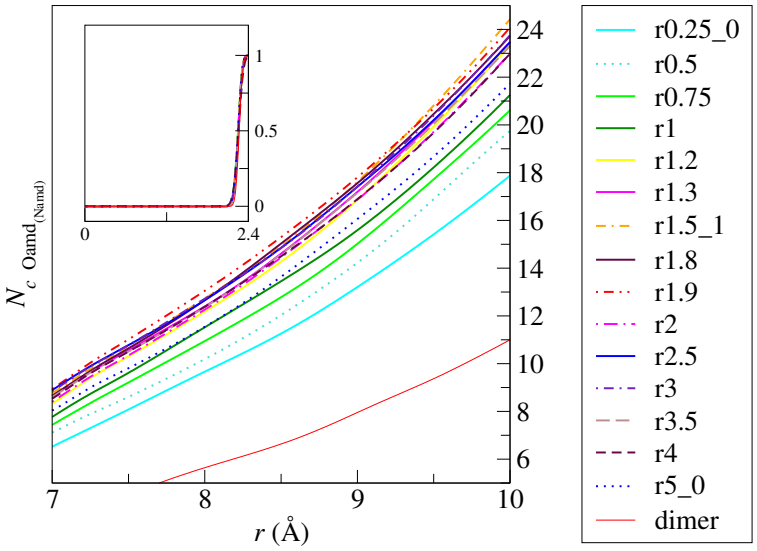

Figure 2.20: Coordination number of nitrogen (Namd) and Oxygen atom (Oamd) in amide bond in 50 dimer system and polymer systems generated from different initial MPD:TMC ratios.

The coordination number of Oamd around Namd (equal to that of Namd around Oamd in this case) at 2.4 Å (the periphery of the first shell) was equal to 1 for all systems, corresponding to the amide bond configuration. If a long coordination distance was taken, the average density of the amide bond in each system could be revealed. At 10 Å, the largest coordination number was found at 24 from the polymer system r1.9. As expected, the lowest coordination number was found at 10 from the dimer system, since this system was not packed at all compared to the polymers. Moreover, systems generated from a medium initial MPD:TMC ratios (such as r1.2, r1.5 and r1.9) demonstrated a tendency to have a denser amide bonds density than systems of extreme ratios (such as r0.25 and r5). This trend was verified by the repetition tests (fig.A5 in Annexes), where systems generated from initial MPD:TMC ratio at 1.5 showed higher amide bond density than systems from initial ratios at 5 and 0.25 at long coordination distance. Therefore, a medium initial MPD:TMC was proven to be more supportive for amide bond formation.

2.4.3.2 State of free amine and carboxylic acid groups

During the polymerization process, the new amide bond was formed based on the distance criteria (≤4 Å) between the closest nitrogen atom in free amine group (Namn) and carbon atom in free carboxylic acid group (Ccbla). It is interesting to have a look at the states of these two atom types in dimer and polymer systems after the relaxation. The RDF of atom pair between Namn and Ccbla ($g_{\mathrm{NamnCcbla}}(r)$) of 50 dimer system and APA polymer systems are presented respectively in fig.2.21 and fig.2.22.

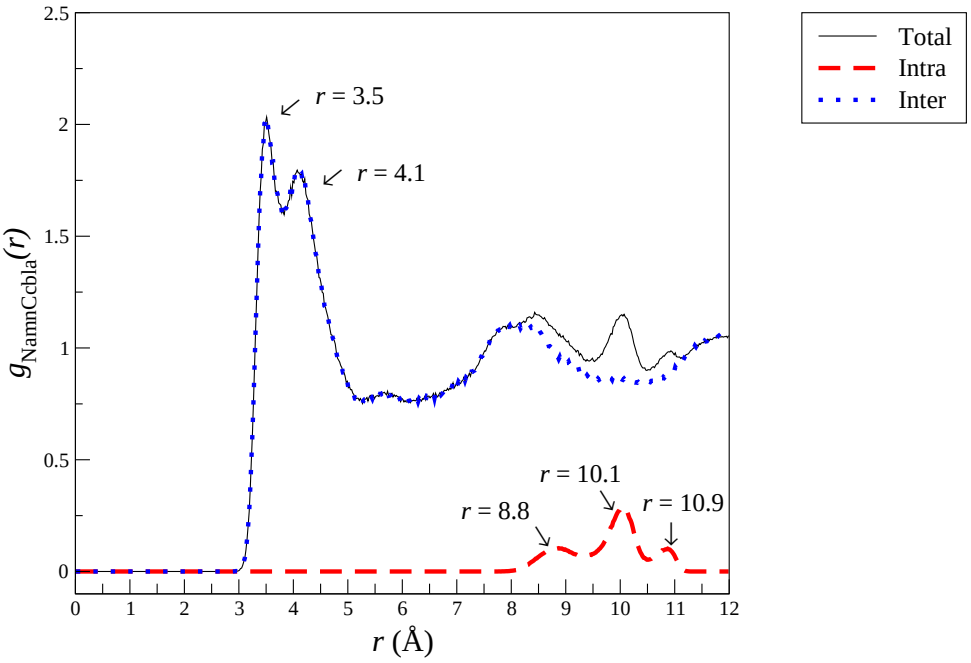

Figure 2.21: Radial distribution function (RDF) between nitrogen atom in amine bond (Namn) and carbon atom in carboxylic acid bond (Ccbla) of 50 dimer system.

The intermolecular peaks between 3.5 Å and 4.1 Å represented the distances between amine and carboxylic acid groups from nearby dimer neighborhoods. Meanwhile, the intramolecular peaks between 8.8 Å and 10.9 Å were the distances between the sole free amine group and one of the two free carboxylic groups inside the same dimer.

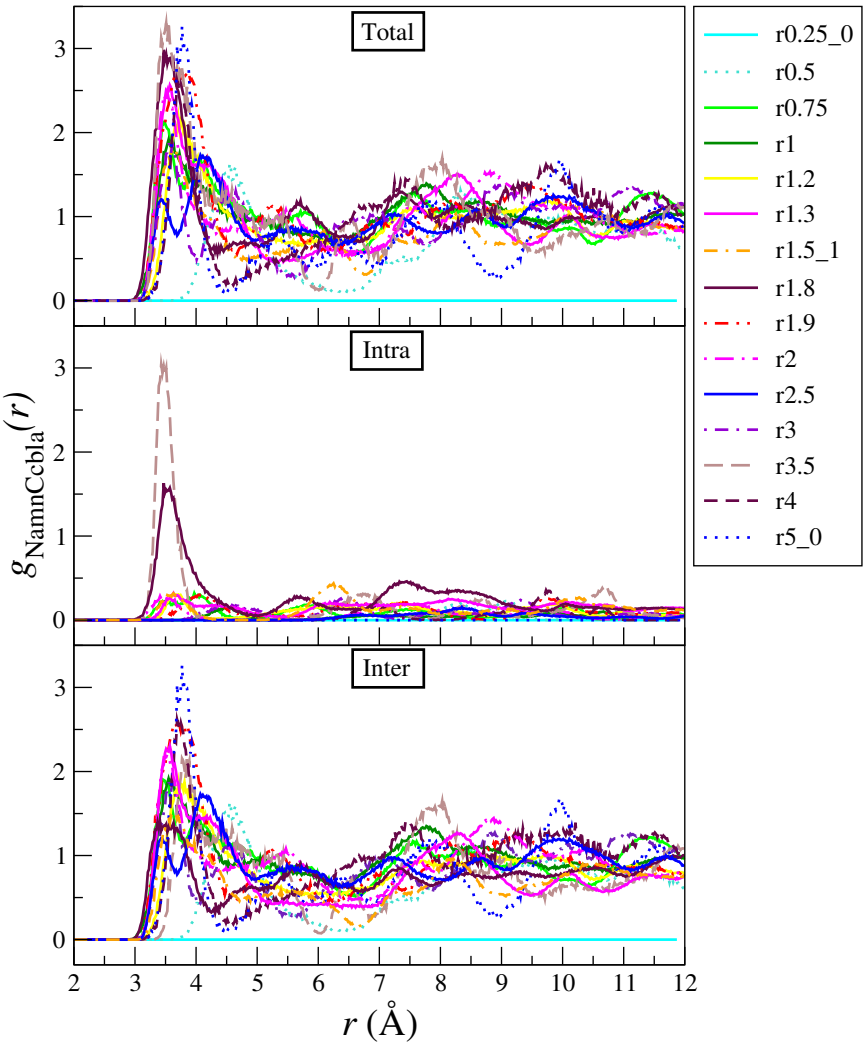

Figure 2.22: Radial distribution function (RDF) between nitrogen atom in amine group (Namn) and carbon atom in carboxylic acid group (Ccbla) of polymer systems generated from different initial MPD:TMC ratios

Overall, the RDFs of atom pair Namn-Ccbla were less regular than that of Namd-Oamd, as there existed a large variability among the polymer systems. Such various performances are supposed to be explained by different local chemical structures and distributions within these polymer systems. As discussed previously in section 2.4.2.2, these APA polymers exhibited various chemical structures as the final $r_{m:t}$ ranged from 0.68 to 2.61, corresponding to f_{ac}/f_{am} varying from 45%/100% to 99%/57%. As a consequence, the quantity and distribution of free acyl and amine groups in these systems were naturally different. System r0.25 had no free amine group, hence its $g_{\mathrm{NamnCcbla}}(r)$ (both inter and intramolecular components) remained at zero. System r5 was rich in free amine groups while its acyl groups were nearly fully saturated. Hence it was difficult to find a

molecule which contained both free amine and carboxylic acid groups. Therefore its intramolecular contribution remained at zero while only intermolecular contribution existed. Distinguished from all other systems, system r3.5 or r4 had a large intramolecular peak around 3.5 Å, which was probably attributed to the random folding configurations between the rarely existent free carboxylic acid groups and free amine groups.

Meanwhile, it should be addressed that for the majority of the systems, there existed a large first peak around 3.8 Å, mainly consisted of intermolecular component. This peak indicated possibilities to find again pairs of a free carbon and nitrogen atoms within 4 Å. Given that such pair didn't exist at the end of polymerization, this observation demonstrated a good structural reorganization for polymer systems after the relaxation stages.

Taking the coordination distance at 4.5 Å, which corresponds to the end position of the first intermolecular peak of $g_{\mathrm{NamnCcbla}}(r)$ for the majority of polymer systems, the coordination numbers of Ccbla around Namn ($N_{c\ \mathrm{Ccbla}_{(\mathrm{Namn})}}$) and Namn around Ccbla ($N_{c\ \mathrm{Namn}_{(\mathrm{Ccbla})}}$) for various polymer systems together with the dimer system, are presented in fig.2.23.

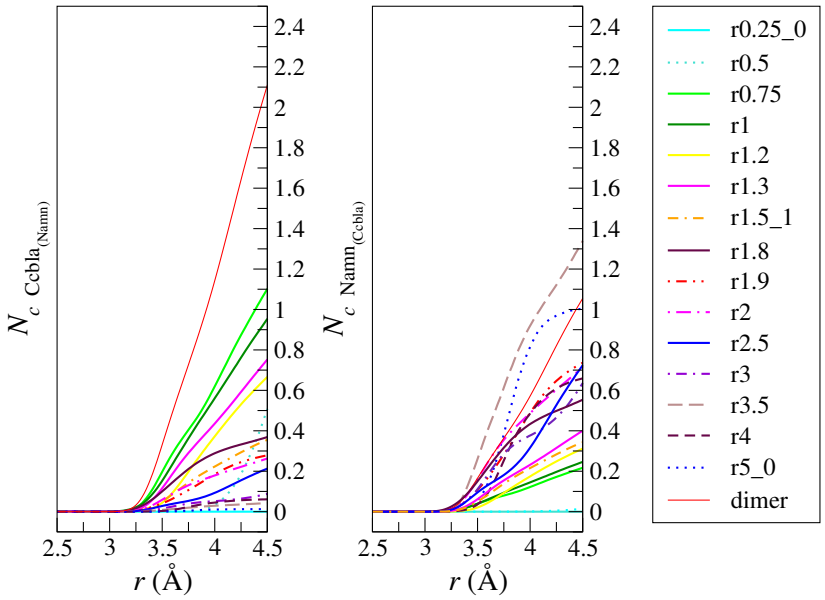

Figure 2.23: Coordination number of Ccbla-Namn atom pair of polymer systems generated from different initial MPD:TMC ratios.

In general, $N_{c\ \mathrm{Ccbla}_{(\mathrm{Namn})}}$ exhibited a decreasing tendency as a function of increasing initial MPD:TMC ratios, as it declined from 1.1 to nearly zero when the initial MPD:TMC ratio increased from 0.75 to 5. This observation was in consistence with previous chemical structure analyses. For systems with low initial MPD:TMC ratios, TMC monomers were excessive during the polymerization, naturally leading to an abundant remaining free acyl groups and poor concentration of free amine groups. Meanwhile, dimer system exhibited the largest $N_{c\ \mathrm{Ccbla}_{(\mathrm{Namn})}}$ as it exhibited the largest free acyl group density.

Vice versa, with respect to the coordination number of Namn around Ccbla ($N_{c\ \mathrm{Namn}_{(\mathrm{Ccbla})}}$), more free

amine groups were found surrounding around free acyl groups in systems with high initial MPD:TMC ratios. Meanwhile, it was noted that the $N_{c\ \mathrm{Namn_{(Ccbla)}}}$ of r3.5 at 4.5 Å was even larger than that of dimer system, which could be explained by polymer's more compacted state.

Given that systems generated from medium initial MPD:TMC ratios (r1.5 $\sim$ r3) had neither evident excess of free acyl or amine groups, these systems were found favorable for a better connection during the polymerization.

2.4.3.3 System's packing state

The packing state of the system could be deduced from RDF and coordination number of the carbon-carbon atom pair in MPD and TMC monomeric units' benzene rings. According to the force field implemented in this study, the carbon atoms in TMC and MPD monomeric units were of the same type for the dimer system, while they were of two different types for polymer systems. Therefore, for dimer system, the RDF of carbon atoms in benzene rings (C_{Ph}), without distinguishing the monomeric unit origins, was investigated ($g_{C_{Ph}C_{Ph}}(r)$); as for polymer systems, the RDFs between carbon atoms in benzene rings of MPD monomeric units (C_{MPD}) and of TMC monomeric units (C_{TMC}) were studied ($g_{C_{MPD}C_{TMC}}(r)$). Since the carbon-carbon pair RDFs of all polymer systems almost shared the same evolution trend, the system r1.5_1 (repetition box n°1) was taken here as example, fig.2.24. More details on $g_{C_{MPD}C_{TMC}}(r)$ of other polymer systems are presented in Annexes fig.A5.

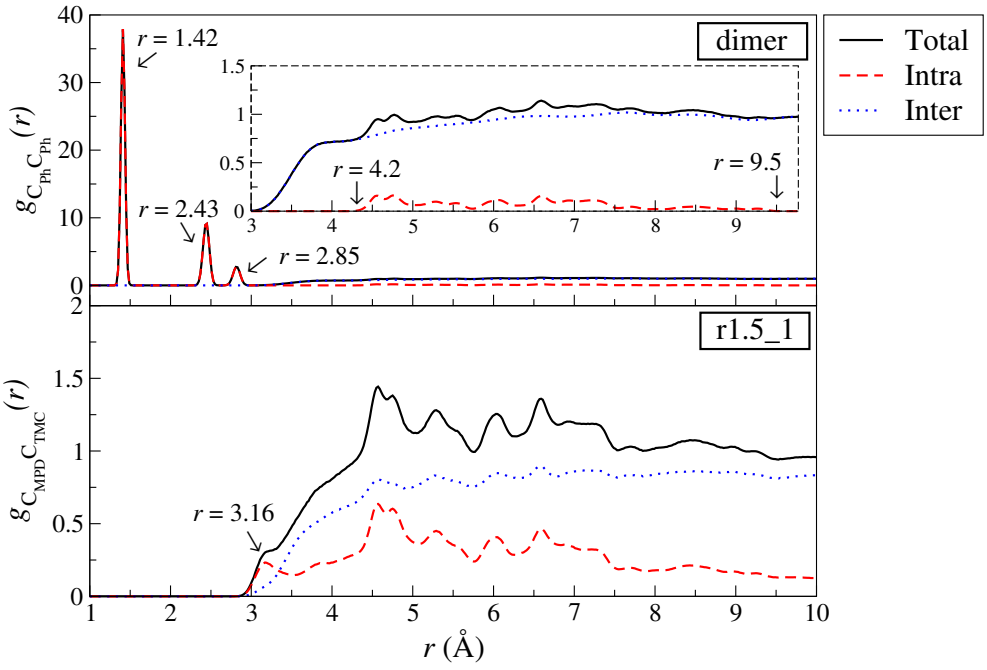

Figure 2.24: Radial distribution function (RDF) between carbon-carbon atom pair from benzene rings of 50 dimer system and polymer system r1.5_1 (repetition box n°1).

With respect to dimer system, the first three peaks located around 1.42 Å, 2.43 Å and 2.85 Å, which were

totally attributed from intramolecular component, representing the distance between any two carbon atoms in the same benzene ring. As for polymer r1.5_1, only the carbon-carbon pairs originated from different benzene rings (one carbon was from MPD while the other one was from TMC monomeric unit) were studied, hence these three peaks were not present. For dimer, the curve of the intramolecular component arose again between 4.2 Å and 9.5 Å, which represented the distances of carbon-carbon atom pairs from two bonded benzene rings. As presented previously in fig.A4, the distance between two neighboring amide bonds was found around 6.5 Å in polymer system r1.5_1, which could also roughly represent the distance between two neighboring benzene rings. In a previous study, Wei *et al.,* (2016)[118] also reported a same distance value between two adjacent benzene rings. Hence for two neighboring benzene rings between which the distance is 6.5 Å, the nearest carbon pair stays 4.2 Å apart, while the farthest one has a distance of 9.5 Å. In terms of the intermolecular component, it firstly arose around 3 Å. It should be noted that this value was even shorter than the distance between the two nearest carbon atoms from two adjacent benzene rings. Meanwhile, it was consistent with the distance between two benzene ring planes of $\pi - \pi$ stacking structure, observed at 3.4 Å by Wei *et al.,* (2016)[118]. The curve of the intermolecular component appeared dull, demonstrating the spatial distribution of dimer system was of irregular nature.

For polymer system r1.5_1, both its intramolecular and intermolecular component peaks firstly arose from 3 Å. The maximums of the first intermolecular and intramolecular peaks were around 3.16 Å, suggesting that the $\pi - \pi$ staking structures existed between benzene rings from both inter- and intra-chains. As analyzed previously, for systems at extreme initial MPD:TMC ratios (e.g. r0.25 and r5, fig.A6), their intramolecular components almost vanished to zero after 10 Å, suggesting a small molecular size with respect to other systems.

2.4.3.4 Estimation of hydrogen bond formation

Since the oxygen in amide bond is electronegative, it is easy to form hydrogen bond with hydrogen atoms in APA system. A hydrogen bond is stronger than the Van der Waals interaction, therefore its existence in polymer system plays an essential role, as it helps shape the polymer into a dense state. The hydrogen bond formation state in dimer and polymer systems could be estimated from the RDF between the oxygen atom in amide bond (Oamd) and the hydrogen atom in amide (Hamd), amine (Hamn) or carboxylic acid group (Hcbla), figure 2.25 for 50 dimers and figure 2.26 for system r1.5_1 (repetition box n°1). It should also be addressed that the hydrogen bond formation not only demands that the distance between the donor hydrogen and the acceptor atom is smaller than 2.5 Å, but also respects that the angles among the related atoms are also important. Hence, the analyses in this section only serve to provide a rough estimation.

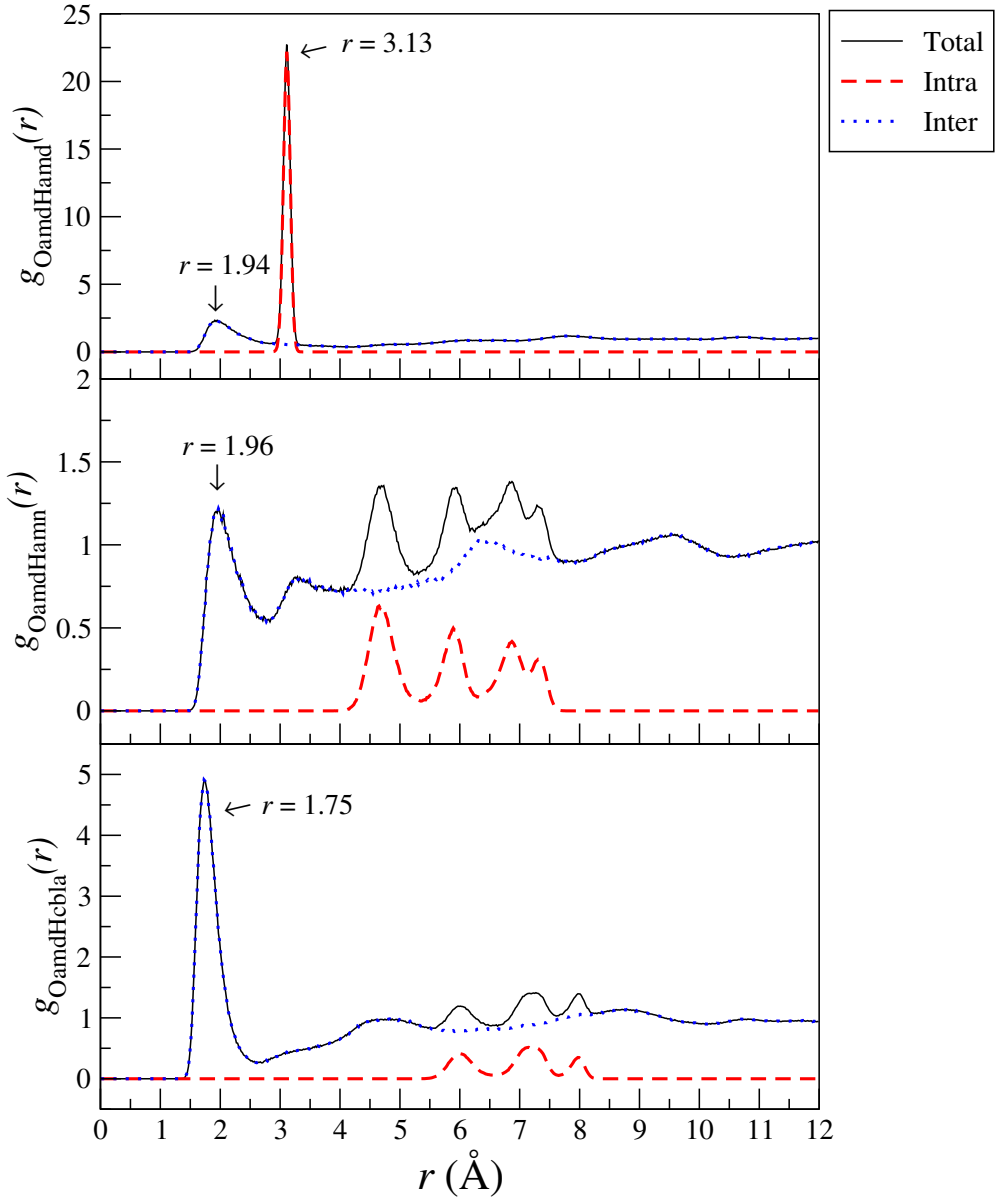

Figure 2.25: Radial distribution function (RDF) between oxygen atom in amide bond (Oamd) and hydrogen atom in amide (Hamd), amine (Hamn) or carboxylic acid group (Hcbla) of 50 dimers.

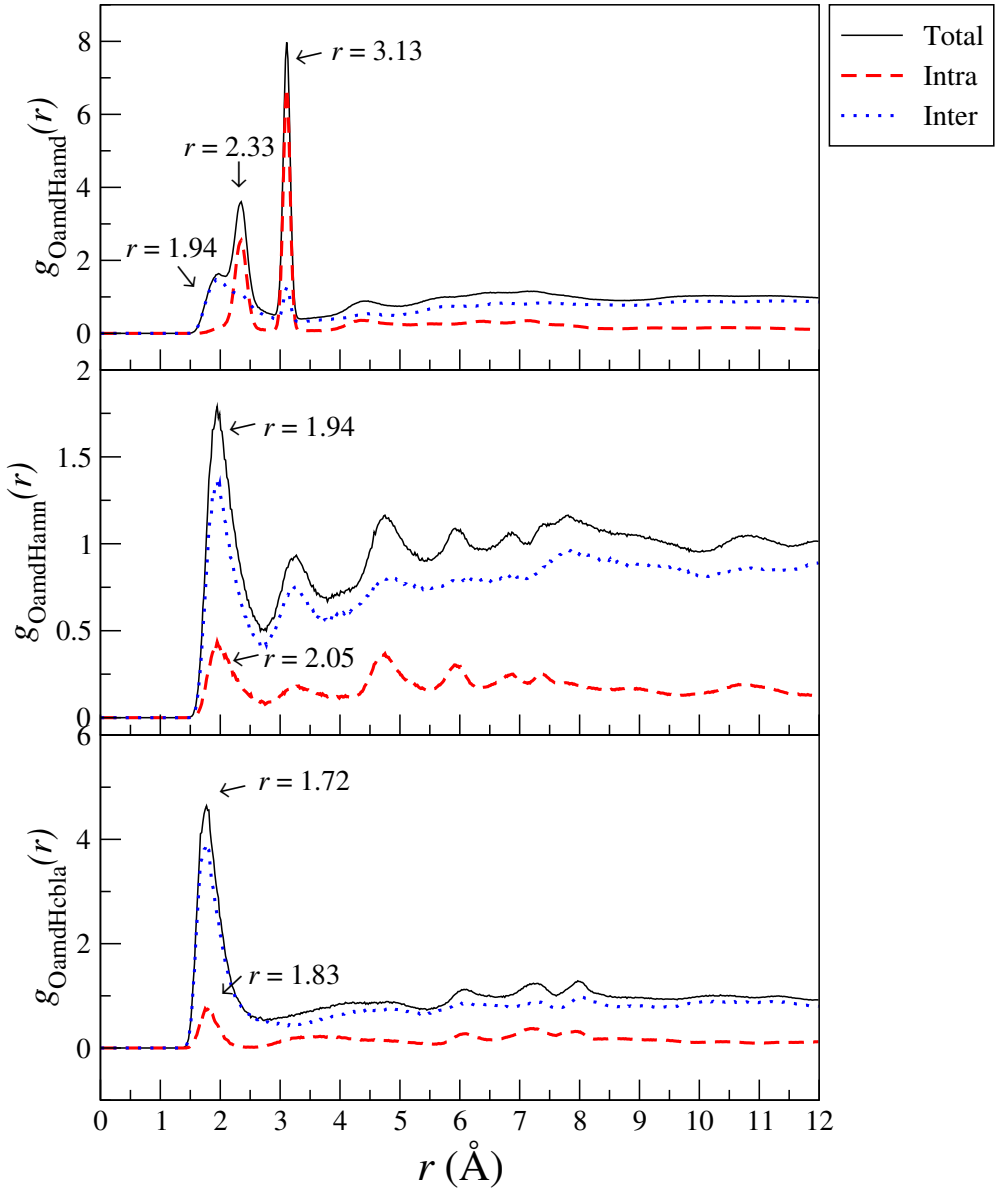

Figure 2.26: Radial distribution function (RDF) between oxygen atom in amide bond (Oamd) and hydrogen atom in amide (Hamd), amine (Hamn) or carboxylic acid group (Hcbla) of polymer system r1.5_1 (repetition box n°1).

As mentioned in previous section 2.4.1.6, the amide bond was of *trans* configuration in dimer system. Therefore the intramolecular peak of $g_{\mathrm{OamdHamd}}(r)$ at 3.13 Å in figure 2.25 represented the distance between the oxygen and hydrogen in the same amide bond in dimer. The first intermolecular peak was found at 1.94 Å, suggesting the possibility of the formation of amide-amide hydrogen bond between one amide oxygen and

one amide hydrogen from a neighboring dimer. In a similar way, the possible amide-amine hydrogen bond is supposed to exhibit a length of 1.96 Å according to $g_{\mathrm{OamdHamn}}(r)$, while the possible amide-carboxylic acid hydrogen bond is supposed to be of 1.75 Å according to $g_{\mathrm{OamdHcbla}}(r)$.

Integrating the RDF with the corresponding hydrogen atom density in bulk region, the coordination numbers of the first hydrogen atom shell (distance = 2.5 Å) in amide, amine and carboxylic acid groups around the oxygen atom in amide bond were of 0.2, 0.2 and 0.5, respectively. The amide oxygen was proven favorable to form the hydrogen bond with the hydrogen in carboxylic acid group in dimer system.

For polymer system, r1.5_1 (repetition box n°1) is presented here as example. In terms of amide-amide hydrogen bond analysis ($g_{\mathrm{OamdHamd}}(r)$), an intermolecular peak was observed at 1.94 Å, same as the dimer system. However, there existed extra intramolecular peaks from 1.5 Å to 2.63 Å, with a peak maximum around 2.33 Å. One possible contribution of these peaks was the hydrogen bond formed between intramolecular chains. The other possible source was the hydrogen bond formed by the amide hydrogen and oxygen of *cis* configuration. On the other hand, intramolecular hydrogen bonds were also observed between the amide oxygen and the amine/carboxylic acid hydrogen according to $g_{\mathrm{OamdHamn}}(r)$ and $g_{\mathrm{OamdHcbla}}(r)$. Identical to the dimer system, the amide-carboxylic acid hydrogen bond had the shortest distance (1.72 Å) with respect to 1.94 Å for the amide-amide/amine case. On the contrast, the coordination number analysis demonstrated that there existed respectively 0.6, 0.1 and 0.2 amide, amine and carboxylic acid hydrogen in the first coordination shell. This variation of hydrogen atom composition could be attributed to more presence of amide bonds and less presence of carboxylic acid groups in the polymer system compared to the dimer one.

Hence, the hydrogen in carboxylic acid group is supposed to be most favorable to form hydrogen bond with the amide oxygen, as the two atoms exhibited the shortest distance (around 1.73 Å). Meanwhile, the amide oxygen is able to form hydrogen bond with amide or amine hydrogen as well. The finally formed hydrogen bond type and amount are supposed to depend on the chemical environment of the system. It should also be addressed that for polymer systems, the hydrogen bonds could be arisen between both intermolecular and intramolecular chains, which promotes the chain folding and leads to a dense structure.

2.4.4 Infrared absorption spectrum

The constraint method of NEWTON code was applied to fix certain chemical bonds in order to identify the characteristic Infrared absorption peaks of typical chemical groups in APA dimers at high frequency, in fig.2.27.

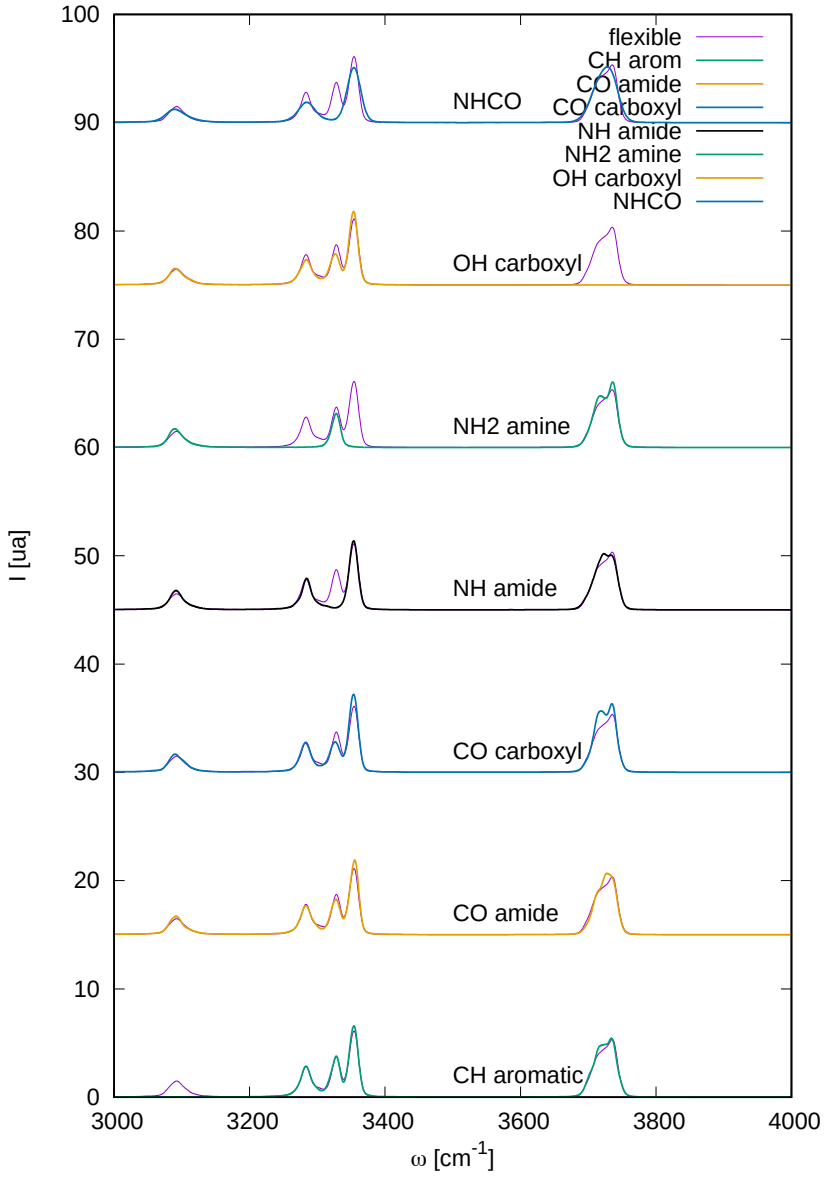

Figure 2.27: Attribution of Infrared absorption spectrum of APA dimer at high frequency, wavenumber 3000 $\sim$ 4000 cm^{-1}.

The IR spectra of polymer systems (r0.25, r1, r1.5, r2 and r5) were obtained via LAMMPS code, fig.2.28.

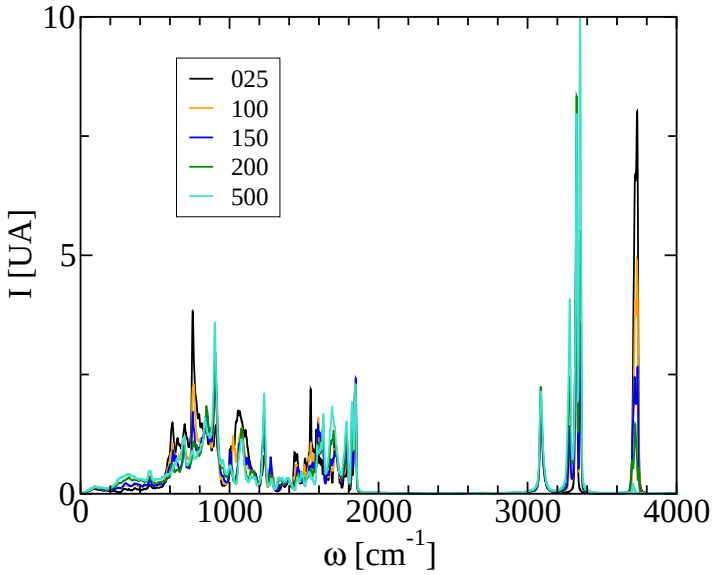

Figure 2.28: Infrared absorption spectra of APA polymer systems generated from different initial MPD:TMC ratios, wavenumber 0 $\sim$ 4000 cm^{-1}.

Polymer systems exhibited similar characteristic peak positions for different chemical groups as the dimer at high frequency (fig.2.28). Based on the attribution analysis above, qualitative analyses of IR spectra of polymer systems were realized at this range, fig.2.29.

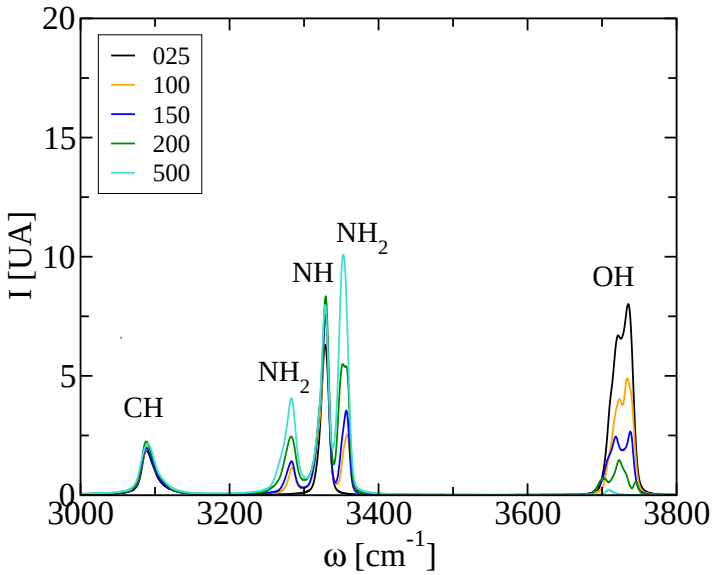

Figure 2.29: Infrared absorption spectra of APA polymer systems generated from different initial MPD:TMC ratios at high frequency, wavenumber 3000 $\sim$ 3800 cm^{-1}.

All polymer systems had an identical peak of CH group, which was consistent with the similar benzene ring densities of these systems. Meanwhile, evident variations were observed for NH_2 and OH groups, which were consistent with the previous chemical structure analysis via N/O map. From r0.25 to r5, f_{am} decreased as the free amine bond number raised, hence an increasing intensity of group NH_2 was observed in IR spectra.

Meanwhile, a decreasing OH stretching was noted, as less free acyl groups remained with increasing MPD:TMC ratios. In addition, our results were consistent with the experimental IR analyses of APA films synthesized from various monomer portions. The authors[27] found the absorbtion peak of NH_2 group around 1670 cm^{-1} was enhanced with a higher MPD concentration. Meanwhile, the peaks of COOH at 1697 cm^{-1} and OH stretching at 3751 cm^{-1} and 3856 cm^{-1} became intenser in presence of a larger TMC portion.

In summary, for simulated polymers, it was verified that the chemical structure variation could be distinguished via the analysis of IR spectra, especially at high frequency. The analysis at low frequency remained complicated due to the overlap of peaks of various chemical groups, which require further investigation. Nonetheless, it should also be addressed that most of the experimental Infrared spectrum analyses on APA films were implemented at low frequency (wavenumber ranging from 1000 to 2000 cm^{-1})[36][84][123]. Hence it will be interesting to have more experimental investigations at high frequency to provide comparative information to our simulation analyses.

2.4.5 Density

In view of the relatively small box dimension used in our study (around $30 \times 30 \times 30$ $Å^3$), no evident void is supposed to form inside the simulated polymer systems. Hence our simulated polymers represented/mimicked the bulk APA polymer or the dense region of the real APA layer instead of the effective APA layer. For each simulated polymer system, the density was calculated as the average density during the last 100 ns of MD under ensemble *NPT iso-stress* (1 bar, 298.15 K). For systems r0.25, r1.5 and r5, their densities were taken as the average values of corresponding 11 repetitions. The obtained results were plotted as a function of $r_{m:t}$ in order to investigate whether there existed structures-density correlations, fig.2.30(a). In the same figure, the densities of typical fully-linear (F-L) and fully-crosslinked (F-C) structures were also plotted, which were estimated based on a group contribution method[116]. Moreover, the experimental dry volumetric densities, obtained in our study via different methods (AFM and profilometry), of the dense region of CPA2 APA layer, together with the average effective volumetric density of APA layers of several uncoated RO and NF membranes reported by Lin *et al.,* (2016)[74], were plotted in fig.2.30(b) as well.

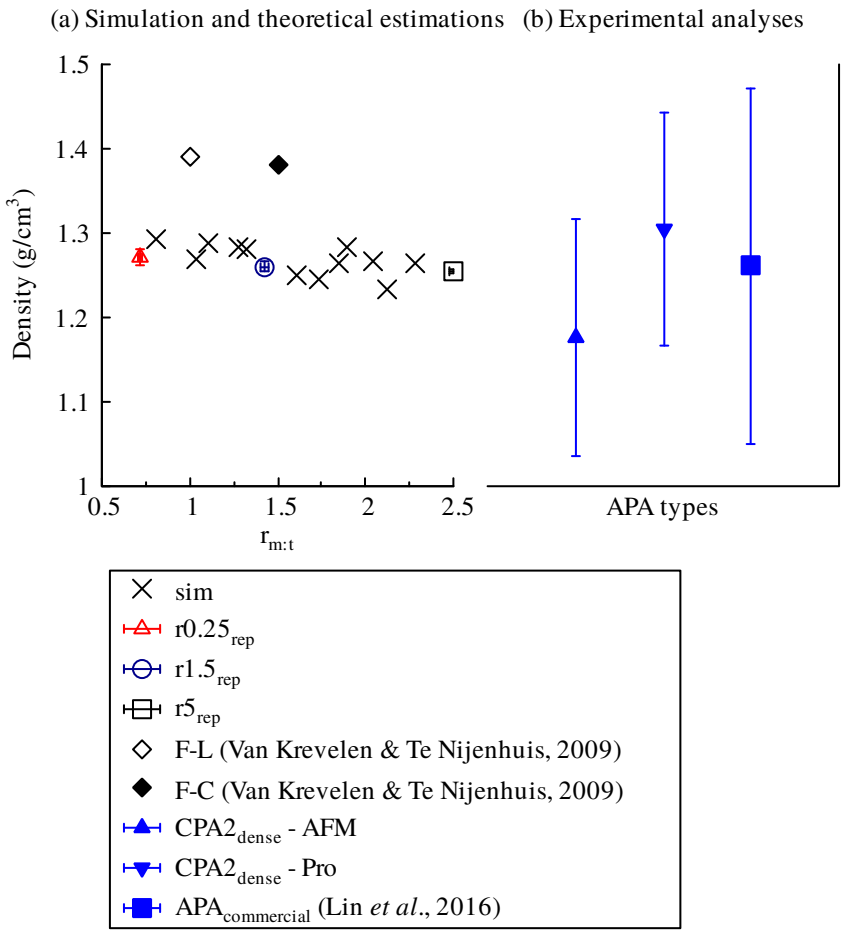

Figure 2.30: Density plotting of simulated APA polymer systems generated from different initial MPD:TMC ratios and experimental density data of commercial APA layers.

A slight decreasing tendency of density as a function of raising $r_{m:t}$ was observed for simulated polymers, fig.2.30(b). In terms of systems with sole repetition, it was difficult to define whether these variations were significant or not due to a weak representability. Meanwhile, the average dry densities of 11 repetition boxes of systems r0.25 (with average $r_{m:t}$ at 0.72), r1.5 (with average $r_{m:t}$ at 1.43) and r5 (with average $r_{m:t}$ at 2.5) were of 1.27 ± 0.01 g·cm^{-3}, 1.26 ± 0.01 g·cm^{-3} and 1.25 ± 0.002 g·cm^{-3}, respectively. Hence, these results demonstrated that the variations were within the analysis error. Since the densities were not significantly different, an average dry density of 1.26 ± 0.003 g·cm^{-3} was calculated for all simulated polymer systems.

The estimations from the group contribution method[116] also demonstrated that the APA's chemical structure did not have a significant effect on its density, as we obtained 1.39 g·cm^{-3} and 1.38 g·cm^{-3} respectively for the fully-linear and fully-crosslinked structures[116]. The above discussions suggested that APA systems with notable unreacted groups (such as excessive free carboxylic acid groups in r0.25 and fully-linear structure, and excessive amine groups in r5) exhibit almost identical densities as systems of a better connection state (such as r1.5 and fully-crosslinked structure). This could be attributed to the establishment of hydrogen bonds between the hydrogen or oxygen atoms in these free groups. As presented previously in the RDF analysis, the oxygen

atoms in amide bonds were able to form hydrogen bonds with hydrogens in amide, free amine and carboxylic acid groups. Therefore, the successful establishment of such hydrogen bonds among linear polymer chains or molecules pieces assists in forming a structure as dense as a well-crosslinked network. Meanwhile, it should be noted that the results obtained from the group contribution method were around 10% higher than the average density of our simulated polymers, which could be attributed to the bias of the applied force field parameters or of the group contribution theory itself. More investigations are demanded to understand this variation.

As presented in the previous chapter, we experimentally investigated the density of the dense region of the APA layer of CPA2 RO membrane from its effective volumetric density and void fraction, obtaining respectively a value at 1.18 ± 0.14 g·cm^{-3} based on thickness analysis via AFM and at 1.30 ± 0.14 g·cm^{-3} via profilometry. These two results roughly led to an average value at 1.24 g·cm^{-3}, with which our simulated average density (1.26 ± 0.003 g·cm^{-3}) was in well consistency.

On the other hand, Lin *et al.,* (2016) have reported an average effective density at 1.26 ± 0.21 g·cm^{-3} for APA layers of NF NF90 and RO XLE, ESPA3 and SWC4+ membranes. Even though this value was very close to our average simulated density, it remained questionable to compare these two values directly, as this experimental value represented effective density rather than that of the dense region. Lin's group reported that these APA layers exhibited void fractions varying from 15% to 32%[75]. Based on these information, the densities of dense regions of these commercial APA layers could be roughly estimated varying from 1.48 to 1.85 g·cm^{-3}. However, these values were unrealistic, as they were even higher than the density of 1.45 g·cm^{-3} of linear para-linked aromatic polyamide p-phenylene terephthalamide (Kevlar). Such unrealistic estimations of the dense density might originate from the inaccurate effective density or void fraction estimation.

Despite density estimations of dense regions of commercial APA layers, the densities of synthesized dense APA nanofilms are also supposed to be close to that of the bulk APA polymer. A highest dry density at 1.26, 1.32 or 1.44 g·cm^{-3} was reported by different authors [20, 32, 59] for their densest synthesized APA nanofilms, which together were little higher than our simulated density. However, as discussed before, it should be addressed that all these experimental results faced the challenge of obtaining an accurate thickness estimation due to the very rough and thin characters of APA films. Moreover, it was revealed that nanofilms could have weak densities inferior to 1 g·cm^{-3} according to synthesis conditions [20, 59]. Hence it remains unclear whether the above reported densest nanofilms exhibited possible void space or not. Overall, no consistent experimental result of the bulk dense APA polymer's density has been reported up to date, mainly due to the lack of accurate thickness estimation and purposeful study.

Various results of the density of the APA molecular model have been reported. Some groups[52, 53, 121] constructed their molecular models by following the chain-bridging methodology of Kotelyanskii *et al.,* (1998)[66], which involved a preset initial hydrated density around 1.38 g·cm^{-3} (or a corresponding dry density around 1 g·cm^{-3}) and predefined water content around 23 wt%. For these studies, final hydrated densities and water content were usually found close to each other, as the water contents fluctuated around 23 wt% and the hy-

drated densities varied from 1.32 to 1.38 g·cm^{-3}, from which a dehydrated density around 1.06 g·cm^{-3} could be deduced. However, this dry density result should be taken with caution, as all obtained thermophysical parameters were close to the initial preset ones, which could be attributed to a short relaxation time (hundreds of ns). As discussed previously, a relaxation time up to several μs is required to well relax APA systems of box dimensions in our study. Since these studies had larger box dimensions than ours, their short relaxation time remained questionable. Moreover, considering the simulation box volume extension due to swelling, the deduced dehydrated densities are supposed to be sub-estimated.

Meanwhile, some studies constructed APA molecular models by connecting monomers (a similar protocol to our study). These studies departed from different preset densities and resulted in final densities varying from 1.28 to 1.33 g·cm^{-3} [6, 118]. It should be addressed that these data were also obtained from a short relaxation time (hundreds of ns). Hence, it remains questionable whether these APA polymers were well relaxed or not after the polymerization. Moreover, Kolev *et al.,* (2014)[64] have established a molecular model with relatively larger dimensions of $7 \times 7 \times 15$ nm^3 and relaxed the system for longer time for one μs. They reported one effective density of 1.2 g·cm^{-3} and the other one excluding the void of 1.3 g·cm^{-3}. The later value represented more the property of the bulk polymer and was close to our average density result at 1.26 ± 0.003 g·cm^{-3}.

2.5 Conclusion

All-atoms molecular models of APA polymer were constructed by forming amide bonds between hydrolyzed trimesoyl chloride (TMC) and *m*-phenylenediamine (MPD) with a set of initial MPD:TMC ratios, varying from 0.25 to 5. We obtained APA systems with various chemical structures, as final MPD:TMC monomer unit ratios ranged from 0.68 to 2.63, corresponding to systems with acyl/amine group connexion degrees at 47%/100% or 100%/59%, respectively. These chemical variations were also detectable via IR spectra analysis in high frequency region. Systems generated from medium MPD:TMC ratios exhibited a better connection state than the ones from extreme ratios, exhibiting larger molecular networks and high acyl/amine group connexion degrees. Our polymer generation results were consistent with the chemical structure evaluation of real APA films synthesized from various monomer ratios reported[27]. Besides, these results also shed light to the APA film's chemical structure formation tendency in different regions during the interfacial polymerization: from the back-surface (interface between organic and aqueous phases) to the top-surface, the MPD:TMC ratio is supposed to decrease progressively, hence the final structure of the back-surface probably has more MPD monomer units and free amine groups than that of the top-surface, vice versa. Meanwhile, it should also be addressed that the real interfacial polymerization is more complicated than the simulated one, as there exist factors such as the hydrolysis of reactive acyl groups at the interface. Such possible depth-dependent heterogeneous structure was confirmed by our experimental chemical structure analysis of the APA layer of CPA2 RO membrane. Its top-surface exhibited a lower $r_{m:t}$ and a higher f_{am} than the back-surface. CPA2's back-surface didn't have a high f_{ac}, because the active acyl groups are supposed to be hydrolyzed by water hence leading to a weak

connection degree. A relaxation time up to several μs was proven indispensable to release the strains raised during the polymerization for the simulated APA polymer systems of box dimensions used in this study (around $30 \times 30 \times 30$ Å^3). $\pi - \pi$ stacking configurations were observed in all polymer systems. And hydrogen bonds were able to be established between the oxygens in amide bonds and hydrogens in amide, amine and carboxylic acid groups. Though the hydrogen atom in carboxylic acid group was proven preferential to form the hydrogen bond with the amide oxygen, the final quantity of the hydrogen bond types was determined by the specific chemical structure of the current system.

Moreover, no correlation was found between APA polymer's chemical structure and density. For all simulated systems, an average dry density was found at 1.26 ± 0.003 g·cm^{-3}. This density was consistent with density results of other APA molecular models generated from a similar 'monomer polymerization' protocol. Moreover, it was in agreement with the experimental density of the dense region of CPA2' APA layer.

Overall, the success of the construction of various molecular models in our study assisted in understanding APA films' formation processes and resulting structures under the effect of different initial MPD:TMC ratios. Besides, this work is the first molecular model study which systematically investigated the APA's structures-properties correlations with a great variety of samples.

Chapter 3

Hydration of APA films and APA molecular models with various chemical structures

3.1 State of the art

3.1.1 Basic theories of sorption isotherms

This section introduces the basic theories developed for the analyses of sorption isotherms. The mathematical models of sorption isotherms, water cluster formation estimation and swelling investigation are presented respectively.

3.1.1.1 Mathematical models of sorption isotherms

The vapor sorption behavior in polymer is complex. Various theories have been developed to mathematically express the relation between the penetrant molecules' density and the corresponding vapor pressure, which in our case is the relation between the water mass uptake and water activity (a_w). The water activity is defined as the ratio between the water vapor pressure (p) and the saturation vapor pressure (p_0) at constant pressure (P) and temperature (T). Hence, the water activity is equal to the relative humidity (RH) divided by 100. It can be expressed as:

$$a_w = \frac{p}{p_0} = \frac{RH}{100} \tag{3.1}$$

According to the classification of International Union of Pure and Applied Chemistry (IUPAC) in 1985, the majority of the physisorption isotherms could be divided into six types[106], as shown in figure 3.1.

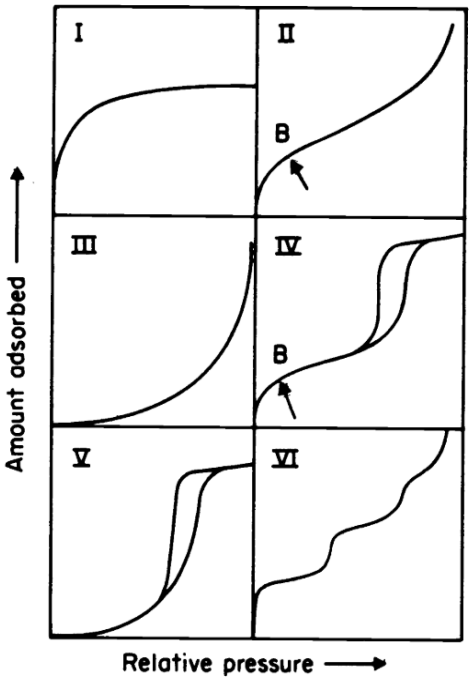

Figure 3.1: Types of physisorption isotherms, from Sing *et al.,* (1985)[106]

The type I isotherms are given by polymer with relatively small external surface, corresponding to the filling of water monomolecular layer at the external and internal surface of the polymer matrix. The water-polymer interactions are the dominant interactions in type I isotherms. A typical type I isotherm is Langmuir isotherm. The type II isotherms are obtained with a non-porous or macro-porous polymer. The water sorption consists of monolayer and unrestricted multilayer formation. The point B in fig.3.1(II), the departing point of the linear middle region, represents the saturation of the monolayer and the beginning of the multilayer formation. Typical type II isotherms include Brunauer-Emmett-Teller (BET) and Guggenheim-Anderson-De Boer (GAB) isotherms. The type III exhibits a convex shape towards the relative pressure axis (or water activity axis). Such isotherm is not common, and water-water interactions are favorable for this type. One example of type III is Flory-Huggins isotherm. The type IV performs similar monolayer-multilayer adsorption at low and middle water activity range as the type II, but exhibits a limited uptake at high water activity. The type V is related to type III, but exhibits a water uptake limitation at high water activity. Similar to type III, such isotherm is not common. The type VI is obtained by progressive multilayer adsorption on a uniform non-porous surface, where the height of each step represents the capacity of each adsorbtion layer.

Principle introduction of various isotherm theories are presented below.

Henry's Law sorption

The sorption following the Henry' law is the simplest mode. It considers the penetrant molecule as an ideal gas, and it is initially constructed to describe the gas solubility into liquid phase at low relative pressure. It could be applied to describe the gas penetration into solid, where polymer-gas and gas-gas interactions are relatively

weak compared to polymer-polymer interactions. The vapor's solubility (s) remains constant as the number density of the adsorbed molecules (n_{ad}, $mol \cdot cm^{-3}$) is linear to p:

$$n_{\mathrm{ad}} = s \cdot p \tag{3.2}$$

Langmuir theory

In Langmuir model, the dominant interactions are the interactions between the sorbate molecules and a solid surface. Water forms monomolecular layer on specific adsorption sites of the solid structure. Before the saturation of adsorption sites, the water mass increases rapidly at first and then raises gradually with the increase of a_w; after the saturation, only few water molecules could still solubilize into the polymer, hence the water uptake curve reaches a plateau. The number density of adsorbed molecules (n_{ad}) compared to total adsorption site density (n_0) is determined directly by a_w ($=p/p_0$) as:

$$\frac{n_{\mathrm{ad}}}{n_0} = \frac{a_w C_{\mathrm{L}}}{1 + a_w C_{\mathrm{L}}} \tag{3.3}$$

With C_{L} is Langmuir constant. C_{L} could be obtained by:

$$C_{\mathrm{L}} = exp(E_{\mathrm{ad}}/k_{\mathrm{B}}T) = exp((E_1 - E_{\mathrm{l}})/k_{\mathrm{B}}T) \tag{3.4}$$

where E_{ad} is the adsorption energy (J), E_1 is the sorption heat on the first layer (J), E_{l} is the heat of liquefaction (J), k_{B} is the Boltzmann constant and T is absolute temperature (K). $E_{\mathrm{ad}}/k_{\mathrm{B}}T$ represent the adsorption affinity. Langmuir theory imposes several assumptions. It assumes that the number of sites on the surface is determined under certain pressure and temperature. Besides, the energy of adsorption for each site is independent and the interactions between the sorbates located at neighboring sites are negligible.

Flory-Huggins theory

The Flory-Huggins model describes the mixing sorption phenomena between a small molecule and a long chain polymer when the solute-solute or solvent-solvent interactions are dominant. The small molecules' solubility raises with the increase of its activity (water molecules are taken as example here), for which the vapor volume fraction (ϕ_1) inside the polymer volume is connected to the Flory-Huggins parameter C_{FH}:

$$ln a_w = ln(\phi_1) + (1 - \phi_1) + C_{\mathrm{FH}}(1 - \phi_1)^2 \tag{3.5}$$

where C_{FH} is equal to the interaction energy of solute/solvent-polymer divided by $k_{\mathrm{B}}T$. Such behavior could be interpreted by two possibilities: a plasticization of the polymer by sorbate molecules or the formation of sorbate clusters when the polymer is relatively hydrophobic.

Brunauer-Emmett-Teller (BET) theory

With respect to the description of water vapor sorption in hydrophilic glassy polymers with polar groups, the Brunauer-Emmett-Teller (BET) model[12] is commonly applied. BET is one of the most fundamental theories that interpret the multilayer sorption isotherms. It describes that water molecules firstly interact with the polymer by occupying the specific adsorption sites, then interact between themselves by forming possible cluster:

$$w_{a_w} = \frac{w_m \bar{c} a_w}{(1 - a_w)(1 + a_w \bar{c} - a_w)} \tag{3.6}$$

where w_{a_w} represents water mass per dry polymer mass at a certain water activity, w_m is the adsorption capacity as water mass per polymer mass when the first layer is saturated, and $\bar{c}$ is the parameter related to the water molecule energy difference between the first layer and higher layers. BET model performs several assumptions: (1) the number of layers condensing on the polymer matrix's surface is infinite; (2) the condensation rate of the first layer is equal to the evaporation rate of the second layer; (3) water molecules in the first layer have the same binding energy; (4) water molecules from the second layer and the other remaining layers are identical to that of pure liquid state. The second and third assumptions are questionable since the sample's surface is not uniform and it is not always correct to ignore the lateral interactions between water molecules in the first layer. In most applications, BET model only shows a good fit with experimental data for low water activities ($aw \leq 0.5$)[5, 106].

Guggenheim-Anderson-De Boer (GAB) equation

The GAB model is called after its developers Guggenheim[46], Anderson[5], and De Boer[19], who independently developed the equation in 1966, 1946 and 1968, respectively. It is a modified BET model and postulates that water molecules in the second layer are identical to those from superior layers but different from those of pure liquid state, hence the water-water interaction inside the polymer is considered weaker than that in bulk water. This model overcomes the limitation of classic BET model as being restricted in the application only for low water activity, showing a good fit for a wide range of water activity up to 0.95[5]. The GAB equation is expressed as:

$$w_{a_w} = \frac{w_m \bar{c} a_w}{(1 - f_{a_w})[1 + a_w(\bar{c} - f)]} \tag{3.7}$$

where f corresponds to parameter measuring the difference between the chemical potentials of molecules in the second absorption layer and in pure liquid state. It is notable that when f is equal to 1, the GAB turns into the BET model. The GAB model accounts for investigating the water bound to the primary adsorption sites. Based on w_m, the number of water adsorption sites per gram of polymer, γ, can be calculated as:

$$\gamma = N_A w_m / MW \tag{3.8}$$

where N_A is Avogadro's number and MW is the molecular weight of water. The isotherms with a sigmoidal shape, such as GAB, are classified as Type II according to IUPAC's classification[106].

Curve fitting efficiency

The curve fitting efficiency is estimated as the mean relative percentage deviation modulus (MRD):

$$\text{MRD} = \frac{1}{N}\Sigma_{i=1}^{N}\frac{|w_i - w_{ip}|}{w_i} \tag{3.9}$$

where w_i is the experimental value and w_{ip} is the corresponding predicted value, N is total number of experimental data. MRD below 10% indicates a good fit[88].

3.1.1.2 Water cluster formation estimation

The information on water cluster formation can be extracted directly from the shape of the water mass uptake curve. On the basis of the statistical mechanics of fluctuation, Zimm and Lundberg[77, 128, 129] developed a mathematical expression to analyze the cluster formation as:

$$\frac{G_{11}}{V_1} = -\phi_2[\frac{\partial(\frac{a_w}{\phi_1})}{\partial a_w}]_{P,T} - 1 \tag{3.10}$$

where G_{11} is the cluster function, V_1 is the partial molar volume of water, ϕ_1 is the volume fraction of water and ϕ_2 is the volume fraction of polymer. ϕ_1 is the ratio between the volume of water V_{water} and the volume of the apparent film V_{film}. We assume that V_{film} remains constant and is equal to the film's volume in dry state. Hence we have:

$$\phi_1 = \frac{V_{\text{water}}}{V_{\text{film}}} = \frac{m_{\text{water}}/d_{\text{water}}}{m_{\text{polymer}}/d_{\text{polymer}}} \tag{3.11}$$

with m_{water} is the mass uptake of water at each water activity and d_{water} is the water density, taken as 0.997 g·cm^{-3} in this study. m_{polymer} is the dry polymer (film) mass and d_{polymer} is dry density of the apparent film, taken as 0.805 g·cm^{-3}, the obtained effective volumetric density of APA layer of CPA2 RO membrane. Thereby, the volume fraction of polymer ϕ_2 is obtained as:

$$\phi_2 = 1 - \phi_1 \tag{3.12}$$

To calculate the derivative in equation (3.10), the $\frac{a_w}{\phi_1}$ is plotted *versus* a_w and this plot is fitted with a polynomial function, which is later differentiated[90].

The function $\frac{G_{11}}{V_1}$ is a measure of the tendency of sorbates to form the cluster. If $\frac{G_{11}}{V_1} < -1$, sorbate molecules segregate one from another or form alternate arrays with molecules of the other component of a binary system; if $\frac{G_{11}}{V_1} = -1$, sorbate molecules dissolve into the polymer matrix randomly; and higher values, $\frac{G_{11}}{V_1} > -1$, suggest

that the clustering of sorbate molecules occurs, as the corresponding concentration is greater than the average concentration in the polymer matrix. Moreover, the cluster's dimension can also be evaluated. Multiplying the quantity $\frac{G_{11}}{V_1}$ by ϕ_1 represents the mean number of sorbate molecules surrounding a sorbate molecule in excess of the mean concentration. Therefore, the mean cluster size (MCS) can be calculated as:

$$\mathrm{MCS} = 1 + \phi_1 \frac{G_{11}}{V_1} \tag{3.13}$$

A MCS value greater than one indicates the formation of sorbate cluster.

3.1.1.3 Swelling investigation

The swelling degree (SW) gives insight to the structural properties of the hydrated APA membrane. It is defined as the ratio of the variation between the wet thickness (L) and the dry thickness (L_0) of the film, and the later:

$$SW = (L - L_0)/L_0 \tag{3.14}$$

For simulated polymer samples, swelling degrees were calculated under the assumption of an isotropic volume expansion. The thickness L was taken as the average value of the three box dimensions. The swelling degree was selected instead of the volume expansion for a better comparison with experimental or other simulation swelling results in the literature.

3.1.2 Implementation of water isotherm study in molecular simulation

3.1.2.1 Osmotic ensemble

The osmotic ensemble accounts for studying biphasic systems with several constituents, which are under a known constraint such as the external/internal pressure P, exchanging the heat with the bath under temperature T. Permitting the deformation of the box, the osmotic ensemble allows specific behaviors such as the system's swelling to be investigated.

The osmotic ensemble is a one phase ensemble, where a polymer-rich phase is constrained to be in equilibrium with a virtual gas phase (water gas in our case). In the polymer-rich phase, the polymer chain number is imposed. The thermodynamic equilibrium of water gas between the polymer-rich phase and the virtual gas phase is achieved by ensuring the equality of the water chemical potential between the two phases via inserting or deleting water molecules with Monte Carlo moves. The water partial pressure of the virtual gas phase is fixed by assuming that it is equal to the fugacity.

3.1.2.2 Monte Carlo method

The Monte Carlo method implements a random method to create a set of configurations of a given physical system. These configurations are obtained by generating a Markov chain. The most widely used algorithm in Monte Carlo method is the importance sampling technique, developed by Metropolis, Rosenbluth and Teller in 1953[82]. Hence it is also called Metropolis algorithm. The general approach to conduct a random walk in Metropolis's algorithm for a partcular point r^N is firstly creating a new configuration ('n') from an old configuration ('o') and then deciding whether to accept the new configuration according to an acceptance probability $acc(o \rightarrow n)$:

$$acc(o \rightarrow n) = min(1, exp\{-\beta'[U(r'^N) - U(r^N)]\}) \tag{3.15}$$

where $U(r'^N)$ is the energy of the old configuration, $U(r^N)$ is the energy of the new configuration, β' is the reciprocal temperature $(1/k_{\mathrm{B}}T)$ and $exp\{-\beta' U(r^N)\}$ is Boltzmann factor. At thermodynamic equilibrium, the collection of created configurations accords with a Boltzmann distribution.

3.1.3 Overview of experimental and molecular simulation investigations on water sorption of APA films

The water sorption and diffusion in the active aromatic polyamide (APA) layer of reverse osmosis (RO) membrane play an important role in determining the performance of RO processes. On the basis of the solution-diffusion model, the water flux (J_{w}) could be described as:

$$J_{\mathrm{w}} = \frac{D_{\mathrm{w}} C_{\mathrm{w}} V_1}{RT\delta}(\triangle P - \triangle \pi) \tag{3.16}$$

where D_{w} is water diffusion coefficient (m^2/s), C_{w} is average water concentration in the active APA layer ($\mathrm{mol \cdot cm^{-3}}$), V_1 is the partial molar volume of liquid water, R is the ideal gas constant ($\mathrm{J \cdot K^{-1} \cdot\ mol^{-1}}$), T is the temperature (K), δ is the APA layer's thickness, $\triangle P$ is the trans-membrane pressure (MPa) and $\triangle \pi$ is the osmotic pressure difference between feed and permeate streams (MPa). Hence, a good knowledge of hydration and water dynamics in the APA active layer is indispensable for understanding the water and solute transports through the membrane.

This section introduces the advancement of experimental and molecular simulation investigations on hydration of APA films.

As introduced in chapter 1, efforts were contributed to understand the water swelling behaviors and water mass uptakes of commercial and synthesized APA films at high water activity[25, 32, 34, 55]. Nonetheless, to the best of our knowledge, only two studies have investigated the water mass uptake curves of APA films as a function of water activity up to date.

Zhang *et al.,*(2009)[127] reported the first water isotherm study of APA films, more specifically of the active layers of RO FT30 and LF10 membranes, via both adsorption and desorption processes. In their study, the APA

active layers were attached to a thin glass substrate with the help of an adhesion layer of polyimide, in order to maintain the films to a similar planar state as in real filtration process. The entire samples were heat cured for 12 h at 200°C. The water uptake analysis was launched for the ensemble of 'APA+polyimide+substrate'. The data of APA were obtained by subtracting the data of 'polyimide+substrate', which were obtained via an independent analysis. A range of water activity varying from 0 to 0.95 was tested at 298 K. The authors reported a water mass uptake of FT30 or LF10 respectively at 12.2 wt% or 12.8 wt% at 95%RH. On the basis of the obtained water content, the authors corrected the FT30's hydrated density from 1.38 g·cm^{-3}[66] to 1.24 g·cm^{-3}. The former value was firstly reported by Kotelyanskii in 1998, and has been widely used in latterly studies as reference. In addition, the authors also reported a hydrated density of 1.22 g·cm^{-3} for LF10. Since the obtained water uptake curves exhibited sigmoid shapes, the authors fitted the water uptake data in low water activity ($0 \sim 0.25$) to Langmuir model and implemented the Flory-Huggins theory for the high water activity range ($0.6 \sim 0.95$). The Langmuir fitting suggested that the adsorption energy of the first water molecular layer was around 3.7 KJ/mol and 2.7 KJ/mol for FT30 and LF10, respectively. From Flory-Huggins fitting, the interaction energies of water and polymer divided by $k_{\mathrm{B}}T$ were found at 1.8 for FT30 and 1.7 for LF10, respectively corresponding to interaction energies at 4.21 KJ/mol and 4.46 KJ/mol. Applying solution-diffusion model with known permeability, the authors also reported the diffusion coefficients of water inside the active layers of FT30 and LF10 were 0.8×10^{-9} m^2/s and 1.2×10^{-9} m^2/s. Despite the interesting information given by this study, it should be noted that FT30 and LF10 are both coated membranes. Their coating, poly vinyl alcohol (PVA), is highly hydrophilic and is supposed to be around 25 nm thick. In addition, the heat curing might deform the sample since the glass-transition temperature of APA ranges between 140°C and 190°C[80]. Based on these above drawbacks, there might exist biases between the obtained data in their study and the properties of uncoated APA films.

In another study, APA layer of RO SW30 membrane and a free-standing synthesized film were characterized[70]. The water mass uptake was analyzed at a water activity range varying from 0 to 0.95 at 298 K and 308 K. The results obtained from the two temperatures turned out identical, suggesting the isotherms were weakly sensitive to temperature within a certain temperature range. Water sorption isotherms were modeled based on Guggenheim-Anderson-De Boer (GAB) theory by using the average data of the adsorption and desorption curves, which is questionable in view of the hysteresis loop. In general, the commercial and synthesized APA films almost performed identical water mass uptakes, figure 3.2.

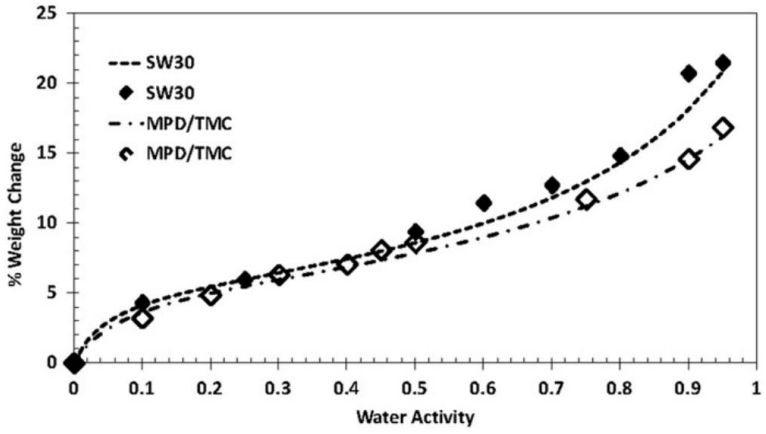

Figure 3.2: GAB fitting of water isotherms of APA layer of SW30 and a synthesized APA film, from Lee *et al.,* (2013)[70].

The water adsorption sites of the two films were both found around 1.9×10^{21} per gram of polymer. The authors also attempted to extract information on water clustering from the water uptake curves by applying the method of Zimm and Lundberg[77, 128, 129]. For both samples, it was found that the cluster formation began from a_w at 0.85 and exhibited an average cluster size around $2.5 \sim 2.7$ at a_w around 0.95. Applying solution-diffusion model, the water diffusion coefficient inside SW30 APA layer was obtained around $0.45 \sim 0.56 \times 10^{-9}$ m^2/s. However, it should be noted that their samples were not prepared in planar state, hence the water sorption surface differed from that during real RO processes. The application of solution-diffusion model in such case remains questionable. The analysis of Positron Annihilation Lifetime Spectroscopy as a function of water activity showed that the free volume cavity size of SW30 decreased firstly and increased afterwards, which was explained by the void filling and swelling mechanism according to the authors.

Overall, these studies provide very interesting information on hydration structures of APA films. Nevertheless, the investigated commercial APA layers above are all coated by PVA, which possibly misled the interpretation of the properties of uncoated APA films.

The transports of water and solutes occur in a molecular level, therefore investigations by the atomistic molecular simulation could give direct insight to the transport mechanisms. Remarkable efforts have been contributed to reveal water/solutes mobility and their interactions inside the polymer. The hydration processes in these studies varied from one to another. Since this process is the essential basis of further analyses, previous works are reviewed here according to the hydration approach applied.

A commonly used approach is to randomly insert water molecules by respecting a target water content. As introduced before, Kotelyanskii *et al.,* (1998) built the first atomistic models of APA polymers. The water molecules were inserted into their APA models, respecting a target water content at 23 wt%[66]. They finally obtained water diffusion coefficients in APA polymers around 0.8×10^{-9} m^2/s, which was an order of magnitude lower than that in bulk water.

In later studies, an interface between water and polymer phases was commonly built to study the water sorption and diffusion in APA polymer. Meanwhile, the water insertion protocol of Kotelyanskii *et al.,* (1998) was also widely adopted in these studies to pre-hydrate the dry polymer.

Hughes *et al.,* (2010)[52] studied the water sorption and salt diffusion (with NaCl concentration at 0.55 or 0.0055 molal) in their APA polymer models by simulating an interface between the a pre-solvated polymer and a water/saline solution phase. The authors finally observed a hydrated density of 1.34g·cm^{-3} with a water content around 21 wt%. In addition, in order to investigate the effect of polysulfone support layer and its porosity on the water diffusion, the authors investigated three arrangements: absence of support layer, presence of support at the back of the polymer phase and presence of support but together with certain water volume at the back of the polymer. To have a good calculation efficiency, the support layer was simplified into layers of atoms placed on a hexagonal lattice. The authors demonstrated that different constructions of polymer, with/without presence of support layer, had negligible effect on water diffusion inside the membrane. Generally, the water diffusion coefficient decreased of an order of magnitude inside the membrane (0.21 $\times 10^{-9}$ m^2/s) compared to in bulk water (2.7 $\times 10^{-9}$ m^2/s).

Xiang *et al.,* (2013)[121] inserted a certain quantity of water molecules into a non-crosslinked APA membrane (consisted of non-crosslinked chains) with presence of a vapor phase above the water-membrane complex, in order to impose a comparative water vapor pressure. After 5 ns MD equilibrium, the authors observed a water content around 23 wt%, a hydrated density around 1.35 g·cm^{-3} and a dehydrated polymer density about 1.1 g·cm^{-3}. It should be noted that in this study, the dehydrated density was identical to the preset dry density at the beginning of box construction. The authors finally observed a stable surface morphology with some variations, which effected the surface-foulant interactions according to the authors. They revealed the binding formation between the carboxylate groups in the surfaces of APA and alginate, which served as a ionic binding bridge in APA-alginate fouling. In addition, similar to other studies, a progressive reduction of water diffusion coefficient was observed along with the diffusion direction into the membrane: 2.3×10^{-9} m^2/s for bulk water, 1.60×10^{-9} m^2/s at the APA surface vicinity, and 0.12×10^{-9} m^2/s inside the membrane.

Ding *et al.,* (2014)[21, 22] surrounded the polymer box by two water reservoirs in Z direction and hydrated the polymer according to a target experimental water content value at 23 wt%. The hydrated system was relaxed in an *NPT* ensemble (300K, 1 atm) for 40 ns. The authors obtained a hydrated density at 1.32 g·cm^{-3}. This value was very close to other simulated hydrated densities introduced above[52, 53, 121]. In this study, it was revealed that the oxygen and hydrogen atoms in carboxylic acid groups and oxygen atom in amide bond are the preferential sites to form hydrogen bond with water molecules. The hydrogen bond number per water molecule was found to be 2.4 (water-water) and 0.4 (water-membrane), compared to 3.8 in bulk water. The dielectric properties were found modified compared to bulk water. Same as other studies, the water diffusion coefficient reduced by an order of magnitude inside the membrane (0.14×10^{-9} m^2/s) compared to in bulk water (2.38×10^{-9} m^2/s).

The above studies provided important information on the interactions between the APA polymer and water or various solutes. Nonetheless, the hydration degrees of these models could not escape from the drawback as being more or less 'artificially' determined. To sum up, a similar hydration protocol was implemented to dissolve water into these polymers. At a first step, water molecules were inserted into the dry polymer model, respecting a previously reported experimental water content of 23 wt% of active APA layer of FT30 RO membrane[66]. Secondly, an interface between the polymer and water phase was established by deposing the pure water/saline solution box next to the polymer one. Finally, the system was relaxed in *NPT* ensemble, allowing of the transfer of water molecules between the polymer and water phases. After an equilibrium time for several or tens of ns, the system was considered equilibrated. There exists several questionable aspects for such hydration protocol. As suggested in the literature, real APA membranes might have depth-dependent heterogeneous chemical structures[17, 33, 35]. The XPS analyses on chemical variation or similarity of active layers of different RO membranes were not in consistence from one to another. Moreover, the polymer models in these studies also performed with various chemical structures. Therefore, it is not correct to consider a uniform preset water content at 23 wt% for all APA models, given that the water sorption capacity is closely linked to the sample's specific chemical structure. Besides, the random water insertion/overlapping might introduce water molecules into well-closed space, which might not be accessible in real conditions. In addition, water molecules are also possibly forced to be present in regions where their presence is unlikely, such as near hydrophobic groups. Correspondingly, such water insertion might lead to an overestimation of the water uptake. Another potential problem raises from the short equilibrium time. As discussed previously, our study showed that an equilibrium time up to μs is indispensable for structural relaxation for dry APA model in a box dimension around $30 \times 30 \times 30$ Å^3. As for the above mentioned studies, the water was inserted simultaneously during the polymer construction (in general via chain-bridging) or after a relaxation time of several ns. Afterwards, the hydrated systems were relaxed only for a short time (less than 40 ns). Considering the large box dimension implemented in these studies compared to ours (introduced in chapter 2), these hydrated polymer models might not be fully relaxed. As a consequence, all these studies demonstrated similar final water contents varying from 21 wt% $\sim$ 23 wt% and hydrated densities varying from 1.32 to 1.35 g·cm^{-3}, which were very close to the corresponding preset values before relaxation.

Meanwhile, other studies also merged a pre-equilibrated water box with the polymer box or inserted water molecules, without presetting any target water content.

Harder *et al.,* (2009)[47] inserted their dry polymer in the middle of a pre-equlibrated water box. The water molecules overlapped with the polymer were deleted and two interfaces in Z direction were created. Then the system was equilibrated in *NPT* (300K, 1 atm) for 1 ns, followed by 4 ns of production duration. They obtained water partition coefficient at 0.21 and a hydrated density of 1.4 g·cm^{-3}. Harder *et al.,* (2009) demonstrated a delay of water diffusion inside the membrane as well. However, they reported high water diffusion coefficients, with 5.1×10^{-9} m^2/s and 0.5×10^{-9} m^2/s in bulk water and inside the polymer respectively, which were almost

as twice as the values reported in other studies (around 2.5×10^{-9} m^2/s in bulk water and around 0.2×10^{-9} m^2/s in polymer[21, 22, 52, 53, 121]). This variation might be attributed to the applications of different forced fields. Applying the Fick's law, the authors calculated the water flux in the membrane based on their APA model, taking a hypothetical thickness of 125 Å. A water flux of 1.4 $\times10^{-6}$ m/s was obtained under 3 MPa, which was in the same order of magnitude with experimental data[101]. The authors also underlined that there existed finite-size artifacts for simulation with interface due to the small size. In a later work[78], an eight times larger APA system (with box dimension around $96 \times 96 \times 96$ $Å^3$) was constructed, giving a corrected hydrated density of 1.34 $g{\cdot}cm^{-3}$, water partition coefficient at 0.3 and water flux at 2.1×10^{-6} m/s.

In the study of Kolev *et al.,* (2014)[64], a water box of a density 0.6 $g{\cdot}cm^{-3}$ was overlapped with the dry polymer. Then energy minimization was applied and the entire system was relaxed in *NPT* ensemble (1 atm and 298.15 K) for 100 ns, followed by 1000 ns long trajectory of equilibrium. Finally, a water mass uptake around $35 \sim 40$ wt% was obtained. The authors claimed that the application of a lower water density could hydrate the polymer with efficiency while avoiding extra stains. The notable high water mass uptake was explained by the existence of evident void. As introduced previously, the authors forced the monomer connection by respecting specific chemical structure criteria, and finally obtained a well crosslinked structure, which at the same time was rigid and porous (with evident voids inside). Consequently, more water would accumulate in these evident voids.

Wei *et al.,* (2016) disposed two water reservoirs at two sides of the dry polymer. Meanwhile, water molecules were randomly inserted. The entire system was equilibrated for 20 ns before launching a heating-annealing process. Finally, this system was relaxed in *NPT* ensemble (298.15K and 1 bar) for 130 ns, performing with a box dimension around $84 \times 85 \times 210$ $Å^3$ at the end. A water content of 20 wt% and a hydrated density of 1.33 $g{\cdot}cm^{-3}$ were obtained. What is interesting in this study is that the authors revealed the effect of heterogeneous chemical structures on the water diffusion. The authors observed a fast pathway for water molecules inside the membrane, and revealed that the water molecules there were more connected by comparing the water molecule coordination number at cut-off distance of 0.33 nm. They obtained that coordination numbers were 4.5, 4.0 and 2.7 in bulk water, along the fast pathway and inside the membrane, respectively. The water molecules were more adjacent to polar groups. In the fast path way, there existed less non-polar atoms in benzene rings and the polymer was less crosslinked. Besides, the water diffusion coefficient varied between 0.2 to 0.6 $\times10^{-9}$ m^2/s inside the membrane, which could be attributed to the heterogeneous chemical environment. Moreover, they revealed that the fast pathway of water had no effect on the membrane's salt rejection, since non ion permeation through the polymer was detected in *NVT* (298K) ensemble for 100 ns.

As stated before, the overlapping of water box and random water insertion in above studies might lead to an overestimation of water mass uptake. In face of such limitation, studies also investigated the water sorption by allowing the water to dissolve freely into the polymer under certain conditions (imposed pressure[23] or volume[112]).

Ding *et al.,* (2016)[23] deposed two water reservoirs on both sides of the polymer box. The water filling was realized via non-equilibrium molecular dynamics simulation. By applying a pressure at 1 bar, the water molecules were pushed into the membrane and finally achieved a water content of 24.1 wt% after 25 ns. Based on the analysis of water-membrane interactions, the authors demonstrated a mixture of cyclic and linear water aggregates at the interior of the membrane, suggesting that there might exist narrow pathways connecting to large voids.

Suzuki *et al.,* (2015)[112] constructed APA models with various chemical structures by varying initial MPD:TMC ratios from 0.25 to 4. Nonetheless, the water diffusion analysis was realized only with the system from initial MPD:TMC ratio at 1. The authors claimed that this system represented the back-surface of the real membrane, as it owned the least free volume and was supposed to be responsible for membrane performance. Similar to Ding *et al.,* (2016), two water reservoirs were placed on both sides of the membrane, forming a sandwich configuration. The water-polymer system was equilibrated for 30 ns in NVT (300 K) ensemble. The partition coefficient was determined at 0.275, which was in agreement with the values obtained by Harder and Luo (0.21 or 0.3)[47, 78]. Moreover, a hydrated density was found at 1.39 g·cm^{-3}, relatively higher than most of the reported simulated hydrated APA densities. In this study, the acyl chloride groups were not converted into carboxylic acid groups. Since these two groups exhibit different hydrophobicity/hydrophilicity and atom molar masses, the presence of chloride might modify the water sorption behavior and molecular mass hence successively leading to a high density value.

To sum up, the above simulation studies revealed important water/solutes - membrane interactions, giving insight to corresponding transfer mechanisms through the membrane. Nonetheless, unsatisfactorinesses such as questionable hydration processes remain to be improved. Moreover, all the studies reviewed so far suffer from the fact that they are limited to single structure analysis. Such analysis has several drawbacks. Firstly, in face of the possible depth-dependent heterogeneous structure of the APA film or the large variety between different APA samples, such investigation might lead to a lack of representability. Secondly, being limited to single structure analysis, correlations between the structures and water sorption properties have not been systematically studied or clearly understood. Moreover, the water uptake behavior of APA as a function of water activity provides interesting insight into the water sorption mechanism, such as the water adsorption site number and the water clustering. Nonetheless, to the best of our knowledge, no such investigation has been reported in the literature up to date.

3.2 Questions raised in this work

Given that there exists only limited experimental water sorption data of uncoated APA films in the literature, our study investigated the water sorption isotherms of four uncoated APA films. One is the active layer of RO CPA2 membrane, which is applied in industrial effluent treatment; and three synthesized films, which were fabricated via free-standing polymerization at -20°C, 0°C and 29°C, respectively. These investigations

are expected not only to give insight to water transport mechanisms through the APA active layer of RO membranes, but also to assist in understanding the effect of various APA structures on final water sorption behaviors.

With the objective to better characterize the water hydration at molecular scale of APA films and to systematically investigate the correlations between chemical structures and resulting properties, the water mass uptakes as a function of water activity of three typical simulated APA polymer systems r0.25_1 (repetition box 1), r1.5_3 (box 3) and r5_0 (box 0) were studied in osmotic ensemble via Monte Carlo method. These systems exhibited similar dry densities of 1.243 g·cm^{-3}, 1.242 g·cm^{-3} and 1.246 g·cm^{-3}, respectively. Meanwhile, their chemical structures were clearly different. r0.25_1 was rich in TMC units and free acyl groups, with MPD:TMC monomer ratio ($r_{m:t}$) at 0.74, connection degree of acyl group (f_{ac}) at 49% and of amine group (f_{am}) at 100%. On the contrary, r5_0 was abundant in MPD units and free amine groups, with $r_{m:t}$ at 2.51, f_{ac} at 99% and f_{am} at 59%. As for r1.5_3, it had a chemical structure with more equivalent monomer unit ratio and better connection, with $r_{m:t}$ at 1.45, f_{ac} at 81% and f_{am} at 83%. Therefore, the investigation on water sorption behaviors of these chemically various systems but of similar dry densities is expected to reveal the chemical structures - thermophysical properties correlations of APA systems.

The swelling degree, water mass uptake, water sorption isotherm and water cluster formation of real APA films and simulated APA systems were compared. The combination of both macro- and micro-investigations is expected to give comprehensive understanding of the water sorption process and hydration structure of APA films.

3.3 Methodology and procedure

3.3.1 Experimental water sorption measurement

The water sorption isotherms of real APA films, CPA2 and the first set of synthesized free-standing films (Syn -20°C, Syn 0°C and Syn 29°C), were established at 20°C from an adsorption process via a dynamic vapor sorption device (DVS, Intrinsic instrument) in flow mode.

The schematic of DVS is presented in Annexes fig.A7. The temperature of the sample chamber was controlled at target temperature. The sample was loaded into the sample pan, which was suspended from a microbalance with a mass sensibility down to 0.1 μg. The RH of the sample chamber was controlled by the passing gas, for which the RH was determined by regulating the saturated water vapor and dry nitrogen gas flow rates. The RH (%) was controlled with a fluctuation around ±1%RH once the equilibrium was achieved.

Sample preparation method was similar to that described in previous density estimation (section 1.1.4.3 in chapter 1). In brief, the APA films after dissection or synthesis were recovered as a pellet and introduced into the DVS for further analysis. Differently, the film areas of the first set synthesized free-standing films remained unclearly defined here. However, this missing information did not play an essential role in isotherm analysis,

as we were only interested in the sample's mass variation along with the evolution of RH (%) but not in its density, contrary to chapter 1. Moreover, it should be noted that the pellet shape of the sample avoided the investigation on water sorption kinetic.

For CPA2, three sets of APA layer samples were dissected and analyzed successively on purpose to offer complementary data. For the first set, CPA2 membrane sample was once conserved at -18°C due to a problem of local storage. The isotherm was investigated at 7 target RH% (0, 5, 10, 80, 85, 90 and 95%RH). For the first stage at 0%RH, which corresponded to a desorption process, the equilibrium time was set at 24 h while for the other stages, the equilibrium time was set at 12 h. As for the second sample set, new CPA2 membrane conserved at proper condition (at 4°C) was analyzed. The isotherm analysis was launched at 8 target RH% (0, 5, 15, 20, 50, 60, 70 and 95%RH). The equilibrium time for each RH stage was set identical at 24 h. In addition, the analysis of the third sample set was conducted at 5 target RH% mainly in the middle range (0, 25, 30, 40 and 75 %RH). The equilibrium time for 0%RH and 75%RH was set at 72h while at 24h for the others. The initial dry masses of three CPA2 samples were 7.88 mg, 9.01 mg and 7.24 mg, respectively. Since these three obtained water sorption isotherm curves overlapped well with each other, these results were finally merged together for further analyses.

With respect to the synthesized films, their isotherms were conducted at 14 RH stages: 0, 10, 15, 20, 25, 30, 40, 50, 60, 70, 75, 85, 90 and 95%RH. A equilibrium time at 24h was set for all RH stages. The initial dry masses of Syn -20°C, Syn 0°C and Syn 29°C samples were 2.74 mg, 0.86 mg and 1.28 mg respectively.

For real films, the water uptake curves were fitted with GAB model for the whole studied a_w range and the corresponding water cluster formations were analyzed via the method of Zimm and Lundberg[77, 128, 129].

3.3.2 Water sorption simulation

The water sorption isotherms at 298.15 K (25°C) of three APA molecular models, r0.25_1 (repetition box 1), r1.5_3 (box 3) and r5_0 (box 0) were obtained in osmotic ensemble via Monte Carlo method by the code GIBBS. Water molecules were modeled by TIP4P model[57]. The saturated water vapor pressure at 298.15 K is 4538 Pa. Fourteen stages of water partial pressure, varying from 50 Pa to 4500 Pa, were imposed to the virtual water gas phase, giving fourteen RH (%) stages ranging from 1 to 99%RH with an interval around 10%RH. The thermodynamic equilibrium of water gas between the virtual water gas phase and polymer-rich phase at each RH% stage was obtained after 400 million Monte Carlo moves.

For the APA molecular models, their swelling degrees and hydrated densities were investigated. Their water sorption isotherms were fitted with Langmuir and GAB models for the whole studied a_w range.

3.4 Results

3.4.1 Water sorption isotherms of real APA films

3.4.1.1 Water sorption isotherms

The water sorption isotherms (at 20°C) of real APA films, CPA2 and synthesized films of the first set (Syn -20°C, Syn 0°C and Syn 29°C), are presented in figure 3.3.

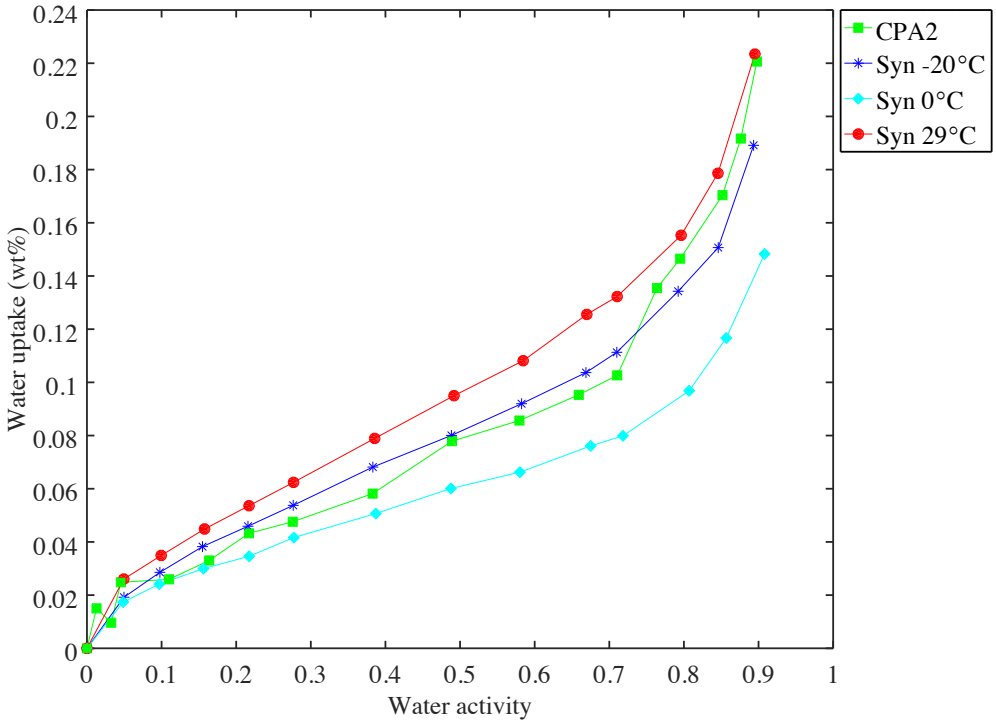

Figure 3.3: Water sorption isotherms of real APA films at 20°C.

The isotherms of real APA films, including CPA2, Syn -20°C, Syn 0°C and Syn 29°C (sample set 1), showed a typical sigmoidal shapes (type II). The isotherms of these samples could be divided into three regions. At low a_w ($0 \sim 0.25$), the curves raised rapidly demonstrating a Langmuir sorption behavior. The water molecules in this region were strongly bound to the polymer, forming the first water layer by interacting with the specific adsorption sites, such as the polar groups, on the external and internal surfaces of the polymer. At the middle a_w range ($0.25 \sim 0.6$), the water molecules became less bound to the polymer as the adsorption sites were supposed to be saturated. The water molecules progressively adsorb on the polymer surface forming multi-molecular layers. The water in this region could be considered in transition state between the bound and free water. At high a_w (>0.6), water molecules accumulated in the large free space such as the voids or large capillaries. They exhibited properties similar to free water and formed water clusters by interacting between themselves.

Among these real films, Syn 29°C exhibited the best water sorption capacity as its water mass uptake curve stayed above the curves of other films and ended with the highest water mass uptake (water mass per gram of

dry polymer mass) of 22.3 wt% at at 90%RH. CPA2 and Syn -20°C had similar water sorption behaviors for the majority of the water activity range, while CPA2 exhibited a higher water mass uptake of 22.1 wt% at 90%RH, compared to 18.9 wt% at 89%RH for Syn -20°C. Moreover, the water uptake curve of Syn 0°C stayed always below the others, and this film exhibited the lowest water mass uptake of 14.8 wt% at 91%RH. Overall, these water mass uptakes were in agreement with the reported values of other commercial APA layers[66, 70, 127] or synthesized films[55], varying between 11 wt% and 23 wt%. The corresponding water mass uptakes at high RH (%) of these real films are summarized in table 3.2.

The different water sorption behaviors of these real films are supposed to be related to their various morphological, topological and chemical structures. CPA2 performed a similar water sorption behavior as Syn -20°C, this might be attributed to their similar film thicknesses (detailed information is presented in fig.1.19, chapter 1). Besides, even though CPA2 exhibited a ridge-and-valley top-surface while Syn -20°C had chimney-like structures, their top-surface morphologies both remained relatively orderly distributed compared to other films. These similar structural feathers might lead to close water adsorption site numbers. In terms of the synthesized films, the high water mass uptake of Syn 29°C might be mainly explained by its high thickness. There might be more free volume inside this film, hence generating a larger internal surface which served as water adsorption sites. A higher water sorption capacity of Syn -20°C than that of Syn 0°C might be mainly attributed to the small and orderly distributed chimney-like structures on the top-surface of Syn -20°C, which led to a higher surface:volume ratio for this sample considering its thin thickness, consequently creating more water adsorption sites per gram of polymer than Syn 0°C. Overall, an accurate analysis of structures-water sorption properties correlations of these real films demands a good knowledge of structural properties such as the free volume and the chemical structure. Nonetheless, further investigations are needed to provide such information for our synthesized films.

In addition, it should be addressed that there exist some biases on the water uptake values of real APA membranes at high relative humidity (compared to the data of water uptake presented in chapter 1, table 1.2). For CPA2, the two analyses were realized at different relative humidity, 19 wt% at 88%RH while 22 wt% at 90%RH. For the synthesized free-standing samples, the data varied because the samples were from different sets. The various water uptake behaviors of these two sample sets might be attributed to different structures. As presented previously in chapter 1, the synthesized films of different sets generally had similar morphologies (fig.1.8). Meanwhile, the films of set 1 exhibited lower average thicknesses than the films synthesized at the corresponding temperature of set 2, according to Profilometry analysis (fig.1.19). Besides, further investigations, especially on the differences or similarities of chemical structures of these two sample sets, are required.

3.4.1.2 GAB model fitting

Since the water isotherms of real APA films established at 20°C all exhibited a typical sigmoidal shape, these isotherms were fitted to GAB model as presented in fig.3.4.

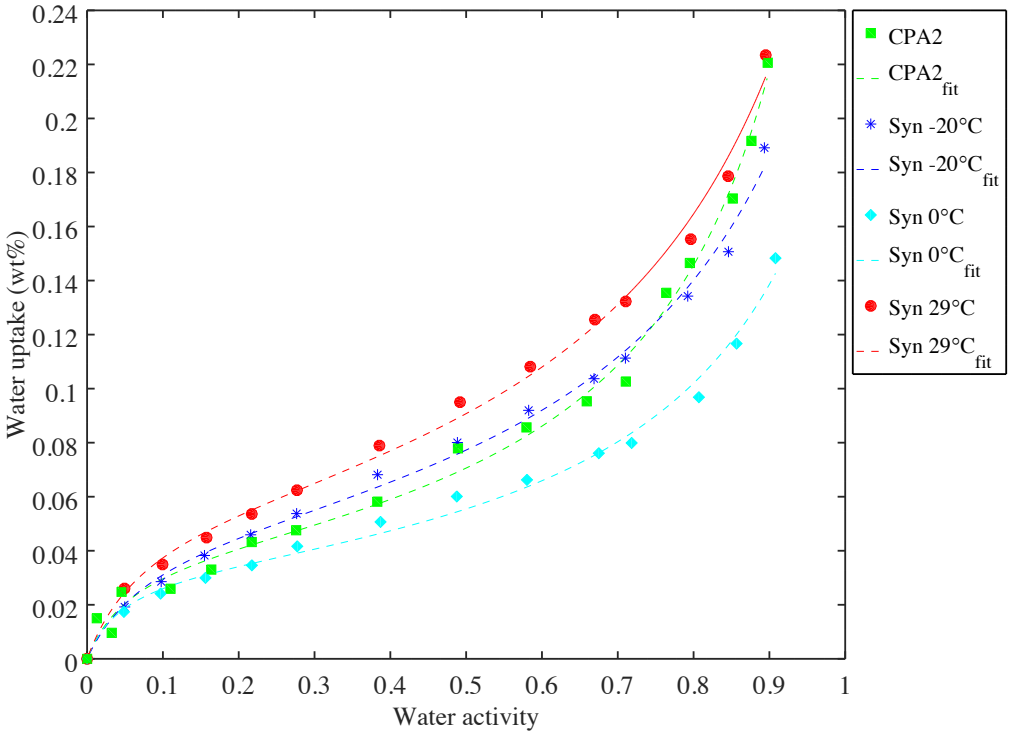

Figure 3.4: GAB fitting of water sorption isotherms of real APA films established at 20°C. The GAB fit is represented by the dotted line.

The obtained GAB parameters are summarized in table 3.1. The GAB parameters of APA layer of SW30 RO membrane and a synthesized free-standing APA film reported by Lee *et al.*, (2003)[70] are presented in the table to provide comparative data. The GAB parameters of APA molecular models are listed as well for further discussions and comparisons.

Table 3.1: GAB parameters characterizing the water vapor sorption for experimental and simulated APA samples.

Samples	w_m	$\bar{c}$	f	γ	MRD (%)
CPA2	0.0412	17.21	0.904	1.38×10^{21}	12.3
Syn -20°C	0.0501	12.14	0.819	1.67×10^{21}	3.7
Syn 0°C	0.0338	21.72	0.844	1.13×10^{21}	4.9
Syn 29°C	0.0583	13.11	0.822	1.95×10^{21}	3.8
r0.25_1	0.0933	5.31	0.170	3.12×10^{21}	9.4
r1.5_3	0.0585	11.21	0.210	1.96×10^{21}	5.5
r5_0	0.0306	5.07	0.362	1.02×10^{21}	8.2
APA+PVA (SW30, Lee *et al.*, (2013)[70])	0.0560	19.16	0.773	1.89×10^{21}	–
APA (synthesized, Lee *et al.*, (2013)[70])	0.0559	13.87	0.696	1.88×10^{21}	–

Overall, the GAB model conducted a good fit for all APA samples as MRD were all below 10% except for

CPA2, which had a relatively larger MRD of 12.3%. For the real APA films, their GAB parameters, w_m varying from 0.033 to 0.058, $\bar{c}$ varying from 12 to 22, f varying from 0.8 to 0.9, were in agreement with parameter ranges of APA layers of SW30 RO membrane and a free-standing APA film reported by Lee *et al.,* (2013)[70]. It should be addressed that the GAB parameters of Syn -20°C and Syn 29°C were very similar to that of Lee's synthesized samples. This was possibly related to similar synthesis conditions. Lee fabricated their free-standing films with MPD initial concentration of 2.5 wt%, TMC of 0.1 wt% and a reaction time around 10 min, which were comparable to our synthesis conditions.

According to the analysis of γ, the numbers of water adsorption site of all real APA films were in the same order of magnitude (10^{21}) and varied between 1×10^{21} and 2×10^{21}. Syn 29 °C exhibited the highest γ of 1.95×10^{21}, very close to the γ value around 1.9×10^{21} for the synthesized APA film reported by Lee *et al.,* (2013). Meanwhile, SW30 exhibited a γ around 1.9×10^{21} as well[70], but it is coated with highly hydrophilic PVA, which might lead to an overestimation of adsorption sites. In addition, Syn 0°C had the lowest γ among the real films. Water adsorption site number is related to the density of polar groups and external/internal surface of the polymer structure. Unfortunately, such detailed information is not available for these real APA films. Hence further investigations are required to clearly reveal the correlations between the structures and the water adsorption site number.

3.4.1.3 Water cluster formation

Complementary information on water clustering could be extracted from the water uptake curves. As presented above, the real films exhibited a Flory-Huggins water sorption behavior at high water activity. Hence, the water clustering formation of these real films were investigated. The evolution of the mean number of water molecules surrounding a water molecule in excess of the mean concentration ($\phi_1 \frac{G_{11}}{V_1}$) and the mean cluster size (MCS) as a function of water activity (a_w) is presented in fig.3.5.

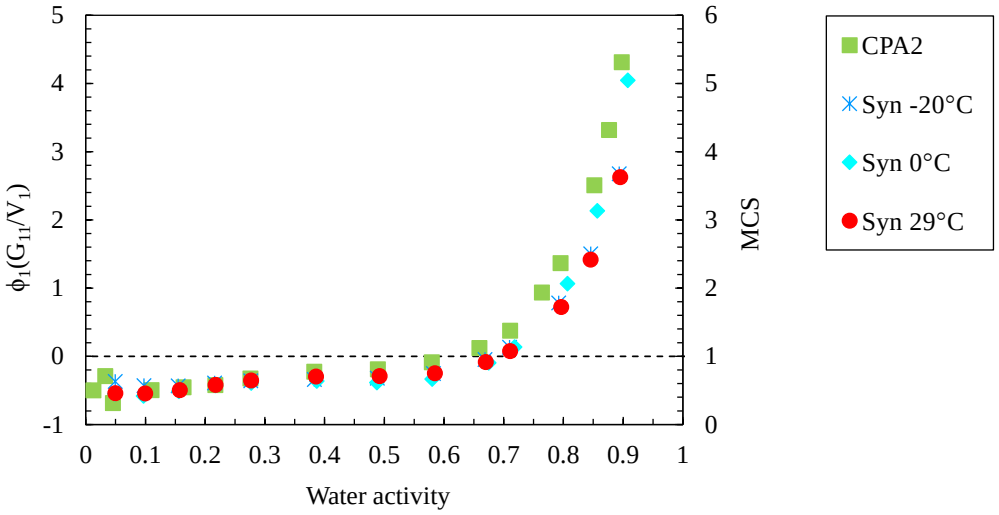

Figure 3.5: Mean number of water molecules surrounding a water molecule in excess of the mean concentration ($\phi_1 \frac{G_{11}}{V_1}$) and mean cluster size (MCS) as a function of water activity (a_w) for the APA layer of CPA2 RO membrane and synthesized free-standing APA films (sample set 1).

For all real APA films, the water clustering was observed. With the increase of water activity (a_w), $\phi_1 \frac{G_{11}}{V_1}$ and MCS values showed a rising tendency. For CPA2, water clusters become to form from a_w around 0.65, as its $\phi_1 \frac{G_{11}}{V_1}$ became superior to zero and MCS became larger than 1, which suggested the presence of surrounding water molecules in excess of the average concentration. At the highest a_w (around 0.9), the CPA2 performed with an average cluster size around 5.3. As for the synthesized films, the water cluster formation started from a_w around 0.7 and finally led to a cluster size about 3.6 for Syn -20°C and Syn 29°C, and 5 for Syn 0°C. The water cluster formation at a larger a_w of these synthesized films suggested better polymer-water interactions. The water clustering confirmed our previous discussions on the water isotherms of these samples: in the region where a_w was larger than 0.6, the water molecules weakly interacted with the polymer matrix but performed with properties close to free water in voids and large capillaries. Overall, our obtained water cluster size results were larger than that of a synthesized APA film reported by Lee *et al.,* (2013) [70]. The authors demonstrated a cluster formation starting from a_w at 0.85 and a cluster size around 2.7 at the highest a_w (around 0.95). The authors also reported a cluster size of 2.5 for the APA layer of SW30, however this value is not comparable here due to the presence of PVA coating.

The notable high water cluster formation of CPA2 APA layer was probably attributed to its loose structure. As presented in chapter 1, CPA2 exhibited a void fraction up to 36 %, compared to 15%∼31% of APA layers of other commercial RO membranes[75]. The presence of evident voids promoted the formation of water cluster. Likewise, Syn 0°C is supposed to exhibit evident voids. Meanwhile, Syn -20°C and Syn 29°C were likely to exhibit certain voids which were smaller than that of the two former samples but close to that of the synthesized film reported by Lee *et al.,* (2013)[70], as they had similar water cluster sizes.

3.4.2 Water sorption isotherms of APA molecular models

3.4.2.1 Water sorption isotherms

The water sorption isotherms at 25°C of APA molecualr models, r0.25_1, r1.5_3 and r5_0 systems, are presented in figure 3.6. The water isotherms (at 20°C) of real APA films are also plotted in this figure for comparison.

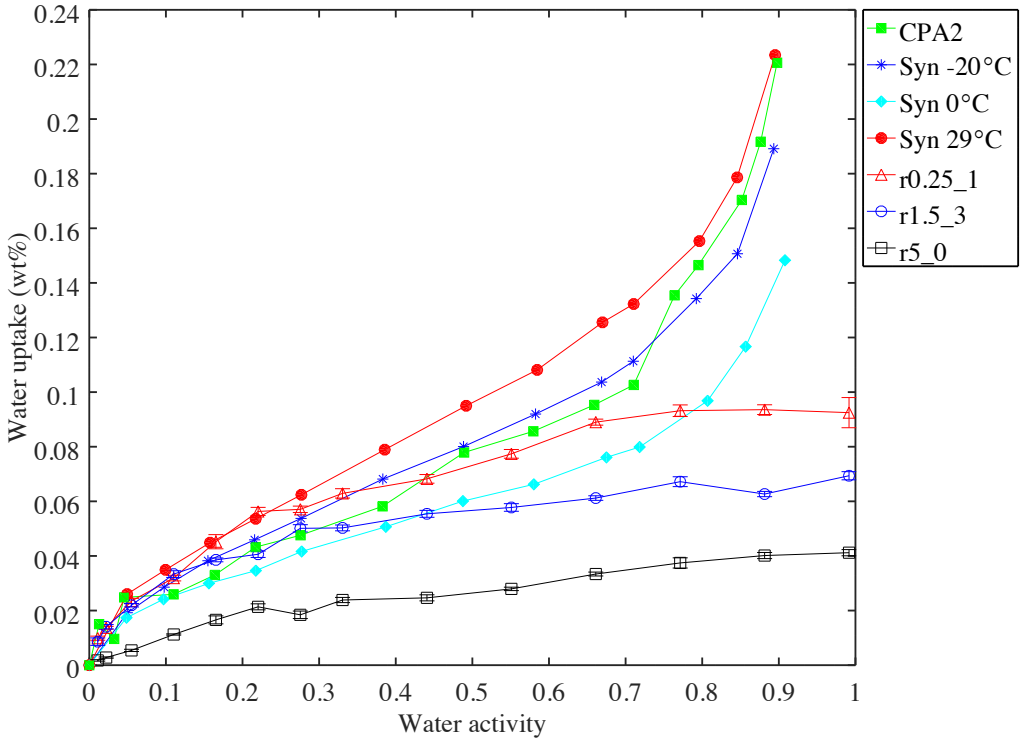

Figure 3.6: Water sorption isotherms of APA molecular models at 25°C and of real APA films at 20°C.

The simulated APA polymers, r0.25_1, r1.5_3 and r5_0, had different isotherm shapes from the real APA films by exhilibiting a type I shape. These samples had similar Langmuir water sorption behaviors as the real membranes at low a_w, indicating similar water-polymer interactions for forming the first water layer, which validated our Monte Carlo simulations. From the middle a_w, the water uptake curves of simulated polymers gradually leveled off while the curves of the real films continued to rise up (fig.3.6). The absence of increasing water uptake for these simulated samples at middle and high a_w could be attributed to the absence of evident voids. Fabricated with relatively small simulation boxes, these simulated APA are supposed to have properties close to the dense bulk APA polymer or the dense region of the CPA2 APA layer. The free space in these samples should be as narrow as the network free volume between polymer chains rather than be evident aggregate voids. It is supposed that once the adsorption sites are saturated at low a_w, only few water molecules are able to continue dissolving into the free space. Even though these water molecules are loosely bound to the polymer, they fail to form clusters due the limited free space inside the polymer.

In addition, water clustering analyses were tested for APA molecular models, the results demonstrated

that their MCS stayed below one during the whole range of water activity. Since our simulated samples did not perform a Flory-Huggins sorption behavior at high water activity, their calculated MCS became even lower than zero when water activity approached to 0.9. Hence, water cluster size analysis seemed not adaptable to the water isotherms of APA molecular models, as no water cluster is supposed to form in these systems. Therefore the corresponding results are not presented here. Besides, our water sorption simulation is still in progress. The water cluster formation is able to be further investigated via direct visualization into the simulation box in our further study.

3.4.2.2 Swelling of APA molecular models

The swelling degrees as a function relative humidity (RH,%) of simulated APA polymers, r0.25_1, r1.5_3 and r5_0, are presented in fig.3.7.

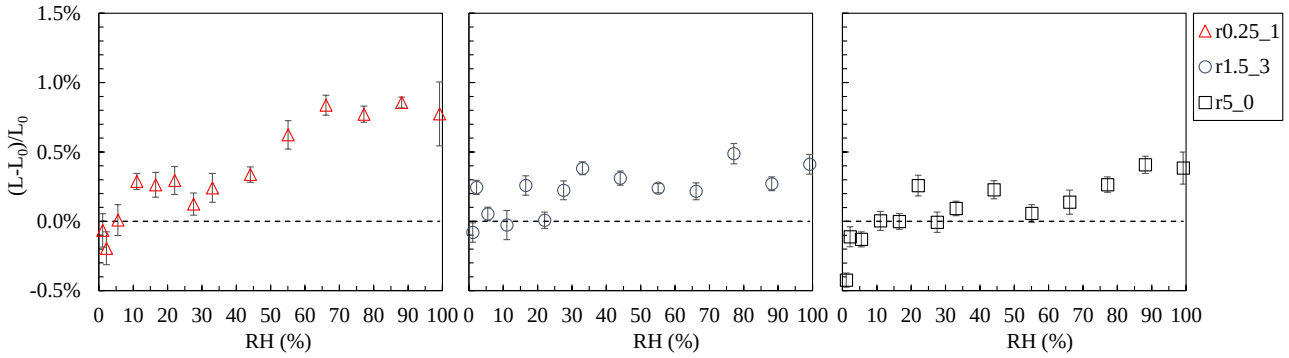

Figure 3.7: The evolution of swelling degree as a function of water activity for simulated APA samples. The dotted line indicates the swelling degree equal to zero.

All three APA polymers exhibited slight swelling with increase of relative humidity (RH, %). At 99%RH, the system r0.25_1 performed with a swelling degree at 0.8%±0.2%, while r1.5_3 and r5_0 had a similar swelling around 0.4%±0.1%. These swelling degrees corresponded to volume expansions around 2.3%±0.9%, 1.2%±0.3% or 1.2%±0.5% respectively for r0.25_1, r1.5_3 and r5_0. Our values were evidently lower than swelling data of other APA molecular models. Ding *et al.,* (2016)[23] reported a volume expansion of 28% on wet basis for their polyamide model, corresponding to a volume expansion around 39% and a swelling degree around 11% on dry basis. Similarly, a swelling degree of 10%∼11% was found for the model of Kolev *et al.,* (2014)[64]. The higher swelling degrees of these APA models are supposed to be related to their larger box dimensions (up to tens of nm) and higher crosslinking degrees, which permitted to create more voids hence leading to larger swelling degrees and higher water mass uptakes, 24 wt%[23] and 35 wt%∼40 wt%[64].

As introduced previously, it was found that the swelling behavior of real APA membranes might vary according to their proper crosslinking states. In our study, we found that the swelling of CPA2 and our synthesized free-standing samples was not evident. Other authors also demonstrated that the swelling of APA films were too weak to detect or not evident considering the thin thickness and high thickness analysis error[34,

70]. Meanwhile, evident high swelling degrees up to 20% or 53% were also reported for synthesized or commercial APA layers[25, 32]. The swelling results of our simulated samples are interesting, because they demonstrated that the swelling behavior might be related to the chemical structures. Among these samples, the system r0.25_1 exhibited many highly hydrophilic acyl groups, consequently performing with the largest water mass uptake and highest swelling degree. Conversely, r5_0 had many less hydrophilic amine groups, leading to the weakest water mass uptake. Hence its swelling was not evident. Meanwhile, even though r1.5_3 had higher water content compared to r5_0, its structure is supposed to be more rigid thanks to a better connection, which hindered the swelling and resulted in a similar swelling degree as r5_0. More investigations of water structures inside the molecular models are needed to provide a deeper insight to structures-water sorption properties correlations.

3.4.2.3 Hydrated density of APA molecular models

The dry density at 0%RH, water mass uptake and hydrated density at high RH of APA molecular models are presented in table 3.2. As introduced previously, the corresponding information of water mass uptakes of real APA membranes, APA layer of CPA2 and free-standing films (set 1), which were used for the analyses of the water sorption isotherm, is presented together to provide comparative information.

Table 3.2: Water mass uptake and density of real APA films (CPA2, Syn -20°C, 0°C and 29°C) and APA molecular models (r0.25_1, r1.5_3 and r5_0)

Samples	Dry density ($g{\cdot}cm^{-3}$)	RH%	Water uptake (wt%)	Hydrated density ($g{\cdot}cm^{-3}$)
CPA2	–	90	22.1	–
Syn -20°C (set 1)	–	89	18.9	–
Syn 0°C (set 1)	–	91	14.8	–
Syn 29°C (set 1)	–	90	22.3	–
r0.25_1	1.242±0.006	99	9.3±0.6	1.327±0.003
r1.5_3	1.242±0.004	99	6.9±0.2	1.312±0.002
r5_0	1.246±0.005	99	4.1±0.1	1.283±0.005

The three simulated polymer systems had similar initial dry densities, varying between 1.242 and 1.246 $g{\cdot}cm^{-3}$. As shown in table 3.2, these systems demonstrated various water sorption capacities. The water mass uptakes at 99%RH decreased with the increase of the initial MPD:TMC ratio, with 9.3 wt%, 6.9 wt% and 4.1 wt% for r0.25_1, r1.5_3 and r5_0, respectively. Accordingly, the hydrated densities of these samples decreased progressively from 1.327 $g{\cdot}cm^{-3}$ to 1.283 $g{\cdot}cm^{-3}$. As discussed above, the water sorption isotherm curves of simulated samples and real films varied from the middle water activity range, which resulted in a variation of water mass uptake at high relative humidity: the water uptake values of simulated APA polymers (< 10 wt%)

were lower than that of CPA2 (22 wt% at 90%RH) or synthesized free-standing samples (14.8 $\sim$ 22.4 wt% around 90%RH for set 1 or 35.6 $\sim$ 65 wt% for set 2). The relative low water mass uptakes at high RH of our simulated samples could be due to the absence of evident void inside the structure, which prevented the water clustering usually formed in large free space.

With respect to water mass uptakes of APA molecular models, the majority of reported data fell into a small range between 20 $\sim$ 24 wt% on dry basis. Meanwhile, Kolev *et al.,* (2014)[64] reported a relatively high mass uptake around 35$\sim$40 wt%. The variations between our simulated water mass uptakes and the results of other simulations could be attributed to different model structures and hydration processes. Firstly, the APA models in other studies had larger box dimensions or even larger crosslinking degrees, which led to more porous structures with larger water sorption capacity at high RH. Secondly, as discussed previously, a general potential problem during the hydration processes of most of other simulations was that the obtained water uptake mass was more or less artificial. Water molecules in these studies were firstly inserted into the polymer box, either via random insertion by respecting an experimental water content of the active layer of FT30 membrane at 23 wt%, either via overlapping the pure box with the polymer one, which led to questionable water uptake results. In our study, such problem was avoided because the insertion of water molecules was based on the equality of water chemical potential in polymer-rich phase and virtual water gas phase at the target partial pressure. We believe that our obtained water mass uptake results are more accurate.

Besides, among our three simulated samples, system r0.25_1 exhibited the highest water mass uptake while system r5_0 had the lowest water sorption capacity. This could be closely related to different chemical group distributions in these systems: r0.25_1 was rich in acyl groups, r1.5_3 had more amide groups, meanwhile r5_0 possessed more free amine groups. These different chemical groups exhibit distinct affinity with water, hence resulting in various water sorption capacities. More discussions on the effect of chemical structures on water sorption are presented in the following section 3.4.2.5. Moreover, according to the water mass uptakes, it could be estimated that the water volume fraction at 99%RH was 11.26$\pm$0.67%, 8.54$\pm$0.18% or 5.09$\pm$0.14% respectively for system r0.25_1, r1.5_3 or r5_0. These values gave rough insight to the free volume fractions that our systems exhibited. It should be noted that the free volumes estimated here were the volumes that could be occupied by water molecules. Considering the chemical groups' possible hydrophobicity, our obtained free volumes were more meaningful to the ones estimated by probing a hard sphere with given Van Der Waals radius[112].

Our simulated samples exhibited hydrated densities ranging from 1.28 to 1.33 g·cm^{-3}, which were close to the reported hydrated densities of APA molecules models varying from 1.24 to 1.4 g·cm^{-3}[23, 47, 52, 78, 112, 118, 121]. Considering the questionable hydration processes applied in most of the other simulations, our results are believed to give more accurate hydrated density estimations of various APA chemical structures.

There exists few experimental hydrated density data of real APA membranes. The hydrated density of the active layer of RO FT30 was reported at 1.38 g·cm^{-3} with a water mass uptake of 23 wt% by Kotelyanskii *et*

al., (1998)[66]. In a recent study, Zhang et *et al.,* (2010) corrected this value into 1.24 g·cm^{-3} with a water content of 11.2 wt%[127], and the authors also reported a hydrated density of 1.22 g·cm^{-3} with a water content of 12.8 wt% for LF10 membrane. Meanwhile, it should note that these commercial layers are all coated by PVA. In terms of synthesized APA films, Foglia *et al.,* (2017) fabricated sub-10 nm APA films with various monomer concentrations, reporting a hydrated density range varying from 1.33 to 1.55 g·cm^{-3}[32] at 100%RH. Besides, our CPA2 sample demonstrated a hydrated density around 1.475 g·cm^{-3}. Overall, our simulated hydrated densities fell into the common range of experimental data.

3.4.2.4 Langmuir model fitting

Since the water sorption isotherms of the APA molecular models exhibited a type I shape, these data were fitted to Langmuir model as presented in fig.3.8. The n_0 was taken as the water concentration obtained at the highest a_w.

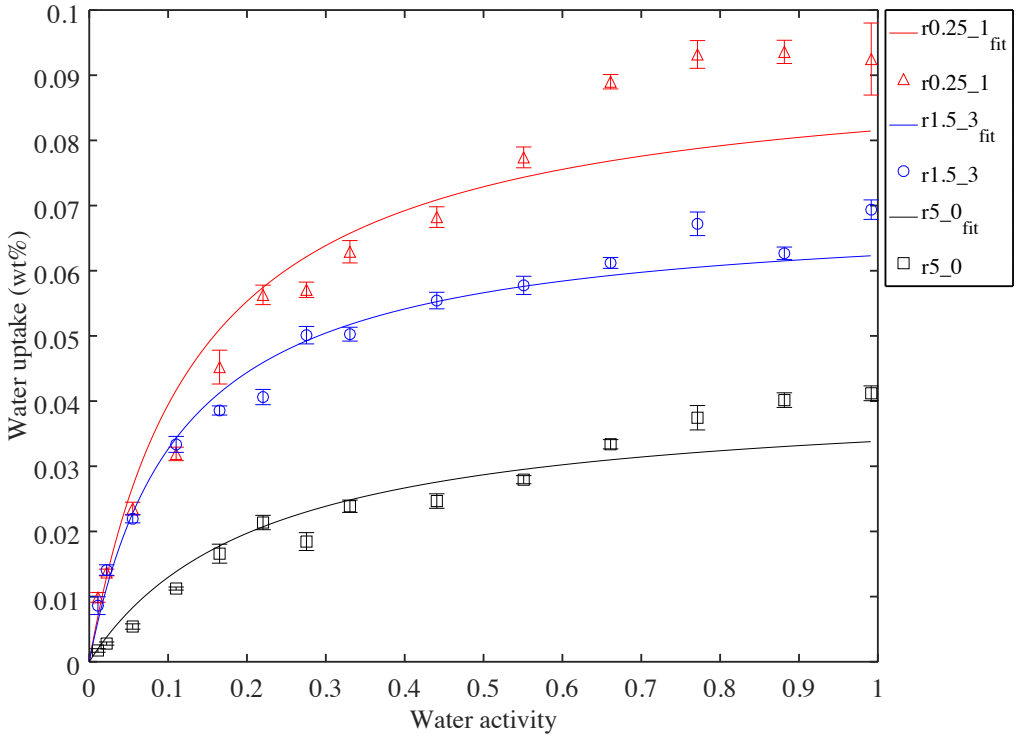

Figure 3.8: Langmuir fitting of water sorption isotherms of APA molecular models established at 25°C. The Langmuir fit is represented by the solid line

The obtained Langmuir parameters are presented in table 3.3. The Langmuir parameters of APA layers of FT30 and LF10 RO membranes reported by Zhang *et al.,* (2009)[127] are presented as well for comparison.

Table 3.3: Langmuir parameters values characterizing water vapor sorption in APA molecular models.

Samples	E_{ad}/k_BT	T (K)	E_{ad} (KJ/mol)	MRD (%)
r0.25_1	1.80	298.15	5.0	10.1
r1.5_3	2.08	298.15	5.4	5.5
r5_0	1.38	298.15	3.8	17.4
APA+PVA (FT30, Zhang *et al.,* (2009)[127])	1.5	298	3.7	–
APA+PVA (LF10, Zhang *et al.,* (2009)[127])	1.1	298	2.7	–

Langmuir model conducted a good fit with systems r1.5_3 with a MCR of 5.5%. The fitting for r0.25_1 was considered still good, as its MCR was only little larger than 10%. However, the data of system r5_0 were not adapted to Langmuir model with a MCR up to 17.4%. The results showed that r0.25_1 and r0.15_3 exhibited an adsorption energy of 5.0 KJ/mol and 5.4 KJ/mol, respectively. These values were in the same order of magnitude as the data reported for APA layers of FT30 and LF10 RO membranes, which were at 3.7 KJ/mol and 3.8 KJ/mol respectively[127]. These films are coated with PVA, hence these results are not directly comparable to ours. A relatively lower adsorption energy of r0.25_1 compared to r1.5_3 suggested a better affinity between water molecules and the polymer. This observation was in consistency with the previous chemical structure analysis. The excessive polar acyl groups in r0.25_1, as the adsorption sites, are supposed to be favorable in forming hydrogen bond with water molecules. However, these obtained adsorption energy results should be taken with caution, as they were deduced from one analysis temperature while the investigation is more accurate with analyses under several temperatures.

3.4.2.5 GAB model fitting

The water isotherms of APA molecular models established at 25°C were fitted to GAB model as shown in fig.3.9. The obtained parameters are summarized in table 3.1.

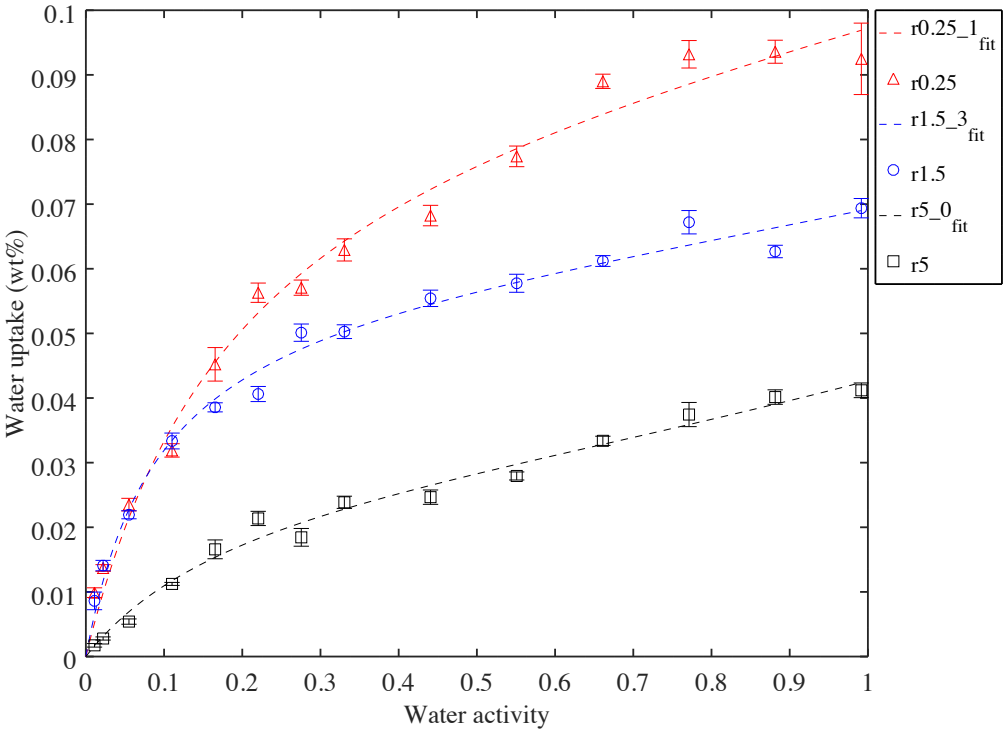

Figure 3.9: GAB fitting of water sorption isotherms of APA molecular models established at 25°C. The GAB fit is represented by the dotted line.

Even though the water isotherms of APA molecular models exhibited a type I shape, the GAB fitting was proven to be reasonable for these samples as the corresponding MCR were all below 10%. Meanwhile, our simulated samples exhibited relatively smaller $\bar{c}$ and f than the real membranes, which could be attributed to the differences in the water layer formation. Therefore, water molecules in real APA membranes intended to form multilayers in large voids formed by dense layers (fig.1.4 in chapter 1), while forming monomolecular layer inside the simulated samples due to the absence of such large voids[106].

With respect to the simulated samples, they demonstrated various water adsorption capacity. With increasing initial MPD:TMC ratio from 0.25 to 5, the adsorption site number decreased progressively from 3.12×10^{21} to 1.02×10^{21}. The total number of available amine, amide and acyl sites in simulation boxes of r0.25_1, r1.5_3 and r5_0 were 6.9×10^{21}, 6.5×10^{21} and 7.1×10^{21} per gram of polymer, respectively. Since the total amine, amide and acyl sites were close and these systems all had similar internal topology (without presence of evident voids) and dry densities, the variety of water adsorption capacity is supposed to be directly related to their various chemical structures. As discussed previously, as a function of increasing initial MPD:TMC ratios, the amine group connection (f_{am}) decreased while the final monomer ratio ($r_{m:t}$) and acyl group connection degree (f_{ac}) increased.

Performing with a f_{ac} of 49% and a f_{am} of 100%, the system r0.25_1 exhibited a notable water adsorption site number at 3.12×10^{21} mainly because it had abundant polar acyl groups. The two oxygen and one hydrogen atoms in carboxylic acid groups are favorable to form hydrogen bond with water molecules[23, 118], thereby

they naturally served as the adsorption sites to form the first water layer. As for r1.5_3, this system exhibited close total number of available amine, amide and acyl sites as r0.25_1, but it had less free acyl groups but more free amine groups with a better f_{ac} of 81% and less f_{am} of 83%. It turned out that though the nitrogen and hydrogens in amine groups are capable as well to form hydrogen bond with water molecules[118], such interaction is supposed to be looser than that of acyl groups, as the water adsorption sites declined to 1.96×10^{21}. The system r5_0 exhibited the largest total number of available amine, amide and acyl sites among the three systems, with an abundance of free amine groups ($f_{am} = 59\%$) but almost no free acyl group ($f_{ac} = 99\%$). This system was found to exhibit the least γ of 1.02 $\times 10^{21}$ per gram of polymer. Thereby, it was clearly shown that free amine groups were less favorable to interact with water molecules as free acyl groups.

The above discussions provided interesting insight into the possible correlations between the chemical structures and water sorption capacities of APA. Carboxylic acid groups are supposed to play an essential role in creating water adsorption sites by establishing hydrogen bonds with water molecules. Meanwhile, amide or amine groups were found to perform looser interactions with water. Experimental investigations are expected to verify whether such correlations exist in real APA films.

3.5 Conclusion

Three APA molecular models with various chemical structures but similar dry densities, r0.25_1, r1.5_3 and r5_0, were hydrated by implementing osmotic ensemble via Monte Carlo method. Compared to real and other simulated APA samples, our simulated polymers performed low water mass uptakes ranging from 4.1 wt% to 9.3 wt% at 99%RH. The weaker water uptakes were possibly attributed to the absence of evident voids, preventing the water cluster formation which only occurs in large voids or capillaries. These films had hydrated densities varying from 1.28 to 1.33 g·cm^{-3}, falling into the reported hydrated density range of real commercial and synthesized APA films. In addition, the weaker water mass uptakes also led to lower swelling degrees, which were 0.8%±0.2% for r0.25_1, and 0.4%±0.1% for r1.5_3 and r5_0. The different swelling behaviors of our simulated samples revealed the possible correlations between the chemical structures and the swelling, assisting in understanding the experimental data in the literature, where various swelling behaviors were reported for synthesized and commercial APA layers.

The water sorption isotherms of APA layer of CPA2, Syn−20°C, Syn0°C and Syn29°C were investigated in a water activity range from 0 to 0.9 via DVS at 20°C. Meanwhile, the water isotherms of three simulated APA polymers were conducted in a water activity range varying from 0 to 0.99 at 25°C. To the best of our knowledge, this is the first water sorption isotherm investigation of the APA film via molecular simulation.

According to the results, the water uptake curves of real films demonstrated a type II shape while that of simulated polymers exhibited a type I shape according to IUPAC's classification[106]. All samples performed Langmuir sorption behavior at low water activity ($0 \sim 0.25$), where water molecules were strongly bound to the polymer by being adsorbed onto the specific adsorption sites on the external/internal surface of the polymer.

The water adsorption site number was analyzed by fitting the water sorption isotherm data to GAB model. All real samples exhibited similar water adsorption site numbers varying between 1.02×10^{21} and 2×10^{21} per gram of polymer. These values were close to that of one free-standing APA film reported in the literature[70]. In terms of simulated films, it was found that with increasing initial MPD:TMC ratio from 0.25 to 5, the water adsorption site number decreased progressively from 3.12×10^{21} to 1.02×10^{21} per gram of polymer. Meanwhile, it should be addressed that these systems exhibited close total numbers of available amine, amide and acyl sites in simulation boxes, with 6.9×10^{21}, 6.5×10^{21} and 7.1×10^{21} sites per gram of polymer for r0.25_1, r1.5_3 and r5_0, respectively. Therefore, the water adsorption site number was proven to be closely related to chemical structures such as the specific chemical groups. For r0.25_1, abundant free acyl groups served as the adsorption sites by firmly interacting with water molecules. Meanwhile, an excess of amine groups was less favorable to create the adsorption sites, as the system r5_0 exhibited the least adsorption sites. Water uptake curves of r0.25_1 and r1.5_3 exhibited a relatively good fit with Langmuir model. It was suggested that the water adsorption was easier in the system r0.25_1 than in r1.5_3, as r0.25_1 showed a lower adsorption energy of 5.0 KJ/mol compared to 5.4 KJ/mol for r1.5_3. Meanwhile, these results should be taken with caution due to the single temperature analysis.

From the middle water activity, the water sorption curves of the real membranes continued rising up while that of the simulated samples leveled off. The distinct water sorption behaviors at middle and high water activity ranges, after the saturation of adsorption sites of the first water monomolecular layer, were probably attributed to different internal topological structures. The real APA films had large voids, which allowed of the formation of water cluster. Meanwhile, the simulated samples are supposed to mimic the bulk polymer or the dense regions of real APA films, only permitting few water molecules to dissolve into the limited free space. As a consequence, water molecules failed to form clusters. Therefore, our simulation provided interesting information on the water sorption behavior of the selective barrier of the membrane, which is responsible for water/solute transports during the filtration.

Since the real films exhibited a Flurry-Huggins water sorption at high water activity, the water cluster formation in these films was further analyzed by implementing Zimm and Lundberg's method[77, 128, 129]. For CPA2 and Syn 0°C, the water cluster occurred at a_w around 0.65 and 0.7 respectively, finally leading to an average cluster size around 5.3 and 5 separately when a_w reached 0.9. Meanwhile, Syn -20°C and Syn 29°C's clustering begun from a_w at 0.7 and resulted in a similar cluster size around 3.6 at high a_w. The delay of the cluster formation of synthesized films suggested better affinity between water molecules and these films compared to CPA2. The larger water cluster sizes of CPA2 and Syn 0°C suggested larger void sizes inside these systems compared to Syn -20°C and Syn 29°C. Moreover, these obtained cluster sizes were all larger than a reported value of 2.7 for another synthesized APA film in the literature[70]. This could be explained by that our films generally had looser structures with larger voids, hence facilitating the formation of larger water clusters. More investigations on the void size/fraction of our synthesized films are needed to perform

more accurate analyses.

General conclusion

This PhD project systematically investigated the structures and structures properties-thermophysical properties correlations of aromatic polyamide (APA) films via two approaches in parallel, experimental characterizations and molecular modeling.

We characterized experimentally the structures of commercial CPA2 reverse osmosis (RO) membrane's active APA layer and a set of free-standing APA films synthesized at four organic solvent temperatures (-20 °C, 0 °C, 15 °C and 29 °C). The APA layer of CPA2 RO showed a typical multi-level structure as 'dense bottom + ridge-and-valley structures upwards' while the free-standing films exhibited a multi-level structure as 'dense bottom + chimney-like structures'. CPA2 APA layer demonstrated a looser structure than other commercial RO membranes reported in the literature, with a dry apparent volumetric density of 0.8 $g{\cdot}cm^{-3}$ accompanied with a void fraction around 35%, which together led to a dry density of 1.24 $g{\cdot}cm^{-3}$ for the dense regions. Besides, it exhibited a water uptake around 19 wt% at 88%RH, leading to a hydrated apparent density of 0.96 $g{\cdot}cm^{-3}$, and 1.48 $g{\cdot}cm^{-3}$ for the dense regions. Meanwhile, applying a new set of chemical structure descriptors, it was found that CPA2 exhibited a depth-dependent heterogeneous structure. From back-surface to top-surface, the MPD:TMC monomer ratios decreased, which might be attributed to the decrease of MPD concentration along its diffusion direction from the interface towards the top-surface during the interfacial polymerization (IP). Besides, the top-surface was better connected than the back-surface. The weaker connection of the latter might be resulted from the hydrolysis of reactive acyl chloride groups into non-reactive carboxylic acid groups at the interface.

In terms of the synthesized films, their back-surfaces were as flat as that of CPA2, which was probably explained by the immiscibility of trimesoyl chloride (TMC) in the aqueous phase. A positively temperature-dependent trend was observed for free-standing films' thicknesses, which was related to the increase of MPD diffusion speed at a higher temperature. The film synthesized at the lowest temperature (-20 °C) performed a remarkable water uptake at 65 wt% at 91%RH, which might be attributed to its orderly distributed and small-size chimney morphology on the top-surface, providing more water adsorption sites. Nonetheless, we didn't manage to estimate the density of our synthesized films. We demonstrated that the thickness estimation remains a very complicated and difficult task in face of thin and highly heterogeneous structures such as our synthesized films.

We successfully constructed all-atoms molecular models of APA polymer with various chemical structures and reported the first investigation on the relationship between the chemical structures and the density of APA polymer. The APA molecular models were polymerized by forming amide bonds between hydrolyzed trimesoyl chloride (TMC) and *m*-phenylenediamine (MPD) with fourteen initial MPD:TMC ratios, varying from 0.25 to 5. For ratios at 0.25, 1.5 and 5, eleven repetition boxes were launched to verify the repeatability of the construction protocol. The obtained APA systems exhibited final MPD:TMC monomer unit ratios ranging from 0.68 to 2.61, corresponding to systems with acyl/amine group connection degrees at 45%/100% and 99%/57%, respectively. These chemical variations were also detectable via IR spectra analysis for high frequency region. The systems generated from medium MPD:TMC ratios exhibited a better connection state than systems from the extreme ratios, forming larger molecular networks with both high acyl/amine group connection degrees. These generation results were consistent with the chemical structure evaluation of real APA films synthesized from various monomer ratios[26]. Besides, our various molecular models are also supposed to mimic APA's possible depth-dependent heterogeneous structures which resulted from the declination of MPD concentration in its diffusion direction during IP (as shown for the chemical structure analysis of CPA2 RO membrane's APA layer), giving insight to these potentially different structures and properties. We developed a relaxation protocol, consisted of a series of minimization, *NVT*, *NPT iso* and *NPT iso-stress* simulations, allowing relaxing the strains created from the polymerization process successively. We also addressed that an equilibrium time up to several μs is indispensable to relax the APA system with box dimension around $30 \times 30 \times 30$ Å^3, while such long equilibrium time was rarely reported in the literature. After being finally well relaxed in molecular dynamics ensemble *NPT iso-stress* (1 bar, 298.15 K), simulated APA polymers were well-packed by forming $\pi - \pi$ stacking structures between benzene rings or hydrogen bonds between chemical groups. We also addressed that chemical structures exhibited little effect on the final density of the polymer. A slight decreasing tendency of density was observed with the increasing MPD:TMC monomer ratio. Whereas, the variations of density were not significant considering the analysis error. An average density around 1.26 g·cm^{-3} was obtained. This value was very close to our experimentally obtained density of the dense region of CPA2 around 1.24 g·cm^{-3}. This good agreement between the simulation and experimental results validated the force field and construction protocol implemented for our molecular models.

We investigated the hydration of real APA films, which serves to complement the very few water sorption isotherm data in the literature and to provide reference data for our molecular simulation as well. Meanwhile, we performed the first water sorption isotherm investigation of APA molecular model by applying simulations in osmotic ensemble via Monte Carlo method. We selected three APA molecular models which were polymerized from different initial MPD:TMC ratios at 0.25 (repetition box 1, r0.25_1), 1.5 (repetition box 3, r1.5_3) and 5 (repetition box 0, r5_0), respectively. These systems were of similar dry densities but various chemical structures, allowing the first investigation on correlations between the chemical structures and water sorption behaviors of APA polymer.

By comparing the real and simulated APA samples, we demonstrated that water sorption behaviors of APA films are significantly effected by the presence/absence of evident voids and by the specific chemical structures. The real films exhibited evident voids, which favored the water clustering at high RH, thereby leading to a sigmoidal water sorption isotherm curve shape and water mass uptakes higher than 14.8 wt%. Conversely, without evident void, simulated systems exhibited no evident cluster formation. Their water isotherm curves leveled off at high RH. Their water mass uptakes, all below 10 wt% at 99%RH, were generally lower than that of real films or other molecular models. Besides, only slight swelling degrees less than 1% were found for our simulated systems, compared to that around 10% for other APA molecular models in the literature. Notably, these variations could also be resulted from different applied hydration methods. The hydrated densities of our molecular models were found ranging from 1.28 to 1.33 g·cm^{-3}, which fell into a common range of the reported values in the literature.

The GAB model fitting demonstrated that the simulated sample r0.25_1, abundant in carboxylic acid groups, exhibited the highest adsorption site number of 3.12×10^{21} per gram of polymer, compared to $1 \times 10^{21} \sim 2 \times 10^{21}$ per gram of polymer for other real or simulated APA systems. It should be addressed that the simulated systems exhibited similar total numbers of available amine, amide and acyl sites in simulation boxes, with 6.9×10^{21}, 6.5×10^{21} and 7.1×10^{21} sites per gram of polymer for r0.25_1, r1.5_3 and r5_0, respectively. Besides, for these simulated systems, an evident raise of water mass uptake was observed with the increase of carboxylic group number. Thereby, carboxylic acid groups are supposed to serve as the water adsorption sites, while amide bonds and amine groups are less favorable to interact with water molecules. More investigations on the water structure inside the simulated polymers such as the hydrogen bond formation are expected to give more accurate analyses on the structures-water sorption properties correlations.

Overall, this work provides interesting information on the structures and structures-thermophysical properties correlations of APA films, serving as a solid base for further investigations on the transport of organic molecules through RO membranes.

The following step of this project is to continue the analyses of the hydrated APA molecular models: the formation of hydrogen bond between water molecules and APA chains will be investigated via radial distribution function. The diffusion coefficient of water molecule inside the models will be studied via the mean-square displacement with molecular dynamics simulations. Since the current simulations focus on investigating the water sorption of the dense regions of real APA films, the effect of the presence of voids will be further investigated, which allows to simulate the corresponding thermophysical properties of the apparent real APA films. Two possible approaches are available to create voids inside molecular models. One is to construct polymer models with simulation box of larger dimensions. A large box size allows of, or promotes, the connection of small voids during the polymerization process, hence leading to the formation of large evident voids. The other approach is to create a 'sandwich' ensemble by inserting a certain void volume between two APA dense molecular models. The void fraction of such ensemble is controllable, hence shedding light to how the void fraction affects the

water sorption of real apparent APA films.

In a further step, small neutral organic molecules with molecular molar mass near 100 $g \cdot mol^{-1}$ but with different chemical structures, such as 2,3-butanediol and furfural, will be inserted into the hydrated APA molecular models with GIBBS code via Monte Carlo method. The molecules-membrane interactions, such as the hydrogen bond formation between chemical groups of organic molecules and polymer chains will be investigated via radial distribution function. For molecules exhibiting aromatic rings, the $\pi - \pi$ interaction between the molecules and the polymer will be characterized. Moreover, the water-polymer partition coefficients of organic molecules and their diffusion coefficients inside the polymer will be calculated. By preparing APA molecular models with various chemical structures and void fractions, we expect to identify factors that dominate the transfer of different organic solutes through the APA film.

With respect to the experimental aspect, more investigations on synthesized films at different synthesis temperatures are to be launched to study experimentally correlations between structural and thermophysical properties of real APA films. New syntheses will be carried out without addition of triethylamine, which helps better investigate chemical structures of these synthesized films and evaluate the corresponding effect of the synthesis temperature. This also assists in investigating the correlation between chemical structures and water sorption behaviors. Moreover, other techniques, such as the analysis of the APA film's cross section by SEM, should be tested for a better characterization of synthesized films' thicknesses. A good thickness estimation is expected to give a better density estimation for these films, which finally shed light to the correlation between the chemical structure and the density of APA films. Moreover, new syntheses at same temperature but with different initial molar ratios of MPD:TMC are also expected. Such syntheses are interesting because they could establish a direct linkage to the current simulation work. The successful experimental characterizations of these films serve as the direct reference to compare or validate the conclusions obtained from the current simulation work. In addition, experimental measurements of water-polymer partition coefficients for several organic solutes are ongoing through batch experiments in the laboratory. The success of these analyses is expected to offer a useful comparison to the future simulation data.

Appendix

A1 Chemical composition of CPA2 active layer with assumption of different support natures

Table A1: Chemical composition of CPA2 active layer, corrected on basis of various assumptions of support types.

Support*		PSf	SPSf (1SO_3H)	SPSf (2SO_3H)	PES	SPES (1SO_3H)	SPES(2SO_3H)
		$C_{27}O_4H_{22}S$	$C_{27}O_7H_{22}S_2$	$C_{27}O_{10}H_{22}S_3$	$C_{12}O_3H_8S$	$C_{12}O_6H_8S_2$	$C_{12}O_9H_8S_3$
CPA2-ots	C%	72±0.8	73.1±0.8	73.4±0.6	73.1±0.6	73.5±0.6	73.7±0.5
	O%	17.0±0.9	16.5±1.0	16.3±0.8	16.5±0.8	16.2±0.8	16.1±0.8
	N%	10.9±0.5	10.5±0.6	10.3±0.5	10.4±0.5	10.2±0.5	10.2±0.5
CPA2-ts	C%	73.1±0.5	74.1±0.8	74.5±0.5	74.1±0.5	74.6±0.5	74.8±0.5
	O%	15.4±0.4	14.9±0.5	14.7±0.3	14.9±0.3	14.7±0.3	14.6±0.3
	N%	11.5±0.4	11.0±0.7	10.8±0.4	10.9±0.4	10.7±0.4	10.7±0.4
CPA2-bs	C%	70.3±0.4	72.6±0.4	73.3±0.2	72.7±0.2	73.7±0.2	74.0±0.2
	O%	15.0±0.4	14.0±0.7	13.7±0.4	14.1±0.4	13.6±0.3	13.4±0.3
	N%	14.7±0.4	13.4±0.6	13.0±0.3	13.2±0.3	12.7±0.3	12.6±0.3

*:PSf, SPEf, PES and SPES are abbreviations for polysulfone, sulfonated polysulfone, polyethersulfone and sulfonated polyethersulfone, respectively.

A2 N/O map plotting for experimental APA layer chemical composition data in the literature

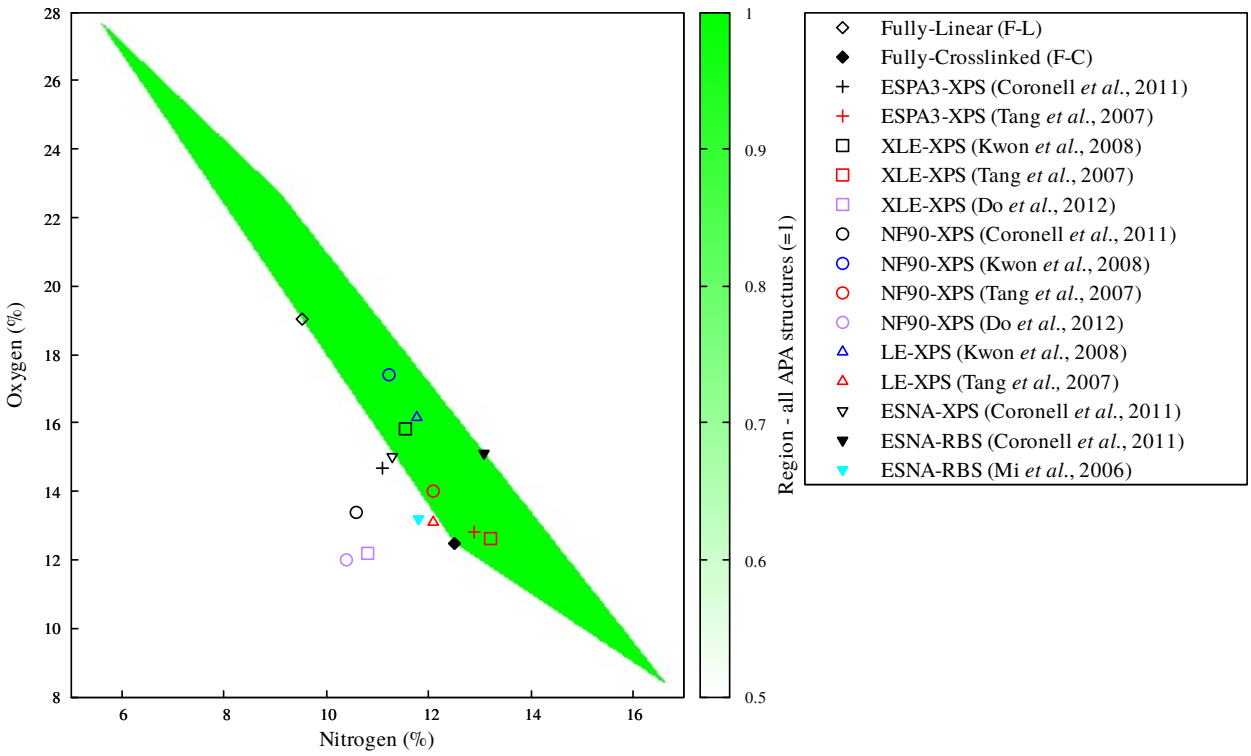

Figure A1: N/O map plotting for experimental chemical composition data of APA layers of RO/NF membranes in the literature[17, 24, 69, 83, 114].

A3 OPLS-AA force field parameter for APA molecular model

The OPLS-AA force field presented below are implemented with functional terms of LAMMMPS.

The Lennard-Jones (LJ) potential is expressed as :

$$U_{\text{Lennard-Jones}}(r_{ij}) = 4\varepsilon_{ij}[(\frac{\sigma_{ij}}{r_{ij}})^{12} - (\frac{\sigma_{ij}}{r_{ij}})^{6}]f_{ij} \tag{A1}$$

where r_{ij} is the distance between the two atoms i and j. r^{-6} is the attractive term while r^{-12} is the repulsive term. ε is the depth of the LJ potential well and σ is the distance at which the LJ potential is zero, for which the standard geometric combining rules are applied as:

$$\varepsilon_{ij} = (\varepsilon_i \varepsilon_j)^{\frac{1}{2}} \tag{A2}$$

$$\sigma_{ij} = (\sigma_i \sigma_j)^{\frac{1}{2}} \tag{A3}$$

The electrostatic (the Coulombic) interaction:

$$U_{\text{electrostatic}}(r_{ij}) = (\frac{q_i q_j e^2}{4\pi\epsilon_0 r_{ij}}) f_{ij} \tag{A4}$$

with q is the charge in electron charge unit, e is the charge of electron, r_{ij} is the distance between the charges on the two atoms, ϵ_0 is absolute dielectric permittivity of classical vacuum, and the ensemble $\frac{1}{4\pi\epsilon_0}$ is the Coulomb constant.

Table A2: Atom class, type, Lennard-Jones parameter and charge.

Atom class	Atom type	Molar mass (g/mol)	ε (kcal/mol)	σ (Å)	q (e)
C90	CA	12.0110	0.070	3.550	-0.1150
C176	C	12.011	0.105	3.750	0.6150
C208	CA	12.011	0.070	3.550	0.0850
C411	C	12.011	0.105	3.750	0.6350
C746	CA	12.0110	0.070	3.550	0.1800
N207	N	14.007	0.17	3.250	-0.3850
N730	NT	14.007	0.17	3.300	-0.9000
H91	HA	1.0080	0.030	2.420	0.1150
H183	H	1.0080	0.000	0.000	0.3000
H212	HO	1.008	0.000	0.000	0.4500
H739	H	1.0080	0.000	0.000	0.3600
O178	O	15.999	0.2100	2.960	-0.5000
O210	O	15.999	0.210	2.9600	-0.4400
O211	OH	15.999	0.1700	3.0000	-0.5300

The bond stretching energy:

$$U_{\text{bond}}(r_{ij}) = K_r(r_{ij} - r_{eq})^2 \tag{A5}$$

where K_r is the constant, r_{ij} is the bond length between atom i and j, r_{eq} represents the corresponding equilibrium bond length.

Table A3: Bond interaction.

Bond type	Bond style	r (Å)	K_r (kcal/mol/Å^2)
CA-CA	harmonic	1.4000	469.00
CA-HA	harmonic	1.0800	367.00
CA-NT	harmonic	1.3400	481.00
C-CA	harmonic	1.4900	400.00
C-O	harmonic	1.2290	570.00
C-OH	harmonic	1.3640	450.00
NT-H	harmonic	1.0100	434.00
HO-OH	harmonic	0.9450	553.00
CA-N	harmonic	1.3810	427.00
N-H	harmonic	1.0100	434.00
N-C	harmonic	1.3350	490.00

The angle bending energy:

$$U_{\text{angle}}(\theta_{ijk}) = K_\theta(\theta_{ijk} - \theta_{eq})^2 \tag{A6}$$

with K_θ is the constant, θ_{ijk} and θ_{eq} are respectively the angle among the atom i, j and k, and the corresponding equilibrium one.

Table A4: Angle interaction.

Angle type	Angle style	θ (deg)	K_θ (kcal/mol/deg^2)
CA-CA-CA	harmonic	120.0000	63.00
CA-CA-HA	harmonic	120.0000	35.00
CA-CA-C	harmonic	120.0000	85.00
CA-C-O	harmonic	120.4000	80.00
CA-C-OH	harmonic	120.0000	70.00
OH-C-O	harmonic	121.0000	80.00
HO-OH-C	harmonic	113.0000	35.00
H-NT-H	harmonic	106.4000	43.60
NT-CA-CA	harmonic	120.0000	70.00
H-NT-CA	harmonic	116.0000	35.00
CA-CA-N	harmonic	120.0000	70.00
CA-N-H	harmonic	119.8000	35.00
CA-N-C	harmonic	121.9000	50.00
H-N-C	harmonic	119.8000	35.00
N-C-O	harmonic	122.9000	80.00
N-C-CA	harmonic	115.5000	70.00

The torsion energy:

$$U_{\text{torsion}}(\beta_{ijkl}) = \sum_{n=0}^{8} a_n [cos(\beta_{ijkl})]^n \tag{A7}$$

where a_n are the constants and β_{ijkl} is the torsion angle.

Table A5: Torsion interaction.

Dihedral type	Dihedral style	$a0$ (kcal/mol)	$a1$ (kcal/mol)	$a2$ (kcal/mol)	$a3$ (kcal/mol)	$a4$ (kcal/mol)	$a5$(kcal/mol)	$a6$ (kcal/mol)	$a7$ (kcal/mol)	$a8$ (kcal/mol)
X-CA-CA-X	nharmonic	7.25	0.00	-7.25	0.00	0.00	0.00	0.00	0.00	0.00
H-NT-CA-CA	nharmonic	2.03	0.00	-2.03	0.00	0.00	0.00	0.00	0.00	0.00
HO-OH-C-O	nharmonic	5.00	0.00	-5.00	0.00	0.00	0.00	0.00	0.00	0.00
CA-CA-C-O/OH	nharmonic	2.1	0.00	-2.10	0.00	0.00	0.00	0.00	0.00	0.00
X-CA-CA-X	nharmonic	7.25	0.00	-7.25	0.00	0.00	0.00	0.00	0.00	0.00
CA-C-OH-HO	nharmonic	7.00	2.00	-5.00	0.00	0.00	0.00	0.00	0.00	0.00
X-CA-CA-X	nharmonic	7.25	0.00	-7.25	0.00	0.00	0.00	0.00	0.00	0.00
H-NT-CA-CA	nharmonic	2.03	0.00	-2.03	0.00	0.00	0.00	0.00	0.00	0.00
CA-CA-N-H/C	nharmonic	2.10	0.00	-2.10	0.00	0.00	0.00	0.00	0.00	0.00
CA-N-C-O	nharmonic	6.089	0.00	-6.089	0.00	0.00	0.00	0.00	0.00	0.00
CA-N-C-CA	nharmonic	7.239	1.15	-6.089	0.00	0.00	0.00	0.00	0.00	0.00
N-C-CA-CA	nharmonic	1.10	0.00	-1.10	0.00	0.00	0.00	0.00	0.00	0.00
H-N-C-O/CA	nharmonic	4.90	0.00	-4.90	0.00	0.00	0.00	0.00	0.00	0.00
CA-C-OH-HO	nharmonic	7.00	2.00	-5.00	0.00	0.00	0.00	0.00	0.00	0.00
HO-OH-C-O	nharmonic	5.00	0.00	-5.00	0.00	0.00	0.00	0.00	0.00	0.00

The improper torsion energy:

$$U_{\text{improper torsion}}(\phi_{ijkl}) = K_\phi[1 + dcos(n\phi_{ijkl})] \tag{A8}$$

with ϕ_{ijkl} is the improper torsion angle and K_ϕ is the constant.

Table A6: Improper dihedral interaction.

Improper type	Improper style	K_ϕ(kcal/mol)	d	n
CA/N-X-X-X	cvff	0.833333	-1	2
C-O-X-X	cvff	3.500000	-1	2

The standard geometric combining rules are applied:

$$\sigma_{ij} = (\sigma_i \sigma_j)^{\frac{1}{2}} \tag{A9}$$

$$\varepsilon_{ij} = (\varepsilon_i \varepsilon_j)^{\frac{1}{2}} \tag{A10}$$

These interactions are applied as well for intramolecular cases when the atoms are separated by at least three bonds as that: $f_{ij} = 0$ if i, j are 1, 2 or 1, 3; $f_{ij} = 0.5$ if i, j are 1,4; otherwise $f_{ij} = 1$. The pair cut distance was set at 10 Å.

A4 Intramolecular interaction parameter comparison between atom type NT and N

Table A7: Intramolecular interaction parameter comparison between atom type NT and N.

Atom type	ε (kcal/mol)	σ (Å)
NT	0.17	3.30
N	0.17	3.25

Bond type	K_r (kcal/mol/Å^2)	r(Å)
NT-H	434.00	1.01
N-H	434.00	1.01
NT-CA	481.00	1.34
N-CA	427.00	1.38

Angle type	K_θ (kcal/mol/deg^2)	θ (deg)
H-NT-CA	35.00	116.00
H-N-CA	35.00	119.80
NT-CA-CA	70.00	120.00
N-CA-CA	70.00	120.00

Dihedral type	a_0	a_1	a_2	a_3	a_4	a_5	a_6	a_7	a_8
H-NT-CA-CA	2.03	0	-2.03	0	0	0	0	0	0
H-N-CA-CA	2.10	0	-2.10	0	0	0	0	0	0

A5 Supplementary information on radial distribution function analysis

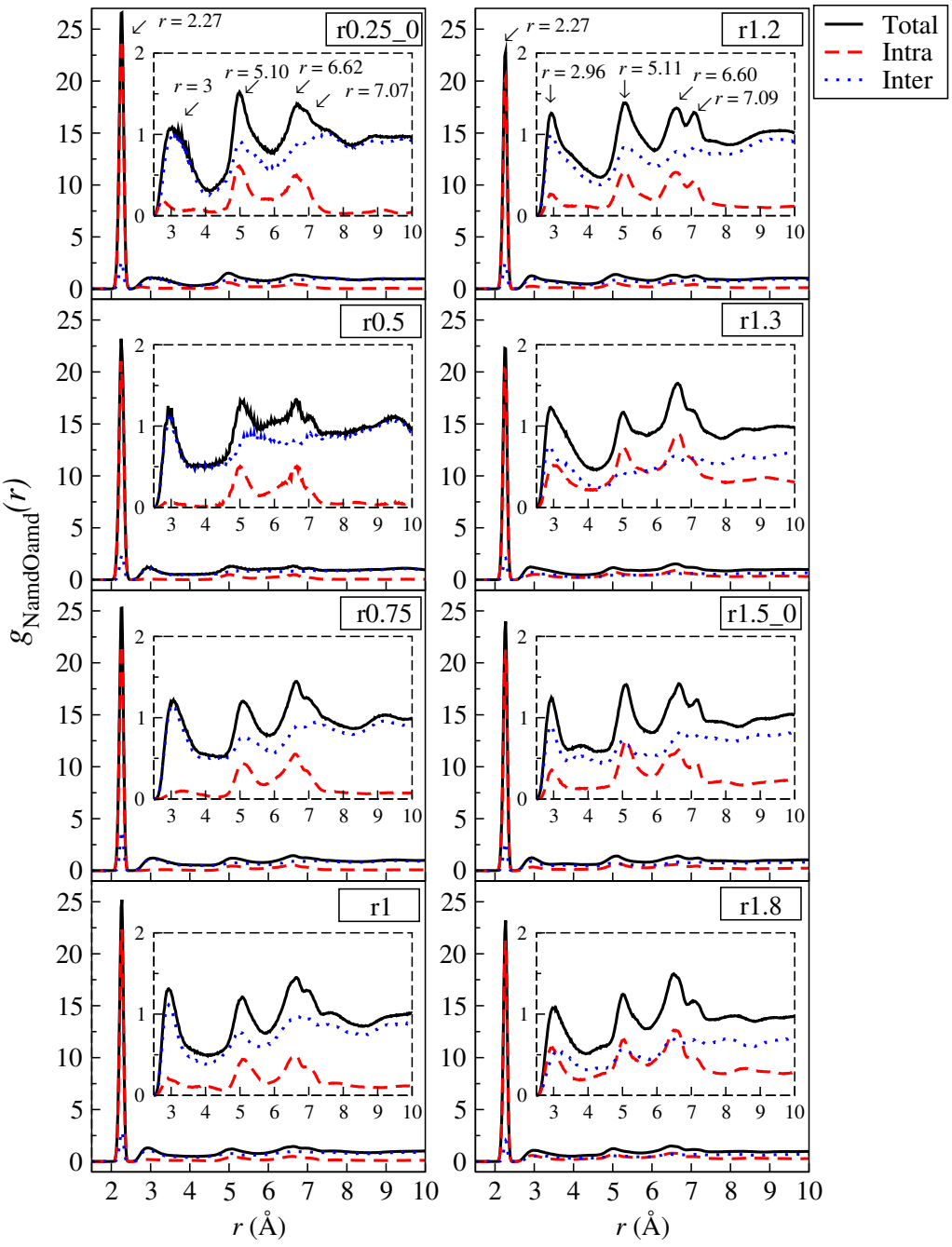

Figure A2: Radial distribution function (RDF) between nitrogen (Namd) and Oxygen atom (Oamd) in amide bond of polymer systems generated from different initial MPD:TMC ratios at 0.25, 0.5, 0.75, 1, 1.2, 1.3, 1.5 and 1.8.

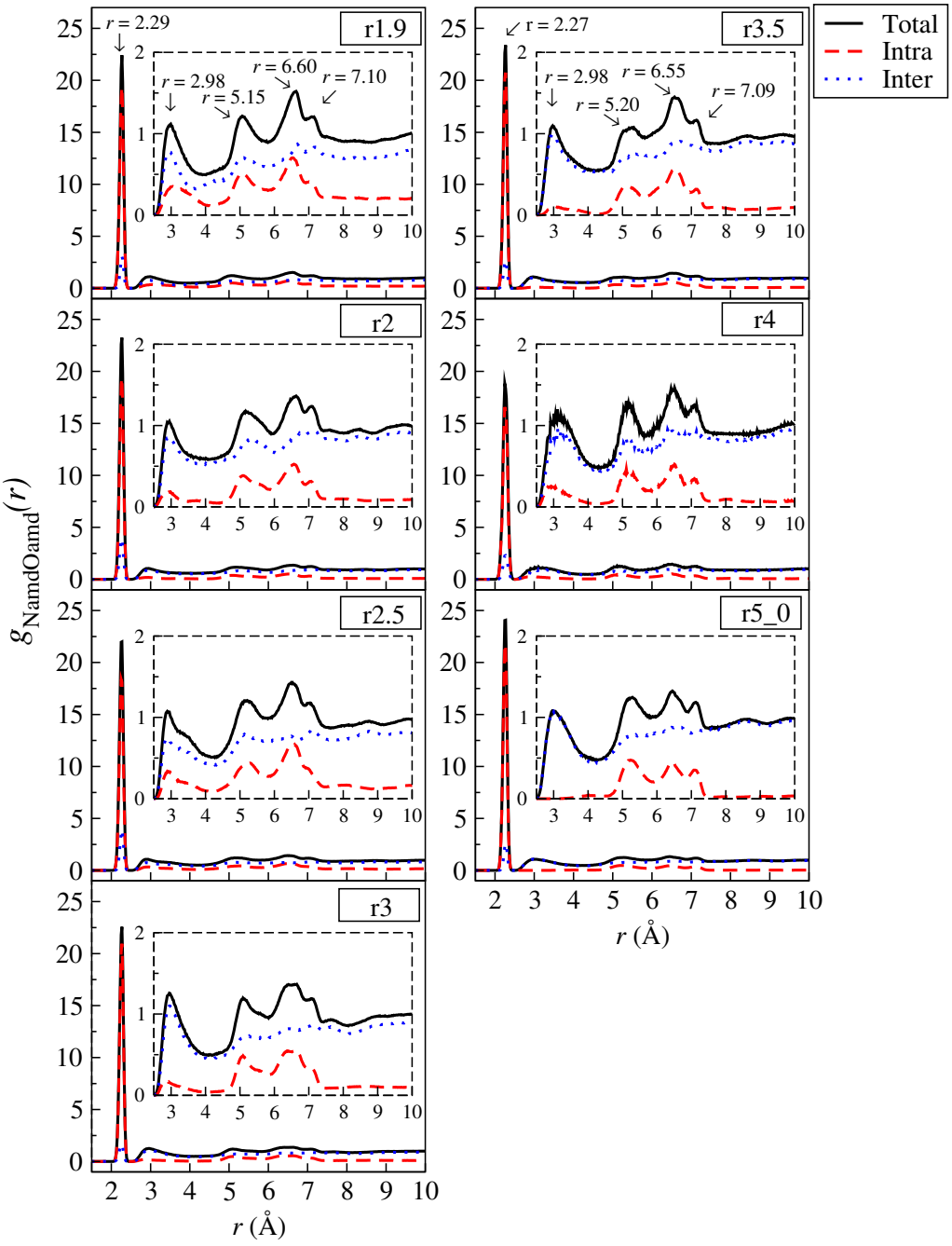

Figure A3: Radial distribution function (RDF) between nitrogen (Namd) and Oxygen atom (Oamd) in amide bond of polymer systems generated from different initial MPD:TMC ratios at 1.9, 2, 2.5, 3, 3.5, 4 and 5.

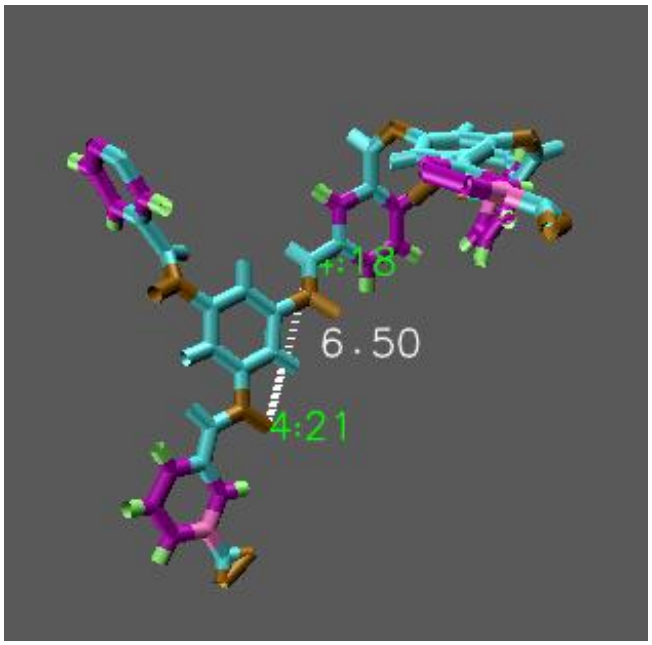

Figure A4: Distance between nitrogen (Namd) and Oxygen atom (Oamd) in closest neighboring amide bond in polymer system r1.5_1 (repetition box n°1).

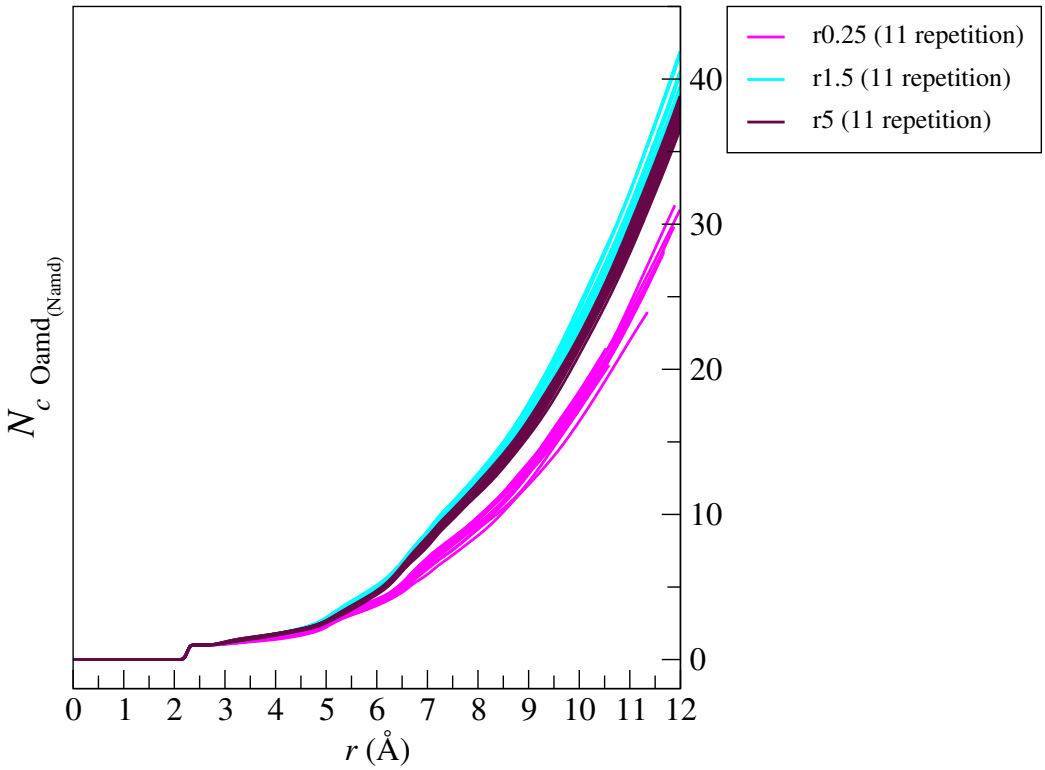

Figure A5: Coordination number of oxygen atom around nitrogen atom in amide bond of polymer systems generated from initial MPD:TMC ratio at 0.25, 1.5 and 5.

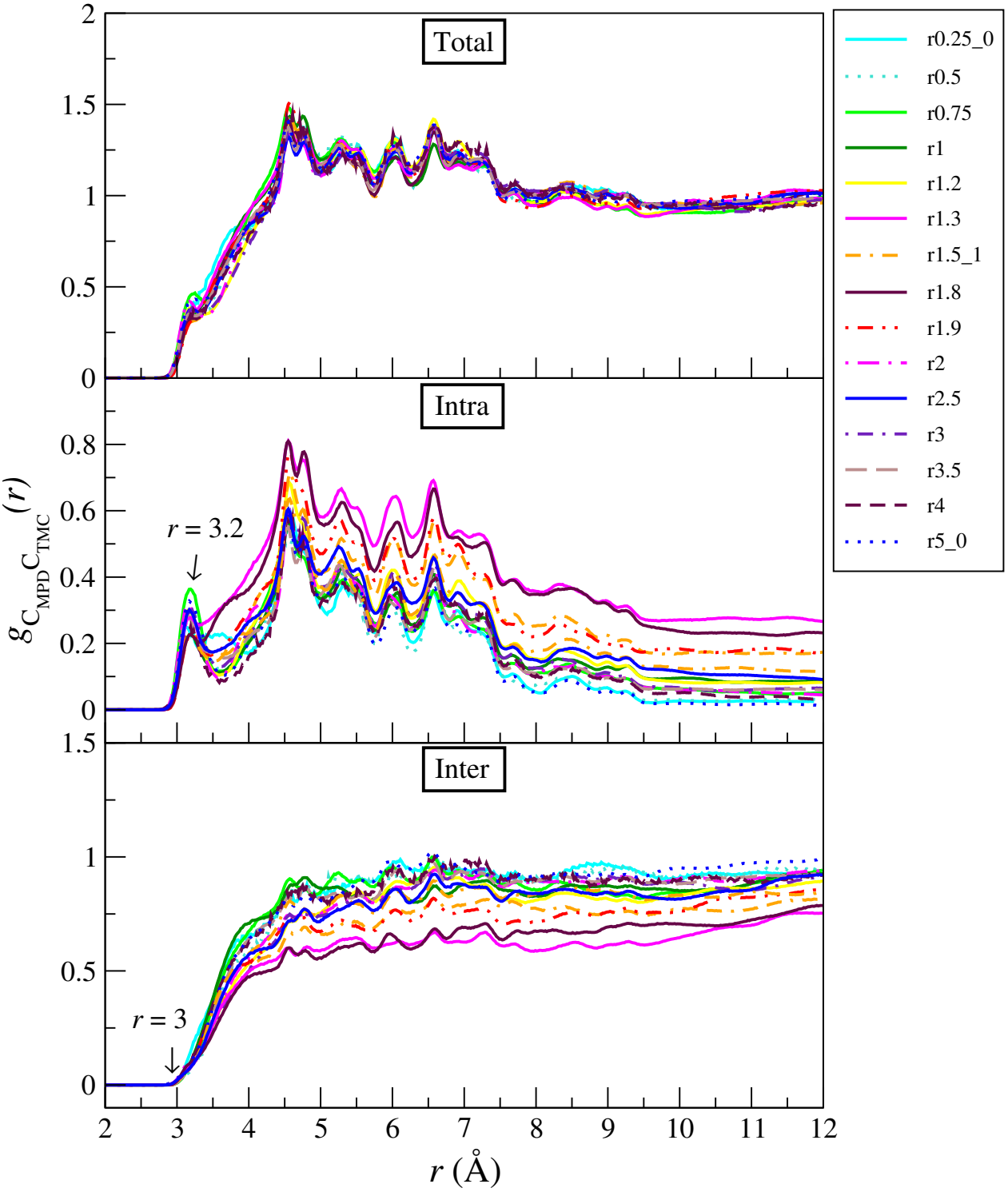

Figure A6: Radial distribution function (RDF) between carbon-carbon atom pair from benzene rings of polymer systems generated from initial MPD:TMC ratios.

A6 Schematic of water sorption measurement equipment

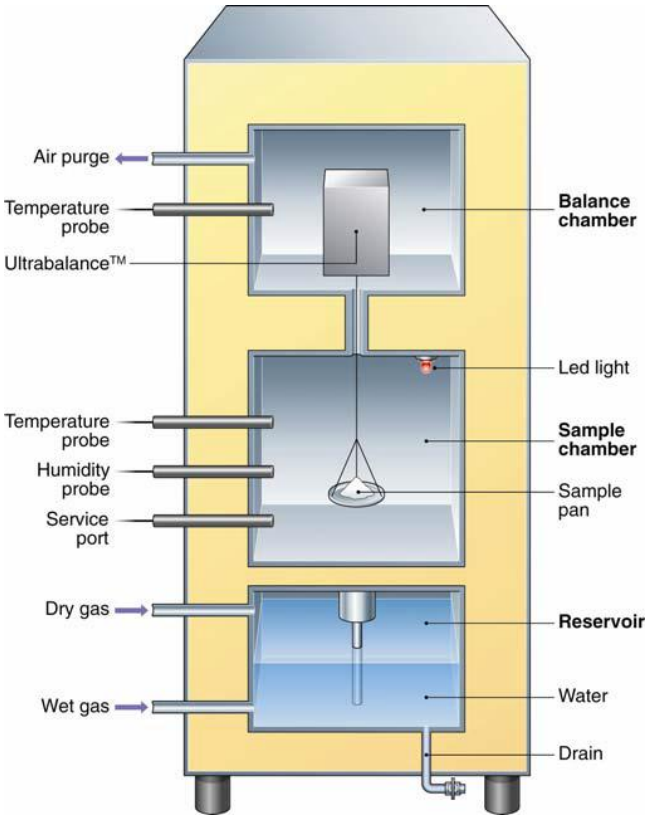

Figure A7: Schematic of water sorption measurement equipment, Dynamic vapor sorption device (DVS), from Surface Measurement Systems, (2004)[111].

Bibliography

[1] O. Akin and F. Temelli. Probing the hydrophobicity of commercial reverse osmosis membranes produced by interfacial polymerization using contact angle, XPS, FTIR, FE-SEM and AFM. *Desalination*, 278 (1-3):387–396, sep 2011. doi: 10.1016/j.desal.2011.05.053.

[2] N. M. Al-Bastaki. Performance of advanced methods for treatment of wastewater: UV/TiO2, RO and UF. *Chemical Engineering and Processing: Process Intensification*, 43(7):935–940, jul 2004. ISSN 02552701. doi: 10.1016/j.cep.2003.08.003.

[3] Z. Ali, Y. Al Sunbul, F. Pacheco, W. Ogieglo, Y. Wang, G. Genduso, and I. Pinnau. Defect-free highly selective polyamide thin-film composite membranes for desalination and boron removal. *Journal of Membrane Science*, 578:85–94, may 2019. doi: 10.1016/j.memsci.2019.02.032.

[4] H. C. Andersen. Molecular dynamics simulations at constant pressure and/or temperature. *The Journal of Chemical Physics*, 72(4):2384–2393, feb 1980. ISSN 0021-9606. doi: 10.1063/1.439486. URL `http://aip.scitation.org/doi/10.1063/1.439486`.

[5] R. B. Anderson. Modifications of the Brunauer, Emmett and Teller equation1. *Journal of the American Chemical Society*, 68(4):686–691, 1946. doi: 10.1021/ja01208a049. URL `https://pubs.acs.org/sharingguidelines`.

[6] T. Araki, R. Cruz-Silva, S. Tejima, K. Takeuchi, T. Hayashi, S. Inukai, T. Noguchi, A. Tanioka, T. Kawaguchi, M. Terrones, and M. Endo. Molecular Dynamics Study of Carbon Nanotubes/Polyamide Reverse Osmosis Membranes: Polymerization, Structure, and Hydration. *ACS Applied Materials & Interfaces*, 7(44):24566–24575, nov 2015. ISSN 1944-8244. doi: 10.1021/acsami.5b06248. URL `https://pubs.acs.org/doi/10.1021/acsami.5b06248`.

[7] R. W. Baker. Membrane technologies and applications. In *Membrane Technologies and Applications*, chapter 5 Reverse, page 201. 2011. ISBN 9781439805275. doi: 10.1201/b11416.

[8] A. Ben-David, S. Bason, J. Jopp, Y. Oren, and V. Freger. Partitioning of organic solutes between water and polyamide layer of RO and NF membranes: Correlation to rejection. *Journal of Membrane Science*, 281(1-2):480–490, 2006. ISSN 03767388. doi: 10.1016/j.memsci.2006.04.017.

[9] A. Ben-David, Y. Oren, and V. Freger. Thermodynamic factors in partitioning and rejection of organic compounds by polyamide composite membranes. *Environmental Science and Technology*, 40(22):7023–7028, 2006. ISSN 0013936X. doi: 10.1021/es0609912.

[10] H. J. C. Berendsen, J. P. M. Postma, W. F. van Gunsteren, A. DiNola, and J. R. Haak. Molecular dynamics with coupling to an external bath. *The Journal of Chemical Physics*, 81(8):3684–3690, oct 1984. ISSN 0021-9606. doi: 10.1063/1.448118. URL `http://aip.scitation.org/doi/10.1063/1.448118`.

[11] E. Bitzek, P. Koskinen, F. Gähler, M. Moseler, and P. Gumbsch. Structural Relaxation Made Simple. *Physical Review Letters*, 97(17):170201, oct 2006. ISSN 0031-9007. doi: 10.1103/PhysRevLett.97.170201. URL `https://link.aps.org/doi/10.1103/PhysRevLett.97.170201`.

[12] S. Brunauer, P. H. Emmett, and E. Teller. Adsorption of gases in multimolecular layers. *Journal of the American chemical society*, 60(2):309–319, 1938. doi: 10.1021/ja01269a023.

[13] J. E. Cadotte. Evolution of Composite Reverse Osmosis Membranes. In *Materials Science of Synthetic Membranes*, pages 273–294. dec 1985. doi: 10.1021/bk-1985-0269.ch012.

[14] J. E. Cadotte, R. J. Petersen, R. E. Larson, and E. E. Erickson. A new thin-film composite seawater reverse osmosis membrane. Technical report, 1980.

[15] G.-Y. Chai and W. B. Krantz. Formation and characterization of polyamide membranes via interfacial polymerization. *Journal of Membrane Science*, 93(2):175–192, 1994. doi: 10.1016/0376-7388(94)80006-5.

[16] O. Coronell, B. J. Mariñas, X. Zhang, and D. G. Cahill. Quantification of Functional Groups and Modeling of Their Ionization Behavior in the Active Layer of FT30 Reverse Osmosis Membrane. *Environmental Science & Technology*, 42(14):5260–5266, jul 2008. ISSN 0013-936X. doi: 10.1021/es8002712. URL `https://pubs.acs.org/doi/10.1021/es8002712`.

[17] O. Coronell, B. J. Mariñas, and D. G. Cahill. Depth heterogeneity of fully aromatic polyamide active layers in reverse osmosis and nanofiltration membranes. *Environmental Science and Technology*, 45(10):4513–4520, 2011. ISSN 0013936X. doi: 10.1021/es200007h.

[18] Y. Cui, X.-Y. Liu, and T.-S. Chung. Ultrathin Polyamide Membranes Fabricated from Free-Standing Interfacial Polymerization: Synthesis, Modifications, and Post-treatment. *Industrial & Engineering Chemistry Research*, 56(2):513–523, jan 2017. ISSN 15205045. doi: 10.1021/acs.iecr.6b04283.

[19] J. H. De Boer. *The dynamical character of adsorption*. Clarendon Press, Oxford, 2nd edition, 1968.

[20] J. M. Dennison, X. Xie, C. J. Murphy, and D. G. Cahill. Density, Elastic Constants, and Thermal Conductivity of Interfacially Polymerized Polyamide Films for Reverse Osmosis Membranes. *ACS Applied Nano Materials*, 1(9):5008–5018, sep 2018. ISSN 25740970. doi: 10.1021/acsanm.8b01129.

[21] M. Ding, A. Ghoufi, and A. Szymczyk. Molecular simulations of polyamide reverse osmosis membranes. *Desalination*, 343:48–53, jun 2014. doi: 10.1016/j.desal.2013.09.024. URL `https://linkinghub.elsevier.com/retrieve/pii/S0011916413004566`.

[22] M. Ding, A. Szymczyk, F. Goujon, A. Soldera, and A. Ghoufi. Structure and dynamics of water confined in a polyamide reverse-osmosis membrane: A molecular-simulation study. *Journal of Membrane Science*, 458:236–244, 2014. ISSN 03767388. doi: 10.1016/j.memsci.2014.01.054.

[23] M. Ding, A. Szymczyk, and A. Ghoufi. Hydration of a polyamide reverse-osmosis membrane. *Journal of Membrane Science*, 501:248–253, 2016. doi: 10.1016/j.memsci.2015.12.036.

[24] V. T. Do, C. Y. Tang, M. Reinhard, and J. O. Leckie. Degradation of polyamide nanofiltration and reverse osmosis membranes by hypochlorite. *Environmental Science and Technology*, 46(2):852–859, jan 2012. ISSN 0013936X. doi: 10.1021/es203090y.

[25] E. Dražević, K. Košutić, and V. Freger. Permeability and selectivity of reverse osmosis membranes: Correlation to swelling revisited. *Water Research*, 49:444–452, 2014. ISSN 18792448. doi: 10.1016/j.watres.2013.10.029.

[26] D. Dutta, A. Bhattacharyya, and B. N. Ganguly. Microstructural study of aromatic polyamide membrane material. *Journal of Membrane Science*, 224(1-2):127–135, oct 2003. ISSN 03767388. doi: 10.1016/j.memsci.2003.08.001.

[27] D. Dutta, A. Bhattacharyya, and B. N. Ganguly. Microstructural study of aromatic polyamide membrane material. *Journal of Membrane Science*, 224(1-2):127–135, 2003. ISSN 03767388. doi: 10.1016/j.memsci.2003.08.001.

[28] A. Ettori. *Vieillissement chimique de membranes d'osmose inverse*. PhD thesis, Université Toulouse III - Paul Sabatier, Toulouse, 2011.

[29] P. P. Ewald. Die Berechnung optischer und elektrostatischer Gitterpotentiale. *Annalen der Physik*, 369 (3):253–287, 1921. ISSN 00033804. doi: 10.1002/andp.19213690304. URL `http://doi.wiley.com/10.1002/andp.19213690304`.

[30] C. Fargues, C. Sagne, A. Szymczyk, P. Fievet, and M. L. Lameloise. Adsorption of small organic solutes from beet distillery condensates on reverse-osmosis membranes: Consequences on the process performances. *Journal of Membrane Science*, 446:132–144, 2013. ISSN 03767388. doi: 10.1016/j.memsci.2013.05.051.

[31] M. N. Fini, H. T. Madsen, and J. Muff. The effect of water matrix, feed concentration and recovery on the rejection of pesticides using NF/RO membranes in water treatment. *Separation and Purification Technology*, 215:521–527, may 2019. ISSN 18733794. doi: 10.1016/j.seppur.2019.01.047.

[32] F. Foglia, S. Karan, M. Nania, Z. Jiang, A. E. Porter, R. Barker, A. G. Livingston, and J. T. Cabral. Neutron Reflectivity and Performance of Polyamide Nanofilms for Water Desalination. *Advanced Functional Materials*, 27(37):1701738, oct 2017. ISSN 1616301X. doi: 10.1002/adfm.201701738.

[33] V. Freger. Nanoscale Heterogeneity of Polyamide Membranes Formedby Interfacial Polymerization. *Langmuir*, 19(11):4791–4797, 2003. ISSN 07437463. doi: 10.1021/la020920q.

[34] V. Freger. Swelling and morphology of the skin layer of polyamide composite membranes: An atomic force microscopy study. *Environmental Science and Technology*, 38(11):3168–3175, 2004. ISSN 0013936X. doi: 10.1021/es034815u.

[35] V. Freger and S. Srebnik. Mathematical model of charge and density distributions in interfacial polymerization of thin films. *Journal of Applied Polymer Science*, 88(5):1162–1169, may 2003. ISSN 00218995. doi: 10.1002/app.11716.

[36] V. Freger, J. Gilron, and S. Belfer. TFC polyamide membranes modified by grafting of hydrophilic polymers: An FT-IR/AFM/TEM study. *Journal of Membrane Science*, 209(1):283–292, 2002. ISSN 03767388. doi: 10.1016/S0376-7388(02)00356-3.

[37] I. Frenzel, D. F. Stamatialis, and M. Wessling. Water recycling from mixed chromic acid waste effluents by membrane technology. *Separation and Purification Technology*, 49(1):76–83, apr 2006. ISSN 13835866. doi: 10.1016/j.seppur.2005.08.010.

[38] L. M. Fry, J. R. Mihelcic, and D. W. Watkins. Water and nonwater-related challenges of achieving global sanitation coverage. *Environmental Science and Technology*, 42(12):4298–4304, jun 2008. ISSN 0013936X. doi: 10.1021/es7025856.

[39] J.-G. Gai, X.-L. Gong, W.-L. Kang, X. Zhang, and W.-W. Wang. Key factors influencing water diffusion in aromatic PA membrane: Hydrates, nanochannels and functional groups. *Desalination*, 333(1):52–58, jan 2014. doi: 10.1016/j.desal.2013.11.028.

[40] J.-G. Gai, X.-L. Gong, X. Zhang, W.-L. Kang, and W.-W. Wang. Key role of hydrates in determining ion rejection by polyamide membrane. *Polymer Engineering & Science*, 55(2):466–473, feb 2015. doi: 10.1002/pen.23882.

[41] A. K. Ghosh and E. M. Hoek. Impacts of support membrane structure and chemistry on polyamide-polysulfone interfacial composite membranes. *Journal of Membrane Science*, 336(1-2):140–148, 2009. doi: 10.1016/j.memsci.2009.03.024.

[42] A. K. Ghosh, B. H. Jeong, X. Huang, and E. M. Hoek. Impacts of reaction and curing conditions on polyamide composite reverse osmosis membrane properties. *Journal of Membrane Science*, 311(1-2):34–45, 2008. ISSN 03767388. doi: 10.1016/j.memsci.2007.11.038.

[43] A. K. Ghosh, B.-H. Jeong, X. Huang, and E. M. Hoek. Impacts of reaction and curing conditions on polyamide composite reverse osmosis membrane properties. *Journal of Membrane Science*, 311(1-2):34–45, mar 2008. ISSN 03767388. doi: 10.1016/j.memsci.2007.11.038.

[44] A. Ghoufi, E. Dražević, and A. Szymczyk. Interactions of organics within hydrated selective layer of reverse osmosis desalination membrane: A combined experimental and computational study. *Environmental Science & Technology*, 51(5):2714–2719, mar 2017. doi: 10.1021/acs.est.6b05153.

[45] L. Greenspan. Humidity fixed points of binary saturated aqueous solutions. *Journal of research of the national bureau of standards*, 81A(1):89–96, 1977. ISSN 0022-4332. doi: 10.6028/jres.081A.011.

[46] E. A. Guggenheim. *Applications of statistical mechanics*. Clarendon Press, Oxford, 1966.

[47] E. Harder, D. E. Walters, Y. D. Bodnar, R. S. Faibish, and B. Roux. Molecular dynamics study of a polymeric reverse osmosis membrane. *Journal of Physical Chemistry B*, 113(30):10177–10182, 2009. ISSN 15206106. doi: 10.1021/jp902715f.

[48] S. Hermans, R. Bernstein, A. Volodin, and I. F. Vankelecom. Study of synthesis parameters and active layer morphology of interfacially polymerized polyamide-polysulfone membranes. *Reactive and Functional Polymers*, 86:199–208, 2015. ISSN 13815148. doi: 10.1016/j.reactfunctpolym.2014.09.013.

[49] J. Hoinkis and V. Panten. Wastewater recycling in laundries-From pilot to large-scale plant. *Chemical Engineering and Processing: Process Intensification*, 47(7):1159–1164, jul 2008. ISSN 02552701. doi: 10.1016/j.cep.2007.12.010.

[50] W. G. Hoover. Canonical dynamics: Equilibrium phase-space distributions. *Physical Review A*, 31(3): 1695–1697, mar 1985. ISSN 0556-2791. doi: 10.1103/PhysRevA.31.1695. URL `https://link.aps.org/doi/10.1103/PhysRevA.31.1695`.

[51] L. Huang and J. R. McCutcheon. Impact of support layer pore size on performance of thin film composite membranes for forward osmosis. *Journal of Membrane Science*, 483:25–33, 2015. ISSN 18733123. doi: 10.1016/j.memsci.2015.01.025.

[52] Z. E. Hughes and J. D. Gale. A computational investigation of the properties of a reverse osmosis membrane. *Journal of Materials Chemistry*, 20(36):7788–7799, sep 2010. ISSN 09599428. doi: 10.1039/c0jm01545h.

[53] Z. E. Hughes and J. D. Gale. Molecular dynamics simulations of the interactions of potential foulant molecules and a reverse osmosis membrane. *Journal of Materials Chemistry*, 22(1):175–184, 2012. ISSN 09599428. doi: 10.1039/c1jm13230j.

[54] L. Janssen and K. Te Nijenhuls. Encapsulation by interfacial polycondensation. I. The capsule production and a model for wall growth. *Journal of Membrane Sctence*, 65(1-2):59–68, 1992. doi: https://doi.org/10.1016/0376-7388(92)87053-Z.

[55] Z. Jiang, S. Karan, and A. G. Livingston. Water Transport through Ultrathin Polyamide Nanofilms Used for Reverse Osmosis. *Advanced Materials*, 30(15):1705973, apr 2018. doi: 10.1002/adma.201705973.

[56] Y. Jin and Z. Su. Effects of polymerization conditions on hydrophilic groups in aromatic polyamide thin films. *Journal of Membrane Science*, 330(1-2):175–179, mar 2009. ISSN 03767388. doi: 10.1016/j.memsci.2008.12.055.

[57] W. L. Jorgensen, J. Chandrasekhar, J. D. Madura, R. W. Impey, and M. L. Klein. Comparison of simple potential functions for simulating liquid water. *The Journal of Chemical Physics*, 79(2):926–935, 1983. ISSN 00219606. doi: 10.1063/1.445869.

[58] W. L. Jorgensen, D. S. Maxwell, and J. Tirado-Rives. Development and Testing of the OPLS All-Atom Force Field on Conformational Energetics and Properties of Organic Liquids. *Journal of the American Chemical Society*, 118(45):11225–11236, jan 1996. ISSN 0002-7863. doi: 10.1021/ja9621760. URL `https://pubs.acs.org/doi/10.1021/ja9621760`.

[59] S. Karan, Z. Jiang, and A. G. Livingston. Sub-10 nm polyamide nanofilms with ultrafast solvent transport for molecular separation. *Science*, 348(6241):1347–1351, jun 2015. ISSN 0036-8075. doi: 10.1126/science.aaa5058. URL `https://www.sciencemag.org/lookup/doi/10.1126/science.aaa5058`.

[60] M. Karthik, J. M. Gohil, and A. K. Suresh. Probing the thickness and roughness of the functional layer in thin film composite membranes. *International Journal of Hydrogen Energy*, 42(42):26464–26474, 2017. doi: 10.1016/j.ijhydene.2017.07.145.

[61] B. Khorshidi, T. Thundat, B. A. Fleck, and M. Sadrzadeh. Thin film composite polyamide membranes: parametric study on the influence of synthesis conditions. *RSC Advances*, 5(68):54985–54997, 2015. ISSN 2046-2069. doi: 10.1039/C5RA08317F. URL `http://xlink.rsc.org/?DOI=C5RA08317F`.

[62] B. Khorshidi, T. Thundat, B. A. Fleck, and M. Sadrzadeh. A Novel Approach Toward Fabrication of High Performance Thin Film Composite Polyamide Membranes. *Scientific Reports*, 6(1):22069, apr 2016. ISSN 2045-2322. doi: 10.1038/srep22069. URL `http://www.nature.com/articles/srep22069`.

[63] S. H. Kim, S.-Y. Kwak, and T. Suzuki. Positron Annihilation Spectroscopic Evidence to Demonstrate the Flux-Enhancement Mechanism in Morphology-Controlled Thin-Film-Composite (TFC) Membrane. *Environmental Science & Technology*, 39(6):1764–1770, mar 2005. ISSN 0013-936X. doi: 10.1021/es049453k. URL `https://pubs.acs.org/doi/10.1021/es049453k`.

[64] V. Kolev and V. Freger. Hydration, porosity and water dynamics in the polyamide layer of reverse osmosis membranes: A molecular dynamics study. *Polymer*, 55(6):1420–1426, 2014. ISSN 00323861. doi: 10.1016/j.polymer.2013.12.045.

[65] V. Kolev and V. Freger. Molecular Dynamics Investigation of Ion Sorption and Permeation in Desalination Membranes. *The Journal of Physical Chemistry B*, 119(44):14168–14179, oct 2015. ISSN 15205207. doi: 10.1021/acs.jpcb.5b06566.

[66] M. J. Kotelyanskii, N. J. Wagner, and M. E. Paulaitis. Atomistic simulation of water and salt transport in the reverse osmosis membrane FT-30. *Journal of Membrane Science*, 139(1):1–16, 1998. ISSN 03767388. doi: 10.1016/S0376-7388(97)00220-2.

[67] S.-Y. Kwak and D. W. Ihm. Use of atomic force microscopy and solid-state NMR spectroscopy to characterize structure-property-performance correlation in high-flux reverse osmosis (RO) membranes. *Journal of Membrane Science*, 158(1-2):143–153, jun 1999. ISSN 03767388. doi: 10.1016/S0376-7388(99)00039-3. URL `https://linkinghub.elsevier.com/retrieve/pii/S0376738899000393`.

[68] S.-Y. Kwak, S. G. Jung, and S. H. Kim. Structure-Motion-Performance Relationship of Flux-Enhanced Reverse Osmosis (RO) Membranes Composed of Aromatic Polyamide Thin Films. *Environmental Science & Technology*, 35(21):4334–4340, nov 2001. ISSN 0013-936X. doi: 10.1021/es010630g. URL `https://pubs.acs.org/doi/10.1021/es010630g`.

[69] Y.-N. Kwon, C. Y. Tang, and J. O. Leckie. Change of chemical composition and hydrogen bonding behavior due to chlorination of crosslinked polyamide membranes. *Journal of Applied Polymer Science*, 108(4):2061–2066, may 2008. doi: 10.1002/app.25657.

[70] J. Lee, C. M. Doherty, A. J. Hill, and S. E. Kentish. Water vapor sorption and free volume in the aromatic polyamide layer of reverse osmosis membranes. *Journal of Membrane Science*, 425-426:217–226, jan 2013. ISSN 03767388. doi: 10.1016/j.memsci.2012.08.054. URL `https://linkinghub.elsevier.com/retrieve/pii/S0376738812006746`.

[71] J. Lee, A. Hill, and S. Kentish. Formation of a thick aromatic polyamide membrane by interfacial polymerisation. *Separation and Purification Technology*, 104:276–283, 2013. doi: 10.1016/j.seppur.2012.11.015.

[72] C. Li, Y. Yang, Y. Liu, and L.-a. Hou. Removal of PhACs and their impacts on membrane fouling in NF/RO membrane filtration of various matrices. *Journal of Membrane Science*, 548:439–448, feb 2018. ISSN 18733123. doi: 10.1016/j.memsci.2017.11.032.

[73] K. P. Licona, L. R. O. Geaquinto, J. V. Nicolini, N. G. Figueiredo, S. C. Chiapetta, A. C. Habert, and L. Yokoyama. Assessing potential of nanofiltration and reverse osmosis for removal of toxic pharmaceuticals

from water. *Journal of Water Process Engineering*, 25:195–204, oct 2018. ISSN 22147144. doi: 10.1016/j.jwpe.2018.08.002.

[74] L. Lin, C. Feng, R. Lopez, and O. Coronell. Identifying facile and accurate methods to measure the thickness of the active layers of thin-film composite membranes - A comparison of seven characterization techniques. *Journal of Membrane Science*, 498:167–179, 2016. ISSN 18733123. doi: 10.1016/j.memsci.2015.09.059.

[75] L. Lin, R. Lopez, G. Z. Ramon, and O. Coronell. Investigating the void structure of the polyamide active layers of thin-film composite membranes. *Journal of Membrane Science*, 497:365–376, 2016. ISSN 18733123. doi: 10.1016/j.memsci.2015.09.020.

[76] Y.-l. Liu, X.-m. Wang, H.-w. Yang, and Y. F. Xie. Quantifying the influence of solute-membrane interactions on adsorption and rejection of pharmaceuticals by NF/RO membranes. *Journal of Membrane Science*, 551:37–46, apr 2018. ISSN 18733123. doi: 10.1016/j.memsci.2018.01.035.

[77] J. L. Lundberg. Clustering Theory and Vapor Sorption by High Polymers. *Journal of Macromolecular Science, Part B: Physics*, 3(4):693–710, 1969. doi: 10.1080/00222346908217114.

[78] Y. Luo, E. Harder, R. S. Faibish, and B. Roux. Computer simulations of water flux and salt permeability of the reverse osmosis FT-30 aromatic polyamide membrane. *Journal of Membrane Science*, 384(1-2):1–9, 2011. ISSN 03767388. doi: 10.1016/j.memsci.2011.08.057.

[79] H. T. Madsen and E. G. Søgaard. Applicability and modelling of nanofiltration and reverse osmosis for remediation of groundwater polluted with pesticides and pesticide transformation products. *Separation and Purification Technology*, 125:111–119, apr 2014. ISSN 13835866. doi: 10.1016/j.seppur.2014.01.038.

[80] S. H. Maruf, D. U. Ahn, A. R. Greenberg, and Y. Ding. Glass transition behaviors of interfacially polymerized polyamide barrier layers on thin film composite membranes via nano-thermal analysis. *Polymer*, 52(12):2643–2649, may 2011. ISSN 00323861. doi: 10.1016/j.polymer.2011.04.022. URL `https://linkinghub.elsevier.com/retrieve/pii/S003238611100303X`.

[81] M. M. Mekonnen and A. Y. Hoekstra. Four billion people facing severe water scarcity. *Science Advances*, 2(2), feb 2016. doi: 10.1126/sciadv.1500323.

[82] N. Metropolis, A. W. Rosenbluth, M. N. Rosenbluth, A. H. Teller, and E. Teller. Equation of state calculations by fast computing machines. *The Journal of Chemical Physics*, 21(6):1087–1092, 1953. ISSN 00219606. doi: 10.1063/1.1699114.

[83] B. Mi, O. Coronell, B. J. Mariñas, F. Watanabe, D. G. Cahill, and I. Petrov. Physico-chemical characterization of NF/RO membrane active layers by Rutherford backscattering spectrometry. *Journal of Membrane Science*, 282(1-2):71–81, 2006. ISSN 03767388. doi: 10.1016/j.memsci.2006.05.015.

[84] B. Mi, D. G. Cahill, and B. J. Mariñas. Physico-chemical integrity of nanofiltration/reverse osmosis membranes during characterization by Rutherford backscattering spectrometry. *Journal of Membrane Science*, 291(1-2):77–85, 2007. ISSN 03767388. doi: 10.1016/j.memsci.2006.12.052.

[85] P. W. Morgan and S. L. Kwolek. Interfacial polycondensation. II. Fundamentals of polymer formation at liquid interfaces. *Journal of Polymer Science*, 40(137):299–327, 1959. doi: 10.1002/pol.1959.1204013702.

[86] J. Muscatello, E. Müller, A. Mostofi, and A. Sutton. Multiscale molecular simulations of the formation and structure of polyamide membranes created by interfacial polymerization. *Journal of Membrane Science*, 527:180–190, apr 2017. ISSN 03767388. doi: 10.1016/j.memsci.2016.11.024. URL `https://linkinghub.elsevier.com/retrieve/pii/S0376738816314909`.

[87] R. Nadler and S. Srebnik. Molecular simulation of polyamide synthesis by interfacial polymerization. *Journal of Membrane Science*, 315(1-2):100–105, may 2008. ISSN 03767388. doi: 10.1016/j.memsci.2008.02.023. URL `https://linkinghub.elsevier.com/retrieve/pii/S0376738808001269`.

[88] S. Naudy, F. Collette, F. Thominette, G. Gebel, and E. Espuche. Influence of hygrothermal aging on the gas and water transport properties of Nafion® membranes. *Journal of Membrane Science*, 451:293–304, feb 2014. ISSN 03767388. doi: 10.1016/j.memsci.2013.10.013.

[89] S. Nosé. A molecular dynamics method for simulations in the canonical ensemble. *Molecular Physics*, 52(2):255–268, jun 1984. ISSN 0026-8976. doi: 10.1080/00268978400101201. URL `http://www.tandfonline.com/doi/abs/10.1080/00268978400101201`.

[90] T. A. Orofino, H. B. Hopfenberg, and V. Stannett. Characterization of Penetrant Clustering in Polymers. *Journal of Macromolecular Science, Part B: Physics*, 3(4):777–788, dec 1969. ISSN 1525609X. doi: 10.1080/00222346908217120.

[91] F. Pacheco, R. Sougrat, M. Reinhard, J. O. Leckie, and I. Pinnau. 3D visualization of the internal nanostructure of polyamide thin films in RO membranes. *Journal of Membrane Science*, 501:33–44, 2016. ISSN 18733123. doi: 10.1016/j.memsci.2015.10.061.

[92] F. A. Pacheco, I. Pinnau, M. Reinhard, and J. O. Leckie. Characterization of isolated polyamide thin films of RO and NF membranes using novel TEM techniques. *Journal of Membrane Science*, 358(1-2):51–59, 2010. doi: 10.1016/j.memsci.2010.04.032.

[93] H. M. Park, K. Y. Jee, and Y. T. Lee. Preparation and characterization of a thin-film composite reverse osmosis membrane using a polysulfone membrane including metal-organic frameworks. *Journal of Membrane Science*, 541:510–518, 2017. doi: 10.1016/j.memsci.2017.07.034.

[94] S.-J. Park, W.-G. Ahn, W. Choi, S.-H. Park, J. S. Lee, H. W. Jung, and J.-H. Lee. A facile and scalable fabrication method for thin film composite reverse osmosis membranes: dual-layer slot coating. *Journal of Materials Chemistry A*, 5(14):6648–6655, 2017. ISSN 20507496. doi: 10.1039/c7ta00891k.

[95] S.-J. Park, W. Choi, S.-E. Nam, S. Hong, J. S. Lee, and J.-H. Lee. Fabrication of polyamide thin film composite reverse osmosis membranes via support-free interfacial polymerization. *Journal of Membrane Science*, 526:52–59, 2017. ISSN 18733123. doi: 10.1016/j.memsci.2016.12.027.

[96] R. J. Petersen. Composite reverse osmosis and nanofiltration membranes. *Journal of Membrane Science*, 83 (1):81–150, aug 1993. ISSN 03767388. doi: 10.1016/0376-7388(93)80014-O. URL `https://linkinghub.elsevier.com/retrieve/pii/037673889380014O`.

[97] E. Polak and G. Ribiere. Note sur la convergence de méthodes de directions conjuguées. *Revue Française d'Informatique et de Recherche Opérationnelle*, 3(R1):35–43, 1969. URL `http://www.numdam.org/conditions`.

[98] S. Qiu, L. Wu, L. Zhang, H. Chen, and C. Gao. Preparation of reverse osmosis composite membrane with high flux by interfacial polymerization of MPD and TMC. *Journal of applied polymer science*, 112(4): 2066–2072, may 2009. doi: 10.1002/app.29639.

[99] H. F. Ridgway, J. Orbell, and S. Gray. Molecular simulations of polyamide membrane materials used in desalination and water reuse applications: Recent developments and future prospects. *Journal of Membrane Science*, 524:436–448, feb 2017. ISSN 03767388. doi: 10.1016/j.memsci.2016.11.061. URL `https://linkinghub.elsevier.com/retrieve/pii/S0376738816318798`.

[100] I. J. Roh and V. P. Khare. Investigation of the specific role of chemical structure on the material and permeation properties of ultrathin aromatic polyamides. *Journal of Materials Chemistry*, 12(8):2334–2338, aug 2002. ISSN 09599428. doi: 10.1039/b109790c.

[101] I. J. Roh, A. R. Greenberg, and V. P. Khare. Synthesis and characterization of interfacially polymerized polyamide thin films. *Desalination*, 191(1-3):279–290, may 2006. ISSN 00119164. doi: 10.1016/j.desal.2006.03.004.

[102] C. Sagne, C. Fargues, R. Lewandowski, M. L. Lameloise, M. Gavach, and M. Decloux. A pilot scale study of reverse osmosis for the purification of condensate arising from distillery stillage concentration plant. *Chemical Engineering and Processing: Process Intensification*, 49(4):331–339, 2010. ISSN 02552701. doi: 10.1016/j.cep.2010.03.002.

[103] M. Shen, S. Keten, and R. M. Lueptow. Dynamics of water and solute transport in polymeric reverse osmosis membranes via molecular dynamics simulations. *Journal of Membrane Science*, 506:95–108, may

2016. ISSN 03767388. doi: 10.1016/j.memsci.2016.01.051. URL https://linkinghub.elsevier.com/retrieve/pii/S0376738816300527.

[104] S. S. Shenvi, A. M. Isloor, and A. F. Ismail. A review on RO membrane technology: Developments and challenges. *Desalination*, 368:10–26, jul 2015. ISSN 00119164. doi: 10.1016/j.desal.2014.12.042.

[105] M. Shi, Z. Wang, S. Zhao, J. Wang, P. Zhang, and X. Cao. A novel pathway for high performance RO membrane: Preparing active layer with decreased thickness and enhanced compactness by incorporating tannic acid into the support. *Journal of Membrane Science*, 555:157–168, 2018. ISSN 18733123. doi: 10.1016/j.memsci.2018.03.025.

[106] K. S. W. Sing, D. H. Everett, R. A. W. Haul, L. Moscou, R. A. Pierotti, J. Rouquérol, and T. Siemieniewska. Reporting physisorption data for gas/solid systems with special reference to the determination of surface area and porosity (Recommendations 1984). *Pure and applied chemistry*, 57(4):603–619, 1985. doi: 10.1351/pac198557040603.

[107] P. Singh, A. Rao, P. Ray, A. Bhattacharya, K. Singh, N. Saha, and A. Reddy. Techniques for characterization of polyamide thin film composite membranes. *Desalination*, 282:78–86, nov 2011. doi: 10.1016/j.desal.2011.04.039.

[108] P. S. Singh, S. V. Joshi, J. J. Trivedi, C. V. Devmurari, A. P. Rao, and P. K. Ghosh. Probing the structural variations of thin film composite RO membranes obtained by coating polyamide over polysulfone membranes of different pore dimensions. *Journal of Membrane Science*, 278(1-2):19–25, 2006. ISSN 03767388. doi: 10.1016/j.memsci.2005.10.039.

[109] A. Sonune and R. Ghate. Developments in wastewater treatment methods. *Desalination*, 167:55–63, 2004. doi: 10.1016/j.desal.2004.06.113. URL www.elsevier.com/locate/desal.

[110] S. A. Sundet. Morphology of the rejecting surface of aromatic polyamide membranes for desalination. *Journal of Membrane Science*, 76(2-3):175–183, 1993. ISSN 03767388. doi: 10.1016/0376-7388(93)85215-I.

[111] Surface Measurement Systems. DVS Intrinsic operation manual Revision 1.1. Technical Report July, 2004.

[112] Y. Suzuki, Y. Koyano, and M. Nagaoka. Influence of monomer mixing ratio on membrane nanostructure in interfacial polycondensation: Application of hybrid MC/MD reaction method with minimum bond convention. *The Journal of Physical Chemistry B*, 119(22):6776–6785, jun 2015. doi: 10.1021/jp512333h.

[113] M. Taheran, S. K. Brar, M. Verma, R. Y. Surampalli, T. C. Zhang, and J. R. Valero. Membrane processes for removal of pharmaceutically active compounds (PhACs) from water and wastewaters. *Science of the Total Environment*, 547:60–77, mar 2016. ISSN 18791026. doi: 10.1016/j.scitotenv.2015.12.139.

[114] C. Tang, Y. Kwon, and J. Leckie. Probing the nano- and micro-scales of reverse osmosis membranes—A comprehensive characterization of physiochemical properties of uncoated and coated membranes by XPS, TEM, ATR-FTIR, and streaming potential measurements. *Journal of Membrane Science*, 287(1):146–156, jan 2007. ISSN 03767388. doi: 10.1016/j.memsci.2006.10.038. URL `https://linkinghub.elsevier.com/retrieve/pii/S0376738806007083`.

[115] C. Y. Tang, Y. N. Kwon, and J. O. Leckie. Effect of membrane chemistry and coating layer on physiochemical properties of thin film composite polyamide RO and NF membranes. I. FTIR and XPS characterization of polyamide and coating layer chemistry. *Desalination*, 242(1-3):149–167, 2009. ISSN 00119164. doi: 10.1016/j.desal.2008.04.003.

[116] D. W. Van Krevelen and K. Te Nijenhuis. *Properties of polymers: their correlation with chemical structure; their numerical estimation and prediction from additive group contributions*. Elsevier, Amsterdam, the Netherlands, 2009. ISBN 9780080548197. doi: 10.1016/B978-0-08-054819-7.X0001-5.

[117] C. J. Vörösmarty, P. Green, J. Salisbury, and B. Richard. Global Water Resources: Vulnerability from Climate Change and Population Growth. *Science*, 289(5477):284–288, 2000. doi: 10.1126/science.289.5477.284.

[118] T. Wei, L. Zhang, H. Zhao, H. Ma, M. S. J. Sajib, H. Jiang, and S. Murad. Aromatic Polyamide Reverse-Osmosis Membrane: An Atomistic Molecular Dynamics Simulation. *The Journal of Physical Chemistry B*, 120(39):10311–10318, oct 2016. doi: 10.1021/acs.jpcb.6b06560.

[119] J. G. Wijmans and R. W. Baker. The solution-diffusion model: a review. *Journal of Membrane Science*, 107:1–21, 1995. doi: 10.1016/0376-7388(95)00102-I.

[120] L. Woodcock. Isothermal molecular dynamics calculations for liquid salts. *Chemical Physics Letters*, 10 (3):257–261, aug 1971. ISSN 00092614. doi: 10.1016/0009-2614(71)80281-6. URL `https://linkinghub.elsevier.com/retrieve/pii/0009261471802816`.

[121] Y. Xiang, Y. Liu, B. Mi, and Y. Leng. Hydrated Polyamide Membrane and Its Interaction with Alginate: A Molecular Dynamics Study. *Langmuir*, 29(37):11600–11608, sep 2013. ISSN 0743-7463. doi: 10.1021/la401442r. URL `https://pubs.acs.org/doi/10.1021/la401442r`.

[122] Y. Xiang, Y. Liu, B. Mi, and Y. Leng. Molecular Dynamics Simulations of Polyamide Membrane, Calcium Alginate Gel, and Their Interactions in Aqueous Solution. *Langmuir*, 30(30):9098–9106, aug 2014. ISSN 0743-7463. doi: 10.1021/la501811d. URL `https://pubs.acs.org/doi/10.1021/la501811d`.

[123] J. Xu, H. Yan, Y. Zhang, G. Pan, and Y. Liu. The morphology of fully-aromatic polyamide separation layer and its relationship with separation performance of TFC membranes. *Journal of Membrane Science*, 541:174–188, 2017. ISSN 18733123. doi: 10.1016/j.memsci.2017.06.057.

[124] H. Yan, X. Miao, J. Xu, G. Pan, Y. Zhang, Y. Shi, M. Guo, and Y. Liu. The porous structure of the fully-aromatic polyamide film in reverse osmosis membranes. *Journal of Membrane Science*, 475:504–510, 2015. ISSN 18733123. doi: 10.1016/j.memsci.2014.10.052.

[125] Y. Yoon and R. M. Lueptow. Removal of organic contaminants by RO and NF membranes. *Journal of Membrane Science*, 261(1-2):76–86, sep 2005. ISSN 03767388. doi: 10.1016/j.memsci.2005.03.038.

[126] Q. Zhang, Z. Zhang, L. Dai, H. Wang, S. Li, and S. Zhang. Novel insights into the interplay between support and active layer in the thin film composite polyamide membranes. *Journal of Membrane Science*, 537:372–383, 2017. ISSN 18733123. doi: 10.1016/j.memsci.2017.05.033.

[127] X. Zhang, D. G. Cahill, O. Coronell, and B. J. Mariñas. Absorption of water in the active layer of reverse osmosis membranes. *Journal of Membrane Science*, 331(1-2):143–151, 2009. ISSN 03767388. doi: 10.1016/j.memsci.2009.01.027.

[128] B. H. Zimm. Simplified relation between thermodynamics and molecular distribution functions for a mixture. *The Journal of Chemical Physics*, 21(5):934–935, 1953. ISSN 00219606. doi: 10.1063/1.1699065.

[129] B. H. Zimm and J. L. Lundberg. Sorption of vapors by high polymers. *The Journal of Physical Chemistry*, 60(4):425–428, 1956. doi: 10.1021/j150538a010.

université PARIS-SACLAY

ÉCOLE DOCTORALE
Agriculture, alimentation, biologie, environnement, santé (ABIES)

Titre : Caractérisation de la structure et modélisation moléculaire de la couche active en polyamide aromatique des membranes d'osmose inverse

Mots clés : Polyamide aromatique, Caractérisation structurale, Sorption d'eau, Modélisation moléculaire

Résumé : Les procédés de filtration tangentielle tel que l'osmose inverse (OI) sont largement utilisés dans le traitement d'effluents industriels et leur recyclage. Mais leurs performances sont difficiles à prévoir, en particulier pour les petits solutes organiques. Ici, des approches expérimentale et de modélisation moléculaire ont été combinées pour aider à la comprehension à l'échelle moléculaire des transferts dans la couche sélective en polyamide aromatique réticulé de ces membranes. Des modèles moléculaires de ce polymère ont été construits par dynamique moléculaire mimant différentes conditions de synthèse. Leurs isothermes de sorption et leur gonflement ont été étudiés par simulation Monte Carlo dans l'ensemble osmotique. En parallèle une membrane commerciale et des échantillons synthétisés à différentes temperatures ont été étudiés (épaisseur, taux de vides, composition chimique, densité, sorption d'eau). Les résultats confirment l'intérêt de la modélisation moléculaire dans ce domaine.

Title: Structural characterization and molecular modeling of the active aromatic polyamide layer in reverse-osmosis membranes

Keywords: Aromatic polyamide, Structural characterization, Water sorption, Molecular modeling

Abstract: Pressure driven filtration processes such as reverse osmosis (RO) are widely used for cleaner industrial processes, but their separation performances are difficult to forecast as far as small organic solutes are concerned. In this work, a chemical engineering approach was combined with a molecular modeling one in order to improve transfer understanding at molecular level through the selective layer of RO membranes (fully aromatic polyamide). Molecular models of the polymer were built by molecular dynamics mimicking different synthesis conditions. Water sorption and swelling were investigated using Monte Carlo method in the osmotic ensemble. Simultaneously, experimental reference data (thickness, void fraction, composition, density, water sorption) on a standard commercial membrane, as well as on free-standing samples synthesized at different temperatures, were obtained. Results confirm the interest of molecular modeling in this field.

Maison du doctorat de l'Université Paris-Saclay
2ème étage aile ouest, Ecole normale supérieure Paris-Saclay
4 avenue des Sciences,
91190 Gif sur Yvette, France